Dissertation

submitted to the

Combined Faculties for the Natural Sciences and for Mathematics

of the Ruperto–Carola University of Heidelberg, Germany

for the degree of

Doctor of Natural Sciences

presented by

Dipl.-Phys. Marco Wilzbach

born in: Frankfurt/Main, Germany

Oral examination: July 4$^{\text{th}}$ 2007

Single atom detection on an atom chip with integrated optics

Referees: Prof. Dr. Jörg Schmiedmayer
Prof. Dr. Joachim Ullrich

Zusammenfassung

Nachweis einzelner Atome auf einem Atomchip mittels integrierter Optik

Gegenstand dieser Arbeit ist die Miniaturisierung und Integration von Detektoren für den Nachweis einzelner Rubidiumatome auf einem Atomchip. Zu diesem Zweck wurden drei verschiedene Detektoren für den Atomnachweis mittels Absorption und Fluoreszenz entwickelt: i) Ein Fluoreszenzdetektor wurde mittels einer fokussierenden Linsenfaser senkrecht zu einer Sammelfaser realisiert. ii) Ein Absoptionsdetektor wurde gebaut, indem eine fokussierende Linsenfaser gegenüber einer Multimodefaser platziert wurde. iii) Ein durchstimmbarer Resonatordetektor wurde aus zwei auf der Atomchipoberfläche befestigten Singlemodefasern aufgebaut. Um die Detektoren auf der ebenen Fläche des Atomchips positionieren zu können, wurde unter Verwendung lithographischer Verfahren eine Haltestruktur entwickelt. Diese Strukturen erlauben eine sehr genaue und stabile passive Positionierung der Fasern. Um die Detektoren im Einzelnen zu testen wurde ein thermisches Ensemble von Rubidiumatomen in einer magneto-optischen Falle präpariert. Danach wurden die Atome in die magnetischen Mikrofallen des Atomchips transferiert und zu einem der Detektoren geleitet. Jeder integrierte Detektor wurde durch verschiedene Messungen bewertet. Von diesen Detektoren erreichte der Fluoreszenzdetektor mit 54% die höchste Effizienz für den Nachweis einzelner Atome. Dadurch war es möglich Messungen der magnetisch geführten Atome auf dem Niveau einzelner Atome durchzuführen und die fundamentalen Eigenschaften der eingeschlossenen Atome zu studieren.

Abstract

Single atom detection on an atom chip with integrated optics

The subject of this thesis is the miniaturization and integration of detectors for the detection of single rubidium atoms on an atom chip. For this purpose three different detectors were developed for atom detection by absorption or fluorescence: i) A fluorescence detector was realized by mounting a tapered lensed fiber perpendicular to a collection fiber. ii) An absorption detector was built by placing a multi-mode fiber in-line with a tapered lensed fiber. iii) A tunable cavity detector was built from two single mode fibers mounted on the chip surface. To mount the detectors on the planar surface of the atom chip retaining structures by means of lithographical techniques were developed. Those structures allow a very accurate and stable passive fiber alignment. To test the individual detectors an atomic ensemble of thermal rubidium atoms was prepared in a magneto-optical trap. Then the atoms were transferred into magnetic micro-traps of the atom chip and were guided to one of the detectors. Each integrated detector has been evaluated by several characterization measurements. With the fluorescence detector the highest single atom detection efficiency of 54% was attained. Thereby it was possible to perform quantitative measurements for the magnetically guided atoms on a single atom level and to study fundamental properties of the confined atoms.

Stets findet Überraschung statt
Da, wo man's nicht erwartet hat.
Wilhelm Busch

Contents

Part I

Introduction

1 Introduction and Motivation

1.1 Introduction

Detecting single neutral atoms state selectively is one of the essential ingredients for developing atomic physics based quantum technologies, and a prerequisite of most quantum information experiments. The key question to be answered is how to perform such measurements using a robust and scalable technology. Ultra-cold atoms can be trapped and manipulated using miniaturized atom chips (Folman et al., 2002).

On an atom chip micro fabricated wires and electrodes generate magnetic and electric fields that can be used to trap and manipulate neutral atoms (Folman et al., 2002, Henkel et al., 2005). The atoms are trapped a few micrometers above the chip surface with high precision and well defined positions. Many components for integrated matter wave technology have been demonstrated. Examples are atom guides (Folman et al., 2000), combined magnetic/electrostatic traps of various geometries (Krüger et al., 2003), motors and shift registers (Hänsel et al., 2001b), atomic beam splitters (Cassettari et al., 2000, Hommelhoff et al., 2005, Müller et al., 2000, Schumm et al., 2005), and Bose-Einstein condensation (BEC) in micro traps (Hänsel et al., 2001a, Ott et al., 2001, Schneider et al., 2003).

Integration of the detection optics on the atom chip is a natural development for integrated matter wave manipulation. Using macroscopically sized detectors, state sensitive detection with near unity efficiency has been realized (Pinkse et al., 2000). Miniaturizing and integrating these highly sophisticated and efficient detectors is essential for further development but is also a difficult challenge.

The scope of this thesis is to explore how one can use the techniques of integrated miniaturized optics for atom detection as proposed in (Eriksson et al., 2005, Horak et al., 2003, Lev et al., 2004, Long et al., 2003, Rosenblit et al., 2004, Wilzbach et al., 2004, 2006) and how to adapt and implement real world devices to the atom chip and to on-chip atom detection. The manufacturing and characterization of miniaturized optics for atom detection on an atom chip will be presented. Three different miniaturized detectors were developed and integrated on an atom chip.

In chapters 2 through 7 the experimental setup will be presented. Measurements characterizing the different integrated detectors using cold rubidium atoms will be given in chapters 9 through 11. The following sections will give a brief introduction on the basic theory on atom detection.

1.2 Detecting single atoms

Single charged particles can be detected through their direct electric interaction with their environment. Neutral atoms however interact rather weakly with the environment. The

coupling of electromagnetic radiation to the atom is characterized by the scattering cross section σ_{scat}

$$\sigma_{\text{scat}} = \frac{\sigma_{\text{abs}}}{1+4\Delta^2}, \tag{1.1}$$

where $\sigma_{\text{abs}} = 3\lambda^2/2\pi$ is the resonant scattering cross section [1] and Δ the normalized detuning given by $\Delta = \frac{\omega-\omega_0}{\Gamma}$. Γ is the atomic line width. The real part of the refractive index results in a phase shift ϕ of the light field. For far off-resonant light fields this becomes

$$\phi = \frac{n_{\text{at}}\sigma_{\text{abs}}}{4\Delta}, \tag{1.2}$$

where n_{at} is the atomic column density. Atoms can be detected by monitoring the fluorescence, absorption, or the imprinted phase shift on a probe light. The efficiency of the detection depends on the coupling strength between the atom and the light, so it is of significant interest to optimize the atom-photon interaction. This requires a high degree of control over the optical fields as well as the dynamics of the atom.

The following restriction will be used in the further context

$$n_{\text{at}}\sigma_{\text{abs}} \ll 1. \tag{1.3}$$

This is the case for detection of small atom numbers and for resonant scattering below atomic saturation.

1.2.1 Measuring the scattered light: Fluorescence Detection

One way of detecting an atom is to observe its fluorescence. The basic idea is to drive a transition of the atom to an excited state with an external light field and to detect the spontaneously emitted photons. In principle one scattered photon is sufficient to detect a single atom. The sensitivity of the detection and its fidelity depend on the detection efficiency of the scattered light and the suppression of background noise.

Modern photo detectors have a near unity efficiency, and atom detection is limited by the amount of light collected. Therefore high numerical aperture collection optics is desirable. In a realistic setting the collection efficiency η_{coll} is much less than unity and it is essential to let each atom scatter many photons. This is best achieved by driving closed transitions. Using a model of a two-level atom with a small number of excitations, the signal to noise ratio for single atom detection using an analog detector is given by:

$$\text{SNR}_{\text{fl}} = \frac{n_{\text{atom}}}{\sqrt{n_{\text{atom}}+n_{\text{background}}}} \tag{1.4}$$

$$= \sqrt{\frac{\eta_{\text{coll}}\sigma_{abs}j_{in}\tau}{A}}\frac{1}{\sqrt{1+f_{\text{b}}A/\sigma_{abs}}}, \tag{1.5}$$

where τ is the measurement time and j_{in} is introduced as the incoming photon flux ($j_{\text{in}} = A\ I_{\text{in}}$). The number of collected fluorescence photons is assumed to be $n_{\text{atom}} =$

[1] For the D2 line of rubidium the on resonant scattering cross section for a cycling transition ($m_F = \pm 2 \rightarrow m'_F = \pm 3$) is given by $\sigma_{\text{abs}}^{\text{Rb}} = 0.29\ \mu\text{m}^2$.

$\eta_{\mathrm{coll}} j_{\mathrm{in}} \tau \sigma_{\mathrm{abs}}/A \gg 1$. f_{b} is the fraction of incoming light which is scattered by anything else in the beam and collected by the fluorescence detector. A is the size of the detection region imaged on the detector, with a total background of $n_{\mathrm{background}} = \eta_{\mathrm{coll}} f_{\mathrm{b}} j_{in} \tau$.

In principle, there is no fundamental limit to the efficiency of a fluorescence detector as long as the atom is not lost from the observation region. For trapped ions it is possible to reach very high detection fidelities (Leibfried et al., 2004). Detection of cold single neutral atoms has been demonstrated in many experiments. For instance, up to 20 atoms trapped in a magneto-optical trap can be counted with a bandwidth of 100 Hz (Miroshnyenko et al., 2003).

The disadvantage of fluorescence detection is the destructive nature of the process. The internal state of the detected atom will be altered, and heating of atoms due to spontaneous emission is almost unavoidable.

1.2.2 Measuring the driving field

While fluorescence detection uses the spontaneously emitted light, the presence of an atom will also influence the driving field. This is described by the susceptibility of the atom. The imaginary part of the susceptibility describes the absorption, and the real part the phase shift on the driving field. By measurements on the driving field a complete atomic signature can be collected.

Absorption on resonance

The atomic density can be measured by monitoring the attenuation of the driving field. In the unsaturated case, this situation is described by Lambert-Beers law. The transmitted light intensity is given by:

$$\frac{I_{\mathrm{trans}}}{I_{\mathrm{in}}} = \exp(-n_{\mathrm{at}}\sigma_{\mathrm{abs}}) \sim 1 - n_{\mathrm{at}}\sigma_{\mathrm{abs}}. \tag{1.6}$$

The absorption signal of Eq. 1.6 provides a direct measure of the atomic column density. For on resonant excitation on the D2 line of rubidium a column density of one atom per µm^2 leads to about 30% absorption. If the mean intensity of the incoming beam is known, the main uncertainty is determined by measuring the transmitted light (due to its fluctuations). The signal-to-noise ratio for an absorption measurement is

$$\begin{aligned} \mathrm{SNR}_{\mathrm{abs}} &= \sqrt{j_{\mathrm{in}}\tau}\frac{1-\exp(-n_{\mathrm{at}}\sigma_{\mathrm{abs}})}{\sqrt{\exp(-n_{\mathrm{at}}\sigma_{\mathrm{abs}})}} \\ &\approx \sqrt{j_{\mathrm{in}}\tau} n_{\mathrm{at}}\sigma_{\mathrm{abs}} \sim \sqrt{N_{\mathrm{abs}} n_{\mathrm{at}}\sigma_{\mathrm{abs}}}, \end{aligned} \tag{1.7}$$

where $N_{\mathrm{abs}} = j_{\mathrm{in}}\tau n_{\mathrm{at}}\sigma_{\mathrm{abs}}$. The minimum number n_{min} of atoms that can be detected with a $\mathrm{SNR}_{\mathrm{abs}} = 1$ is then given by:

$$n_{\mathrm{min}} = \frac{A}{\sigma_{\mathrm{abs}}}\frac{1}{\sqrt{j_{\mathrm{in}}\tau}} = \frac{1}{\sigma_{\mathrm{abs}}}\sqrt{\frac{\mathrm{A}}{I_{\mathrm{in}}\tau}}. \tag{1.8}$$

Equation 1.7 assumes that the mean incident photon flux is known to high precision. In absorption imaging it is common practice to relate the absorption of the atoms to a

reference image by dividing the two images. Then the noise of the reference image has to be fully considered. For small absorption, the signal-to-noise ratio of Eq. 1.7 is reduced by a factor $1/\sqrt{2}$. This increases the necessary minimum number of detectable atoms by a factor $\sqrt{2}$.

To reach unity detection efficiency in absorption imaging it seems natural to reduce the beam waist as much as possible as indicated by Eq. 1.8. This is however not a successful strategy[2] as pointed out by van Enk (2004), van Enk and Kimble (2000, 2001).

Another strategy to improve the sensitivity is to increase the measurement time. The scattered photons will however heat up the atoms and expel them from the observation window. If the atom is trapped by a dipole trap, the measurement time can be increased significantly (See section 6.3.1). There is no fundamental limit to the detection efficiency of a single atom via absorption, if it can be kept localized long enough.

Refraction

For large detunings ($\Delta \gg 1$) the absorption decreases as $\propto \Delta^{-2}$ as can be seen from Eq. 1.1. In addition the transmitted beam acquires a phase shift ϕ_{atom}. This is caused by the refractive index of the atoms. The phase shift decreases only with $\phi_{\mathrm{atom}} \propto \Delta^{-1}$ as shown by Eq. 1.2. The phase-shift has been used to image clouds of cold atoms and include Mach-Zehnder type interferometers (Kadlecek et al., 2001), for phase-contrast imaging (Andrews et al., 1996), or in line holography by de-focussed imaging (Turner et al., 2004).

The minimal detectable phase shift $\Delta\phi$ in an interferometer is given by the number / phase uncertainty relation $\Delta\phi\Delta N = 1$ resulting in $\Delta\phi_{\mathrm{min}} = 1/\sqrt{j_{\mathrm{in}}\tau}$ (neglecting absorption). From these scaling laws for the scattered light and the phase shift one finds for the signal-to-noise ratio for dispersive atom detection:

$$\mathrm{SNR}_{\mathrm{disp}} = \frac{\phi}{\Delta\phi} \sim \sqrt{N_{\mathrm{scat}} n_{\mathrm{at}} \sigma_{\mathrm{abs}}}, \tag{1.9}$$

with $N_{\mathrm{scat}} = j_{\mathrm{in}}\tau n_{\mathrm{at}}\sigma_{\mathrm{scat}}$. $\mathrm{SNR}_{\mathrm{disp}}$ depends only on the total number of scattered photons N_{scat}. In fact it is the same as for on resonant detection, and the optimal achievable SNR for classical light as shown by Hope and Close (2004a,b), Lye et al. (2004). Going off resonance does not help in obtaining a better measurement compared to plain absorption.

The off-resonant detection of atoms however has significant advantages in combination with cavities (Hope and Close, 2004a). Non-destructive and shot noise limited detection becomes possible.

1.2.3 Cavities

Cavities enhance the interaction between the light and atoms. The photons are given multiple chances to interact with an atom located in the cavity. The number of interactions is increased by the number of round trips. The latter is determined by the cavity finesse $n_{\mathrm{rt}} = \mathcal{F}/2\pi$. This can be used to improve the signal-to-noise ratios. Even with moderate finesse cavities single atom detection can be achieved.

[2] A strongly focused beam is not optimally overlapped with the radiation pattern of the atoms. The absorption cross section for such a strongly focused beam becomes smaller with a decreased spot size.

Absorption on resonance

The probability for absorption during each round trip is determined by the ratio between the atomic absorption cross section $\sigma_{\mathrm{abs}} = 3\lambda^2/2\pi$ and the beam cross section inside the cavity $A = \frac{\pi}{4}w_0^2$. A natural figure of merit for cavity assisted absorption is therefore

$$C_1 = \frac{\mathcal{F}}{2\pi}\frac{\sigma_{\mathrm{abs}}}{A} = \frac{3\lambda^2}{\pi^3}\frac{\mathcal{F}}{w_0^2}. \tag{1.10}$$

This quantity is identical to the cooperativity parameter $C_1 = g_0^2/2\kappa\Gamma$ (Berman, 1994), which relates the single photon Rabi frequency of the atom-photon system g_0 to the incoherent decay rates of the cavity field κ and atomic excitation Γ. Interestingly, a reduced cavity mode waist can compensate for a small cavity finesse (Horak et al., 2003).

When the cooperativity parameter is smaller than unity and the atomic saturation is low, the signal-to-noise ratio for shot-noise limited single atom detection becomes

$$\mathrm{SNR} = \sqrt{j_{\mathrm{in}}\tau}\frac{\kappa_T}{\kappa}C_1 = \frac{3\lambda^2}{\pi^3}\sqrt{j_{\mathrm{in}}\tau}\frac{\kappa_T}{\kappa}\frac{\mathcal{F}}{w_0^2} \sim \sqrt{\frac{\kappa_T}{\kappa}N_{\mathrm{abs}}^C C_1}, \tag{1.11}$$

where $N_{\mathrm{abs}}^C = j_{\mathrm{in}}\tau\frac{\sigma_{\mathrm{abs}}}{A}\frac{\kappa_T}{\kappa}n_{\mathrm{rt}}$, κ_T is the mirror transmittance rate, and κ the total cavity decay rate (Horak et al., 2003). For a fixed measurement time an increased signal-to-noise ratio can be obtained by increasing the cooperativity parameter. This can be done by increasing the cavity finesse, or by decreasing the beam waist.

Refraction

Similarly, the phase shift induced by the atom in the cavity increases with the each round trip. Accordingly the signal to noise ratio Eq. 1.9 is then increased to

$$\mathrm{SNR} = \sqrt{j_{\mathrm{in}}\tau}\frac{\kappa_T}{\kappa}\frac{C_1}{\Delta} \sim \sqrt{\frac{\kappa_T}{\kappa}N_{\mathrm{scat}}^C C_1} \sim \sqrt{\frac{\kappa_T}{\kappa}N_{\mathrm{abs}}^C C_1}/\Delta, \tag{1.12}$$

where $N_{\mathrm{scat}}^C = j_{\mathrm{in}}\tau\frac{\sigma_{\mathrm{scat}}}{A}\frac{\kappa_T}{\kappa}n_{\mathrm{rt}}$. When the cooperativity parameter is larger than unity, non-destructive detection with low photon scattering becomes possible (Hope and Close, 2004a).

Many atoms in a cavity

These considerations apply to the coupling of a single atom to a cavity. This can be extended to the many-atom case by introducing a many-atom cooperativity parameter $C = N_{\mathrm{eff}}C_1$, where N_{eff} is an effective number of atoms in the cavity mode, which takes into account the spatial dependence of the coupling constant $g(\vec{r}) = g_0\psi(\vec{r})$, given by the cavity mode function $\psi(\vec{r})$, and the atomic density distribution $\rho(\vec{r})$. The fraction N_{eff} of the total atom number N, which are maximally coupled to the cavity mode, is given by the overlap integral of both functions

$$N_{\mathrm{eff}} = N\int d^3r\,\rho(\vec{r})|\psi(\vec{r})|^2. \tag{1.13}$$

The absorptive and dispersive effects of the atoms on the cavity amplitude (Haase, 2005, Horak et al., 2003) scale linearly with this effective atom number as long as the atomic saturation is low.

L	w_0	$\mathcal{F}$	g_0	g_0/Γ	g_0/κ	C_1
[µm]	[µm]		$2\pi\times$[MHz]			
200	30	20000	12	4.0	0.65	1.3
50	7.5	5000	97	32	0.32	5.2
20	5	5000	230	77	0.31	11.8
10	2.5	5000	650	217	0.43	47
10	2.5	1250	650	217	0.11	11.8
10	2.5	250	650	217	0.02	2.3
10^4	2.5	250	21	6.9	0.68	2.3
10^5	2.5	250	6.5	2.2	2.2	2.3
10^5	2.5	50	6.5	2.2	0.43	0.47

Table 1.1: Properties of various cavities as a function of mode geometry and finesse. The cooperativity parameter C_1 stays high if the mode waist is kept small even at moderate cavity finesse. For small mode volumes the single photon Rabi frequency can become very high.

1.2.4 Concentric cavity

As seen above, a small mode diameter w_0 is advantageous. Such a small w_0 can be obtained by using a near-concentric cavity. Consider the case when the cavity is formed by two identical mirrors with radius of curvature R separated by a distance L. The beam waist w_0 in the cavity center is given by

$$w_0^2 = \frac{\lambda}{2\pi}\sqrt{L(2R-L)}. \tag{1.14}$$

The concentric geometry occurs when the mirror separation L approaches the value $2R$. The waist size w_0 becomes small but the beam size on the cavity mirrors

$$w^2 = \frac{R\lambda}{\pi}\sqrt{\frac{L}{2R-L}}, \tag{1.15}$$

becomes large as one approaches the concentric limit. A large mirror spot size requires very uniform mirrors, as deviations from a spherical mirror shape will lower the optical finesse drastically. Furthermore, as the concentric point is approached, the cavity also becomes extremely sensitive to misalignments and vibrations. For more details on cavities see Siegman (1986). An experimental proof of detecting atoms with low finesse cavities and small waist can be found in Haase (2005) and Haase et al. (2006).

1.2.5 Miniaturization

The principle advantage of miniaturizing the cavities is that for a fixed geometry, i.e. for a constant ratio of R and L, the mode diameter scales with the size (see Eq. 1.14 and Eq. 1.15). This automatically increases the cooperativity parameter. In fact C_1 scales like $C_1 \propto w_0^{-2}$ and high values for C_1 can be reached even for moderate finesse as illustrated in Table. 1.1. Miniaturization allows to build cavities with a very small mode volume $V_m = \int d^3\vec{r}|\psi(\vec{r})|^2$. A small cavity volume has the advantage that photons will interact more strongly with atoms localized inside the cavity as the light intensity per

photon increases. The interaction between the photon and the atom is described by the atom-photon coupling constant (single photon Rabi frequency) $g_0 = \sqrt{3\Gamma c\lambda^2/(4\pi V_m)}$. It determines how much the dressed atomic energy levels inside the cavity are shifted by the presence of a single photon. As g_0 is increased, single atom - single photon coupling becomes feasible if $g_0 \gg (\kappa, \Gamma)$ can be satisfied.

Since for a fixed finesse the cavity line width κ becomes larger with decreasing length L ($\kappa \propto L^{-1}$) the fulfillment of the above condition for strong coupling and CQED does not improve as dramatically as the cooperativity parameter $C_1 \sim w_0^{-2}$. One has $g_0/\Gamma \sim 1/w_0\sqrt{L}$ and $g_0/\kappa \sim \sqrt{L}/w_0$ so the length must be chosen precisely to achieve strong coupling (see Table 1.1). It is however always an advantage to choose w_0 small.

For the detection of atoms the increased cooperativity parameter is the main benefit of miniaturization. Miniaturized cavities with moderate finesse can detect single atoms. Therefore miniaturization is much more beneficial for atom detection than for cavity QED experiments.

Part II

Experimental Setup

2 Overview

The following chapters describe the experimental setup providing the basis for atom detection. First the fundamental theory of magneto-optical and magnetic trapping of neutral atoms is characterized in chapter 3. A brief description how electromagnetic fields can be used to cool and trap neutral atoms is given in section 3.1. Then pure magnetic traps are explained in section 3.2. A short overview over basic magnetic trap geometries are shown as well as some special trap geometries used in the experiment.

Since experiments with magnetic traps need ultra high vacuum (UHV) conditions, the vacuum system and the necessary tools to obtain UHV are explained in chapter 4. For mounting the atom chip in the vacuum chamber, a copper structure called "chip mounting" is fixed to the inner vacuum chamber. Section 4.2 describes this mounting and its functions. The design of the copper structures for creating different magnetic fields and the electrical feedthrough are discussed in detail.

After the basis of trapping and UHV is laid, the laser system is described in chapter 5. The laser system provides the laser light needed for the different aspects of the experiment. The description will be divided into several main parts which are specific to this experiment: magneto-optical trapping, diode laser setup and spectroscopy, the setup to provide the light for the fibre detectors and the imaging system. Moreover the methods to stabilize the lasers frequency are presented in section 5.3. This is essential to match the atomic resonances, which require a relative frequency stability better than 3×10^{-9} for the used wavelength. The basic theory of passively stabilizing the laser with a grating and actively with electronic methods is introduced. The frequency modulation stabilization and the frequency offset stabilization are covered in this section. The electronics were developed during this thesis and are now used by (at least) two groups in quantum optics and cold matter physics.

Chapter 6 is concentrating on the atom chip. The atom chip combines the best of two worlds: Cold atoms, a well controllable quantum system, with the immense technological capabilities of nano-fabrication in microelectronics and micro optics to manipulate quantum states. Through miniaturization, atom chips offer a versatile new technology for implementing quantum optics, quantum measurement and quantum information processing. A short overview over the production of such an atom chip will be presented. The production of the fibre cavity, which is integrated on the chip, will be briefly presented here. In great detail the manufacturing process as well as novel techniques to improve the fiber cavities is described in the diploma theses of Schwarz (2004) and Wicker (2006).

Then the integration of the fibre detectors is described in section 6.4. A novel method of mounting and aligning the fibres on the flat surface of the atom chip is developed. The chapter will conclude with the mounting of the atom chip on the chip mounting and the necessary electrical connections.

Finally in chapter 7 the computer interface is introduced. A brief overview over the computer system and the necessary interfaces to control the experiment will be given.

The following list summarizes the chapters of the experimental setup:

- Trapping atoms (MOT, magn.traps) in chapter 3
- Vacuum system (chamber and chip mounting) in chapter 4
- Laser system (for MOT, probing atoms, imaging) in chapter 5 Means of laser frequency stabilization in section 5.3
- Atom Chip (Atom chip production, integration of fibres, chip bonding and integration on the chip mounting) in chapter 6
- Computer control in chapter 7

3 Trapping atoms

Cooling and trapping neutral atoms with lasers and magnetic fields are the prerequisites for our experiment. The underlying method is based on the interaction of the atoms with the environment via the coupling of electromagnetic radiation. That is why a brief description on how electromagnetic fields can be used to cool and trap neutral atoms will be given. Firstly fundamental details on magneto-optical traps are explained in section 3.1, where the atom-laser interaction and the basic theories are introduced. Finally pure magnetic traps are illustrated in section 3.2. A short overview over basic trap geometries is given as well as some special trap geometries, which are used in the experiment.

3.1 Magneto optical trap - MOT

Trapping neutral atoms in momentum space by optical molasses and by magnetic fields in position space was first accomplished in 1985 in Gaithersburg (USA) (Chu et al., 1985). Simultaneous cooling and trapping was realized 1987 in Bell-Labs (Raab et al., 1987) with a so called magneto-optical trap (MOT). For the experimental realization and the theoretical description the Nobel prize in physics was awarded 1997 to C.Cohen-Tannoudji, S.Chu and W.D.Phillips. Their Nobel lectures (Chu, 1998, Cohen-Tannoudji, 1998, Phillips, 1998) are an excellent source to get an overview over this subject. Since with those type of traps neutral atoms can be cooled down to the µK regime, they are used as a preliminary stage for Bose-Einstein condensates and in 2001 the Nobel prize in physics was awarded to E.Cornell, C.Wieman and W.Ketterle (Ketterle, 2001, Wieman and Cornell, 2002) for the experimental realization. Another complete description of the theory of cooling and trapping neutral atoms with laser light can be found in (Metcalf and van der Straten, 1999).

3.1.1 Atom–Laser interaction

Light pressure To describe the action of laser light onto the movement of atoms, a simple picture of a two level atom is utilized. The lifetime of the excited state is τ and the atom interacts with a monochromatic planar laser wave. The decay rate of the excited state is given as $\Gamma = 1/\tau$. The ratio of the laser intensity I to the saturation intensity I_0 of the atomic transition is given by the resonant saturation parameter $s = I/I_0 = 2\Omega^2/\Gamma^2$. Ω is the Rabi frequency. The laser frequency ω is detuned from the atomic resonance frequency ω_0 by $\delta = \omega - \omega_0$. Since the atom is in general not at rest, the Doppler shift must be considered. In the rest system of the atom the laser frequency is Doppler shifted by $\Delta\omega_D = -\vec{k}\vec{v}$. Each photon in the light field carries the momentum $\hbar k$. Using the rotating-wave and dipole approximation the excitation rate of the atom caused by the

laser field can be written as:

$$\kappa = \frac{\Gamma}{2} \frac{s}{1 + s + \left[\frac{2(\delta - \vec{k}\vec{v})}{\Gamma}\right]^2}. \tag{3.1}$$

When a photon is absorbed the atom gets excited and additionally receives a momentum $\hbar k$. This momentum transfer is directed, since the laser field is unidirectional. When the atom falls back to the ground level it spontaneously emits a photon. This is radiated isotropically and therefore the average momentum transfer is zero The average force acting on the atom is

$$\vec{F} = \hbar\vec{k}\kappa = \hbar\vec{k}\frac{\Gamma}{2} \frac{s}{1 + s + \left[\frac{2(\delta - \vec{k}\vec{v})}{\Gamma}\right]^2}. \tag{3.2}$$

If the laser is red detuned ($\delta < 0$) and the atoms are propagating against the direction of the laser field, a force acting against the direction of motion is the result. For high intensities ($s \gg 1$) the result is a maximal force of $\hbar\vec{k}\frac{\Gamma}{2}$.

3.1.2 Optical molasses

Only from the atomic resonance red detuned laser frequencies will be used in the following. If two counter propagating laser beams with the same frequency, intensity and polarization are considered, then the light forces are compensated only for an atom at rest. The result of an atom moving along one direction of the laser beams is a force. This force is directed against the direction of motion of the atom. Therefore the atom is slowed down (cooled). The force in one dimension is the sum of $F(k)$ and $F(-k)$. This is only valid for small intensities ($s \ll 1$), because only then the stimulated emission can be neglected. For a detuning of $\delta = -\frac{\Gamma}{2}$ and for low intensities the light pressure force of the single lasers can be added up to form the total light force F_{total}:

$$F_{total} = \hbar k \frac{\Gamma}{2} \left[\frac{s}{1 + \left(\frac{2(\delta - |\Delta\omega_D|)}{\Gamma}\right)^2} - \frac{s}{1 + \left(\frac{2(\delta + |\Delta\omega_D|)}{\Gamma}\right)^2} \right]. \tag{3.3}$$

In Fig. 3.1 F_{total} is plotted. The total force slows down the atoms in both directions (along the laser axis). For small velocities of the atom ($v \ll \Gamma/k$) and with

$$\alpha = 2\hbar k^2 \frac{2s(-2\delta/\Gamma)}{\left[1 + (2\delta/\Gamma)^2\right]^2}, \tag{3.4}$$

this can be simplified to a viscous force $F_{total} = -\alpha v$, which is linear in v and acting against the direction of motion of the atom. Due to the Doppler shift a moving atom preferably scatters photons out of the counter propagating laser beam, because it is closer to the atomic resonance. Therefore the velocity is damped. The kinetic energy, which the atom looses in that process can be expressed as a loss rate

$$\left(\frac{d}{dt}E_{kin}\right)_{cool} = \vec{F}_{total}\vec{v} = -\alpha v^2. \tag{3.5}$$

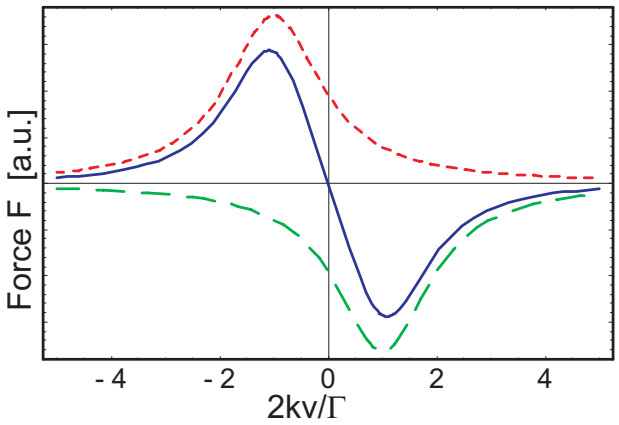

Figure 3.1: Total light force (solid line) acting on an atom as a function of the atom's velocity and a detuning of $2\delta/\Gamma = -1$. The total force is the sum of the forces of the single counter propagating laser beams (dashed lines).

The lasers cool down the atoms, that is why they are called "cooling lasers". When extending this one dimensional treatment to three dimensions it is called optical molasses. The optical molasses encloses the atoms in momentum space only and not in position space. A more detailed theory of optical molasses can be found for example in Lett et al. (1989).

For these considerations only the average light pressure was taken into account, leading to zero velocity and to zero temperature. This non physical state can not be obtained, since the isotropic radiation of the spontaneous emission always transfers a discrete momentum $\hbar k$ on the atom. The result is a kind of Brownian motion in momentum space. The average square of the momentum is not vanishing and counteracts on the cooling. This leads to the Doppler limit (Wineland and Itano, 1979) for a laser detuning of $\delta = -\Gamma/2$:

$$k_B T_{Doppler} = \frac{\hbar\Gamma}{2}. \tag{3.6}$$

For rubidium the Doppler limit is $T_{Doppler} = 141$ µK. But this not the limit of laser cooling. In experiments temperatures way below the Doppler limit have been measured. The abberation can be explained by other effects like the polarization gradient cooling, where temperatures of a few 10 µK can be reached (Dalibard and Cohen-Tannoudji, 1989, Metcalf and van der Straten, 1999).

3.1.3 Magneto-optical trap

Sofar the atoms are only trapped in momentum space, but not in position space. In an optical molasses the movements are damped, but not restricted (in position). Because of the thermal movement, the atoms diffuse.

The energy shift of the atomic states in an external magnetic field (Zeeman effect) can be used to enclose the atoms also in position space. In an external magnetic field the (2F+1) degenerate magnetic levels are split. Taking a two-level atom with the ground state $|g, F = 0\rangle$ ($m_F = 0$) and the excited state $|e, F = 1\rangle$ ($m_F = -1, 0, 1$) in an inhomogeneous magnetic field of the form $B(z) = a \cdot z$, the excited state splits into 3 Zeeman levels. The strength of the splitting depends on the magnetic field and therefore on the position. Only for $z = 0$ there is no splitting, since the field is zero. The resonance frequency for each of the 3 components ($m_F = -1, 0, 1$) for $z \neq 0$ is different and depends on the position. The transition from the ground state to the excited state also depends on the polarization of the light. For an optical transition with $\Delta m_F = -1$ or $\Delta m_F = 0$ or $\Delta m_F = +1$ photons

with the polarization σ^- or π or σ^+ must be absorbed. In Figure 3.2 such a splitting in a magnetic field is shown. This corresponds to a one dimensional magneto-optical trap. Two laser beams are overlapped and have opposite circular polarizations. Both are

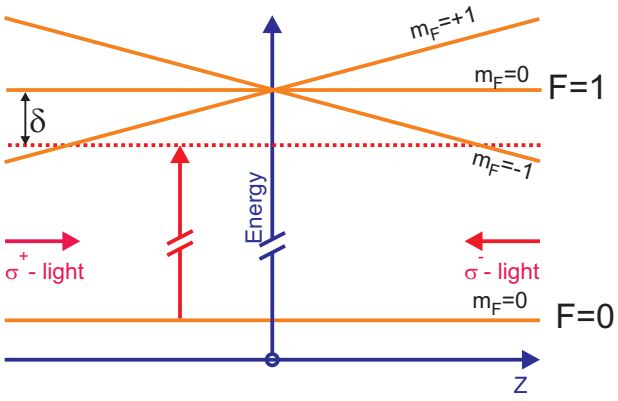

Figure 3.2: One dimensional MOT. The dotted line is a laser red detuned by δ from the field free resonance of the atom at rest. Due to the magnetic field of the form $B(z) = a \cdot z$ the excited states are Zeeman split. For $z > 0$ the atomic transition $|0, 0\rangle \rightarrow |1, -1\rangle$ is closer to resonance to the laser from the right (σ^- light). The laser beam coming from the left (σ^+ light) is further off resonance. Therefore the atom will be pushed into the center, where the magnetic field vanishes.

detuned by $\delta < 0$ from the field free atomic resonance. For $z > 0$ the energy of the state $|F = 1, m_F = -1\rangle$ is lowered and the energy of the state $|F = 1, m_F = +1\rangle$ is raised with respect to the atomic resonance without a magnetic field. If the laser beam polarizations are chosen in such a way, that the beam from the positive z-direction (σ^-) excites the atom into the excited state with $m_F = -1$, then an atom at positions $z > 0$ prefers to scatter photons out of that beam. Therefore a force acts onto the atom, which pushes it into the direction of the magnetic field zero (at $z = 0$). For $z < 0$ the laser beam (σ^+) coming from the negative z-direction is closer to resonance with the excited state $m_F = +1$ and the resulting force moves the atom again into the center. In total one gets a position dependent force, which pushes the atoms into the direction of the vanishing magnetic field ($z = 0$). The atoms are trapped. Additionally to the inclusion in momentum space an inclusion in position space is achieved. Expanding the treatment to 3 dimensions, then for each direction two laser beams are overlapped. A magnetic field similar to $B(z) = a \cdot z$ is a quadrupole field.

3.1.4 Mirror MOT

One speciality is the use of an atom chip, and therefore two of the six laser beams necessary for a MOT are blocked. Nevertheless a MOT can be formed by reflecting two of the six MOT beams under an angle of 45° from the surface. Because of the reflection at the surface (mirror) this type of MOT is called mirror MOT. The principles are the same as for the 6-beam MOT. A more detailed description can be found in Folman et al. (2000), Lee et al. (1996), Reichel et al. (1999).

3.2 Magnetic traps

The first trapping of neutral atoms was accomplished 1985 (Chu et al., 1985). A prerequisite for trapping neutral atoms was the laser cooling. The MOT is used as a preliminary

stage for Bose-Einstein condensates (Ketterle, 2001, Wieman and Cornell, 2002) in pure magnetic traps. In this experiment a BEC was not created. Further pieces of information can be found in Anderson et al. (1995), Bradley et al. (1995), Davis et al.. In the following section the fundamental principles of magnetic trapping of neutral atoms will be discussed.

3.2.1 Magnetic wire traps

The manipulation of neutral atoms by a magnetic field is based upon the interaction of the magnetic dipole moment $\vec{\mu}_{atom}$ of the atom with the magnetic field $\vec{B}$. In an inhomogeneous magnetic field a force $\vec{F} = \vec{\nabla}(\vec{\mu}_{atom} \cdot \vec{B})$ will act on the atom. For the first time this relation was shown 1922 in the experiment of Stern and Gerlach (Stern, 1921, Stern and Gerlach, 1922) by splitting a beam of silver atoms. The measured discrete deflection of the atoms is a result of the quantization of the magnetic moment of the atom $\vec{\mu}_{atom} = m_F g_F \vec{\mu}_B$, where m_F is the magnetic quantum number, g_F the Landee's g-factor for the respective atomic hyperfine level and $\vec{\mu}_B$ the Bohr magneton. This interaction can be used to form magnetic traps for neutral atoms. Many types of magnetic traps exist nowadays (Bergeman et al., 1987, Wieman et al., 1999). One restriction of magnetic traps is the adiabatic constraint. The spin of the atom must be able to follow the magnetic field. This is the case for

$$\frac{\mathrm{d}}{\mathrm{dt}} \frac{\vec{B}}{\left|\vec{B}\right|} < \omega_{Larmor} = \frac{\vec{\mu}_{atom} \cdot \vec{B}}{\hbar}, \tag{3.7}$$

where ω_{Larmor} is the Larmor frequency of the atom in the magnetic field. For an atomic ensemble, whose magnetic levels m_F are statistically distributed two species of atoms can be identified. Depending on the relative orientation of the atomic magnetic moment with respect to the magnetic field, the force is directed to the field maximum ($g_F m_F < 0$) or the field minimum ($g_F m_F > 0$). These two atomic classes are called "high field seekers" and "low field seekers". In this experiment only low field seekers are trapped. As a consequence the atoms must be prepared in a magnetic state with $g_F m_F > 0$ just before magnetic trapping.

Two basic traps will be introduced in the following, the quadrupole trap and the Ioffe-Pritchard trap. After the introduction of these basic traps, planar wire traps will be described.

Quadrupole trap The behavior of the absolute magnetic field close to the center of a magnetic trap can be described in lowest order with a linear or quadratic (harmonic) approximation.

A quadrupole magnetic field is zero ($B_0 = 0$) in the center and has a linear field increase in all directions. The simplest realization of a 3 dimensional quadrupole field is with two coaxial coils with counter propagating electric currents (anti Helmholtz configuration). The magnetic field is proportional to

$$\vec{B} \propto \begin{pmatrix} x \\ -2y \\ z \end{pmatrix}. \tag{3.8}$$

The first magnetic storage of neutral atoms was realized in a quadrupole trap (Migdall et al., 1985).

Majorana losses The disadvantage of the quadrupole trap is the vanishing magnetic field at the trap center. The orientation of the field changes faster than the atomic magnetic moment can follow. Therefore the spin of the atom can turn down, the atom is no longer trapped and becomes lost. These losses are called Majorana spin flips. They become important for high trapping frequencies and cold atoms . Further details can be found in Gov et al. (2000), Sukumar and Brink (1997). The losses can be overcome by other trap geometries, like the Ioffe-Pritchard type trap, which will be described in the following.

Ioffe-Pritchard type trap A trap which has similar properties as the quadrupole trap, but with $B_0 > 0$ is the Ioffe-Pritchard type trap. At the trap minimum the Ioffe-trap is harmonic in all directions. This kind of trap for neutral atoms was first proposed and realized by Pritchard (Bagnato et al., 1987, Pritchard, 1983). In most cases the trap is made of four straight wires, which generate a two dimensional quadrupole field. The atoms are therefore confined into the radial direction. For axial confinement two so called pinch coils (with co-propagating currents) are used. The resulting magnetic field has a non zero minimum in the center. The trapping is usually strongly anisotropic, since the longitudinal confinement (parallel to the wires) is much weaker than the transversal (perpendicular to the wires) one. It is convenient to describe the trap by the trap frequencies ω_i of an atom at the trap minimum.

$$\omega_i = \sqrt{\frac{\mu_{atom}}{m_{Rb}} \frac{d^2B}{dx_i^2}}, \tag{3.9}$$

for all the directions $i = x, y, z$ in space.

3.2.2 Basic wire traps

In many experiments the fields for the magnetic traps are created outside the vacuum chamber. The necessary coils and supporting structures become quite large. Another disadvantage of this approach is the lack of spatial resolution and the limit of the achievable field gradients. Consequently the idea was to use microscopic magnetic traps, which are generated by micro-fabricated wires on surfaces which are directly put into the vacuum chamber. Nowadays many groups (Folman et al., 2002) have realized the scheme of an so called atom chip. With this kind of technology the distance of the field generating structures from the trapped atoms can be minimized down to a few microns.

First experiments on the way to miniaturization used free standing wires (Denschlag et al., 1999a,b). Atoms with magnetic states which are attracted by high fields, circled around the wire in stable orbits. Along the direction of the wire however they were free to move.

A next step was to form a trap, which is called side guide. The basic idea is to superpose a magnetic field generated by a wire by an orthogonal (to the wire) homogeneous bias field B_{Bias}. A magnetic minimum is formed aside the wire, and low field seeking atoms can be trapped. This was realized for free standing wires by Denschlag et al. (1999b), Fortagh et al. (1998). Therefore it is also possible to put the wire onto a surface. That has the advantage of robustness and also high flexibility. On surfaces lithographic methods can

be used to define various structures. Integrated planar wire traps mounted on a microfabricated surface have been demonstrated by Dekker et al. (2000), Folman et al. (2000), Müller et al. (1999), Reichel et al. (1999). If a homogeneous field component B_{IP} is added along the wire, the zero field at the trap minimum is removed and the two dimensional quadrupole trap will be harmonic close to the minimum. This type of trap is also called Ioffe-Pritchard type trap. Why the miniaturization is important will be obvious when looking at the scaling laws of such a side guide trap for an infinitesimally long and thin wire. The distance r_0 of the trap minimum to the wire is given as

$$r_0 = \left(\frac{\mu_0}{2\pi}\right)\frac{I_{Wire}}{B_{Bias}}. \tag{3.10}$$

Close to the minimum the gradient is given as

$$\left.\frac{dB}{dr}\right|_{r_0} = \frac{2\pi}{\mu_0}\frac{B_{Bias}^2}{I_{Wire}} = \frac{B_{Bias}}{r_0}. \tag{3.11}$$

To achieve a high gradient only reducing r_0 will be a proper solution. Since the wire has a finite extension the wire extension itself must be minimize too, in order not to hit its surface. The potential around the minimum is harmonic in two directions and the trapped atoms oscillate transversely with the angular frequency

$$\omega_r = \sqrt{\frac{\mu_B g_F m_F}{m_{Rb}}\left(\frac{d^2B}{dr^2}\right)} = \frac{B_{Bias}}{r_0}\sqrt{\frac{\mu_B g_F m_F}{m_{Rb}B_{IP}}}. \tag{3.12}$$

The atoms are trapped in two dimensions only. To trap the atoms in three dimensions the trap has to be closed with endcaps. This can be realized in many different ways. A possible solution is the bending of the wire to form a “U” shape or to create a “Z“ structure. The second realization has the advantage that the field configuration has a minimum different from zero, such that it prevents Majorana losses without the need of an external field along the wire B_{IP}. In the following only the U and Z shaped traps are briefly discussed, since those are the only ones (additionally to the side guide) used in this setup. Both geometries and their potentials are plotted in Fig. 3.3. Further details can be found in Folman et al. (2002), Haase et al. (2001). A nice overview of the properties and the field parameters can be found in Schneider (2003). Those two structures allow to generate a quadrupole and Ioffe trap on an atom chip with one conducting layer only. More sophisticated structures are available, which allow the tailoring of the magnetic potentials. An overview of the production can be found in Groth (2006).

Another special feature of this experiment is the “U”-shaped copper wire beneath the atom chip. Together with an external bias field it is used to form a 3-dimensional quadrupole field. For the creation of a MOT a quadrupole field is necessary. With the “U”-shaped copper wire extra coils outside the vacuum chamber for generating this field become unnecessary. Also the optical access becomes better. A detailed description of this novel method can be found in Becker (2002), Wildermuth et al. (2004).

Finite size effects When the atoms are trapped close to the surface the finite size of the wires must be considered. The above calculations all were done assuming an infinitely thin

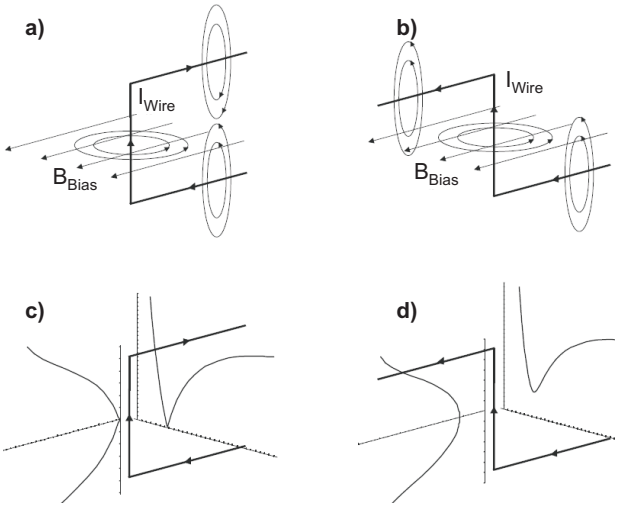

Figure 3.3: **a)** and **b)** show the geometries for the U and the Z trapping wires, the currents I_{Wire} and the bias field B_{Bias}. In **c)** and **d)** the corresponding radial and axial trapping potentials are shown. The "U"-shaped wire creates a field configuration similar to a 3-dimensional quadrupole field with a zero in the trapping center. For a "Z"-shaped wire a Ioffe Pritchard type trap is obtained.

and long wire. But for an infinitely long wire with a cross section of $h \times w$, the magnetic field close to the wire will differ from the magnetic field calculated for an infinitely thin and long wire. The wire is extended in the x-direction from $-w/2$ to $w/2$ and in the z-direction from $-h/2$ to $h/2$ and infinite in the y-direction. With $x_\pm = x \pm w/2$ and $z_\pm = z \pm h/2$ the magnetic field can be calculated analytically:

$$\begin{aligned} B_x(x,y,z,w,h) &= \frac{\mu_0 \cdot I}{4\pi w \cdot h}\left[x_+ \ln\left(\frac{x_+^2+z_-^2}{x_+^2+z_+^2}\right) + x_- \ln\left(\frac{x_-^2+z_+^2}{x_-^2+z_-^2}\right)\right. \\ &\quad +2z_+\left(\arctan\frac{x_-}{z_+} - \arctan\frac{x_+}{z_+}\right) \\ &\quad \left.+2z_-\left(\arctan\frac{x_+}{z_-} - \arctan\frac{x_-}{z_-}\right)\right], \end{aligned} \tag{3.13}$$

$$B_y(x,y,z,w,h) = 0, \tag{3.14}$$

$$B_z(x,y,z,w,h) = -B_x(z,y,x,h,w). \tag{3.15}$$

I is the current and $j = I/(w \cdot h)$ is the current density, which is assumed to be constant over the whole wire. To illustrate the finite size effects, the magnetic potential is plotted in Fig. 3.4 for an infinitely thin wire and for a wire with a cross section of $w \times h = 50 \times 10\ \mu\text{m}^2$. As a rule of thumb one can use an easy relationship. If the formula for the distance for the infinitesimally thin wire yields a trap minimum, which is farther away than the wire is wide, then the relative distance error by using the infinitely thin wire approximation will be smaller than 5%. This may not be valid for all possible geometries, but is correct for the ones used in the current setup. But Eq. 3.13 remains the better choice. For more complicated structures and even smaller distances numerical methods can be utilized. Specific programs are already available, e.g. programs which use a finite element method (FEM) to find the solution for a set of parameters[1].

Influence of gravity In the magnetic traps gravity plays a role. The magnetic trap is modified in one dimension only (in this case into the z-direction). The magnetic trap

[1] e.g. Comsol Multphysics. FEMLAB GmbH, Göttingen, Germany.

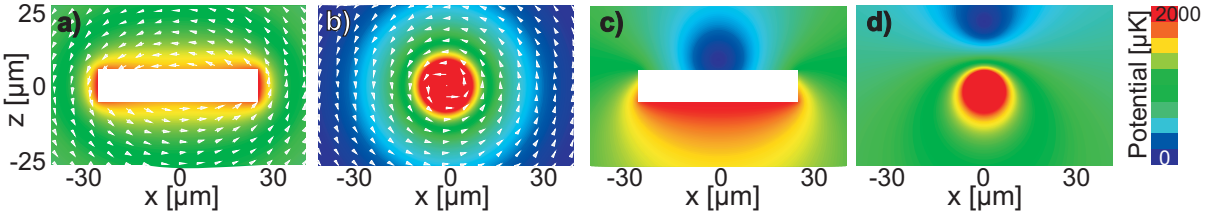

Figure 3.4: The magnetic potential is plotted for an infinitely long wire by a color plot (red: high magnetic potential, dark blue: low magnetic potential). In **a)** the cross section of the wire is 50×10 µm^2. An infinitesimally thin wire is depicted in **b)**. The direction of the field is indicated by arrows. **c)** and **d)** show the magnetic potential additionally with an offset field along the x-axis. The magnetic potential has a minimum above the wires. Due to the finite size effects the minima of the wires are not at the same position. For the broad wire the trap minimum is actually closer to the surface.

minimum is shifted into the direction of gravity. This is usually not a problem, since the vertical trap frequency and the vertical confinement respectively are high/strong enough. The trap gradient is modified by

$$\frac{\mathrm{d}\tilde{B}}{\mathrm{dz}} = \frac{\mathrm{d}B}{\mathrm{dz}} \pm m_{Rb} \cdot g, \tag{3.16}$$

where m_{Rb} is the mass of the rubidium atom and g is the acceleration due to gravity.

4 Vacuum system

4.1 Vacuum chamber

Experiments with magneto-optical and magnetic traps are carried out in an ultra high vacuum (UHV) environment. Since all experiments with magnetic traps are very sensitive to magnetic fields, the main vacuum chamber consists of stainless steal with a low magnetization[1]. It has an octagon shape and an outer diameter of 17 cm. The inner diameter is 11 cm. In Fig. 4.1 a schematic view of the vacuum chamber is shown. The complete technical drawings of the vacuum chamber can be found in appendix D. The

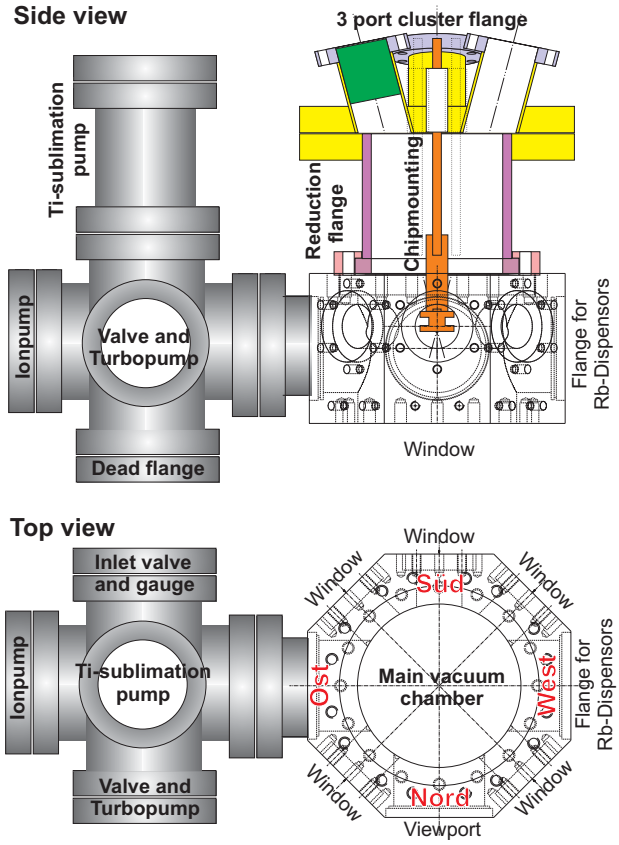

Figure 4.1: Schematic side and top view of the vacuum chamber. The main vacuum chamber is connected to a six-way cross. The six-way cross is linked to the titanium sublimation pump, the ion getter pump, a valve and turbo pump. Another way is connected to the gauge, and is closed with a valve and an inlet valve. Opposite to the titanium sublimation pump one way is blocked with a blind flange. On top of the main vacuum chamber a reduction flange is connected. The reduction flange is connected to a 3-port cluster flange. The 3-port cluster flange holds the chip mounting and has the electrical and optical feedthrough for operating the MOT, chip and fibre detectors.

vacuum chamber is optically accessible through high quality[2] windows. One big window with a free diameter of 11 cm from below and 5 windows with a free diameter of 3 cm

[1] 316LN (1.4429 ESU) and permeability of $\mu_r < 0.005$.

[2] BK7 glass, with a surface roughness better than $\lambda/10$. Also both sides of the windows are coated with an anti-reflecting coating for $\lambda = 780$ nm and angles of 0° to 45° . The coating is from Lens Optics GmbH, Allershausen, Germany.

at the sides of the chamber. These windows are sealed with Helicoflex gasgets[3]. A sixth window on the side is a standard CF63 viewport[4]. Another flange on the side of the vacuum chamber holds two high current feedthroughs, to which two rubidium dispensers[5] are connected from the inside. When sending a current through the dispensers they will heat up and emit rubidium atoms.

The main vacuum chamber is additionally connected to a six-way cross. The six-way cross is linked to the titanium sublimation pump[6], the ion getter pump[7], a valve and a turbo pump[8]. Another way of the cross is connected to the gauge, and is closed with a valve and an inlet valve. Opposite to the titanium sublimation pump one way is blocked with a blind flange.

On top of the vacuum chamber a reduction flange[9] is connected. At the top the reduction flange is linked to a 3 port cluster flange[10]. The 3-port cluster flange holds the chip mounting and has the electrical and optical feedthroughs for operating the MOT, chip and fibre detectors. In the first port a 35x electrical feedthrough[11] for the atom chip and in the second port a 8x electrical feedthrough is integrated. At the third port the flange with the fibre feedthrough is connected. Actually 4 pairs of fibers can be fed into the vacuum chamber. Another 4 high current feedthroughs are welded into the 3 port cluster flange. All the different feedthroughs are summarized in tab. 4.1. The chip mounting in the vacuum is fixed on the 3 port cluster flange. Details on the use of the different feedthroughs and the chip mounting will be given in chapter 4.2. After baking[12] out the

Type	Number of pins	Use
Chip	35	magn. traps and mirror-MOT
Cu-Structures (Z, 2xI)	8	Ioffe trap
Cu-Structures (H)	4	used as “U” for MOT quadrupole field
Dispenser	2	providing rubidium atoms
optical fibers	4x2	connecting fibre detectors

Table 4.1: Summary of the different feedthroughs into the vacuum chamber.

chamber, pressures of $< 1.1 \times 10^{-10}$ mbar are reached. This can be considered ultra high vacuum and is sufficient for laser cooling and magnetic trapping of the rubidium atoms.

Four coils are attached at the sides “West”, “Ost” (WO), “Nord” and “Süd” (NS). One coil is wrapped around the reduction flange (Up-Down). The coils and their strengths are summarized in 4.2. Note that the Up-Down field is generated by one coil only. This leads to a magnetic field gradient. Due to the large diameter of the coil, the gradient is small enough that no disadvantages can be observed during MOT phase.

[3]Type HLV290B, Garlock GmbH, Neuss, Germany.
[4]CF63 viewport, Hositrad Holland B.V., Hoevelaken, The Netherlands.
[5]SAES Getters S.p.A., Milan, Italy.
[6]Mini-Ti Ball, Varian Inc., Torino, Italy.
[7]Vaclon Plus, Varian Inc., Torino, Italy.
[8]Pfeiffer Vacuum GmbH, Asslar, Germany.
[9]DN160CF-DN100CF, Caburn-MDC Europe Ltd., United Kingdom.
[10]CF160-40-3, Caburn-MDC Europe Ltd., United Kingdom.
[11]IFA35, Caburn-MDC Europe Ltd., United Kingdom.
[12]First the chamber was baked out at 200°C. When the chip mounting containing the fibres was built in, the chamber was baked out a second time, but only up to 110°C.

Pair of coils	Strength
Nord-Süd	2.56 G/A
West-Ost	2.87 G/A
Up-Down	1.56 G/A

Table 4.2: List of coils and their magnetic field strengths in Gauss per Ampere.

4.2 Chip mounting

The chip mounting has several functions. The copper structures for creating different fields are included in the chip mounting as well as the necessary electrical connections to provide access to the atom chip from outside the vacuum chamber. Mainly the mounting is set up of rather large copper structures, which are (electrical independently) connected to a common base of the vacuum system. At several positions these copper structures are held together by insulating Shapal pieces. At the top of the chip mounting an insulating Shapal piece is designed to hold the atom chip and provides a stable base for electrically connecting the chip with the electrical wires leading to the outside of the vacuum chamber. In the following the design will be presented in more detail.

The chip mounting is connected at the 3 port cluster flange. It includes the copper structures beneath the chip and the mounting of the chip. The technical drawings are given in appendix C. The 3 port cluster flange holds the copper structures for creating different magnetic fields. The Cu-H structure is connected to 4 high current feedthroughs, the Cu-Z structure to 4 pins of the 8x feedthrough and the 2xCu-I structures to 4 pins of the 8x feedthrough. One port is for 4x2 fiber feedthroughs and one port holds a 35x feedthrough for connections for the chip. The H-structure is used as an "U"-structure to create the quadrupole field for the MOT, the Z- and the two I-structures can be used as a Ioffe-Pritchard trap with a higher trapping volume than the chip-Z trap. One speciality are the fiber feedthroughs. Four (0.32 cm) stainless steel Swagelok[13] connectors are welded into a CF40 flange. A solid cylinder of teflon is machined to match the dimensions of the ferrules that are usually used with the Swagelok. Details on this kind of feedthrough for optical fibers can be found in Abraham and Cornell (1998). Each teflon cylinder has two 300 µm holes in it. Through the holes a fiber (outer coating diameter 250 µm) can be feed through into the vacuum. Then with the Swagelok system the teflon ferrule is compressed and the gaps are closed[14]. The system is compatible with UHV vacuum and pressures below 10^{-10} mbar are reached.

Several images of the chip mounting are shown in Fig. 4.2. On top of the mounting the structures are held together by a copper block and two Shapal[15] blocks. In the upper Shapal block the copper structures and the pins[16] are countersunk. The chip has a free opening of equivalent size in the Shapal block. The depth in the Shapal is 0.65 mm, whereas the thickness of the chip is 0.7 mm. That ensures the right positioning of the chip

[13] Stainless steel fitting SS-2-TA-1. Swagelok company, Solon, Ohio, USA. www.swagelok.com

[14] One ferrule was tested with a fibre and the the Swagelok was tightened up to the block. The fibre did not break and no difference in the transmitted intensity can be measured. Usually closing the Swagelok halfway is enough.

[15] Aluminium nitride, see for example (Goodfellow, 2007) for further physical properties of the material.

[16] Copper-Beryllium was used, since it is harder than pure copper.

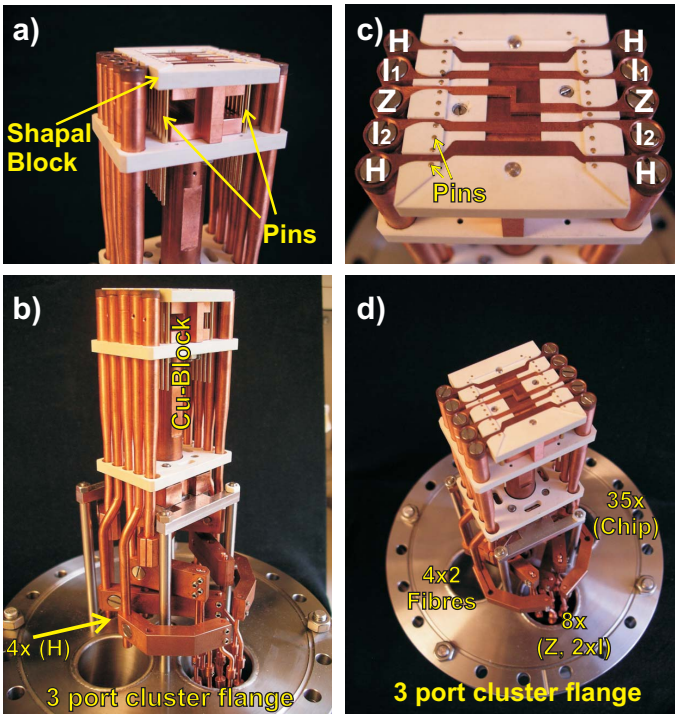

Figure 4.2: Pictures of the chip mounting. The 3 port cluster flange holds the copper structures. The Cu-H structure is connected to 4 high current feedthroughs, the Cu-Z structure to 4 pins of the 8x feedthrough and the 2xCu-I structures to 4 pins of the 8x feedthrough. One port is for 4x2 fiber feedthroughs and one port holds a 35x feedthrough for connections for the chip. On top of the mounting the structures are held together by a copper block and two Shapal blocks. In the upper Shapal the copper structures and the pins are countersunk. The chip has a free opening of equivalent size in the Shapal block. The chip is not yet integrated on the pictures.

in the mounting, which is important to align the copper structures with the chip. Due to the 0.05 mm lower walls of the Shapal the optical access to the chip is not obstructed. The copper block and the Shapal block are used because of their high thermal conductivity[17] to quickly dissipate the heat arising from the Ohmic resistivity of the wires. The pins are connected on their lower part with the 35x feedthrough with copper wires. The head of the pin is used as a bonding pad for the electrical connections to the chip. The heads of the pins are polished[18] to ensure good contact for the bonding wires. With polishing the pins and a stable mounting in the bonding machine[19], it is possible to have >10 bonding wires for each electrical connection to the chip. This is important for obtaining high currents without the risk of burning the small bonding wires.

[17] Shapal has a thermal conductivity of 100 W/m/K.
[18] 0.03 µm polishing paper for optical fibres was used.
[19] Manual bonding station at KIP, University of Heidelberg, 25 µm aluminium bonding wire. Ch1: (PWR 5.3, Time: 5.3), Ch2: (PWR: 5.0, Time: 5.0), bond force 14.8, speed 6.85, loop 13.9, reset 2.85, A-search 12.35, B-search 8.25, tool heat 3.8.

5 Laser system

The laser system provides the laser light needed for the different aspects of the experiment, like for the MOT or probing the atoms. Since ^{87}Rb is used in the experiment, the following sections will be restricted to that isotope, whereupon in general the setup is not restricted to this frequency. The description will be divided into several main parts: magneto-optical trapping, lasers and frequency stabilization, the setup to provide light for the fibre detectors and the imaging system.

5.1 MOT

The MOT is a prerequisite for pure magnetic trapping. The theory for magneto-optical trapping neutral atoms with laser light in general was described in section 3.1. In the following the specific properties of the laser system for magneto-optical trapping of rubidium will be pointed out. For the creation of a magneto-optical trap (MOT) for neutral atoms, a strong atomic transition is needed. The D2-line in Rubidium ($\lambda = 780$ nm) is one of the strongest transitions. The level scheme for ^{87}Rb-D2 is drawn in Fig. 5.1**(a)**. Also the different transitions for operating a MOT are indicated. Two lasers are needed, one "re-pump" laser (Alberto) and one "cooling" laser (Wimp+TA) to confine the atoms in momentum space. The necessary quadrupole field to confine the atoms in position space is provided by a copper-U structure (Wildermuth et al., 2004) beneath the chip (one half of the copper-H was used) and coils attached outside to the chamber.

For laser cooling, for absorption/fluorescence imaging of the atoms with a camera and in most of the cases for the fibre detectors the $5^2S_{1/2}\,|F=2\rangle \rightarrow 5^2P_{3/2}\,|F'=3\rangle$ transition is used. In one out of 1000 cycles the atom can leave this cycling transition and fall to the $5^2S_{1/2}\,|F=1\rangle$ ground state. This state is about 6.8 GHz away, which is not resonant to the cooling laser anymore. To pump back the atom one needs a "re-pump" laser, which is on resonance with the $5^2S_{1/2}\,|F=1\rangle \rightarrow 5^2P_{3/2}\,|F'=2\rangle$ transition. From the $5^2P_{3/2}\,|F'=2\rangle$ the atom can fall back into the $5^2S_{1/2}\,|F=2\rangle$ ground state, where it enters again the cooling cycle.

After the MOT and optical molasses phase the atoms are prepared in the $5^2S_{1/2}\,|F=2, m_F=2\rangle$ ground state. This state is trapped strongest in magnetic traps. A laser (Marcone) is used to provide light for "optically pumping" the atoms via the $5^2S_{1/2}\,|F=2\rangle \rightarrow 5^2P_{3/2}\,|F'=2\rangle$ transition.

For optically trapping, 6 laser beams coming from all 6 directions and intersecting in one point are needed. Since an atom chip is used at the center, a mirror-magneto-optical trap (MMOT) is prepared. This is very common and details can be found in Folman et al. (2000), Lee et al. (1996), Reichel et al. (1999), thus only technical details will be discussed very briefly. The optics for operating the MOT are drawn in Fig. 5.2. The re-pump laser beam is widened by a telescope. Then it hits the atom chip from beneath the chamber

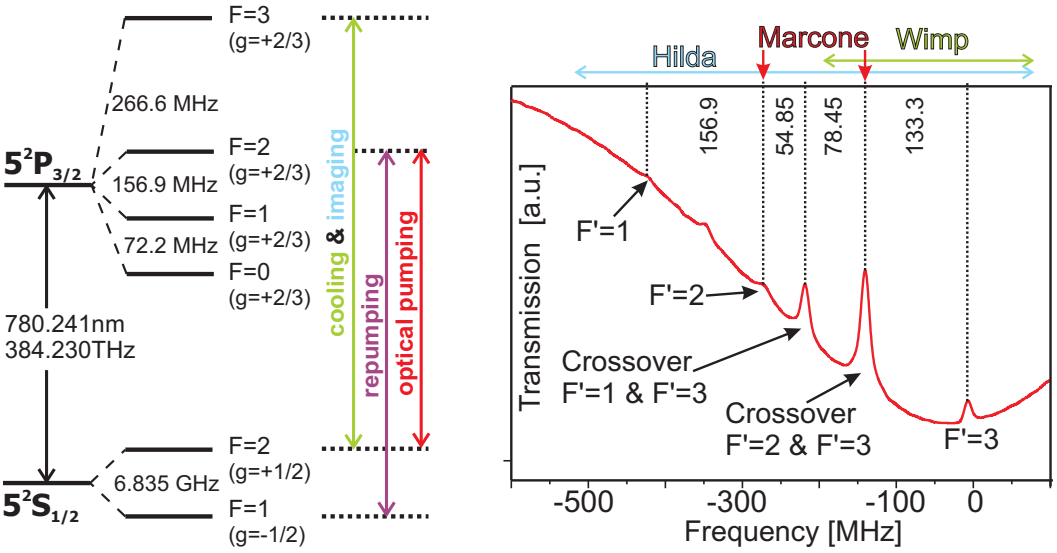

(a) Level scheme of the D2 line in ^{87}Rb. (b) Spectroscopy of the D2 line of ^{87}Rb.

Figure 5.1: **(a)** Relevant level scheme and transitions for ^{87}Rb used in the experiment. The transitions used for laser cooling/imaging, re-pumping and optical pumping are marked. The hyperfine level splitting is taken from Steck (2001). **(b)** Spectroscopy of the $5^2S_{1/2}\,|F=2, m_F\rangle \rightarrow 5^2P_{3/2}\,|F', m'_F\rangle$ line of rubidium in a rubidium spectroscopy cell. The available frequency ranges of the lasers are marked. (The re-pump laser is not shown, since it sits further away.) The complete spectroscopy of the D2 line is given in appendix A.

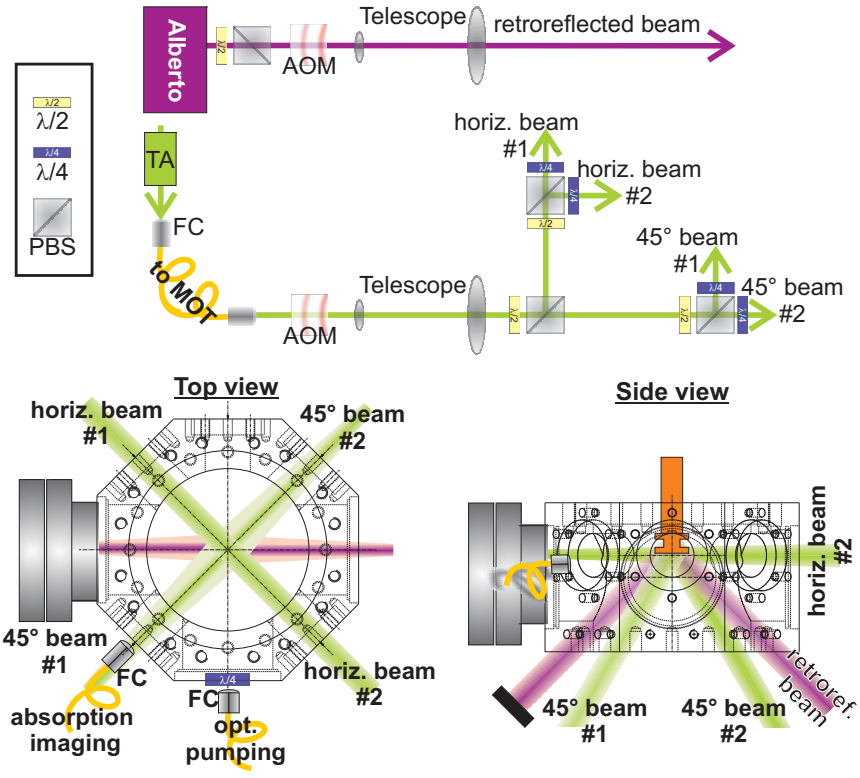

Figure 5.2: Optics for the MOT. Cooling and re-pumping beams are shown. Only optics essential to comprehend the setup are shown at the upper drawing. The beams at the chamber are shown from the side and from the top in the lower part of the drawing. Additionally the fibre couplers for absorption imaging and for optical pumping are indicated in the lower left drawing.

under almost 45°. After leaving the chamber, the beam is retro reflected again. Thus

the re-pump laser beam passes by the atoms 4 times[1]. For the re-pump beam it is not necessary to arrive from all 6 directions. The cooling laser is also widened by a telescope. The beam is then split into 4 beams. Two enter the chamber from the side, two from below under 45°. The beams from below are reflected at the atom chip. Thus "virtually" 6 cooling beams intersect at the atom chip. The beams of the two lasers can be switched by acousto-optic modulators (AOM) and additionally with mechanical shutters[2]. The AOMs[3] receive their RF power from AOM drivers[4], which generate a RF signal. The RF power can be controlled via an analog input. Additionally the RF power can be switched off with a TTL signal.

5.2 Diode lasers

In the experiment only diode lasers are used. Most of them are Rohm[5] laser diodes, which are also used in CD-ROM burners. Except one all lasers are grating stabilized in Littrow configuration. Table 5.1 summarizes the different lasers and their function. Most of them were given "names", to make it easier for the experimentalist to remember. Two lasers are stabilized in frequency via the frequency modulation (FM), and two lasers via the frequency offset (FO) locking technique. For the FO technique a frequency master laser is needed. A heterodyne signal is used to lock the slave laser with a certain frequency offset onto the master laser. With the frequency locks, the frequency stability is better than $\Delta\nu/\nu < 3 \times 10^{-9}$. That corresponds to a line width of ≈ 1 MHz, which is smaller than the natural line width of the D2 line of rubidium ($\Gamma = 2\pi \times 6.0$ MHz). Details on the methods how to lock a laser will be given in section 5.3. Only the two dipole lasers[6] are not locked onto a frequency. Their maximum drifts are smaller than 0.1 nm and no resonance is "close" by.

For magnetically trapping the atoms they are pumped into the $|2, 2\rangle$ state. This is accomplished via shining in σ^+ polarized laser light at the frequency for the $|F = 2, m_F = 2\rangle$ to $|F' = 2, m'_F = 2\rangle$ transition. A small magnetic field is applied to provide the quantization axis. The light is provided by a diode laser (Marcone), which also acts as the frequency master for the probing (Hilda) and master cooling laser (Wimp). The probing laser (Hilda) provides the light for absorption imaging and for the fibre detectors.

The lasers for the magneto-optical trap are the re-pumper (Alberto) and the cooler (Darth) laser. To have more laser power the master cooling laser (Wimp) seeds the tapered amplifier(TA)[7] (Darth). The TA is build by ourselves and details will be given in (Heine,

[1] First on the way to the atom chip, them directly after being reflected at the atom chip and on the way back from the mirror. The beam is "recycled" and higher intensities are reached at the position of the MOT.

[2] Because of the high power cooling laser it is prudent to switch off the AOM first, before closing the shutter. Otherwise the shutter will become a pinhole.

[3] Standard AOMs and some out of laser printers.

[4] Wildsau Lingam Elektonik.

[5] Rohm RLD78PZW2.

[6] The dipole lasers are grating stabilized, thus providing line widths of 1 MHz, but temperature drifts are not compensated. The drifts are smaller than 0.1 nm, thus it was not necessary to lock them.

[7] eagleyard Photonics GmbH, Berlin, GERMANY, Tapered Amplifier EYP-TPA-0780-01000-3006-CMT03-0000.

Name	Type	Function	Locking mode
Marcone	Rohm diode	Frequ. master for FO and opt.pump.	FM
Hilda	Rohm diode	Absorption imaging + fibres	FO
Alberto	Rohm diode	MOT Re-pumper	FM
Wimp	Rohm diode	Master laser for TA(Darth)	FO
TA(Darth)	Tapered Amp.	MOT Cooler	Seeded
Dipole 786nm	Rohm diode	Dipole laser	-
Dipole 840nm	Toptica diode	Dipole laser	-

Table 5.1: Diode lasers used in the experimental setup, their function and method of locking. Marcone provides light for optical pumping the atoms into the $|2,2\rangle$ state for magnetic trapping the atoms. Hilda provides the light for the absorption imaging and for probing the atoms with the fibre detectors. The lasers for the magneto-optical trap are Alberto (repumper) and Wimp+Darth (cooler). Wimp is the master laser for the tapered amplifier(TA) Darth. The TA is seeded with the light coming from Wimp.

2007), who designed it. In terms of power stability, there is no match on the market.

The laser system is shown in figures 5.3 and 5.4 Each laser has its own spectroscopy and

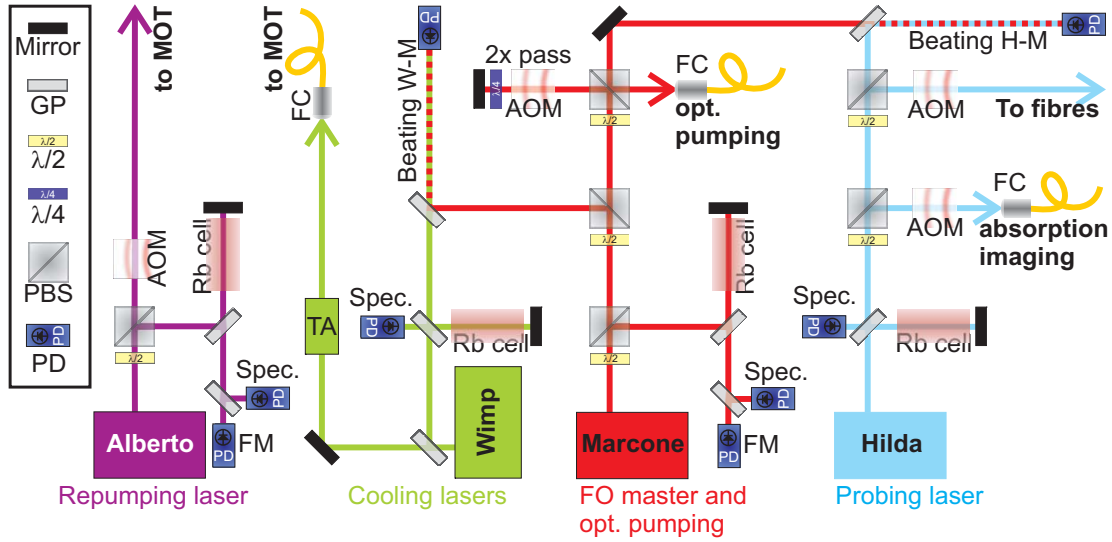

Figure 5.3: Schematic view of the laser system. Most optical components are omitted, like lenses, pinholes, mirrors, when they are not necessary for understanding the setup.

those locked via FM additionally have a fast avalanche photodiode[8]. In the schematics in Fig. 5.3 additional optics are omitted. The optical isolator after each laser diode is not shown, as well as the lenses in front and after the AOM's. Also several mirrors are not shown, like for coupling light into the AOM's or the fiber couplers. All the optics are shown in Fig. 5.4. The cooling laser (TA) is fibre coupled and the re-pump laser (Alberto) is directly pointed to the MOT optical setup. The light for optical pumping and for absorption imaging is fibre coupled. The fibre coupling for those three light sources is

[8]Physikalisches Institut, Universität Heidelberg, V160.

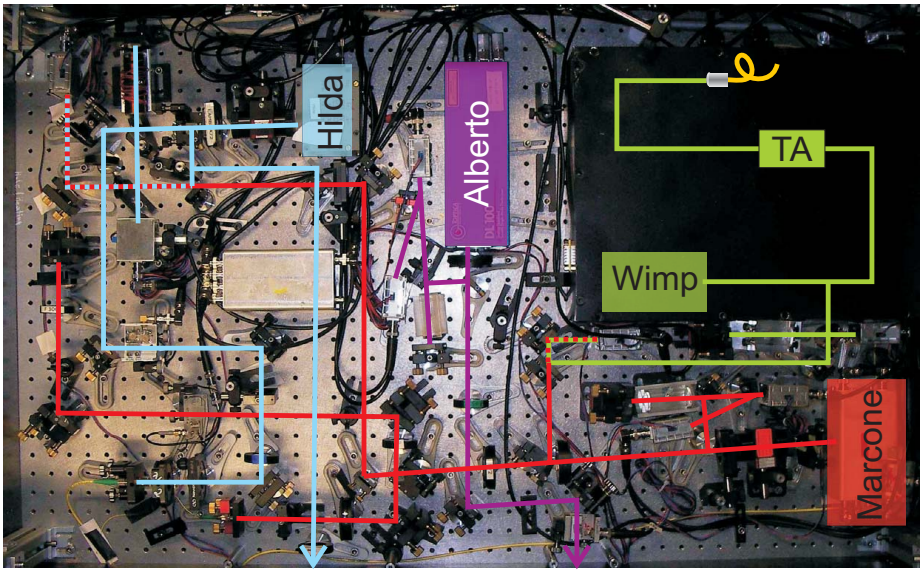

Figure 5.4: Reality looks a "bit different". Picture of the laser setup, with indicated beam paths.

implemented with polarization maintaining (PM) fibres[9]. Additionally all light sources pass through an AOM and a mechanical shutter. This is necessary for switching the light. The AOM can be switched on a µs scale, whereas it takes some milliseconds for the shutter to open/close.

5.3 Means of Laser Frequency Stabilization

To be able to create a MOT or to probe the atoms, the frequency of the used lasers has to be controlled with an accuracy of one MHz. The necessary electronic system for active frequency stabilization of laser diodes was developed during this thesis. Therefore a brief overview of the used laser frequency stabilization will be given.

Grating stabilized Diode Lasers Diode lasers are well suited for frequency stabilization since they are quite sensitive to optical back-reflections (Wieman, 1991). This fact can be exploited via re-coupling a part of the light that is emitted by the laser diode. If a small wavelength band can be selected to be coupled back, then the laser diode will be forced to emit on this wavelength. The laser line width can be reduced with this method from several 100 MHz to several MHz.

One possibility of external back-reflection is the Littrow configuration (Ricci et al., 1995). In this configuration an external holographic reflection grating is used. The zeroth order of the grating is coupled out and can be used for the experiment. The first order is reflected back into the diode (feed back). Via changing the angle of the grating with respect to the diode, the back-reflected wavelength can be selected. Additionally to the narrowing of the line width of the diode, the free running wavelength can be altered by a few nanometers with the grating. For coarse wavelength changes the grating is turned with the mounting.

[9]This makes it necessary to have a $\lambda/2$ wave plate and sometimes a polarizer in front of the fibre coupler.

For small frequency changes of up to 50 GHz an actuator on the back of the grating is used. When turning the grating the diode will not continuously change its wavelength. The frequency can be scanned by typically 5-10 GHz, before "mode-hops" appear (Petermann, 1988). This is usually enough for a stable experiment. Further details on this kind of setup can be found in Wilzbach (2002).

Electronic Stabilization The grating stabilization is usually not enough to keep the laser diode on a constant wavelength. Due to temperature changes, diode current instabilities or aging the wavelength of the diode will drift. To compensate these effects the laser must be stabilized actively. This case is called "locking" the laser onto a frequency. The prerequisite is to measure the actual frequency of the laser. There is a manifold of means to provide the frequency reference. Several methods will be referred to in the following text. For absolute frequency measurements an atomic spectroscopy of the relevant transition can be used. Doppler free saturation spectroscopy (Feld and Letokhov, 1973, Letokhov and Chebotayev, 1977, Shimoda, 1976) gets rid of the broadening effects due to the movement of the thermal atoms in the spectroscopy cell. A typical spectroscopy taken with one of the lasers can be found in appendix A. The frequency reference is not necessarily an atomic transition. As a reference also a cavity or a different laser can be used.

In the following the basics of two important locking techniques will be evaluated. First the frequency modulation (FM) method is introduced. It relies on the Pound-Drever-Hall (PDH) method. The FM method can be used to lock cavities onto lasers or an atomic transition, or lasers onto cavities or atomic transitions (Black, 2001, Drever et al., 1983).

The basic principle underlying the FM method is that the laser is modulated in frequency (in the order of several MHz). This can be accomplished by external devices (e.g. with electro-optical modulators) or in the case of a diode laser by modulating the current of the diode with a RF signal. The phase relation between the central frequency (carrier) and the two additional frequencies (sidebands) at $\pm$ the RF-frequency can be measured on a fast photodiode. The sidebands contain usually less than 1-2% of the power in the carrier. If the laser hits a resonance (of the cavity or the atomic transition) the interference of the two sidebands will vanish and the error signal is zero. If the laser is not exactly at resonance there will be a phase difference of the two sidebands and a beating will remain. This can be used to generate an error signal, which is zero only at resonance. Its polarity changes, when crossing a zero. This is an error signal, which can be used to stabilize the frequency of the laser onto the resonance. Also locking chains are possible. For example a laser can be locked onto a cavity and then the cavity can be locked on an atomic resonance. The applications are manifold. A main advantage of this technique compared to standard lock-in techniques is the high frequency used. Technical noise goes as $1/f$ and can be almost neglected. The lock can also compensate for frequency drifts within the range of the distance of the sidebands. More details and theoretical calculations of the error signal can be found in Wilzbach (2002). Also the references Bertinetto et al. (2001), Bjorklund (1979), Bjorklund et al. (1983), Camy et al. (1982), Ducloy and Bloch (1984), Jaatinen (1995), Raab et al. (1998), Raj et al. (1980), Schenzle et al. (1982), Shirley (1982), Supplee et al. (1994) include a nice experimental and theoretical overview. The necessary electronics was developed during this thesis and can be found in appendix B. With the setup and diode lasers the measured relative stability is better than 3×10^{-9},

which corresponds to one MHz laser line width.

The second method is the frequency offset (FO)method, where a laser (frequency master) is used as a reference for a second laser (slave). To measure the frequency difference of both lasers, their beams are overlapped on a fast photodiode. On the photodiode the beating signature (the frequency difference) of the two lasers can be measured. With an electronic circuitry (see appendix B) and mixing with a RF signal, the beating signal can be used to create an error signal. The slave laser can be locked with a PID controller onto the master laser with a certain frequency difference. This difference can be changed via changing the frequency of the RF-source[10]. This method is very useful, since the slave laser can be tuned in frequency with respect to the (fixed) master laser. With the electronics the slave laser can be typically tuned over several hundred MHz.

5.3.1 Transmission grating Laser

Since fibre coupling needs a high accuracy in beam pointing stability, a novel grating stabilized laser was designed. It uses a fixed transmission grating instead of a (turnable) reflection grating. The advantage is a higher pointing stability of the zeroth order of the emitted laser beam, which will not be displaced by turning the grating. The frequency tuning is accomplished by coupling back the first order of the transmission grating via an external mirror. The mirror can be moved and provides the frequency selection, but leaves the zeroth order unchanged. Figure 5.5 shows the setup. The output power of

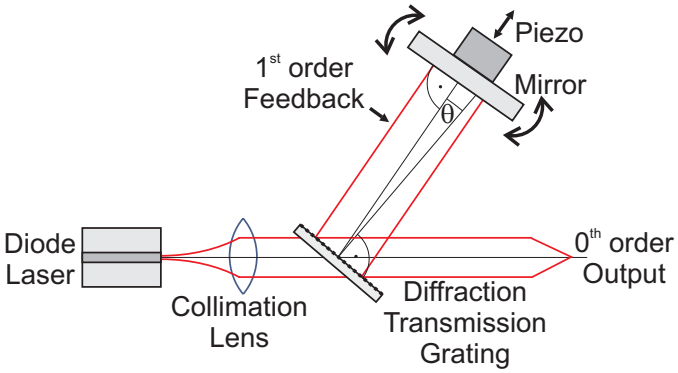

Figure 5.5: External-cavity diode laser in transmission grating configuration. The zeroth order of the emitted laser beam is not changed by the transmission grating. The first order is feed back with an external mirror into the laser diode. The zeroth order is left unchanged. Technical details can be found in Wicker (2006).

this laser is (17.5 ± 0.5) mW at a diode current of 77 mA. The line width of the laser is estimated by a beating measurement with a known reference laser. It is measured to be (1.7 ± 0.2) MHz, which is higher than the width for the reflection grating stabilized lasers. One difference here is the shorter external cavity design, which results in a higher line width. The frequency scanning range is measured to 2.3 GHz and with current feed-forward a scanning range of over 8 GHz is feasible. The beam pointing stability is superior to other designs. Therefore the transmission grating laser is used for seeding the home-made tapered amplifier system (Heine, 2007). Over one Watt of laser power is achieved with that kind of setup with a long time stability unmatched by commercial systems.

[10]Via a voltage controlled oscillator one can tune the frequency by changing the voltage externally.

5.4 Fibre optics

The setup for the fibre optics is shown in Fig. 5.6. Two dipole lasers and the imaging

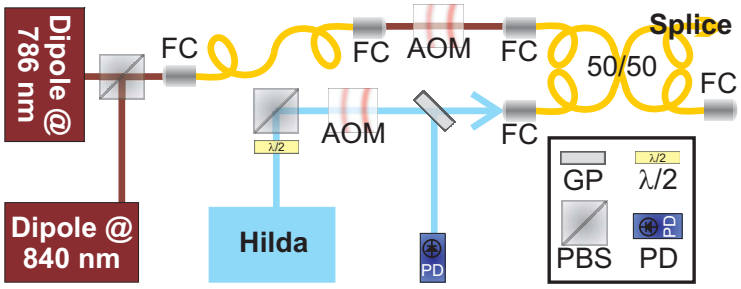

Figure 5.6: Schematic view of the laser system leading to the fibres. Only the components relevant for the fibre detection of the imaging laser "Hilda" are shown.

laser (Hilda) can be coupled into a 50/50 fibre coupler[11]. All lasers can be switched with AOM's and mechanical shutters. The imaging light can be intensity stabilized after the AOM or after the 50/50 fibre coupler. One end of the 50/50 fibre coupler leads to the fibre detectors in the vacuum chamber. Further details on the fibre detectors will be given in chapter 8.

5.5 Imaging system

To probe the atoms in all steps of the experiment, the experimental area is imaged with CCD cameras. The imaging system is made of two 12bit CCD cameras[12]. The cameras have a quantum efficiency of 20% at 780 nm. The system consists of an ultra compact camera head, which is connected to a standard PCI board via a high speed serial data link. The available exposure times range from 5 µs to 65 s. A digital temperature compensation is integrated instead of a thermo-electrical cooling unit. All camera functions can be remotely accessed and controlled via the digital interface (PCO AG, 2007). The resolution is 1392 × 1024 pixels and the pixel size is 6.45 × 6.45 µm^2.

One camera is placed at the chamber window opposite to the fiber coupler for absorption imaging (see fig 5.3). This will give a picture of the atoms from the side. The used lenses[13] have a focal length of $f_1 = 300$ mm and $f_2 = 140$ mm. The magnification factor is $m_T = 0.84$. The distance of the chip center to the first lens (with f_1) is $s_{01} = 203$ mm. The distance of the first lens to the second lens is $d = 28$ mm. The distance of the second lens to the CCD chip is $s_{i2} = 177$ mm. For a given pair of lenses the optimal parameters are connected via the formulas (Hecht, 2005)

$$s_{i2} = \frac{f_2 d - f_2 s_{01} f_1/(s_{01} - f_1)}{d - f_2 - s_{01} f_1/(s_{01} - f1)}, \tag{5.1}$$

$$m_T = \frac{f_1 s_{i2}}{d(s_{01} - f_1) - s_{01} f_1}. \tag{5.2}$$

[11]Newport Single-Mode Coupler: 2x2 50/50 (3 dB) Coupler F-CPL-S22855.
[12]Pixelfly QE CCD camera, PCO AG, Kehlheim, Germany.
[13]MGLA1 and 309099, Melles Griot, Bensheim, Germany.

A negative magnification means, that the picture is reverted (headfirst). The resolution is measured with a different chip. The chip[14] used for resolution measurements has structures of sizes 100 µm down to 4 µm. A pair of structures placed next to each other can be resolved (distinguished) down to a size of 6.6 ± 0.9 µm. The diffraction limit is given as $\alpha \approx 1.22\lambda f_1/a$, where $\lambda = 550$ nm is used for the resolution measurement. The window is the limiting aperture and has a diameter of $a = 30$ mm. The first lens has a focal length of $f_1 = 300$ mm, thus $\alpha_{550nm} \approx 6.7$ µm is the limit. This becomes worse by a factor of 780/550 for the imaging laser light. The second camera images the chip from beneath the vacuum chamber. It has a standard camera objective[15].

Absorption and fluorescence imaging Both cameras can image the atoms in fluorescence and the camera from the side additionally images the atoms in absorption. This standard technique is described e.g. in Engeser (2002). With fluorescence imaging the atom cloud is illuminated by a resonant laser beam. The atoms scatter the absorbed light, which is collected by the cameras.

For absorption imaging a resonant laser beam is hitting the atoms from the side and is imaged by a lens system on the other side onto the CCD chip of the camera. Two (three) consecutive pictures are made. The first picture with atoms and the second picture without atoms. (The third picture is done without the laser beam and defines the background.)

From the three pictures the column density can be calculated[16]. The absorption is calculated pixel-wise for the three pictures:

$$I_{abs} \quad = \quad 1 - \frac{I_{with\,atoms} - I_{background}}{I_{without\,atoms} - I_{background}}. \tag{5.3}$$

For a low background, the calculation can be simplified by leaving out $I_{background}$.

It is possible to image the atoms while they are being trapped in the magnetic field (in-situ). Then the frequency of the laser must be adjusted to be on resonance with the atoms in the magnetic field. For temperature measurements, the atoms are released from the trap. Gravity will pull them downwards. During the fall the atomic cloud will expand freely. From a series of pictures the extension of the cloud can be determined and the temperature can be calculated. This is called time-of-flight (TOF) imaging. From the absorption images one can also calculate the number of atoms (Engeser, 2002).

To get information about the distance of the atomic cloud from the chip surface, light must be shone in under a very small angle. The angle must be chosen in such a way, that the light directly hits the camera on the other side. Also a part of the beam must be reflected at the chip surface and hit the camera on the other side. Then (up to a maximum distance) the atomic cloud is present twice on the image. The distance between the two clouds is two times the distance of the cloud from the atom chip. An example of the absorption imaging is shown in Fig. 5.7.

[14] Chip layout hybrid161003.gds, see (Groth, 2006).
[15] Nikon Nikkor 50 mm, 1:1.4.
[16] It is a 2-dimensional projection of the 3-dimensional atom cloud onto the CCD chip.

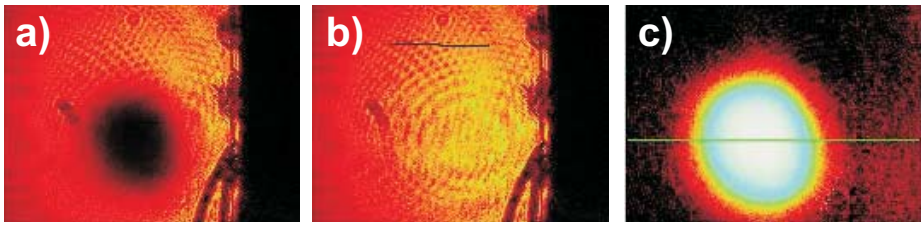

Figure 5.7: Example of an absorption imaging. The dark structure on the pictures **a)** and **b)** on the right is the shadow of the atom chip and the bonding wires. The bonding wires partly obstruct the beam. For future experiments the central region of the atom chip must be kept clear of bonding wires to improve the imaging. **a)** shows the picture with atoms, **b)** a picture without atoms and **c)** shows the division of both pictures according to Eq. 5.3. The line in the last picture indicates the position, where the imaging program tries to make a Gaussian fit to the atom cloud (not shown here).

6 Atom Chip

Atom chips are robust and extremely powerful toolboxes for quantum optical experiments, since they allow to create exceptionally precise magnetic traps for neutral atoms with minimal field modulations. Accurate manipulation of trapped atoms is feasible with magnetic and electric fields created on the atom chip. Therefore atom chips with high quality surfaces and extremely well defined wires were build (Groth, 2006).

In section 3.2 the theoretical basis for magnetic traps was established. In the following the technical aspects of the production of an atom chip will be introduced (section 6.1). Then the properties and the required steps for manufacturing a fibre cavity will be summarized in section 6.2. In section 6.3 the fluorescence and the absorption fibre detector will be addressed. Moreover the technology for integration of fibres on the atom chip will be concentrated on in section 6.4. The chapter will conclude with the integration of the chip on the chip mounting in section 6.5.

6.1 Atom Chip production

A typical production cycle is shown in Fig. 6.1. For further details, see Groth (2006). The design of the chip is carried out with the program dw2000[1]. Then the structures are

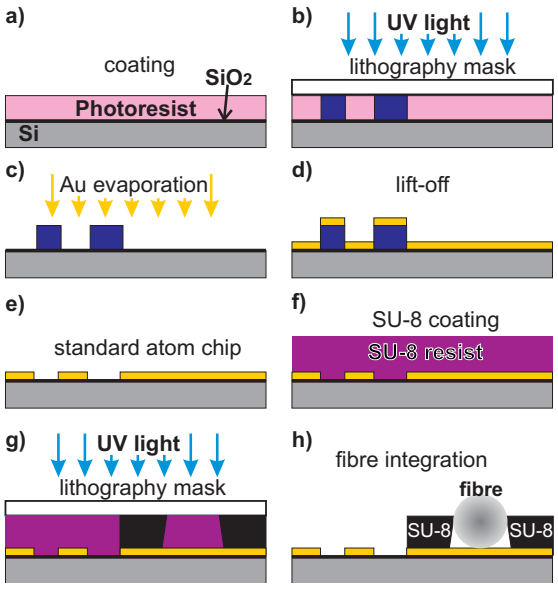

Figure 6.1: The fabrication process is illustrated in this figure. **a)** The Si substrate with its SiO_2 cover layer is spin coated with photo resist. **b)** The resist is exposed through a lithography mask. **c)** After development the sample with its resist pattern is evaporated with titanium and gold. **d)** Lift-off removes the resist and the metal on top of it. **e)** The standard atom chip is ready. More details for the process until this step are given in Groth (2006). **f)** Spin coating with SU-8 photo resist. **g)** The resist is exposed through a lithography mask. **h)** After development the sample with its resist pattern is used to integrate the fibres.

transferred to a lithography mask with an electron beam machine. A silicon substrate is covered with silicon-dioxide for electrical insulation. Then the substrate is spin coated with photo resist, and the resist is exposed with UV light through the lithography mask.

[1]Design workshop technologies, dw2000, www.designw.com

After the development of the resist it will stay at the non exposed places on the substrate's surface. Then an evaporation with titanium (to have better contact) and gold is performed. The final step in the standard production cycle is to remove the rest of the resist (lift off), where the metal on top of the resist is also removed. Groves without gold define the structures on the chip. In that way, the whole substrate (except for some grooves) is covered with gold and can be used as a mirror for the operation of a mirror MOT. In this special case with the integrated detectors there are several further steps. The next one is to spin coat the chip with SU-8 photo resist. After development structures capable of holding optical fibres are left on the chip. The final step is to insert the fibres.

6.2 Properties of Fiber Cavities

The advantage of fibers is that they can be easily handled using well established techniques. For instance, transfer mirror coatings can be directly glued to the fibers. Different fibers can be melted together using commercially available fusion splicers. The fabrication of fiber optical components does usually not require expensive and time consuming lithographic techniques. Fibers also have the advantage that they have very low optical loss, usually less than 3 dB/km.

For miniaturization of optical components for atomic physics several proposals on atom chip integration have been presented in Armani et al. (2003), Horak et al. (2003), Lev et al. (2004), Liu et al. (2005), Moktadir et al. (2004), Rosenblit et al. (2004), Wilzbach et al. (2004). In this approach optical fibers are attached to the chip to form fiber-based cavities and to make small dipole traps. For fiber cavity experiments it is interesting to put atoms into the optical resonator. To place the atom inside the cavity it is possible to cut the fiber into two pieces and place the atom in the fiber gap. The production of the fibre cavities itself will only be summarized here. In detail this is covered in the diploma theses of Schwarz (2004) and Wicker (2006). The manufacturing process as well as novel techniques to improve the fiber cavities are presented there.

It is also possible to use a hollow fiber and guide the atom inside of it (Key et al., 2000). Because it is quite difficult to load atoms into a hollow fiber, especially if it is mounted on a micro-structured surface, the following section deals with fiber-gap-fiber configurations as the ones outlined in Fig. 6.2.

One realization of a fiber cavity is to implant mirrors into the fibers, such as Bragg gratings or dielectric coatings inserted between fiber pieces. See Fig. 6.2a). This has the advantage that the interaction volume (the gap through which the atoms pass) is defined only by the bare fiber tips. Thus only the fiber itself has to be mounted on the atom chip with little or no need for alignment actuators. Mirrors and tuning actuators can be placed far from the gap. This allows a higher integration of the optics. A disadvantage of this method is that the cavity becomes quite long and that the extra interfaces increase the optical loss of the cavity. Using a long cavity will increase the mode volume and therefore also reduce the single photon Rabi frequency g_0 (see Eq. 1.10). For atom detection the length of the cavity is fortunately not a very important parameter, as indicated by Eq. 1.11.

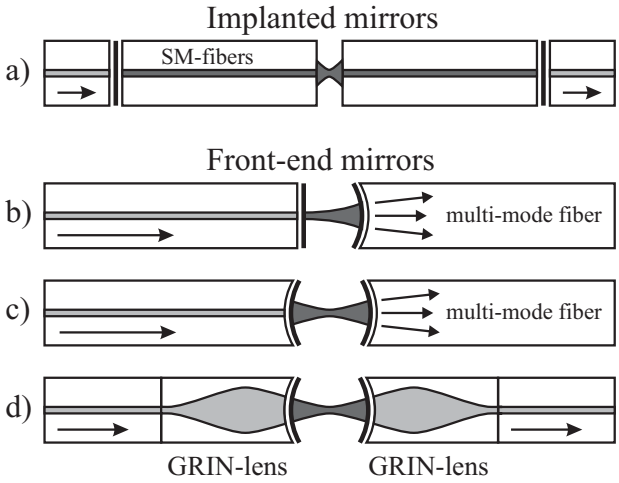

Figure 6.2: a) A cavity with implanted mirrors. This cavity requires little alignment of the gap, but the mode volume is large. This configuration can be realized using only single mode fibers. b) A plano-concave cavity. Incoupling from a single mode fiber is efficient, but the mode diameter becomes large at the location of the atom. Outcoupling to a single mode fiber is not optimal, but a multi-mode fiber can collect the transmitted light well. c) A concave-concave cavity. The mode diameter can be controlled, but coupling to single mode fibers is not optimal. d) Focussing optics can be integrated to optimize the fiber-cavity coupling efficiency. Cavities b) - d) require active alignment of the gap.

6.2.1 Loss mechanisms for a cavity

The quality of an optical resonator is described by its finesse. The finesse is related to the losses by:

$$\mathcal{F} = \frac{\pi}{\sum_i \alpha_i}, \tag{6.1}$$

where α_i are the loss probabilities for the different loss channels. For example, a cavity mirror transmittance of $T = 0.01$ corresponds to $\alpha = 0.01$. As long as $\Sigma_i \alpha_i \ll 1$ the cavity finesse is accurately calculated by Eq. 6.1. Further details on resonators can be found in Siegman (1986). For atom detection it is desirable to obtain a high signal-to-noise ratio. This does not automatically mean that the finesse has to be maximized. The signal-to-noise ratio for atom detection in the weak coupling and low atomic saturation is given by Eq. 1.11, where $\kappa_T \propto \alpha_T$ describes the mirror transmittance and $\alpha_{\text{tot}} = \alpha_T + \alpha_{\text{other}}$ is the total cavity loss. This implies that SNR $\propto \alpha_T/(\alpha_T + \alpha_{\text{other}})^2$ which is maximized for $\alpha_T = \alpha_{\text{other}}$. For each kind of cavity there is an optimal choice of the mirror transmittance.

When the cavity contains a gap (wee Fig. 6.2a) the main loss mechanism is related to the reduced coupling efficiency across the gap. This loss depends mainly on three factors. (1) It is clear that the mode matching of the two fibers is not optimal and losses will occur as the gap is traversed. This loss increases with the gap size. (2) Also, in the case of transverse misalignment of the two fibers modes are not well-matched at the fiber facets. (3) A tilt between the two fibers also increases the mismatch between the two modes. In this case the loss also increases with the length of the fiber gap.

Figure 6.3 shows these misalignments of the gap. The power coupling efficiency η for two fibers can be calculated in the paraxial approximation by the overlap integral of the

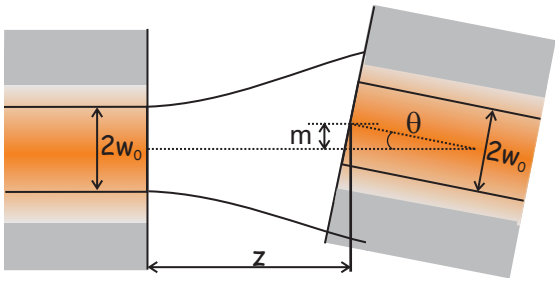

Figure 6.3: The fiber light mode diverges, after leaving the fiber on the left with a mode field diameter of $2w_0$. The second fiber on the right has a longitudinal displacement of z, a transversal displacement of m and an angular misalignment of θ.

involved transverse mode functions.

$$\eta = \frac{\left|\iint_{\mathbf{A}} \Psi_1(\vec{r})\Psi_2^*(\vec{r})dA\right|^2}{\iint_{\mathbf{A}} \Psi_1(\vec{r})\Psi_1^*(\vec{r})dA \iint_{\mathbf{A}} \Psi_2(\vec{r})\Psi_2^*(\vec{r})dA}, \tag{6.2}$$

where $\Psi_1(\vec{r})$, $\Psi_2(\vec{r})$ are the fiber optical field modes, and $\mathbf{A}$ is the plane coinciding with one of the fiber facets. In this text this measure is used to describe cavity losses.

Losses due to the gap length

It is obvious that the losses rise with increasing gap size z. The light leaving the first fiber at z diverges until it hits the opposite fiber at $z = 0$. The light leaving the first fiber can be described as

$$\Psi_1(x,y,z) = \sqrt{\frac{2}{\pi}}\frac{1}{w(z)}\exp\left(-\frac{ik\,(x^2+y^2)}{2R(z)}\right) \times \exp\left(-\frac{x^2+y^2}{w(z)^2}\right)\exp\left(ikz - i\Phi(z)\right), \tag{6.3}$$

where $w(z) = w_0\sqrt{1+z^2/z_0^2}$ the beam radius, w_0 is the Gaussian waist at the first fiber facet, $R(z) = z + z_0^2/z$ the radius of curvature, $z_0 = \pi w_0^2/\lambda$ the Rayleigh length, and $\Phi(z) = \arctan(z/z_0)$ the Gouy-phase. The wavelength is $\lambda = \lambda_0/n$ and the wave number is $k = k_0 n$ in the medium between the fibers with refractive index n. The wavelength and the wave number in vacuum are λ_0 and k_0, respectively. Assuming that the two fibers are identical, the mode function at the facet of the second fiber is

$$\Psi_2 = \Psi_1(x,y,0) = \sqrt{\frac{2}{\pi}}\frac{1}{w_0}\exp\left(-\frac{x^2+y^2}{w_0^2}\right). \tag{6.4}$$

The loss α_{gap} due to the length of the gap can be calculated from the overlap between Eq. 6.3 and Eq. 6.4.

$$\begin{aligned}\alpha_{\text{gap}}(z) &= 1 - \left|\int_{-\infty}^{\infty}\int_{-\infty}^{\infty} \Psi_1(x,y,z)\Psi_2^*(x,y,0)dx\,dy\right|^2 \\ &= \frac{z^2}{4z_0^2+z^2} \approx \left(\frac{z}{2z_0}\right)^2 = \left(\frac{\lambda^2}{4\pi^2 w_0^4}\right)z^2.\end{aligned} \tag{6.5}$$

Here the transverse and angular misalignments are assumed to be zero. A plot of a finesse measurement with varying gap size z is shown in Fig. 6.10a. In this case mirrors with a

loss of 1% are assumed to be located inside the fibers. This loss is decreased if the gap between the fibers is small and the fiber has a small numerical aperture i.e. a large w_0. However, to detect atoms w_0 must be small, as indicated by Eq. 1.11.

Losses due to transversal misalignment

If the two fibers are transversally misaligned to each other there will also be a mode mismatch when the light is coupled between the fibers. This loss can easily be calculated from Eq. 6.2. Using normalized Gaussian mode functions for two identical fibers (with $z = 0$) with waist w_0 choosing the gap and angular misalignment to be zero one has

$$\begin{aligned} \Psi_1(x,y,0) &= \sqrt{\frac{2}{\pi}}\frac{1}{w_0}\exp\left(-\frac{x^2+y^2}{w_0^2}\right), \\ \Psi_2(x,y,0) &= \Psi_1(x-m,y,0) \\ &= \sqrt{\frac{2}{\pi}}\frac{1}{w_0}\exp\left(-\frac{(x-m)^2+y^2}{w_0^2}\right), \end{aligned} \tag{6.6}$$

where m is the transverse misalignment of one of the fibers. This gives a loss due to the transversal misalignment α_{tra}:

$$\begin{aligned} \alpha_{\mathrm{tra}}(m) &= 1 - \left| \int_{-\infty}^{\infty}\int_{-\infty}^{\infty} \Psi_1(x,y,0)\Psi_2^*(x,y,0)dx\,dy \right|^2 \\ &= 1 - \exp\left(-\frac{m^2}{w_0^2}\right) \approx \frac{m^2}{w_0^2}, \end{aligned} \tag{6.7}$$

where the last approximation is valid only for $m \ll w_0$. A plot of a finesse measurement with varying transversal misalignment is shown in Fig. 6.10b.

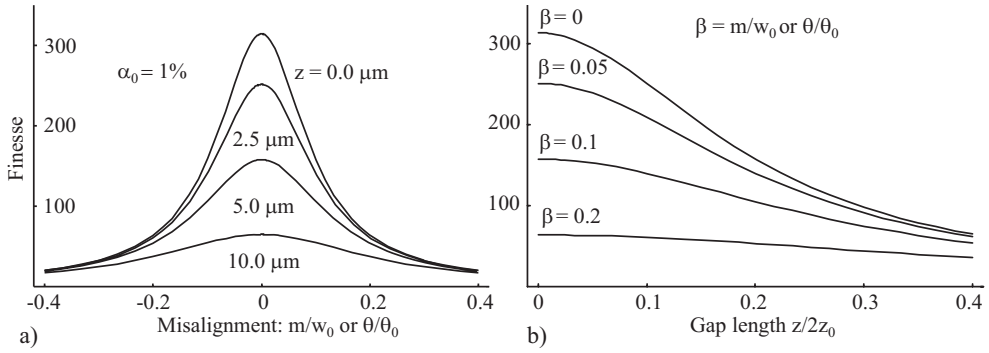

Figure 6.4: Theoretical calculations were conducted for an implanted mirror cavity. The fiber mode radius was $w_0 = 2.5$ µm at a wavelength of 780 nm. All losses except the gap losses were set to 1%. Plot a) shows the finesse as a function of θ and m, which were normalized to θ_0 and w_0, respectively. θ_0 is given by $\lambda/(\pi w_0) = w_0/z_0$. The different curves correspond to different gap lengths starting with the highest finesse at $z = 0$ µm and ending with the lowest at $z = 10$ µm. In b) the finesse is plotted as a function of $z/2z_0$. The different curves correspond to different β, where β is either θ/θ_0 or m/w_0. β ranges from 0 to 0.2

Losses due to angular misalignment

Another kind of loss emerges from angular misalignment of the two optical axes of the fibers. This is calculated by performing a basis change of Eq. 6.3 and evaluating the overlap given by Eq. 6.2. The mode leaving the first fiber (see Fig. 6.3) is approximately described by

$$\Psi_1(x,y,z) \approx \sqrt{\frac{2}{\pi}}\frac{1}{w_0}\exp\left(-\frac{x^2+y^2}{w_0^2}\right)\exp\left(ikz\right), \tag{6.8}$$

for small $z \ll z_0$ neglecting diffraction effects. A small rotation θ around the y-axis is given by

$$\begin{aligned}\begin{pmatrix} x \\ y \\ z \end{pmatrix} &= \begin{pmatrix} \cos\theta & 0 & \sin\theta \\ 0 & 1 & 0 \\ -\sin\theta & 0 & \cos\theta \end{pmatrix}\begin{pmatrix} x' \\ y' \\ z' \end{pmatrix} \\ &\approx \begin{pmatrix} 1 & 0 & \theta \\ 0 & 1 & 0 \\ -\theta & 0 & 1 \end{pmatrix}\begin{pmatrix} x' \\ y' \\ z' \end{pmatrix}.\end{aligned} \tag{6.9}$$

Transforming $\Psi_1(x,y,z)$ into the coordinate system (x',y',z') the mode function for the incident beam at the input plane $z'=0$ of the second fiber becomes

$$\Psi_1(x',y',z'=0) \approx \sqrt{\frac{2}{\pi}}\frac{1}{w_0}\exp\left(-\frac{x'^2+y'^2}{w_0^2}\right)\exp\left(ikx'\theta\right). \tag{6.10}$$

The mode function for the second fiber at the input plane $z'=0$ is given by

$$\Psi_2(x',y',z'=0) = \sqrt{\frac{2}{\pi}}\frac{1}{w_0}\exp\left(-\frac{x'^2+y'^2}{w_0^2}\right). \tag{6.11}$$

The loss α_{ang} due to a pure angle misalignment can be calculated from the overlap between Eq. 6.10 and Eq. 6.11.

$$\begin{aligned}\alpha_{\text{ang}}(\theta) &= 1 - \left|\int_{-\infty}^{\infty}\int_{-\infty}^{\infty}\Psi_1(x',y',0)\Psi_2^*(x',y',0)dx'\,dy'\right|^2 \\ &= 1-\exp\left(-\frac{\pi^2 w_0^2}{\lambda^2}\theta^2\right) \approx \left(\frac{\theta}{\theta_0}\right)^2,\end{aligned} \tag{6.12}$$

with $\theta_0 = \lambda/(\pi w_0) = w_0/z_0$. In general these misalignments are not independent of each other. The combined formula for all the misalignment losses is given by (Saruwatari and Nawate, 1979):

$$\begin{aligned}\alpha(\theta,m,z) = 1-\eta \approx 1-\mu(z)\times \\ \exp\left[-\mu(z)\left(\frac{m^2}{w_0^2}+\frac{\pi^2\theta^2 w_0^2}{\lambda^2}+\frac{\theta^2 z^2}{2w_0^2}-\frac{m\theta z}{w_0^2}\right)\right],\end{aligned} \tag{6.13}$$

with $\mu(z) = 4z_0^2/(4z_0^2+z^2)$. A measurement with transversal and longitudinal displacement and angle misalignment is plotted in Fig. 6.10. One experimental advantage is that the loss rate depends quadratically on small misalignments.

Fresnel reflections

Another effect that has to be taken into account is the reflection of light at the interfaces between the fibers and the introduced gap. It results from the step in the refractive index and is called Fresnel reflection. For a typical fiber ($n_1 = 1.5$) in air or vacuum ($n_2 = 1$) a fraction of $R_F = (n_2 - n_1)^2/(n_2 + n_1)^2 = 4\%$ of the incident light is reflected from a polished flat connector. In the case of a fiber gap cavity, these additional reflections lead to a system of three coupled resonators. While for any system of coupled resonators stationary solutions exist, i.e. eigenmodes of the electromagnetic field, they will in general not be equidistantly distributed in the frequency domain.

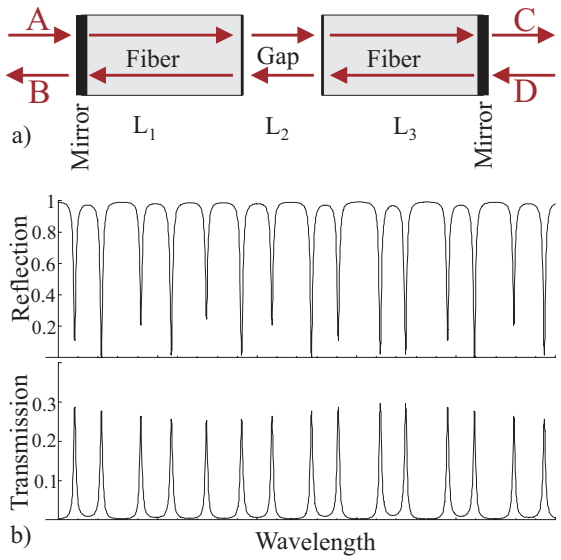

Figure 6.5: a) Schematic description of the cavity formed by the three coupled resonators. b) Reflectance and transmittance of a cavity formed by three coupled resonators. The system is constituted by Mirror-Fiber-Gap-Fiber-Mirror and has $\alpha = 0.05$. In addition $L_1 \neq L_3$ and $L_2 = \lambda/4$ plus an integer multiple of $\lambda/2$. The period of the envelope is given by the length difference of the two fiber pieces.

In a simple one-dimensional model, the coupled cavity system can be treated as a chain of transfer matrices (Siegman, 1986). Figure 6.5 shows the calculated reflected and transmitted intensities for a model resonator of rather low finesse.

The light intensity inside the gap depends on the specifics of the mode. This changes the overall losses, as can be seen in Fig. 6.5b. Consequently the reflected and transmitted intensities vary from mode to mode. The effect is strongest when the gap length is a multiple of $\lambda/2$. In experiments coupling atoms to the light field it has to be considered that the intensity inside the gap depends on the order of the mode and on the exact length of the gap. In absorption experiments only the relative change of transmitted light intensity is measured, which remains mode independent for light intensities well below saturation. Nevertheless it leads to a mode dependent signal-to noise ratio. Using fibers with n=1.5 and intensities below atomic saturation the SNR changes by roughly 15%

6.2.2 Building fiber cavities

So far cavities with curved and planar mirrors at the front-end of two fibers, and cavities with implanted mirrors made out of one piece of fiber with a gap for the atoms similar to the ones shown in Fig. 6.2 are realized.

The mirror coatings are attached to the fibers using a *transfer technique*. These fibre cavities were developed during this thesis and are explained in detail in Schwarz (2004).

In this process, dielectric mirror coatings with a transmittance of 0.1% to 1% are manufactured on a glass substrate. The substrate is either flat or contains an array of spherical micro lenses for curved coatings. The adhesion between the coating and the glass substrate is fairly low. When the coating is glued to an optical fiber it is possible to transfer the coating[2] from the substrate to the fiber. A series of pictures showing this transfer is given in Fig. 6.6.

The transmittance T is chosen to be around 1% for cavities with implanted mirrors (Fig. 6.2a) because of the higher loss. For the front-end mirrors (Fig. 6.2b-d), the loss is lower therefore it is more suitable to choose a mirror with transmittance around 0.1% to obtain a high SNR for the detection of atoms.

The higher losses for cavities with implanted mirrors have several origins in addition to the ones caused by the gap. For some of the cavities the main intrinsic loss source are the glue layers holding the mirror coatings to the fibers. These glue layers are typically a few micrometers thick. The transversal confinement of the fiber is absent in the glue layers as well as in the mirror coatings. This leads to losses similar to the ones discussed for the gap length, i.e Eq. 6.5. Glued mirrors are also sensitive to angular misalignment, which can be treated by Eq. 6.12.

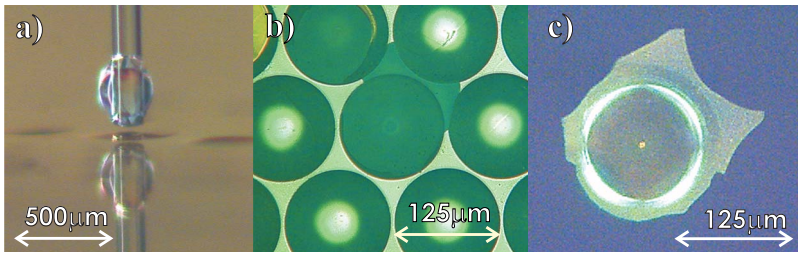

Figure 6.6: Picture a) shows a fiber with a drop of glue on the tip. The fiber is hovering 100 microns above a micro lens with dielectric mirror coating. The lower part is a mirror image of the real fiber. Once the fiber is glued to the coating it can be removed by gently pulling the fiber away from the substrate. In picture b) one can see the micro lens array from above. A closer look reveals that coatings are missing from two of the lenses. One of these is attached to the fiber shown in c). Additionally in c) light was coupled in from the other side of the fiber, so one can see the fiber core in the center of the picture.

Curved coatings may be used to build a concave cavity with front-end mirrors. With this design finesses of greater than 1000 can be reached as shown in Fig. 6.7. Complications due to Fresnel reflections do not exist for the front-end cavity. The quality of the mirrors and their alignment determine how high the finesse may become. The mode profile of the optical fiber does usually not match the cavity mode leading to a poor coupling into the front-end cavity. The problem can be solved by transferring the mirror coatings to a tapered fiber, or a small grin lens to focus the light into the cavity mode. Unfortunately a more complicated and error prone fabrication process is the result. In addition, a cavity with front-end mirrors must be mounted on alignment actuators for efficient tuning of the cavity. This makes miniaturization and integration of multiple cavities harder.

A cavity with the geometry shown in Fig. 6.2a) was built by inserting two planar mirrors into a fiber with length about 10 cm. This fiber cavity is subsequently cut into two halves

[2] Optische Interferenz Bauelemente GmbH (2004)

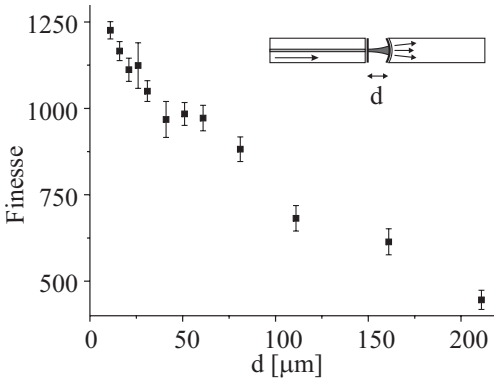

Figure 6.7: Finesse measurement of a cavity with a flat mirror on a single mode fiber on the side to couple in and a curved mirror with $r = 350$ µm on a multi-mode fiber on the side to couple out, as the one illustrated in Fig. 6.2b. Both mirrors have an reflectance of R=99.9%. The finesse stays above 400 for fiber separations smaller than 200 µm and has a maximal value of 1200 for small mirror separations.

and the new surfaces are polished. This cavity has the advantage that it is very easy to align and mount. An actual cavity of this kind is shown in Fig. 6.8c) where the cavity is mounted on an atom chip using a SU-8 structure to hold the fibers. The drawback of this cavity geometry is that the finesse is rather low compared to the front-end mirrors, mainly because of the fiber gap and the glue layers as described above. Cavities with inserted mirrors typically reach a finesse of a few hundred instead of a few thousand as for the front-end cavities. The losses due to the glue layers can be reduced by direct coating of the fiber instead of using the transfer technique. The losses due to the gap itself can also be reduced by introducing collimation optics in the gap, such as a small grin lens or a tapered fiber. Such additional optics will however introduce additional Fresnel reflections and may also require active alignment of the gap, as for the front-end cavity.

6.3 Other fiber optical components for the atom chip

Not only cavities can be mounted on the surface of an atom chip. Miniaturization offers various advantages for several other optical components. Lenses with extremely short focal lengths can be used to focus light to small areas. Such devices can be used to generate very tight dipole traps (Reymond et al., 2003, Schlosser et al., 2001, 2002), or to collect light from very well-defined volumes (Eriksson et al., 2005).

6.3.1 Fluorescence and absorption detectors

A fluorescence detector can be built using a single mode tapered lensed fiber and a multi-mode fiber. In this case, the tapered fiber is used to optically pump the atom. The multi mode fiber is used to collect the fluorescent light. For this configuration the multi mode fiber is put at any angle with respect to the tapered lensed fiber. At small angles, atoms located in the focus of the tapered lensed fiber will scatter light *away* from the multi mode fiber. This constitutes an absorption detector. Such a device is illustrated in Fig. 6.8b). If the angle between the two fibers is sufficiently large only the fluorescent emission from the atom will be *collected* by the multi mode fiber. A picture of a 90° fluorescence detector setup is shown in Fig. 6.8a). If no atom is present in the beam focus, very little light is scattered into the fiber. As soon as an atom is present, this signal increases. If these two techniques are sensitive enough for single atom detection will be evaluated experimentally. Definitely photon recoils will expel the atom from the detection region and the multi mode

fiber only collects a few photons. To circumvent the loss one must trap the atom(s) in the tapered lensed fiber focus. This can be accomplished by a dipole trap.

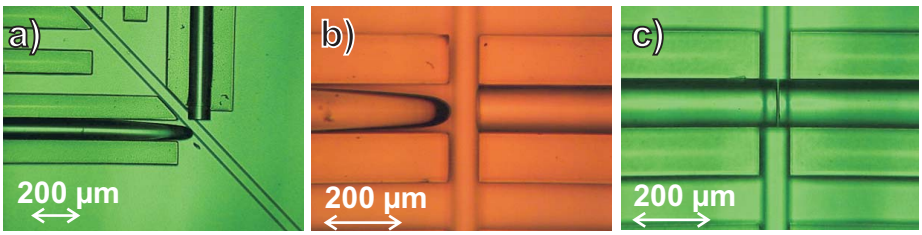

Figure 6.8: a) The image shows the 90° fluorescence fiber detector setup. It is made of a tapered fiber (the horizontal fiber) used for a dipole trap and optical probing. The vertical fiber is a multi-mode fiber used to collect scattered light. **b)** shows a tapered fiber facing a multi-mode fiber. This setup can be used for absorption detection of a few atoms. **c)** shows a fiber cavity with a gap of a few microns.

6.3.2 A single mode tapered lensed fiber dipole trap

To increase the number of detectable photons, the atom can be trapped inside the area where it interacts with the light. One possibility is to hold the atom in place with a dipole trap. An atom with transition frequency ω_0 is attracted to the intensity maximum of a red-detuned laser beam ($\omega < \omega_0$). A focussed laser beam forms an atom trap in the beam focus. For a far-detuned dipole trap quantities such as trap depth, lifetime and number of scattered photons can be estimated easily. A detailed derivation of dipole trap parameters discussed in the following paragraph can be found in Grimm et al. (2000). The potential depth of a dipole trap for an alkali atom is

$$U_{\mathrm{dip}}(\vec{r}) = \frac{\pi c^2 \Gamma}{2\omega_0^3}\left(\frac{2}{\Delta_{D2}} + \frac{1}{\Delta_{D1}}\right) I(\vec{r}), \tag{6.14}$$

and the scattering rate is given by

$$\Gamma_{\mathrm{sc}}(\vec{r}) = \frac{\pi c^2 \Gamma^2}{2\hbar\omega_0^3}\left(\frac{2}{\Delta_{D2}^2} + \frac{1}{\Delta_{D1}^2}\right) I(\vec{r}), \tag{6.15}$$

where Δ_{D2} and Δ_{D1} are the detunings of the laser with respect to the D2 and D1 lines of the alkali atom. The formulas apply to alkali atoms with a laser detuning much larger than the hyperfine structure splitting and a scattering rate far from saturation. It follows that the scattering rate for a given potential can be decreased by choosing a larger detuning and a higher laser intensity. The potential depth scales as $\sim \Gamma/\Delta$, whereas the scattering rate scales as $\sim \Gamma^2/\Delta^2$.

The D2 line of Rubidium, ${}^2S_{1/2} \rightarrow {}^2P_{3/2}$, has a wavelength of 780 nm, and the D1 line ${}^2S_{1/2} \rightarrow {}^2P_{1/2}$ has a wavelength of 795 nm. A standard tapered lensed fiber generates a typical beam radius of $w_0 = 2.5$ µm at a wavelength of 780 nm. Far off resonance dipole traps can be realized with easy to use, high power diode lasers. Standard single mode lasers diodes are available with a power up to 150 mW. Assuming a coupling efficiency into the fiber of around 20%, one gets 30 mW of laser power in the dipole trap. These

parameters yield a trap depth of 3.9 mK, and a transverse (longitudinal) trap frequency of 80 kHz (6 kHz). The heating rate for the dipole light is almost negligible. Experiments have shown that the lifetime is mainly limited by the background pressure of the vacuum chamber (Miller et al., 1993).

Using resonant light to detect an atom increases the number of scattered photons as well as the heating rate enormously. In this case the trap lifetime drops to below a millisecond, which yields several thousands scattered photons before the atom is lost.

6.4 Integration of fibers on the atom chip

A method for mounting fibers accurately is needed to integrate the above devices on atom chips. Fibers can be held at the right place with the help of fiber grippers, aligned and finally glued to the chip. This strategy will not work well for fiber cavities because they need to be actively aligned during operation (See Fig. 6.2b-d). For active alignment of an on-chip cavity an actuator is needed. Useful actuators, such as piezoelectric stacks, are quite large compared to the fibers. Typical dimensions exceed 2x2x2mm. This places restrictions on the level of optical integration one can obtain on the chip. Components that do not need active alignment, such as the cavities with implanted mirrors (see Fig. 6.2a) or tapered fibers for dipole traps, can be directly integrated on the chip. To obtain a high degree of precision in the mounting a lithographic method was developed where a thick photoresist is patterned to form the mounting structures (Liu et al., 2005).

6.4.1 The SU-8 resist

To mount fibers on the atom chip a lithographically patterned photoresist called SU-8 is used. SU-8 is an epoxy based negative resist with high mechanical, chemical and thermal stability. Its specific properties facilitate the production of thick structures with very smooth, nearly vertical sidewalls (Liu et al., 2005). It has been used to fabricate various micro-components. Examples include optical planar waveguides with high thermal stability and controllable optical properties. Mechanical parts such as microgears (Seidemann et al., 2002) for engineering applications, and microfluidic systems for chemistry (Duffy et al., 1998) have also been built. The SU-8 is typically patterned with 365-436 nm UV-light.

To assess the quality of the alignment structures, the SU-8 structures are used to hold fiber optical resonators. The finesse of the resonator strongly depends on losses introduced by misalignment as described by Eq. 6.13.

Structure requirements The alignment structures for the fiber resonator must meet some specific requirements. They must be able to tolerate temperature changes and gradients. In typical experiments with atoms trapped in microscopic potentials, the currents carried by the metallic structures lead to a local temperature increase of as much as 100 ℃. Furthermore, the structure must be taller than the fiber radius ($r = 67.5$ µm) and an exposure in thick resist is needed. To prevent lateral and angular misalignment, i.e., parallel and perpendicular to the substrate plane, an undercut sidewall profile is superior to a vertical sidewall profile. With such a profile, the separation between the sidewalls decreases proportional to the distance from the substrate surface (see Fig. 6.9(c)), thus clamping the

fiber. To meet these requirements, SU-8 is highly suitable, because of its thermal stability and outstanding lithographic performance. The undercut sidewall profile can be obtained by optimization of the lithographic process steps. The optimization techniques include fine-tuning of the exposure dose and the post-exposure bake (PEB) time.

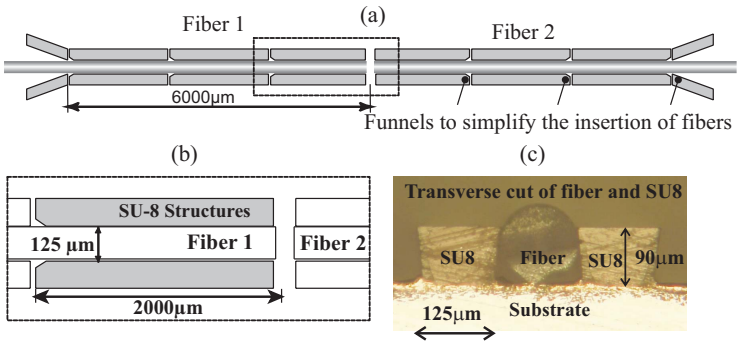

Figure 6.9: a) Layout of the alignment structure and a magnified part (rectangle) in b). c) Fiber in a SU-8 structure mounted on a gold coated atom chip. The atom chip and the SU-8 structures have been cut with a wafer saw. The SU-8 maintains structural integrity during the cutting.

The layout of the desired alignment structure with fibers is shown in Fig. 6.9. This design includes funnels to simplify the insertion of the fiber. To avoid angular misalignment, the total length of the alignment structure was chosen to be 6000 µm, and it is divided into several subsegments to reduce stress induced by thermal expansion.

Quality of the SU-8 structures The quality of the SU-8 fiber splice is determined indirectly by first measuring the finesse of an intact fibre resonator and then splitting and inserting it into the structures. The transmitted light intensity is recorded while scanning the laser over several free spectral ranges of the fiber resonator. A model function is fitted to the data, yielding the finesse according to Eq. 6.1. The results are averaged over several hundred runs of the experiment. The finesses of two intact resonators are found to be $\mathcal{F}_1 = 110.4 \pm 0.3$ and $\mathcal{F}_2 = 152.8 \pm 1.1$. After cutting the resonators and polishing the surfaces, the pieces are introduced into the SU-8 structures. The fiber ends are observed under a microscope and the gap size is minimized to touching fibers. The finesses are measured to be $\mathcal{F}_1 = 101.1 \pm 0.5$ and $\mathcal{F}_2 = 132.0 \pm 1.3$, thus giving an additional average loss of $\alpha = (0.29 \pm 0.04)\%$ or (0.013 ± 0.002) dB. Neglecting other additional losses, this corresponds to a pure lateral misalignment of $m = 150$ nm or a pure angular misalignment of $\theta = 6.3 \times 10^{-3}$ rad $\approx 0.36°$. These losses are an upper limit for the SU-8, since many other losses are unaccounted for, eg. the fibre core-cladding eccentricity or the polished fibre facets.

To test thermal stability, the temperature of the substrate is varied between 20 and 70 ℃. The finesse of the inserted fiber resonator shows no change during heating. Another test for the quality of the SU-8 structures is a finesse measurement as a function of the gap size. One measurement is done in the SU-8 structures and one outside the structures. The measurement outside is performed with nano positioning stages, which in principle can be tuned to a few nanometers. With the positioning stages the finesse is optimized. Nevertheless, the finesse obtained inside the SU-8 structures always remains higher than the ones obtained using the positioning stages. The results of these measurements are shown in Fig. 6.10a). The structures have also allowed long-term stability of a fibre cavity

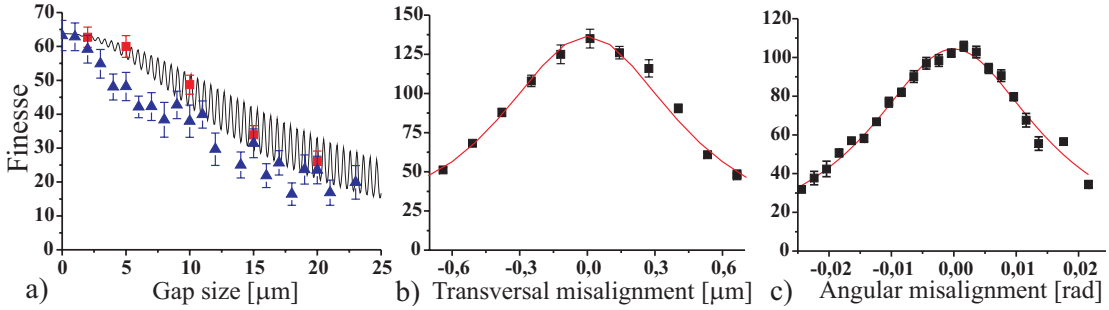

Figure 6.10: Measurement of the finesse of a fiber cavity as a function of the gap size is shown in a). The oscillating function shows the theoretical curve for the finesse with varying gap size. The oscillation of the finesse is due to the multiple reflections between the facets and the mirrors. The red squares correspond to the finesse measured for a cavity mounted inside a SU-8 structure. The blue triangles correspond to a finesse measurement where the cavity is held by precision translation stages. Graph b) shows the finesse of a different cavity measured as a function of transversal misalignment. In c) the finesse is plotted as a function of angular misalignment.

in a high-vacuum environment. The fibre cavity used in the setup keeps its finesse of ≈ 20 for over one year without realignment.

In summary, a method for aligning fibers on a flat surface by using SU-8 superstructures was developed. The aligned fibers represent a Fabry-Perot-type resonator for atomic physics to detect atoms. Then the layout of the SU-8 alignment structures was introduced, which enables easy positioning and alignment, and because of the undercut sidewall profile, also offers a method of fixing the fiber position. To achieve this structure, the lithographic process was optimized. Furthermore a technique for quantifying the losses due to misalignment is demonstrated with the help of the fiber resonator itself. The finesse measurement indicated that the SU-8 superstructures are of superior quality.

Structures specific to this experiment

The process of the SU-8 structure fabrication was explained in the last section. In the experiment three different types of fibre detectors are implemented. The cavity and the absorption detector need a straight SU-8 design, whereas for the fluorescence detector a 90° design of the SU-8 structures is used. Figure 6.11 shows the used setup. The atom chip and the lithography mask for the SU-8 structures is aligned with the help of several markers around the atom chip. Due to surface tension the SU-8 photo resist is contracting at the edges of the sample. This will change the thickness of the resist. To have a stable repeatable process (and to have these effects far out), the chip substrate has a dimension of $\approx$ 50x50 mm^2 in the beginning.

The used fibres diameter is 125 ± 1 µm. Due to the (small) variation in diameter 7 trenches are integrated with the SU-8 structures (Fig. 6.11). The difference is the trench width, which ranges from 123.5 µm to 126.5 µm with 0.5 µm steps between. To find the right width, each trench had to be tested with a cavity.

For the 90° SU-8 structures only 3 trenches were integrated. For the fluorescence detector the accuracy was less critical, than for the cavity. The trench widths in this case are

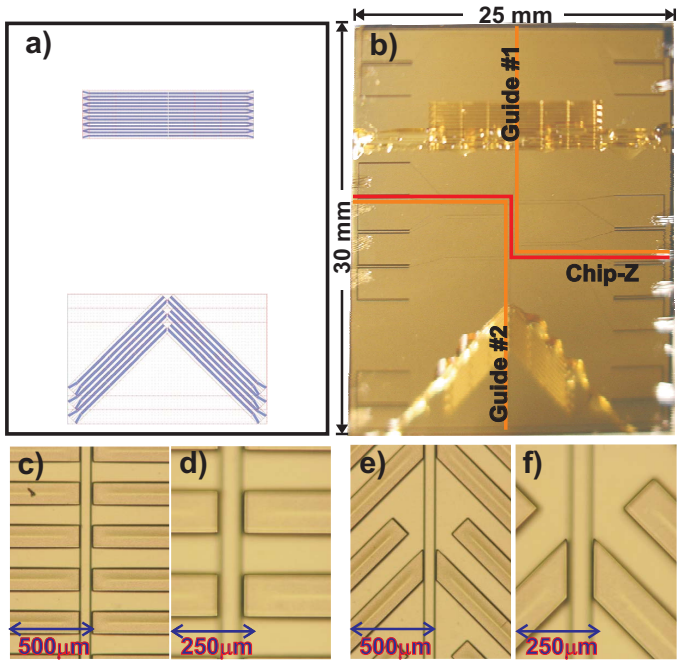

Figure 6.11: SU-8 structures on the atom chip. **a)** shows the mask for the SU-8 structures. In **b)** the chip with the applied SU-8 structures is shown. **c)-d)** shows a magnification of the straight SU-8 structures. **e)-f)** shows a magnification of the 90° SU-8 structures. In the middle of the magnified pictures the wire guide can be seen. Two separate wire guides are used. The first leads to the cavity and absorption detector, the second to the fluorescence detector.

124.5 µm, 125.0 µm and 125.5 µm.

After the SU-8 integration, the chip is cut to the final dimensions of 30×25 mm^2 with a wafer saw[3] also removing the markers for alignment.

6.5 Chip bonding and integration on the mounting

The achieved precision with the SU-8 structures is necessary for the cavity. For the absorption and fluorescence detector however, the precision does not need to be better than 2 µm. Thus for the latter two detectors the SU-8 structures are very well suited for the integration of the fibres on a flat surface. Figure 6.12 shows several pictures of the integration process of the chip on the chip mounting and of the fibres on the chip. After the chip is cut it is attached to the chip mounting. The upper Shapal block has a counterbore of the same dimensions as the chip. Its height is only 0.65 mm, whereas the chip's height is 0.7 mm. Thus the optical access to the chip's surface is not blocked by the Shapal from the sides. One side of the Shapal block is open, thus the chip can be slid in. The advantage of the counterbore is the self-alignment of the chip on top of the mounting. The chip is then glued to the block. The next step is to connect the chip to the copper pins via bonding wires (see also section 4.2). After that the fibres are integrated. This must be done under a microscope and with the help of µm translation stages. As soon as the fibres are threaded into the SU-8 structures, they are additionally glued onto the chip (although the fibres are already clamped down by the SU-8 structures).

The ready chip mount is then integrated into the vacuum system. Moderate back-out temperatures[4] can be used to improve the final vacuum.

[3] The accuracy of the saw is better than 5 µm. Institut für TI Mannheim.
[4] Up to 100°C.

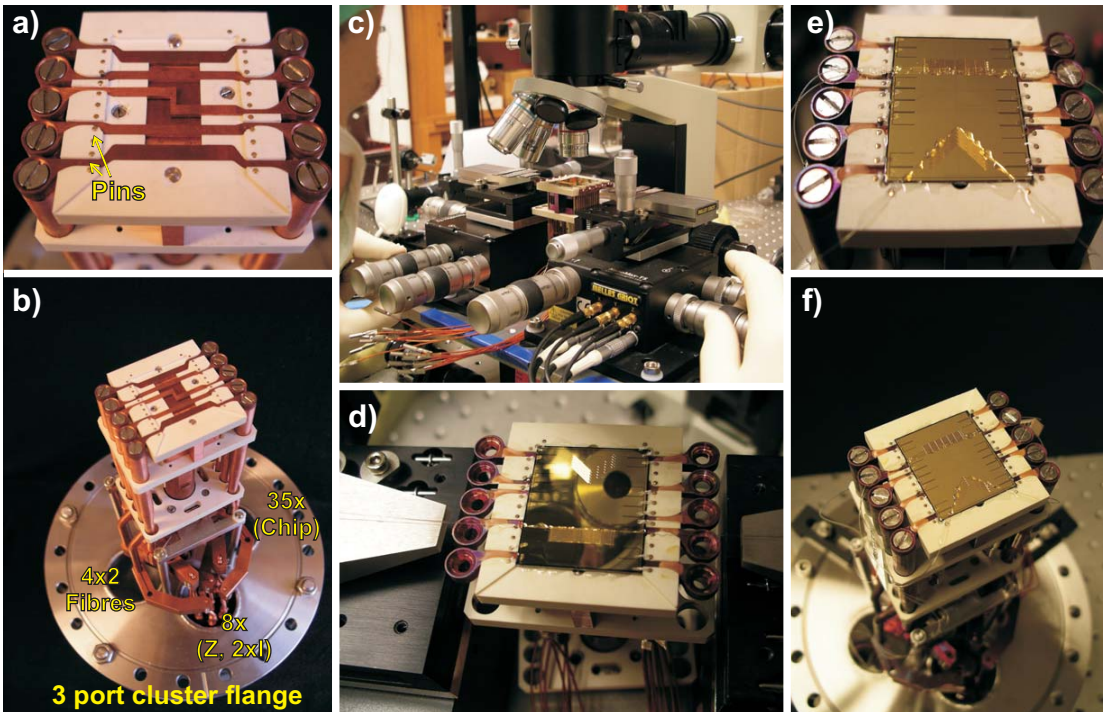

Figure 6.12: Chip integration. **a)** and **b)** show the chip mounting without the chip. In **c)** and **d)** the chip is glued to the mounting and the fibers are being integrated. This is done under a microscope and with the help of µm translation stages. **e)** and **f)** show the final result of the chip mounting with the chip and the three fibre detectors integrated.

7 Computer control and data acquisition

7.1 Labiew Control

The heart of every modern experiment is the computer interface. In the following a brief overview over the computer system will be given. This system mainly consists of data acquisition (DAQ) devices from National Instruments[1]. These are available as PCI-bus type computer cards. For TTL signals, which require precise timing, FPGA programable

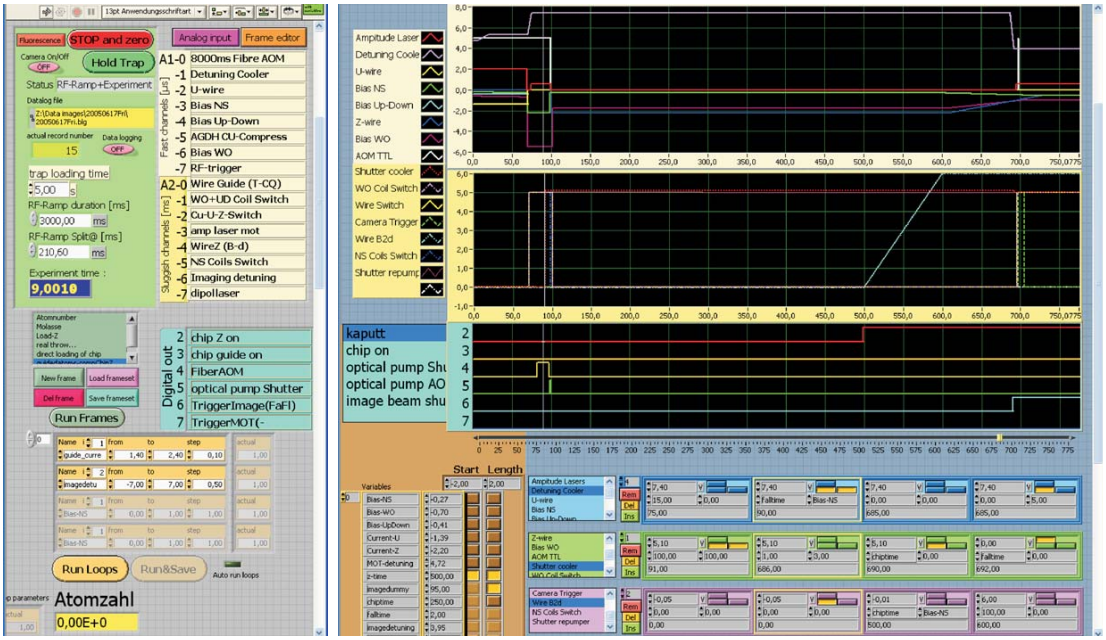

Figure 7.1: Screen shot of the main experimental control program. It was written in Labview. 16 analog-out, 8 digital-out and 16 analog-in channels can be controlled with the program.

devices[2] are used. The FPGA offers several advantages. Complicated pulse trains can be generated with high timing accuracy. Logical tests can be performed without modifying the hardware, as is usually done using regular TTL-electronics. These can be programmed in Labview and via an USB interface. The PCI cards have to be distributed between several computers. To have the computers on the same grounding as the rest of the experiment,

[1] National Instruments Germany GmbH, München, Germany.

[2] Physikalisches Institut, Universität Heidelberg. Now available as "Nembox" at W-IE-NE-R, Plein und Baus GmbH, Burscheid Germany.

the computers are integrated into the experimental setup. The computers are connected by an opto-electronic and wireless network card not to be connected to the ground of the computer network. The main control program is shown in Fig. 7.1. The program is written in Labview, a programming language from National Instruments (NI). With the program 16 analog-out, 8 digital-out and 16 analog-in channels can be controlled. The card with the digital pulses provides the master trigger. All the DAQ-cards in the other computers and the FPGA boxes are triggered by this digital card.

One card is used to acquire the data from the different detectors (NI-6221). Analog-in channels or counter-channels (max. 2 counters) can be used to collect the data. For taking the pictures with the two cameras of the imaging system two PCI interface cards are available. They are connected with the cameras via a network cable. The camera software is written in Labview and provides some preliminary data analysis of the pictures (Heine, 2007). The cameras can be controlled via TCP/IP from the main control program.

The cards and hardware for controlling the experiment are summarized in table 7.1.

Hardware	Function	Channels
1x NI-6602	digital out	8
2x NI-6713	analog out	2×8
1x NI-6035E	analog in	1-2
1x NI-6221	analog/digital in	2
2x FPGA	digital out	2×8

Table 7.1: Hardware used for generating analog/digital signals and for data acquisition. Only a certain number of channels was used for each card. This is specified in the last column.

The signals for in-/output are connected to custom built in- and output boxes[3], which provide opto-coupling (for TTL signals) and buffer amplifiers (for analog signals). Noise, ground loops and cross talk can be minimized with these boxes. The buffers in the boxes are better suited to drive (longer) BNC cables than the PCI cards only. For the circuit diagrams and further details see Wilzbach (2002).

[3]Labview Steuerungsboxen A374-0, A373-0, Physikalisches Institut, Universität Heidelberg.

Part III

Fibre Detection

8 Introduction and Overview

8.1 Experimental setup

The following part deals with the detection of atoms by integrated fibres on the atom chip. First a brief overview of the experimental setup for the fibre detection will be discussed. Then the experimental methods are outlined. Important quantities such as background signals, intensity stability and detector properties will be evaluated. To be able to measure a signal at the detector several experimental steps are necessary. The atoms are collected in the MOT, then loaded to a magnetic trap on the chip and finally transferred to the magnetic guide. The guide leads the atoms to the fibre detectors. A typical timing of the experimental parameters for the detection is discussed at the end of this chapter

The purpose of the chip is to guide atoms to three different detectors. This is accomplished by two magnetic guides that can funnel atoms from the initial magnetic trap through the detection zones. A full view of the atom chip and its detectors is shown in Fig. 8.1. The three main structures on the atom chip for magnetically trapping (Chip-Z) and guiding (guide 1, 2) the atoms are indicated. Guide 1 leads to the absorption detector **(b)** and the fibre cavity **(a)**. The absorption detector is first passed by the atoms, before they enter the cavity. Guide 2 leads to the fluorescence detector **(c)**. Note that only one guide and one detector can be operated at the same time. For each type of fibre detector a single mode fibre and a multi mode fibre are fed through into the vacuum chamber. To have the probe light in the detectors, it must be coupled from the probe laser beam into one of the detectors. The fibre coupling of laser light is shown in Fig. 8.2. Two lasers can be coupled into two independent fibre couplers at once. To be able to switch off the lasers, the imaging/probing laser and the dipole laser each go through an AOM[1] and the first diffraction orders are coupled into a 2x2 fibre coupler[2]. Light that is coupled into any of the four ports, leaves the coupler at two ports on the other side, with a split ratio of 50/50. One port is connected via a fibre splice[3] to a single mode fibre of one of the fibre detectors. The other 50% of the light which leave the 50/50 coupler are used for intensity stabilization. In the case of very low intensities, the light intensity must be stabilized before coupling into the 50/50 coupler. A beam sampler[4] is placed after the AOM and a part of the light is used to intensity stabilize the imaging/probing laser. To be able to insert an optical bandpass filter the light leaving the vacuum chamber is coupled out by a fibre coupler. After passing though the optical bandpass filter the light is coupled into a fibre leading to the detector. The setup is shown in Fig. 8.3. The signal of the detector is then recorded with a computer data acquisition system.

[1] Crystal technology acousto-optic modulator. Model 3110-120.
[2] Newport Single-Mode Coupler: 2x2 50/50 (3 dB) Coupler F-CPL-S22855.
[3] Newport fibre optical splice F-SK-SA.
[4] Thorlabs beam sampler BSP10-B1.

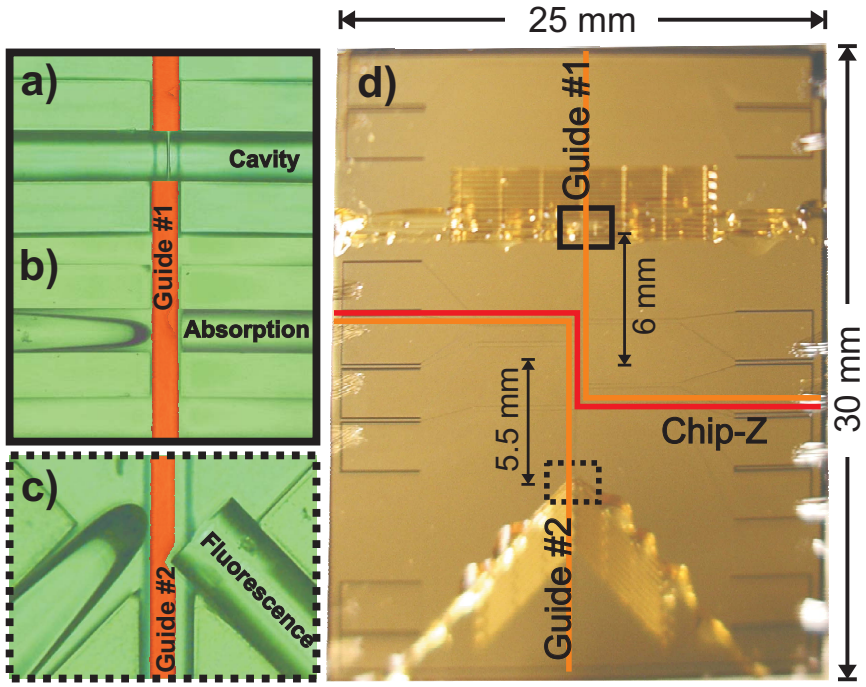

Figure 8.1: Overview of the atom chip and the different integrated detectors. The complete chip is shown in **(d)**. The three main structures for magnetically trapping and guiding the atoms are emphasized. With the Ioffe-Pritchard trap (Chip-Z) the atoms are initially trapped. Afterwards the atoms can be transferred to guide 1 or to guide 2. Guide 1 leads to the absorption detector **(b)** and the fibre cavity **(a)**. First the atoms enter the absorption detector and then the cavity. Guide 2 leads to the fluorescence detector **(c)**. The distances from the center of the chip-Z to the detectors were 5.5, 6.0 and 6.5 mm for the fluorescence detector, absorption detector and the cavity.

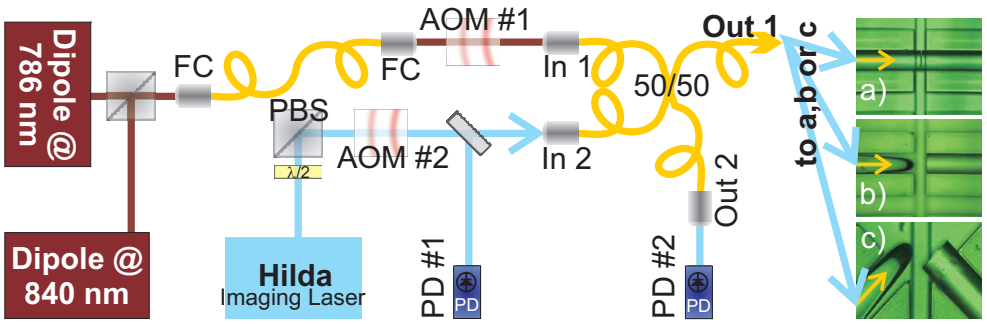

Figure 8.2: Coupling of the probe and dipole laser light into the fibres leading into the vacuum chamber. To be able to switch the lasers, they go through AOMs. Both lasers are coupled into a 50/50 fibre coupler (In 1 and In 2). One output (Out 1) or a part of the beam before In 2 can be used to intensity stabilize the imaging laser. The part of fibre leading to Out 2 is inserted into a SM fibre polarization controller. That enables the control of the polarization of the light. Out 2 is connected via a fibre splice to the single mode fibre, which leads to one of the detectors **a), b)** or **c)**. Note, that additional optics like lenses, pinholes etc. were omitted here, when they were not important for understanding the setup.

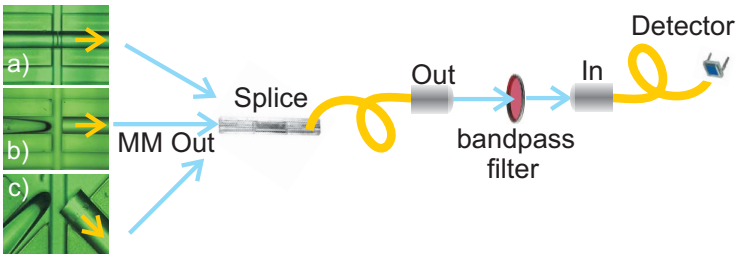

Figure 8.3: Output from fibres out of the UHV chamber. The multi mode fibre leaving the chamber is connected via a splice to a second multi mode fibre. This fibre leads to a fibre coupler. In the beam path different optical elements, like bandpass filters, can be placed. Then the light is again coupled into a multi mode fibre, which is connected to the detector.

8.1.1 Intensity stabilization

To have a stable light source for probing the atoms, it must not only be stable in frequency but also in intensity. This section will describe the method of light intensity stabilization. As shown in Fig. 8.2 there are two options, where the fibre coupled light can be intensity stabilized. One option uses the light directly after the AOM, the second one uses the light leaving the 50/50 fibre coupler. The advantage of stabilizing the light after the 50/50 coupler is to include fluctuations in the coupler. The disadvantage appears at very low light levels, when the signal is too weak to use it for intensity stabilization. Then the light directly after the AOM must be used. The PID controller[5] was built at the institute. The function of the PID is shown in Fig. 8.4. The input signal from the photodiode is compared to an adjustable offset of the PID card. The control signal of the PID card then is connected to the amplitude control of the AOM driver for the imaging laser. The light

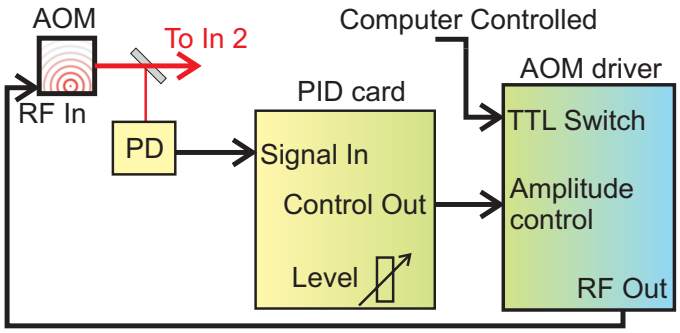

Figure 8.4: Schematic feedback loop for intensity stabilization. A part of the diffracted laser light is detected on a Photodiode (PD). This signal is compared on the PID card with an adjustable signal level. If the difference is unequal to zero, the PID card will change the voltage of the amplitude control of the AOM driver to adjust the intensity. Additionally the AOM driver can be switched off via a TTL pulse from the computer control system.

level for intensity locking is held constant. When a different intensity is needed, only the fibre coupling is changed by inserting optical density filters or by misaligned fibre couplers. The reason for this procedure is the AOM itself. The relationship between applied RF power and the light power diffracted into the different orders is linear only in a small band. If possible only minor intensity adjustments are done via setting the level on the

[5]Physikalisches Institut, PI-Regler A368F.

PID card. A typical lock shows intensity fluctuations of 0.8 nW on an overall light level of 160 nW. Thus the intensity is stabilized to a ratio better than 5/1000. It is important to mention that the intensity is stabilized *before* entering the fibre into the vacuum chamber. What happens in the fibre on the way into the vacuum can not be controlled. A standard procedure during an experimental cycle is to switch off the AOM's via the TTL input of the AOM drivers. At first sight this seems to be a problem for the intensity lock, since it tries to compensate for the sudden switch off. That means the control voltage is set to a maximum by the PID controller. As soon as the TTL switch is deactivated, the AOM will run at full power. It turns out to be no problem, since the lock can recover in less than 1 ms. Only for the first millisecond the light levels are quite high. At this time the atoms are still a few millimeters away from the detection zone.

Measurement of the fluctuations In the following paragraph the intensity stabilization will be quantified with the help of a statistical analysis of the measured light fluctuations. For a laser well above threshold, the light intensity has a Poissonian distribution. That leads to the following relation for a constant light intensity X:

$$\frac{\mathrm{var}(X)}{\langle X\rangle} = 1, \tag{8.1}$$

with the variance $\mathrm{var}(X)$, the expectation value $\langle X\rangle$ and the dataset X. The dataset X consists of several data points. Another dataset Y is introduced, which expresses additional (non Poissonian) fluctuations of the laser light. It is assumed to be independent from X and has the following properties:

$$Y = \{y_1, y_2, \ldots, y_N\} \tag{8.2}$$
$$\langle Y\rangle = 0. \tag{8.3}$$

One easily calculates the following properties:

$$var(X+Y) = var(X) + var(Y) + covar(X,Y) = var(X) + var(Y), \tag{8.4}$$
$$\langle X+Y\rangle = \langle X\rangle + \langle Y\rangle = \langle X\rangle, \tag{8.5}$$

where the covariance $covar(X,Y) = 0$ for independent data sets.

If a binning for the dataset is introduced, the result is a new dataset ${}_BX$. B is an integer divisor of the length of the dataset X.

$$X := \{x_1, x_2, \ldots, x_N\} \tag{8.6}$$
$${}_BX := \left\{ \sum_{i=1}^{B} x_i, \sum_{i=B+1}^{2B} x_i, \ldots, \sum_{i=(m-1)B+1}^{N} x_i \right\}, \tag{8.7}$$

where $N = m \times B$ and $B, m \in \mathbb{N}$. For a Poissonian distribution the variance and expectation value can be calculated to $var({}_BX) = B\, var(X)$, $\langle {}_BX\rangle = B\langle X\rangle$. This yields

$$\frac{\mathrm{var}({}_BX)}{\langle {}_BX\rangle} = 1\,,\ \forall B.$$

For no binning ($B = 1$) the sampling interval was 10 µs, which was the maximum resolution of 100 kHz of the counter card. If there are only Poissonian fluctuations from the laser light, then the above fraction always becomes one, independent of the used binning **B**. But if additional fluctuations Y are taken into account, then the variance and expectation value become

$$var\left({}_B(X+Y)\right) = var({}_BX) + var({}_BY) = B\,var(X) + var({}_BY) \tag{8.8}$$

$$\langle {}_B(X+Y)\rangle = \langle {}_BX\rangle + \langle {}_BY\rangle = B\langle X\rangle. \tag{8.9}$$

Now the variance over the expectation value looks different:

$$\frac{var\left({}_B(X+Y)\right)}{\langle {}_B(X+Y)\rangle} = \frac{B\,var(X) + var({}_BY)}{B\langle X\rangle} = 1 + \frac{var({}_BY)}{B\langle X\rangle}. \tag{8.10}$$

This can be simplified for some cases to

$$var({}_BY) \propto \begin{cases} B & \text{if } y_i \text{ are random numbers} \\ B^2 & \text{if } y_i \text{ correlate to } x^k,\ k \geq 1 \\ B^2 & \text{if } y_i \propto \sin(2\pi k) \text{ and } 2\pi k \ll B\Delta t \\ 0 & \text{if } y_i \propto \sin(2\pi k) \text{ and } 2\pi k \gg B\Delta t. \end{cases}$$

The variance for a sinusoidal fluctuation approaches zero, as soon as the binned time interval becomes larger than the period. If the period is much greater than the binned time interval, then a sinusoidal fluctuation is not smoothed out by the binning.

$$\frac{var({}_BY)}{B\langle X\rangle} \propto \begin{cases} 1 & \text{if } y_i \text{ are random numbers} \\ B & \text{if } y_i \text{ correlate to } x^k,\ k \geq 1 \\ B & \text{if } y_i \propto \sin(2\pi k) \text{ and } 2\pi k \ll B\Delta t \\ 0 & \text{if } y_i \propto \sin(2\pi k) \text{ and } 2\pi k \gg B\Delta t. \end{cases}$$

Figure 8.5 shows a few measurements to specify fluctuations additionally to the Poissonian fluctuations. Note, that the stabilization is done with a photodiode at a much higher light level outside the vacuum chamber, but the measurement is done at low count rates with a single photon counting module (SPCM). The photons are collected with one of the fibre detectors. Low count rates are used to be in a linear regime of the SPCM. The fraction $var({}_B(X+Y))/\langle {}_B(X+Y)\rangle$ is plotted as a function of the binning **B**. The binning is given in multiples of the resolution limit of 10 µs. One plot shows a measurement with high fluctuations. The slope of the fitted line is 3.0×10^{-3}. The reason for the high fluctuations was the multi mode fibre leading to the detector. Both fibre facets were flat polished. This leads to internal reflections generating interferences and intensity fluctuations. The fibre was exchanged with an angle polished fibre, where the facets show a 8° angle. Interferences can not build up. In the second plot (**b)** two measurements with the new fibre are shown. The one with the (relatively) high slope (9.4×10^{-5}) is without intensity stabilization, the one with the smaller slope (1.7×10^{-5}) is with the intensity stabilization activated.

The measurements show that $var({}_B(X+Y))/\langle {}_B(X+Y)\rangle$ rises linear for a binning up to 2000 (20 ms). This means, that the periods of the fluctuations are smaller than 20 ms (50 Hz). Assuming linear or slow fluctuations the order of magnitude of the fluctuations

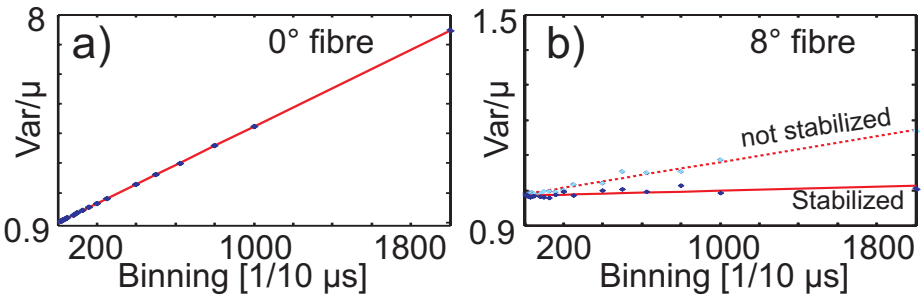

Figure 8.5: The variance over the expectation value is plotted as a function of the binning. **a)** shows a measurement with high fluctuations. The slope of the fitted line is 3.0×10^{-3}. The reason for the high fluctuations was the multi mode fibre leading to the detector. Both fibre facets were flat polished. This leads to internal reflections generating interferences and intensity fluctuations. The fibre was exchanged with an angle polished fibre, where the facets show a 8° angle. Interferences can not build up. In **b)** two measurements with the new fibre are done. The one with the high slope (9.4×10^{-5}) is without intensity stabilization, the one with the smaller slope (1.7×10^{-5}) is with the intensity stabilization activated.

can be expressed with the following expression:

$$1 + \frac{var({}_B Y)}{B\langle X\rangle} = 1 + \frac{var(Y) \times B^2}{B\langle X\rangle} \tag{8.11}$$

$$= 1 + \frac{var(Y)}{\langle X\rangle} B. \tag{8.12}$$

The slope is given by

$$c = var(Y)/\langle X\rangle,$$

and can be measured. Some exemplary measurements are given in Fig. 8.5. This yields the $var(Y)$ for no binning:

$$var(Y) = c \times \langle X\rangle.$$

The standard deviation is then

$$\sigma(Y) = \sqrt{var(Y)} = \sqrt{c\langle X\rangle}.$$

For the slopes in Fig. 8.5, the following results are calculated

$$\sigma(Y) = \begin{cases} 0.076 & \text{for a } 0° \text{ fibre} \\ 0.017 & \text{for a } 8° \text{ fibre, intensity unstabilized} \\ 0.0075 & \text{for a } 8° \text{ fibre, intensity stabilized.} \end{cases}$$

Translating this table into intensities, the non-Poissonian laser light fluctuations are given as $\Delta I/I = \sigma(Y)/\langle X\rangle$ and are

$$\frac{\Delta I}{I} = \begin{cases} 3.9\% & \text{for the } 0° \text{ fibre} \\ 0.55\% & \text{for the } 8° \text{ fibre unstabilized} \\ 0.22\% & \text{for the } 8° \text{ fibre stabilized.} \end{cases}$$

Exchanging the fibre to an angle polished one decreases the intensity fluctuations by a factor of 7, whereas intensity stabilizing the laser again decreases the fluctuations by almost a factor of 2. This is comparable to the directly measured 0.5% fluctuations on the photodiode used for stabilization. The decrease in fluctuations by a factor of ≈ 2 may not be worth the effort of stabilization. But most methods to improve the signal are scaling with a square root, thus in principle a factor of $2^2 = 4$ is gained in accuracy. Moreover long term drifts in intensity are not included in the above error treatment. These will be eliminated by the intensity stabilization, too. This will allow to take longer sequences of measurements, which is important for statistical analysis. Stabilizing the light intensity is therefore a prerequisite, if one has to take data for statistical analysis.

8.1.2 Detector calibration

With the results of the characterization of section 8.1.1 in mind, the properties of the different detectors used can be specified. In the experiment different light levels are faced, that is why different detectors have to be used. Each detector is well suited for a limited range of light intensity. A single photon counting module (SPCM), a photomultiplier tube (PMT) and a silicon photodiode (PD) is used. The SPCM is used for light levels ranging from 0 pW up to 2.5 pW, the PMT for powers ranging from a few pW up to a nW. The PD can be used from the pW regime up to one mW. The noise figures are best for the SPCM; the PMT noise figures are better than those of the PD.

SPCM The single photon counting module (SPCM) used in the setup[6] has the characteristics summarized in tab. 8.1. It detects single photons with a quantum efficiency of about 57% (at λ =780 nm). As each photon is detected, a TTL pulse is created with a typical pulse length of 31 ns. This signal is acquired with a counter card[7] at a clock rate of 100 kHz.

Parameters	Typical value
Dark Counts	250 Hz
Max.light count	15 MHz
Dead time	55 ns
Pulse width	31 ns
Afterpulse prob.	0.5%

Table 8.1: Typical parameters for the single photon counting module according to the data sheet. Some parameters will be checked by own measurements.

Mandel's parameter A laser well above threshold has a Poissonian photon distribution. Let k be the number of photon counts in a time interval and $\langle k \rangle$ the expectation value. $\langle k \rangle$ is then given by a proportionality factor η_I and the intensity I_D at the detector.

$$\langle k \rangle = \eta_I I_D.$$

[6] PerkinElmer SPCM-AQR-12-FC.
[7] National Instruments PCI-6221.

A complete derivation can be found in Hillesheim and Müller (2003), Müller (2004). The Mandel's Q factor is a parameter to characterize the photon count distribution and is given by

$$Q = \frac{var(k) - \langle k \rangle}{\langle k \rangle}.$$

For a Poissonian distribution $Q = 0$ holds, which implies that the variance is equal to the mean. Since photon detectors are not ideal, there are effects which must be taken into account. For a SPCM this can be a after-pulsing probability as well as a dead-time, after a photon is counted. These effects will result in an abberation of the measured distribution. Mathematically the effects of the dead time and the after-pulses change the computation of the Q parameter (Finn et al., 1988) to

$$Q = 2p_a - 2\langle k \rangle f_s \tau_d = 2p_a - 2I\tau_d,$$

where $I = \langle k \rangle \times f_s$ is the photon count rate (in Hz), f_s the sampling frequency, p_a the after-pulsing probability and τ_d the dead-time. If Q is plotted vs. the count rate, the plot will be linear with a slope of $-2\tau_d$ and a y-intercept of $2p_a$.

Dead-time and After-pulsing probability In Figure 8.6 Mandel's parameter is plotted as a function of the count rate for the used SPCM. A linear fit yields a dead-time of (60 ± 5) ns and an after-pulse probability of $(1.6 \pm 0.3)\%$. The device specific data-sheet includes a dead-time of 55-60 ns, which agrees with the measurement. A general data-sheet states a typical after-pulse probability of 0.5%. The measurement shows a deviation from the given number.

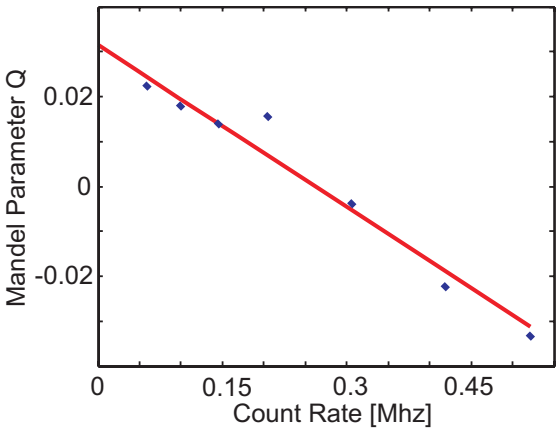

Figure 8.6: Plot of Mandel's Q parameter as a function of the count rate. A line is fitted to the data. The slope is a measure of the dead-time of the system. The y-intercept is related to the after-pulse probability. The used SPCM has a dead-time of (60 ± 5) ns and an after-pulse probability of $(1.6 \pm 0.3)\%$.

Noise equivalent power A useful quantity for the characterization of photodiodes is the noise equivalent power (NEP). The NEP (www.hamamatsu.com, 2007) is the amount of light equivalent to the noise level of a device. Stated differently, it is the light level required to obtain a signal-to-noise ratio of unity. In data sheets the NEP values are usually given for the peak wavelength λ_p. Since the noise level is proportional to the square root of the frequency bandwidth, the NEP is measured at a bandwidth of 1 Hz.

$$NEP = \frac{I_C}{S_\lambda},$$

where the noise current I_C is given in $A/\sqrt{Hz}$ and the photo sensitivity S_λ is given in A/W.

Photomultiplier Tube The photomultiplier tube[8] (PMT) has a quantum efficiency of 8% and a radiant sensitivity of 60 mA/W at λ=780 nm. The specified internal gain was measured to be $(4.5 \pm 0.2) \times 10^5$ at a supply voltage of 1250 V, which fits to the number given in the data sheet. The advantage of the PMT is the noise free intrinsic amplification between the dynodes. The amplification afterwards (not free of amplification noise) therefore can be smaller by that factor. This allows in turn to increase the bandwidth of the overall electronics chain.

Photodiode The silicon PIN detector[9] under investigation has a responsitivity of 0.52 A/W at λ=780 nm. The noise equivalent power (NEP) is given with $1.2 \times 10^{-14}\,\mathrm{W}/\sqrt{\mathrm{Hz}}$. For a signal to noise ratio of unity and a bandwidth of 100 kHz and 1 kHz the minimal detectable power is 3.8 pW and 0.38 pW. This fully agrees with the measurements. The diode capacitance is $\mathrm{C_J}$=20 pF and the bandwidth for a given load $\mathrm{R_{Load}}$ is

$$\mathrm{f_{BW}} = \frac{1}{2\pi \mathrm{R_{Load}} \mathrm{C_J}}.$$

Table 8.2 compares the photodiode with the PMT. The bandwidth is given according to the amplifiers datasheet[10] and the responsitivities to the detectors' data sheet. The other parameters are measured or calculated. A low power limit at a signal to noise ratio (SNR) of one gives the smallest detectable power difference at the given bandwidth. With the PD and a bandwidth of 1 kHz it is possible to measure a light intensity difference of 0.4 pW with a SNR of one.

	Photodiode	Photomultiplier Tube
Gain (intrinsic)	1*	$(4.5 \pm 0.2) \times 10^5$
Amplification	10^{9}*	10^{5}*
Bandwidth	1 kHz *	400 kHz [1 kHz]*
lower limit (SNR=1)	(0.4 ± 0.07) pW	(1.2 ± 0.2) pW [60 fW]
NEP	$(1.2 \pm 0.2) \times 10^{-14} W/\sqrt{Hz}$	$(2 \pm 0.4) \times 10^{-15} W/\sqrt{Hz}$
Responsitivity	0.52 A/W *	60 mA/W *

Table 8.2: Comparison of the parameters for the photodiode and the photomultiplier tube. Note that for the PMT two different bandwidths are given. The lower bandwidth of 1 kHz in [brackets] is not used in the experiment. It is given here to have a comparison to the photodiode, where the amplification must be 10^9 (and therefore the bandwidth is 1 kHz). Values marked with an asterisk are taken from the data sheets, the remaining values are measured or calculated. Linear responses can be expected for powers up to 1 mW and 2 nW for the photodiode and the PMT (without amplifiers).

The given lower power limit is valid only as long as the shot noise of the light is not becoming bigger than this limit. In the case of 0.4 pW (at 1 kHz) the absolute power must

[8] Hamamatsu R636-10 PMT, HA Coating.
[9] Thorlabs DET110.
[10] Femto DLPCA 100 low noise current amplifier.

not get above 640 nW – of course then the amplification has to be changed at such high light levels to avoid saturating the amplifier).

8.1.3 Experimental Cycle

The above detectors are used in the experiment for atom detection. To be able to measure a signal at the detector several experimental steps are necessary. First the MOT is loaded, then the atoms are magnetically trapped on the chip and finally the atoms are transferred to the magnetic guide. The guide leads the atoms to the fibre detectors. A typical timing of the experimental parameters for the detection is displayed in Fig. 8.7.

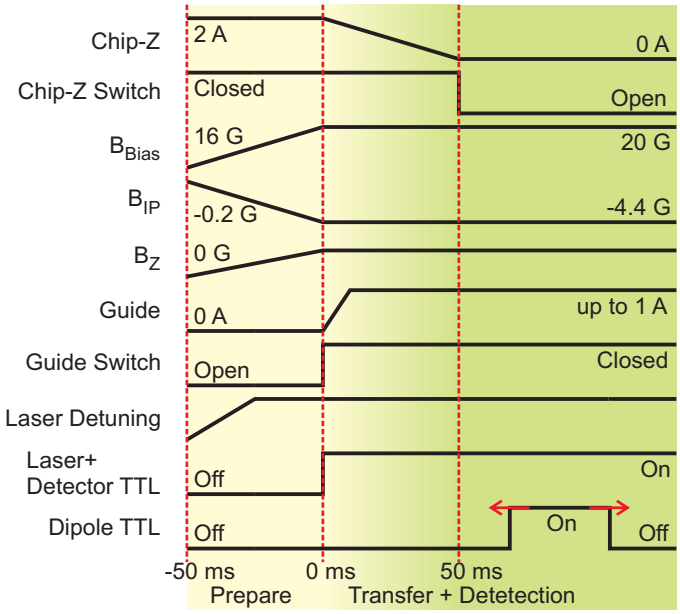

Figure 8.7: Timing diagram for fibre detection. The steps can be divided into three main steps. **Prepare** runs from -50 to 0 ms. **Transfer** from 0 to 50 ms and **Detection** runs from 0 to 1000 ms.

The timing can be divided into three, overlapping sequences:

Prepare (-50 to 0 ms) The magnetic fields are ramped up in such a way that a good mode match of the chip-z magnetic trap with the magnetic trap of the guide is achieved. The vertical magnetic field B_z is usually zero, but for some measurements it is ramped up in the preparation process. The imaging laser is set to the probing frequency by the frequency offset lock.

Transfer (0 to 50 ms) The current source of the guide is switched on and ramped up in 10 ms from zero to the final value. (The guide is established at 10 ms.) Meanwhile the current of the chip-z is ramped down in 50 ms to zero and is completely kept at zero with the switch after that 50 ms.

Detection (0 to 1000 ms) The detection starts already at 0 ms. The imaging laser and the dipole laser can be switched on/off at any time during detection by acousto-optical modulators and mechanical shutters. For most measurements however the imaging laser was simultaneously switched on with the detector and the data recording.

9 Fluorescence Detector

9.1 Overview

One way of detecting an atom is to observe its fluorescence. The basic idea is to drive a transition of the atom to an excited state with an external light field and to detect the spontaneously emitted photons. In principle one scattered photon is sufficient to detect a single atom. The sensitivity of the detection and its fidelity depend on the detection efficiency of the scattered light and the suppression of background noise. Atom detection is limited by the amount of light collected. Therefore high numerical aperture collection optics is desirable. In a realistic setting the collection efficiency is much less than unity and it is essential to let each atom scatter many photons. This is best achieved by driving closed transitions. In principle, there is no fundamental limit to the efficiency of a fluorescence detector as long as the atom is not lost from the observation region. The disadvantage of fluorescence detection is the destructive nature of the process. The internal state of the detected atom will be altered, and heating of atoms due to spontaneous emission is almost unavoidable.

In this chapter the fibre fluorescence detector is characterized with the help of different measurements. First it starts with the description of the background signals and how to prevent/reduce them. That is an important quantity, since fluorescence detectors are only limited by the background (and the measurement time). The detection efficiency is explained and derived. Then a typical signal is shown. The arrival time of the atoms agree with a 1-D Maxwell-Boltzmann distribution. The distribution is calculated and is extended with a Monte Carlo simulation to cover the complete experimental situation. The standard measurement procedure is to keep all parameters constant and take the atom signal for one cycle, and change parameters only for the next experimental cycle. Therefore a timing information is always acquired.

It is important to understand how the levels behave due to the Zeeman shift in the magnetic guide. That is why the next step is to take the spectroscopy of the $|2, m_F\rangle \rightarrow |F', m'_F\rangle$ transition and to compare the measured with the theoretical values. Then the transition to the $|3, m'_F\rangle$ excited state is evaluated for different laser powers and laser detunings. Another point is to determine the number of atoms in the magnetic guide. Three different methods are used. One is to use absorption imaging with the external camera system, the other method is to use the $|2, m_F\rangle \rightarrow |1, 1\rangle$ transition to determine the number of atoms. The third one is a statistical approach. The different methods will be explained and their advantages and disadvantages are discussed in detail. Also the number of photons which are scattered per atom can be derived. This leads to the detection probability for a single atom.

The multi mode fibre has a limited field of view. The atoms may already scatter outside that field of view. Therefore geometrical detection effects will be examined. This will be

accomplished with the help of different illumination techniques.

Then different tomographic pictures of the magnetic guide are taken. Therefor the minimum of the guide is shifted perpendicular to the chip wire as well as sidewards. From these measurements pieces of information about the atomic distribution in the magnetic guide are acquired. Finally the tomographies are repeated for radio-frequency (RF) cooled atoms. Both measurements are compared and the effect of cooling onto the distribution of the atoms in the magnetic guide can be evaluated.

9.2 Background evaluation

In the following the background of the fluorescence detector will be evaluated. This is one of the most important quantities of a fluorescence detector. The MOT beams hitting the chip with a power of 185 mW cause high background light levels in all detectors. The power of the stray light out of the MOT that is coupled into the 90° MM detector is measured to be 320 pW[1]. This relates to a suppression factor of almost 10^{-9}. Still, the 10^9 photons/s reaching the detector are too much for a single photon detector. For that reason special attention has to be payed during operation of sensitive detectors, e.g. by closing a shutter or by switching off the detector during the MOT phase. In this case the sensitive detectors were switched off during high light levels. Most of the background noise sources can be

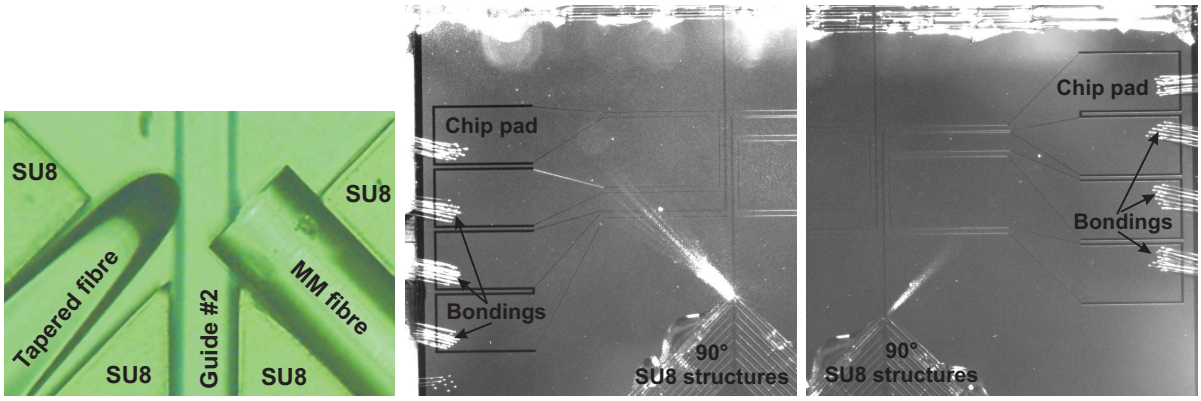

(a) Microscopic picture of the 90°detector.

(b) Light emerging from the MM fibre.

(c) Light emerging from the tapered fibre.

Figure 9.1: (a) Microscopic image of the 90° fluorescence detector. Top view of the atom chip with light emerging from the 90° fluorescence detector. Light was coupled into the MM fibre (b) and into the tapered fibre (c). The emitted light is visible as stray light on the chip as it hits the surface and the SU-8 structures of the absorption detector at the top of the picture. Several modes are visible as light is emitted from the MM fibre (b).

eliminated by simply switching off the source during atom detection or by using a bandpass filter[2]. This filter has a (theoretical) transmittance of better than 99% for light at 780 nm. The transmittance is suppressed by a factor of 10^{-7} for wavelengths diverging more than 12 nm from the central wavelength 780 nm. Light that is coupled into the tapered fiber is

[1]Thorlabs DET210 and an Electronic Workshop current amplifier.
[2]Semrock LL01-780 optical filter.

being detected by the MM[3] fibre with a suppression factor of 3.0×10^{-10}. This factor does not include the detectors efficiency of 57%, it only describes the geometrical suppression effect. Many background sources can be switched off, those are summarized in tab. 9.1. Sources, which can not be switched off are summarized in tab. 9.2.

Source	photons/s detected
MOT beams	6.9×10^8
Room light	4800
Gauge	0.54×10^6
Titan subl. pump	$\gg 15 \times 10^6$
Sum	$\approx 10^9$

Table 9.1: Typical count values for the different background sources detected by the 90° detector. The sources in this table can be eliminated by switching them off. The detectors efficiency is 57% for the wavelengths used and is already taken into account. For some sources like the titan sublimation pump one has to take care of unintentionally starts of its operation, because its high background levels can harm the detector.

Source	photons/s w/o bandpass	photons/s with bandpass
Room light	4800	≈ 0
Dispensers	2.0×10^6	40
Dipole laser	1.6×10^8	≈ 10
Sum	$\gg 10^8$	50

Table 9.2: Different background sources detected by the 90° detector. Most of the sources can be almost eliminated by using two bandpass filters, providing a suppression of 10^{-14} for light deviating more than 12 nm from 780 nm. The detectors efficiency is 57% for the used wavelengths. The light from the dipole laser running at 840 nm with a power of 40 mW itself is already smaller by a factor 3×10^{-10} because of the geometrical suppression factor of the detector setup. The remaining 10 photons may arise from the amplified spontaneous emission (ASE) background of the dipole laser diode, which is typically several 10 nm broad. Or light can enter the fibre leading to the detector after the filters. This was tried to be avoided by an opaque fibre shielding.

These numbers must be compared to the expected signal of an atom. A realistic time interval for the atom to stay in the detection region is in the order of $\Delta t \approx 50$ µs. This time interval follows out of the mode diameter (≈ 5 µm) of the exciting light and the speed of the atoms (of a few cm/s) in the guide. For the rubidium D2 line at saturation (s=1) theoretically

$$\frac{\Gamma}{2}\frac{s}{s+1}\Delta t \approx 470$$

photons are scattered[4] in 50 µs. $\Gamma/2 \times s/(s+1)$ is the scattering rate, where s is the

[3] Thorlabs GIF625. Graded index multi mode fibre with 62.5 µm core diameter, NA=0.275 and with an attenuation of 3.6 dB/km$\sim 0.57 \times 10^{-3}$ loss per m.

[4] Note that although the laser is on resonance with the $F = 2 \rightarrow F' = 3$ cycling transition, it can be excited to $F' = 2$. From there it can undergo an optical transition into the $F = 1$ ground state. That process happens on average every 1000 photons scattered. Then it is 6.8 GHz detuned.

saturation parameter. Later it will be derived that much less photons than theoretically expected are scattered. The different effects are compared in tab. 9.3. Thus up to one nW of light at 780 nm can be coupled into the tapered fibre resulting in less than one background count per second. Together with a bandpass filter this allows us to use dipole lasers with powers of a few hundred milliwatts. A more disturbing background source is mainly caused by black body radiation[5], which is suppressed by 10^{-7} "only", leaving 40 photons/s. The so called dead counts of the SPCM constitute the biggest part in the background rate (250/s). This rate can be reduced by better detectors with dead counts below 25/s.

Source	Counts/50µs	Overall Suppression
geometrical suppression	0.5×10^{-4}	3×10^{-10}
background/bandpass filter	2.5×10^{-3}	3×10^{-7}
Dead counts SPCM	1.3×10^{-2}	1

Table 9.3: Comparing all kinds of background sources and their remaining average effect at a time scale of 50 µs. Theoretically it becomes feasible to distinguish between the contribution of a single atom and that of the background sources, since 4 counts in 50 µs are expected per atom. Experimentally however, a much lower scattering rate than the theoretically predicted will be measured, which means that the detection efficiency drops as the number of scattered photons per atom drops.

9.2.1 The bandpass filter setup

The setup for the bandpass filter[6] consists of two stable mirrors[7] and two fibre couplers. Each fiber coupler is built out of one z-translator[8] and one mounted aspheric lens[9], which is used to adjust the focusing of the light from the fibre. The light emerging from the MM fibre from the detection area in the vacuum chamber is coupled out at the first fiber coupler. Then the light hits the two mirrors, which are used to couple the light into the second fiber coupler. For MM to MM fibre coupling, the efficiency is >80%. Afterwards the two bandpass filters are attached in front of the second fiber coupler. The MM fiber from the first fiber coupler is connected to the detector and is covered with an opaque shielding[10]. No effect of the bandpass filters on the light at 780 nm can be measured. For alignment the wavelength for detection must be used, since the lenses behave differently for varying wavelengths. If light at 780 nm is optimally coupled into the fibre coupler, then light at other wavelengths will be less efficiently coupled in, resulting in an additional suppression of that wavelength.

[5] When the dispensers were almost empty, almost 16 A were pushed through them. This caused an immense rise in background photons. With that high currents, the dispensers had to be switched off a few seconds before magnetic trapping, so that the remaining black body radiation stayed small enough. The dispensers were changed and with a set of new ones, it was sufficient to drive 8 A of current.
[6] Semrock LL01-780 optical bandpass filter.
[7] Radiant Dyes.
[8] Thorlabs SM1Z Cage System Translator.
[9] Thorlabs C240TM-B.
[10] Hosepipe Aldi Nord Ultrabar Season 05.

9.2.2 Detection efficiency

The 90° detector has a certain detection efficiency for photons, which are emitted into the complete solid angle in the detection area. Many facts contribute to this efficiency. There is the acceptance angle of the MM fibre, which is related to the numerical aperture of it. Figure 9.11 shows an overview of that. Secondly there is one splice loss in between the MM fibre coming out of the chamber and the MM fibre leading to the bandpass filter system. The bandpass filter system itself has a limited coupling efficiency. Finally the detector has a certain quantum efficiency. The different loss mechanisms are summarized in tab. 9.4. So almost 0.8% of all isotropically emitted photons in the detection area are detected. It

Source	Coupling	Improved system
MM fibre	0.019 (NA 0.275)	0.10 (NA 0.60)
Splice	0.95	-
Bandpass Filter	0.80	0.9
SPCM	0.57	0.57
Fresnell losses	0.96	-
Overall efficiency	0.80%	5.13%

Table 9.4: Overall detection efficiency is made of the MM fibre acceptance of 1.9%, a splice coupling of 0.95%, a bandpass filter system coupling of 80%, the quantum efficiency of the detector of 57% and one Fresnel loss at the MM facet in the chamber (and one Fresnel loss at the detector if the detector is not anti reflex coated). The overall detection efficiency is roughly 0.8%. The improved system is feasible with the technology available. One can even think of using two MM fibres, which increase the overall efficiency to $2 \times 5.13\%$.

is feasible to increase that efficiency with taking a MM fibre with a higher[11] numerical (NA=0.60) aperture or to have a detector with a higher quantum efficiency. The splice loss can be eliminated by leaving that one out, by simply connecting the MM fibre from the detection area directly with the bandpass filter system. But to allow that, the first MM fibre must be long enough, unfortunately this was not the case in this setup. The two Fresnel losses, which result from light that enters an optically more dense medium, can be eliminated by coating the fibre facets with an AR coating. To improve the bandpass filter system is a bit more difficult but reducing the losses by a factor of two becomes feasible (0.9). This improved system can have a photon detection efficiency of more than 5.13%. Even using two MM fibres can increase the overall photon detection efficiency to $2 \times 5.13\%$. These MM can easily be placed facing each other, or being placed under 45° with respect to the tapered fibre. One of the MM fibres then blocks the magnetic guide after the detection region. If the actual system with all its losses and detectors is kept and only the MM fibre is replaced with two high NA MM fibres, an overall photon detection efficiency of $2 \times 4.16\% = 8.32\%$ is feasible.

[11] Fibres with NA>0.6 are available on the market (www.crystal-fibre.com) and one can think of special fabricated fibres with even higher NA's. For the estimation a fibre which is on stock is used.

9.3 Typical atomic signal from the guide

For the first test with the 90° detector the atoms were directly moved from the MOT down onto the chip close to the 90° detection area by ramping the bias fields. A signal was clearly visible and the cumulative count rate was 4000 with atoms and 400 without atoms. From that point on, it was clear that the detector worked and attempts to magnetically trap the atoms on the chip and guide them through the detector were started.

A typical signal with magnetically guided atoms is recorded with the SPCM and a Counter Card[12] and is shown in Fig. 9.2. During one measurement run, the fields and the laser detuning stay constant. The atoms are released into the guide at $t_0 = 0$ ms. The counts are recorded for one second, during which the light stays on for most of the measurements. The curve complies with a 1D Maxwell-Boltzmann distribution. First the distribution for the case where all atoms start from the same point and at the same time is derived. This condition is fulfilled if the atoms are transferred to the guide in less than a millisecond. But usually the atoms are not released at once. The transfer of the atoms to the guide is accomplished via ramping down the chip-z trap in a few 10 ms. This ramping effect will be addressed after the derivation of the "simple" case (release at once). We will not leave out the derivation, since we found a constant relation between the simulations and the following derivation. The probability of finding a particle with velocity v in the infinitesimal element dv in the one dimensional case it is given as:

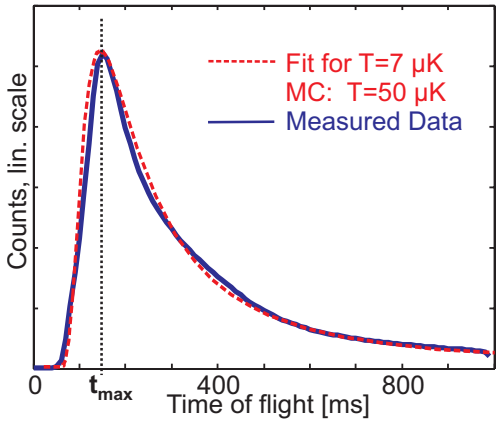

Figure 9.2: Typical signal from the SPCM. The signal is taken for a set of magnetic fields and laser detuning. During the guiding time of one second, these parameters are not changed. The x-axis runs from 0 ms to 1000 ms, whereas the y-axis shows the counts recorded in a 10 µs time bin for each point. In this case the maximum atom number arrives at the detector after (150 ± 5) ms. Even after one second there are still atoms arriving at the detector. The red (dotted) line is a fit of a simple 1D Boltzmann distribution to the data and yields a temperature of the atoms of (7.0 ± 0.3) µK. The function used for fitting is derived in this section. The time t_{max} of the arrival of the peak is also marked. Including the transfer process of the atoms, a Monte Carlo simulation yields a temperature of (50 ± 5) µK.

$$f(v)dv \quad = \quad \sqrt{\frac{m_{Rb}}{2\pi k_B T}} \exp\left(-\frac{mv^2}{2k_B T}\right), \tag{9.1}$$

where $f(v)$ is the velocity probability density, m_{Rb} the mass of an Rubidium atom, k_B Boltzmann's constant and T the temperature. It is normalized to one $\int_{-\infty}^{\infty} f(v)\,dv = 1$.

[12] NI-6221, 16-Bit, 250 kS/s, 16 Analog Inputs, 2 Counters.

Now a new distribution $ft(t)$ can be calculated, which is the arrival time probability density. The velocity v can be expressed with the distance d_0 from the start of the atoms to the detector and the time of arrival t as

$$v = \frac{d_0}{t}.$$

With

$$\frac{dv}{dt} = -\frac{d_0}{t^2}$$

and, similarly to the velocity probability density, the probability to find a particle at t in the infinitesimal element dt in the one dimensional case is given as:

$$ft(t)dt = f(d_0/t) \times \frac{-dv}{dt}dt \tag{9.2}$$

$$= f(d_0/t) \times \frac{d_0}{t^2}dt. \tag{9.3}$$

The dv gets an additional minus, because the intervals changes sign (direction). The maximum atom number is found via $\frac{d}{dt}ft(t) = 0$ for t_{max}:

$$t_{max} = d_0\sqrt{\frac{m_{Rb}}{2k_BT}}. \tag{9.4}$$

Now the temperature can be expressed as a function of the peak arrival time:

$$T = \left(\frac{d_0}{t_{max}}\right)^2 \frac{m_{Rb}}{2k_B}. \tag{9.5}$$

Some of the properties are shown in Fig. 9.3. For a more accurate calculation one hast to take into account that the atoms do not start from a singular point, but from a certain volume. Furthermore reflections can exists. Those can bring back the atoms which started into the "wrong" direction first. For the general case one has to take an integration over the atomic density distribution $\rho(\vec{x})$ times the time probability density $ft(t) = f(d_0/t) \times \frac{d_0}{t^2}$. Of course d_0 is a function of the path, the atom has to travel until reaching the detector. This is analytically not solvable anymore. Therefore Monte Carlo simulations are a better tool to calculate the atomic arrival time probability density.

Monte Carlo simulation of the atom transfer The calculation for the Maxwell-Boltzmann distribution is valid, if the atoms are released at the same time. This is not the case in the experiment, where the transfer takes place in a few 10 ms, by lowering the potential of the initial magnetic trap (chip-z). Since this can not be solved analytically, a Monte Carlo simulation is used to provide theoretical values for the selected properties. The simulation yields almost the same curves as for the calculations of the instantaneous release with one difference: In this special case the peak arrival times t_{max} are delayed by a factor of 2.6. Since the temperature scales like $1/t_{max}^2$, the temperatures must be corrected by a factor of $2.6^2 \approx 7$. Still one can use the formalism of instantaneous release, calculate the temperature and then apply the correction. For the case given in 9.2 the actual temperature therefore is 50 ± 5 µK.

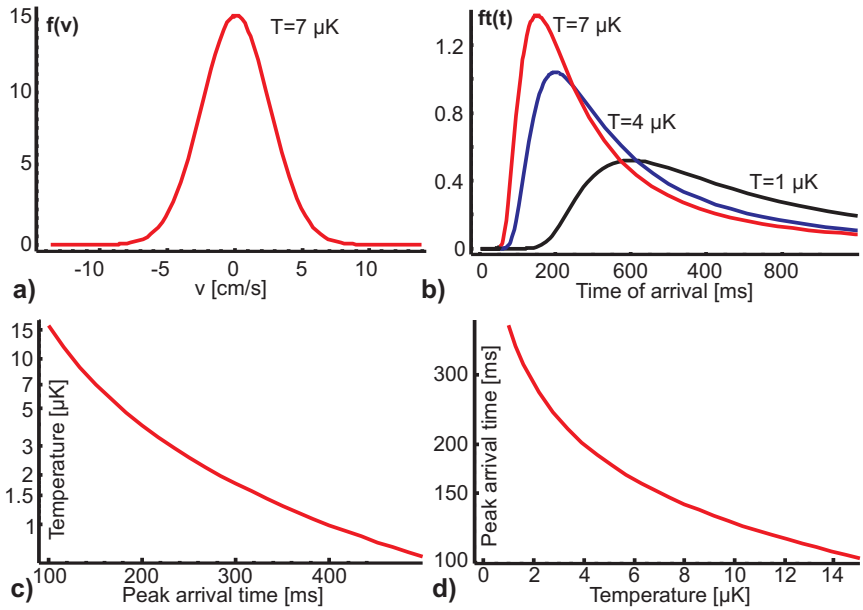

Figure 9.3: Selected properties of the velocity probability density and the time probability density are calculated. For the distance from the start of the atoms to the detector $d_0 = 5.5$ mm is used for all graphs. In **a)** $f(v)$ is plotted for a temperature of 7 µK. **b)** shows the time probability density for several temperatures (7, 4, 1 µK). The temperature is plotted as a function of the peak arrival time in **c)**, whereas the peak arrival time is plotted as a function of the temperature in **d)**.

9.4 Spectroscopy of the $|2, m_F\rangle \rightarrow |F', m'_F\rangle$ transition

For the fluorescence detector it is important to have as much scattered photons per atom as possible. The hyperfine splitting of the rubidium atom leads to different optical transitions. These vary in frequency and transition strength. In a magnetic field the degenerate levels are further split by the Zeeman shift. For the experiment it is important to understand the behavior of the atoms in the magnetic guide. From the measured frequencies the properties of the magnetic field can be calculated. An advantage of a spectroscopy in the magnetic guide is the low temperature of the atoms. The line broadening due to the Doppler shift for an atomic ensemble with a temperature of ≈ 50 µK is only 200 kHz, whereas at room temperature the line broadening is in the order of 520 MHz.

The atoms in the guide, which are trapped in the $|2, 2\rangle$ state can undergo optical transitions. The measurements were performed for the D2-line of ^{87}Rb , which can have the transitions $5^2S_{1/2}\,|F = 2, m_F\rangle \rightarrow 5^2P_{3/2}\,|F', m'_F\rangle$. The optical selection rules $\Delta F = F' - F$ and $\Delta m_F = m'_F - m_F$ must be equal to ± 1 or zero. The line strengths are given by the square of the appropriate Clebsch-Gordan coefficients (Steck, 2001), thus $|2, m_F\rangle \rightarrow |3, m'_F\rangle$, $|2, m_F\rangle \rightarrow |2, m'_F\rangle$ and $|2, m_F\rangle \rightarrow |1, 1\rangle$ transitions' relative strength are (1, 0.3, 0.07). The level diagram is plotted in Fig. A.1 and the appropriate Clebsch-Gordan coefficients are summarized in Fig. A.2.

In the underlying case the light is polarized, thus the given line strengths can not be used. The relative peak heights of the transition can be easily changed by changing the

polarization via the fibre paddles[13]. Unfortunately no direct measurement of the polarization of the light leaving the tapered fibre is possible, which means that the exact degree of polarization is unknown. The spectroscopy is not taken in a field free environment, but the atoms are magnetically guided. This leads to a shift in the spectrum due to a Zeeman level splitting. Figure 9.4 shows the complete spectroscopy with the frequencies given relative to the field free $|2, m_F\rangle \rightarrow |3, m'_F\rangle$ transition. Negative detunings are red shifts. The counts

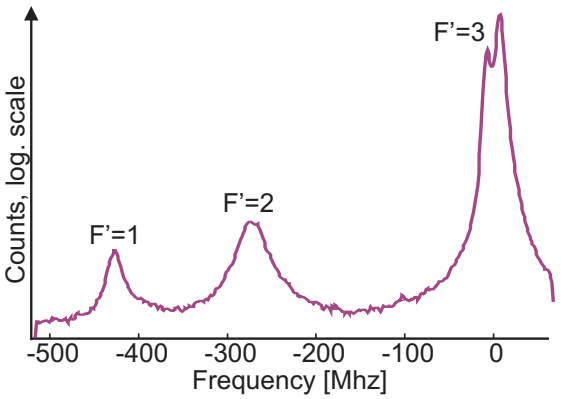

Figure 9.4: Plot of $|2, m_F\rangle \rightarrow |3, m'_f\rangle$ transitions. The counts are on a logarithmic scale to make the small transitions better visible. Note that the F'=3 peak is split into two peaks. This is due to the Zeeman shift of the strongest peaks ($|2, \pm 2 \rightarrow\rangle\ |3, \pm 3\rangle$). The Zeeman shift is not resolved for the other transitions. The relative peak heights are (0.025 / 0.0482 / 1.0) for the $|2, m_F\rangle \rightarrow |3, 1\rangle$ (left peak) and (0.0148 / 0.0284 / 1.0) for the $|2, m_F\rangle \rightarrow |3, 3\rangle$ (right peak) transition. The theoretical relative line strengths are (0.07 / 0.30 / 1.00) for unpolarized light.

are plotted on a logarithmic scale, in order to make all transitions visible. Lorentzian fits are applied to the peaks and the results are summarized in tab. 9.5. The Zeeman splitting in energy is $\Delta E = g_F \mu_0 B$. The Landee's factor for the ground (excited) states is $g_F = 1/2$ ($g_F = 2/3$). Assuming a magnetic field of $B = (4.4 \pm 0.4)$ Gauss the splitting for the allowed transitions is much smaller than the line width. Therefore only one peak as a sum of many should become visible. Of course the transition probabilities influence this result (proportional to the square of the appropriate Clebsch-Gordan coefficients). This will be evident for the cycling transitions from $|F = 2, m_F = \pm 2\rangle$ to $|F' = 3, m'_F = \pm 3\rangle$ for σ^+ and σ^- light. Those transitions are much stronger than the other transitions and are separated by more than a line width. Therefore these two peaks can be distinguished from the otherwise unresolved sum of the single peaks. Two Lorentzian fits were applied to those two peaks. The results are 6.2 ± 0.1 MHz and -7.6 ± 0.1 MHz. The positive shift fits well to the expected shift of 6.16 MHz for a magnetic field of 4.4 G. The negative shift should be at (-6.16 ± 0.6) MHz, but it is at (-7.6 ± 0.1) MHz. The lasers frequency can not be measured to an accuracy better than 1 MHz and the summation over many peaks also can falsify the fit, thus the measured frequencies comply within the errors.

Since the guiding took place for one second, the data contains the spectroscopy of the atoms for different detector arrival times. Figure 9.5 shows such a spectroscopy with a frequency and a time axis. The most important thing to mention is that the transition frequencies do not change with time.

Because of the non-trivial structure of the $|2, m_F\rangle$ to $|3, m'_F\rangle$ transition it has to be investigated further before it reliably can be used for the detection experiments.

[13]Thorlabs manual SM fibre polarization controller.

F'	g_F	$\nu(B=0)$	Max. shifts $\Delta\nu(B=4.4\pm0.4G)$	Measured $\Delta\nu$
1	2/3	-424.3 MHz	$\pm(4.1\pm0.4)$ MHz	(-4.2 ± 0.5) MHz
2	2/3	-267.1 MHz	$\pm(5.1\pm0.5)$ MHz	(-5.9 ± 1) MHz
3	2/3	0 MHz	$\pm(6.2\pm0.6)$ MHz	(6.3 ± 0.1) MHz (-7.6 ± 0.1) MHz

Table 9.5: Spectroscopic data for the transitions $|2, m_F\rangle$ to $|F', m'_F\rangle$. The given errors are only the fitting uncertainties. Other errors are not included here. The ground state's $|2, m'_F\rangle$ Landee's factor is $g_F = 1/2$. The frequency shifts for the hyperfine lines are given with respect to the field free $5^2S_{1/2}\,|F=2, m_F\rangle \rightarrow 5^2P_{3/2}\,|F', m'_F\rangle$ transition. Also the maximum Zeeman splitting are given for a magnetic field of 4.4 ± 0.4G. Each line consists of all optically allowed transitions. The splitting between each Zeeman line is approximately 1 MHz, which is much smaller than the natural line width. Thus the single Zeeman splitting can not be observed. Only the transition $|2, m_F\rangle$ to $|3, m'_F\rangle$ have two strong cycling transitions for σ^+ and σ^- polarization ($m_F = \pm2 \rightarrow m'_F = \pm3$). The peaks in between are rather suppressed. Thus for $|2, m_F\rangle \rightarrow |1, m'_F\rangle$ and $|2, m_F\rangle \rightarrow |2, m'_F\rangle$ a single peak fit was applied whereas for the $|2, m_F\rangle \rightarrow |3, m'_F\rangle$ a peak fit with two Lorentzian lines was applied. The experimental values are $B_{\text{Bias}} = 20$ G, $B_{IP} = -4.4$ G for the offset fields, the guide's current is $I_{Guide} = 0.627$ A. The wire field compensates B_{Bias} and reaches a value of $B_{62\mu m} = 0.4$ G at a height of 62 µm. The absolute value of the magnetic field in the guide center at a height of 62 µm is $\approx |B| = 4.4$ G. The detuning in a magnetic field is approximately 1.4 MHz/G$\times\Delta(m_F \times g_F)$.

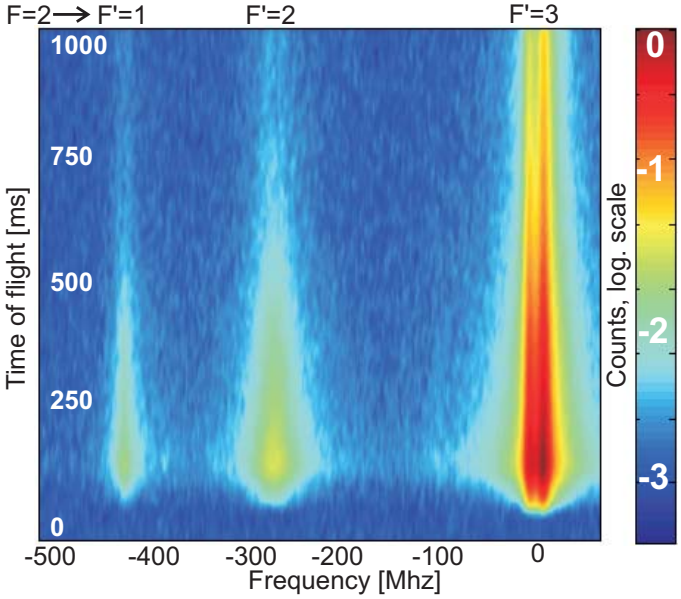

Figure 9.5: Logarithmic plot of the (to 1) normalized count rate as a function of the laser detuning with respect to the field free $|2, m_F\rangle \rightarrow |3, m'_F\rangle$ transition and as a function of time of flight of the atoms in the guide before reaching the detection area. Note that the F'=3 peak is split into two peaks. This is due to the Zeeman shift of the strongest peaks ($|2, \pm2 \rightarrow\rangle\ |3, \pm3\rangle$). The Zeeman shift is not resolved for the other transitions.

9.5 Spectroscopy for different intensities

9.5.1 Spectroscopy of the $|2, m_F\rangle \rightarrow |3, m'_F\rangle$ transition for different intensities

In the last section revealed a level splitting in the spectroscopy due to the Zeeman shift. The $|2, m_F\rangle \rightarrow |3, m'_F\rangle$ is the strongest transition. The strongest transition must be used in

order to get as many photons per atom as possible. Now the $|2, m_F\rangle \rightarrow |3, m'_F\rangle$ transition will be investigated in detail for different intensities. Therefore the laser detuning is scanned over 160 MHz and the intensities are varied between 125 pW and 117 µW. The signals are plotted in Fig. 9.6. The maximum count rate is reached at 150 nW, at higher intensities the counts drop again. It is evident, that the separation of the two main peaks increases with intensity. Together with that effect the counts between the two peaks (at 0 MHz) decrease with increasing intensity. At 33 µW there are only background counts left at 0 MHz. The results of the peak positions and peak heights are shown in Fig. 9.7. The dip

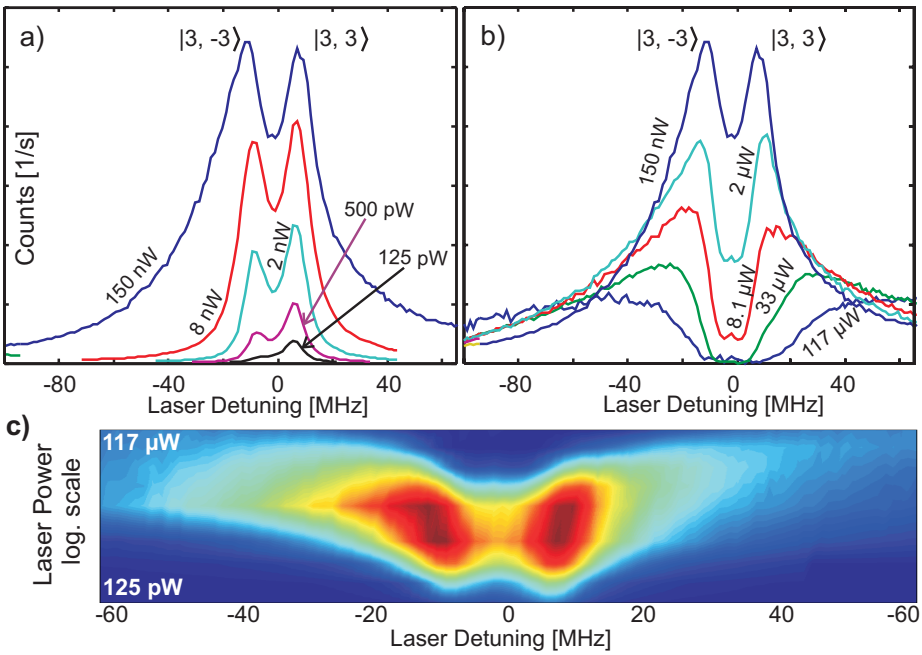

Figure 9.6: Counts for $|2, m_F\rangle \rightarrow |3, m'_F\rangle$ as a function of detuning and intensity. The experimental parameters were $B_{\text{Bias}} = 19.9$ G, $B_{IP} = -4.4$ G, $B_{62\mu m} = -0.13$ G, $I_{guide} = 0.627$ A, yielding an optimal height of the magnetic guide at $r_0 = 2I/B_{\text{Bias}} = 62.9$ µm. **(a)** The intensities for the different curves were (0.125, 0.5, 2, 8, 150) nW. In this plot higher intensity means also higher counts. **(b)** The intensities for the different curves were (0.15, 2.0, 8.1, 33, 117) µW. In this plot higher intensity means lower counts. So at 150 nW the maximum count rate is reached and is decreasing with increasing intensity. **(c)** The contour plot shows the data of a) and b). The y-scale is a logarithmic scale for the different laser powers and runs from 125 pW to 117 µW.

gets also broader if the spectroscopy is evaluated for slower atoms. An possible explanation of a reduced scattering rate with increasing intensity is the start of the scattering process of the atoms already outside the most efficient collection volume of the MM fibre. This will be further investigated and discussed in section 9.6.

Optical pumping For very low powers the transition to the $|3, -3\rangle$ excited state is smaller than to the transition to $|3, 3\rangle$. That can be explained by optical pumping. The atom starts from the ground state $|2, 2\rangle$ and first has to be optically pumped to reach the cycling transition from $|2, -2\rangle$ to $|3, -3\rangle$ (by several transitions of σ^- polarized light).

The ratio of the maximum of right peak and the left peak is plotted in Fig. 9.8. The

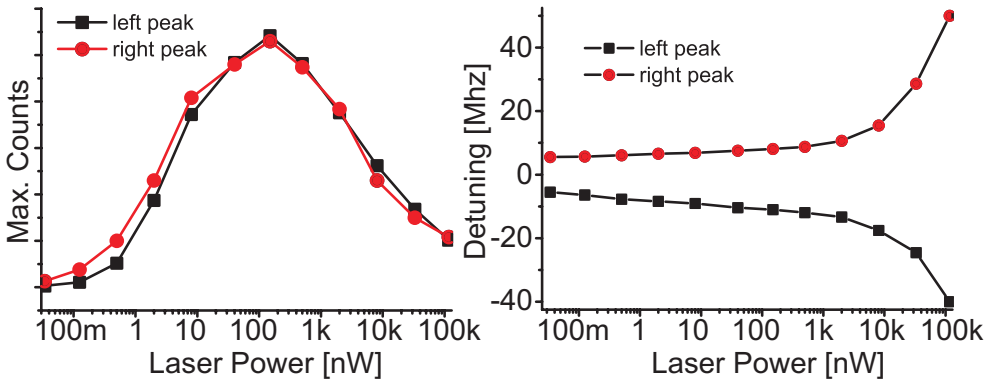

Figure 9.7: Peak position and counts at the maximum as a function of the laser power (1 nW$\leftrightarrow$ $s \approx 3$). The experimental parameters were $B_{\text{Bias}} = 19.9$ G, $B_{IP} = -4.4$ G, $B_{62\mu m} = -0.13$ G, $I_{guide} = 0.627$ A, yielding an optimal height of the magnetic guide at $r_0 = 2I/B_{\text{Bias}} = 62.9$ µm. The peak position detuning behaves like a square root function. The power broadened line width of a transition scales like $\sqrt{1+s}$, where s is the saturation parameter.

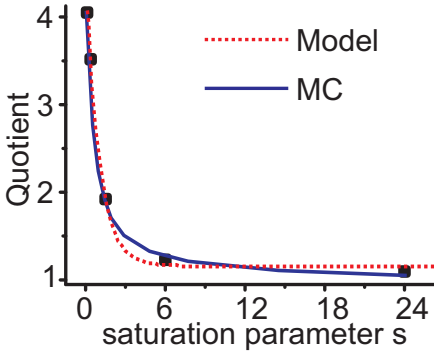

Figure 9.8: The graph shows the ratio of the peak maxima for the right ($|2,2\rangle$ to $|3,3\rangle$) and left ($|2,-2\rangle$ to $|3,-3\rangle$) peak as a function of the saturation parameter s. Taking the ratio of both signals will cancel out geometrical effects of illuminating different volumes for different intensities. Only pumping effects will remain. The red (dotted) line can be calculated with the model presented in the text. The Monte Carlo simulation is shown as the blue (solid) line and also fits to the data points.

problem of the different scattering rates for the left and right peak can not be solved analytically, but can be approximated with an intensity dependent scattering rate Λ

$$\Lambda = \Lambda(s) = \Lambda_0 \times f(s). \tag{9.6}$$

The best fit for the available data yields the following intensity dependent model function:

$$f(s) = \left(1 - e^{-s}\right) \frac{s}{s+1} + e^{-s} \frac{s}{s+1+(2\zeta)^2}, \tag{9.7}$$

where ζ is the detuning of the laser frequency with respect to the $|2,2\rangle$ to $|3,3\rangle$ transition (in units of the natural line width Γ) and s the saturation parameter. The first term corresponds to the resonant transition, the associated ground state becomes populated when the saturation parameter increases. The second term describes the off resonant pumping starting from the $|2,2\rangle$ state. Only for the left peak and for low saturation parameters the second term dominates the scattering rate.

To figure out more about the model function, more measurements are necessary. A Monte Carlo simulation describing the situation of the atom to start in the $|2,2\rangle$ ground state and incorporating the different light polarizations, light frequencies and transition rates yields a similar result. The simulation for a saturation parameter of $s = 0.1$ and $s = 10$ is shown in Fig. 9.9.

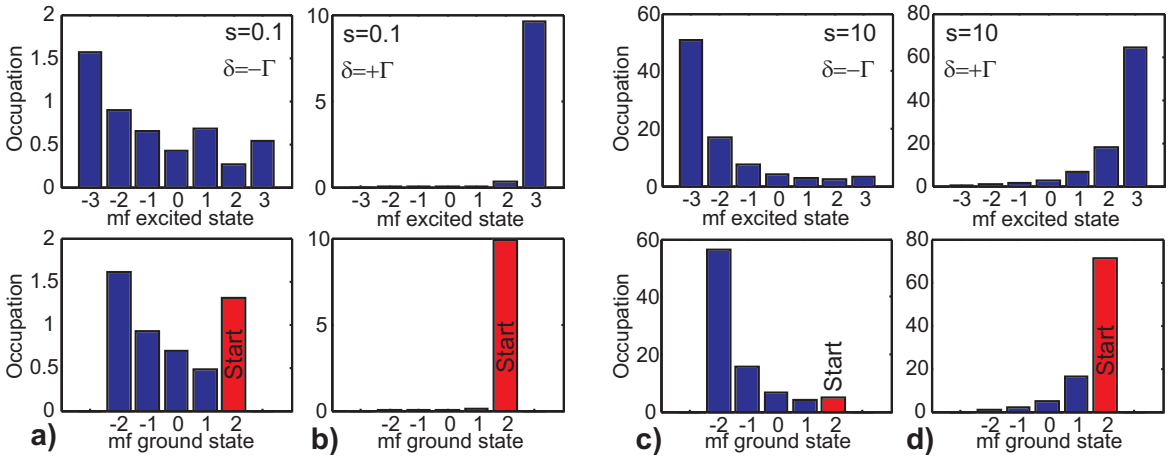

Figure 9.9: A Monte-Carlo simulation is used to calculate the occupation of a certain m_F ground state and the excited state for a fixed time of 10 µs. The atom starts from the $|2,2\rangle$ ground state. The maximum detuning for $\sigma^{\pm}$ polarized light caused by the magnetic field is chosen to be $\pm\Gamma$ (as in the experiment). The fraction of the different light polarizations is set to $|\sigma^-,\pi,\sigma^+\rangle = \frac{1}{7}|3,1,3\rangle$. The plots show the occupancy of the different m_F levels. Two pairs of plots are shown, one for a laser detuning of $\delta = -\Gamma$ and the other for $\delta = +\Gamma$. **a)** and **b)** are the results of a simulation for a saturation parameter of $s = 0.1$, whereas **c)** and **d)** are the results of a simulation for a saturation parameter of $s = 10$. For low intensities ($s = 0.1$) and a laser detuning of $\delta = -\Gamma$ it takes several steps to pump the atom from the $m_F = 2$ to the $m_F = -2$ ground state. For higher intensities ($s = 10$) the pumping process is of less importance. The sum of the different occupations is the total number of scattered photons.

The problem of the optical pumping occurs for very low powers only and only for the left peak. To overcome the measured problems one has to use the right peak ($|2,2\rangle$ to $|3,3\rangle$) and smaller remaining magnetic fields at the guide center, so the maximum Zeeman splitting is within the natural line width of the atom.

9.5.2 Spectroscopy of the $|2,m_F\rangle \rightarrow |1,1\rangle$ transition for different intensities

In the last section a difference in the signal strength of the cycling transitions to the $|3,-3\rangle$ and $|3,3\rangle$ excited state can be seen for low intensities. With a similar measurement for the $|2,m_F\rangle \rightarrow |1,1\rangle$ transition it is possible to confirm, that the above effect arises due to optical pumping. The $|2,m_F\rangle \rightarrow |1,1\rangle$ transition has a much simpler ground level structure ($m_F = 0,\pm 1$). Moreover the atom is lost into dark states after scattering 1.4 photons on average. This will exclude any optical pumping, because the atom simply can not reach any other levels (before being lost).

The measurement for the $|2,m_F\rangle \rightarrow |1,1\rangle$ transition is plotted in Fig. 9.10. The splitting starts much later at higher intensities than for the $|2,m_F\rangle \rightarrow |3,m'_F\rangle$ transition. This can be explained by the absence of optical pumping and a higher saturation intensity needed for that transition. In this case the dip can be explained fully geometrically, because for higher intensities atoms at resonance start to scatter already outside the optimal MM

collection volume. For a frequency shift from resonance the scattering rate drops, which will relocate the first scattering process again back into the optimal MM collection volume.

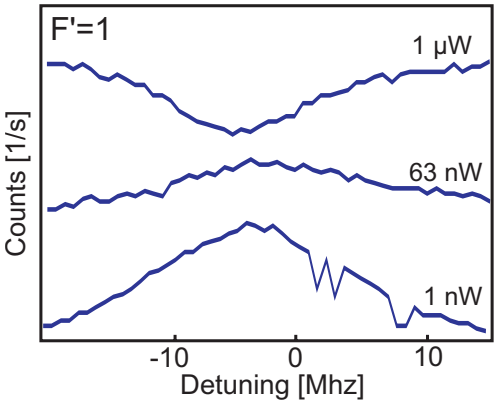

Figure 9.10: Counts for $|2, m_F\rangle \rightarrow |1, 1\rangle$ as a function of the laser detuning and laser power. The intensities are equal to 1, 63 and 1000 nW. The individual lines are shifted in absolute count rate, to get an better overview. The dip can be explained geometrically.

The last section about the spectroscopy for different intensities is summarized in the following:

- The count rate first rises and then decreases again with increasing laser power. The maximum is obtained at a laser power of 150 nW. This is an geometrical effect. For increasing intensities the atoms start to scatter outside the optimum collection region of the MM fibre. At a certain light intensity, the atoms will scatter all photons outside the detection volume. This effect will be further evaluated in detail in section 9.6.

- Not only the $|2, 2\rangle$ to $|3, 3\rangle$ transition starting from the magnetically trapped state can be measured, but all possible transitions. Thus the atoms need not to stay magnetically trapped to get a signal. Gravity needs 700 µs to pull an atom 2.5 µm away. This becomes evident for the two "opposite" transitions to the exited state $|3, 3\rangle$ and $|3, -3\rangle$. The $|3, 3\rangle$ can only decay into the trapped ground state $|2, 2\rangle$, whereas the $|3, -3\rangle$ state can only decay into the not trapped $|2, -2\rangle$ state. The $|2, -2\rangle$ is even repelled from the magnetic trap with the same strength as the $|2, 2\rangle$ state is captured.

- For very low powers the transition to the $|3, -3\rangle$ excited state is smaller than to the transition to $|3, 3\rangle$. That can be explained by optical pumping. First the atoms starting from the ground state $|2, 2\rangle$ must be optically pumped to reach the cycling transition from $|2, -2\rangle$ to $|3, -3\rangle$ (by several transitions of σ^- polarized light). Before they reach this cycling transition the atoms are farther detuned from the laser light, thus the scattering rate in the beginning is much smaller.

- The absolute magnetic field at the guide center (4.4 ± 0.4 G) leads to a Zeeman-splitting and optical pumping. To avoid those effects in the future, one has to choose the smallest possible remaining magnetic field at the guide center. It must be small enough, that the Zeeman-splitting is much smaller than the natural line width of the atomic transition.

- The two peaks of the transitions $|3,-3\rangle$ and $|3,3\rangle$ are not symmetric. The transition to $|3,-3\rangle$ is extended much further to red detunings than the $|3,3\rangle$ extends into blue detunings. This can be explained by the expelled atoms in the $|2,-2\rangle$ ground state, which move further than the trapped atoms in the $|2,2\rangle$ ground state. Therefore these atoms reach higher magnetic fields, which explains the higher red detunings.

- For the $|2,2\rangle$ to $|1,1\rangle$ transition is no optical pumping. The atom first has to be excited to the $|1,1\rangle$ state. From there it goes with a probability of 5/6 (see Fig. 9.15) to the F=1 ground state, which is 6.8 GHz away. Only in 1/6 of all cases it is falling back to a F=2 ground state. In 60% of these cases it falls back to the $|2,2\rangle$ ground state. Therefore the dip evolving with increasing laser power is explainable geometrically. For high powers the atoms scatter outside the detection volume of the MM fibre. The scattering rate drops for detunings from the transition, therefore it is then more likely that the atom again scatters inside the detection region of the MM fibre.

Considering the above aspects a high performance fluorescence detector has to be operated at saturation intensity (to avoid losses outside the optimum detection volume of the MM). It has to be on resonance with the cycling transition $|2,2\rangle$ to $|3,3\rangle$. One has to choose the experimental parameters in such a way, that the remaining magnetic field in the guide center is as small as possible to avoid distracting optical pumping effects.

9.6 Geometrical detection effects

As was evaluated in the last section, the collected signal drops at high intensities. This was explained by losing scattered photons already outside the detection volume of the MM fibre. In Fig. 9.11 the fluorescence detector and the collection efficiency of the MM fibre as a function of the position of the atoms are depicted. The curve for the collection efficiency is not symmetric around the y-axis, since the MM fibre is rotated by 45° with respect to the magnetic guide. It is important to figure out, if the atoms in the guide are kicked out by scattered photons from the tip of the tapered fibre or by scattered photons from other surfaces. Here the geometrical effects of the collection efficiency of the MM fibre are discussed. If the intensity is high enough, the atoms start to scatter already outside the collection volume.

Comparing different illumination techniques To measure the strength of the effect, a measurement with a pulsed illumination of the atoms is performed and compared to the signal of a continuous (cw) illumination. This is achieved by leaving on the probing beam the whole time the atoms are guided through the detector. In a different trial the illuminating laser is not switched on for the whole experiment, but pulsed with 10 ms. The counts for cw and pulsed laser operation are shown in Fig. 9.13a). The counts of the 10 µs pulse are integrated. No significant difference between the signal acquired at once and the signal acquired stepwise is observed.

Having a closer look at the 10 ms pulses (see Fig. 9.12), an overshoot is visible in the beginning. The overshoot peak grows with rising laser power. The overshoot decays with a decay constant of $\tau \approx (480 \pm 80)$ µs for all intensities. In 480 µs the atoms in the

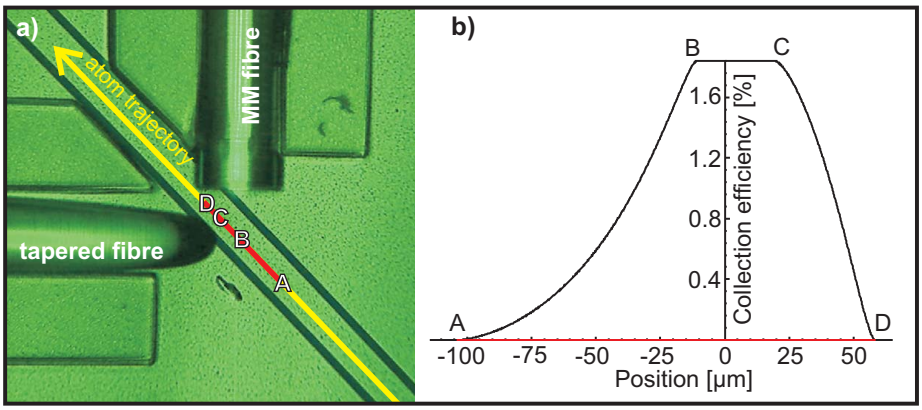

Figure 9.11: In **a)** a picture of the fluorescence detector is shown. The atomic trajectory in the guide is marked with four points (A,B,C,D) in front of the MM fibre. Photons from atoms that scatter at **A** or **D** are not collected anymore. The maximum collection efficiency of the MM fibre is reached between the points **B** and **C**. The collection efficiency is plotted in **b)** as a function of the atomic position. Position zero means that the atoms are on the centerline of the MM fibre and the tapered fibre. The maximum collection efficiency of 1.9% can be calculated from the numerical aperture of the MM fibre.

peak travel 48 ± 8 µm. This distance corresponds within errors to the distance (B-C) in Fig. 9.11, where the MM fibre has its maximum collection efficiency.

The following model is used for the fit

$$Y_{Data} = y_0 + A \times \exp\left(-\frac{X_{Data}}{\tau}\right),$$

where y_0 is the offset, A the amplitude of the exponential decay and τ the decay constant. The difference is not visible in Fig. 9.13a), since the overshoot does not change

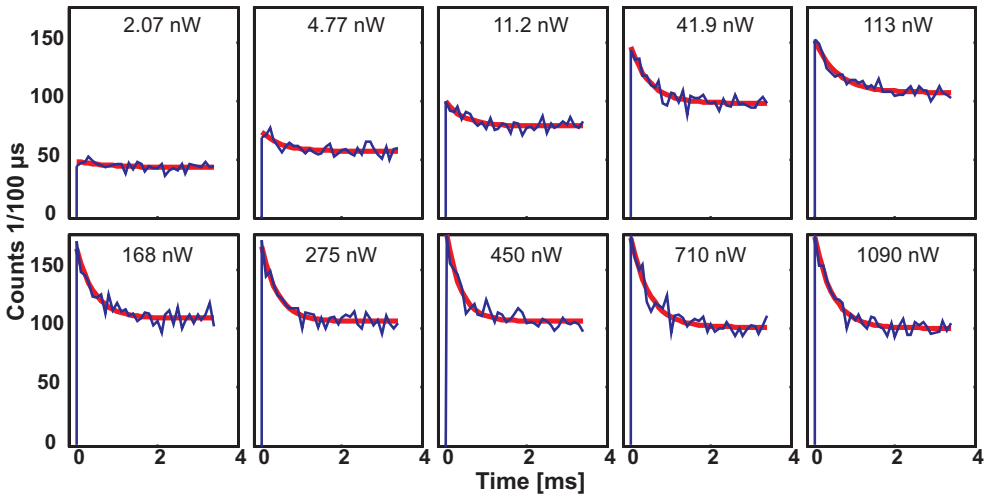

Figure 9.12: The first 4 ms of the pulsed signal are shown in this graph as a function of laser power. The signal shows an overshoot at the beginning, which decays with a decay constant of $\tau \approx (480 \pm 80)$ µs for all intensities. Each signal is an average over 5 measurements and is binned to 100 µs.

the integrated counts. The contribution of the overshoot is less than 1% to the complete 10 ms interval. Figure 9.13b) plots the amplitude of the overshoot $(y_0 + A)$ divided by the amplitude of the remaining signal (y_0). The smooth line is a fit of the radius^2 (where the

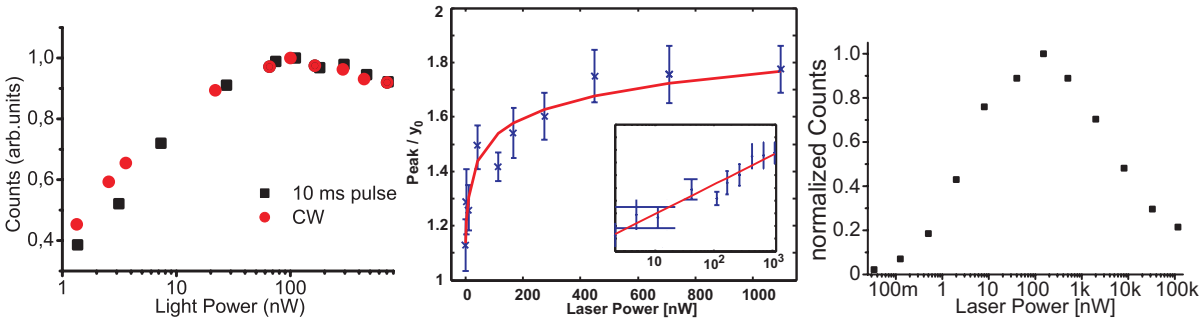

(a) Summed 10 ms pulse. (b) Overshoot divided by y_0. (c) Scattering rate.

Figure 9.13: **a)** Counts plotted as function of the laser power. The two curves differ in the method of applying the light. One is recorded with a pulsed laser (black squares) with a pulse length of 10 ms and the second curve (red circles) was measured with the light continuously left on. Both curves are normalized with the same factor. There is no significant difference for the methods. **b)** The amplitudes of the overshoots $(y_0 + A)$ are divided by the amplitudes of the remaining signal (y_0) for different intensities. The smooth line is a fit of the radius^2 (where the intensity has dropped to a certain value) as a function of laser power. **c)** Maximum scattering rate as a function of the laser power. At high powers $\gg$ 500 nW the signal drops again. This can be explained by the fact that the atoms interact with the light already outside the collection volume of the MM fibre.

intensity has dropped to a certain value) as a function of the laser power.

For even higher intensities an additional measurement for cw illumination was made . This is shown in Fig. 9.13**c**. The signal rise was as expected and leveled out at a certain point. The coupled powers got as high as 100 nW without an obvious decrease in the signal. Then for very high powers there is a drop in the number of counts. This can be explained by the fact, that the atoms interact with the light already outside the collection volume of the MM fibre. Most measurements are performed with laser powers in the nW range. That is why most of the measurements are carried out with the light on for the complete guide time of one second, since the losses of 10% seem to be acceptable.

When the guide is switched off, the atoms fall out of the detection region. Gravity will pull them away. Figure 9.14 shows that process. Applying an exponential decay to the data, yields for $\tau = 0.74 \pm 0.2$ ms. The question still remains what the main cause for this decay is. When the atomic ensemble is released from the trap it will expand, move and fall downwards due to gravity. Detuning effects due to the switching off of the magnetic fields[14] can be excluded, because a broadband light source (actually the ASE[15] of the dipole laser at 786.2 nm) is used. Also pushing due to light force can be neglected, because the average scattering rate per atom was $\ll 1$ photons. The dominating effect strongly depends on the temperature of the atoms, thus to determine the temperature with simulations, further measurements with different preconditions must be performed.

[14] During the switch off the magnetic fields will vary strongly.
[15] Amplified spontaneous emission is common in diode lasers.

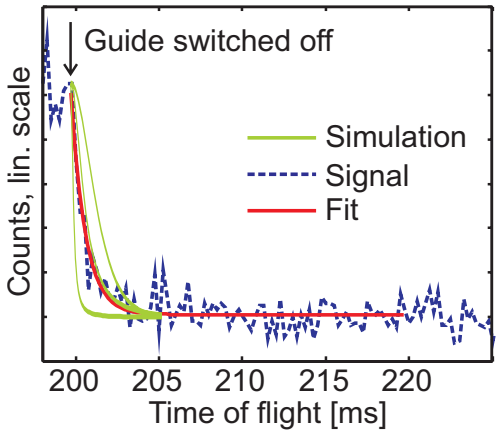

Figure 9.14: The magnetic guide is switched off at $t = 200$ ms. The atoms fall out of the illumination zone. A fit applied to the signal decay yields a decay constant of $\tau = 0.74 \pm 0.2$ ms. The reason of the signal decay may have different reasons. The atomic ensemble will expand, move and fall downwards after it is released from the trap. Also a simulation of the expansion and falling of a thermal cloud is drawn for three different temperatures.

The geometrical effects can be summarized to the following points:

- To increase the number of atoms imaged, one has to increase the light intensity. At a certain laser power it becomes more important to use pulsed light instead of cw illumination. Otherwise the atoms will start to scatter outside the most effective detection volume and are lost before reaching the detection center. One must not get tricked by the signal increase. A larger volume means also a less efficient average detection. If one can prepare and guide atoms through the waist of the tapered fibre, one must use saturation power only.

- For large imaged volumes at high laser powers pulsing the light can increase the collected photons by a factor of 1.8. In $\tau = 480 \pm 80$ µs the atoms in the peak of the distribution travel 48 ± 8 µm. This distance corresponds within errors to the length, where the MM fibre has its maximum collection efficiency.

Geometrical effects do not always need to be considered. The probing intensity depends on whether it is important to illuminate as many atoms as possible, or to detect the atoms as effective as possible. To image a large volume the intensity must be chosen quite high ($\gg s_0$) and the laser must be pulsed to have no signal losses outside the most efficient detection volume. Saturation intensity is best suited for an efficient probing of the atoms, since no signal is lost outside the most efficient detection volume.

9.7 Determination of the number of atoms

An important quantity is the number of atoms in the magnetic guide. In the following section the relation of the measured signal to the number of atoms contributing to the signal will be evaluated. As soon as this relation is know, one can derive the number of scattered photons per atom. This number will directly lead to the detection efficiency of a single atom, which is an important quantity of the fluorescence detector.

In the following the number of atoms will be measured with three different methods. First the external camera system is used to perform an absorption imaging, then the number of atoms is measured with the help of the $|2, m_F\rangle \rightarrow |1, 1\rangle$ transition. Finally the number of atoms is derived via a statistical approach, which will be discussed in detail.

9.7.1 Number of atoms via absorption imaging

With the help of absorption imaging the atoms with the camera system, the transfer efficiency from the MOT to the magnetic chip guide is measured. The atom numbers in the guide are quite inaccurate, because of a very weak signal close to the scattering surface of the chip. Also the electrical connections (bonding wires) to the chip partially obstruct the view of the camera to the magnetic guide. This is tried to be overcome by taking sufficient data samples to make a statistical analysis. A typical transfer process is summarized in tab. 9.6. The measurement yields $(1.0 \pm 0.2) \times 10^5$ atoms in the guide.

Step	Number of atoms	Ratio	Temperature µK
MOT	8×10^6	100%	300
Molasse	8×10^6	100%	< 40
Chip-Z Start	1.1×10^6	13.8%	> 200
Chip-Z End	0.5×10^6	6.3%	150-200
Guide	0.1×10^6	1.25%	50-100

Table 9.6: Transfer efficiency for the atoms from the MOT to the magnetic chip guide. Only 1.25% of the atoms in the MOT are transferred to the magnetic guide leading to the 90° detector. This is a very low number, but still the 10^5 atoms are more than enough for the desired purpose. The numbers in this table were calculated using absorption imaging.

9.7.2 Number of atoms via the $|2, m_F\rangle \rightarrow |1, 1\rangle$ transition

There is a second possibility to measure the number of atoms in the guide. If the number of scattered photons per atom is known, the number of atoms can be calculated. For the $5^2S_{1/2}\,|F = 2, m_F = 2\rangle \rightarrow 5^2P_{3/2}\,|F' = 1, m'_F = 1\rangle$ transition an atom scatters 1.44 photons on average, before it is lost into a "dark" (far off resonant) state. This can be deduced from the term schematics in Fig. 9.15, where the transition matrix elements are plotted. From each excited F'=1 state there exist two more transitions to the F=1 ground state with a strength of 25 in each case. They were omitted here to keep the figure clearer.

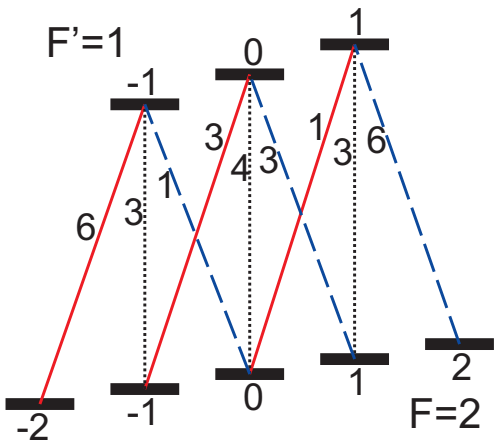

Figure 9.15: Transition matrix elements are plotted for the $5^2S_{1/2}\,|F = 2, m_F = 2\rangle \rightarrow 5^2P_{1/2}\,|F' = 1, m'_F = 1\rangle$ transition. From each excited F'=1 state there exist two more transitions to the F=1 ground state with a strength of 25 in each case. They were omitted here to keep the figure clearer. Once the atom is in the F=1 ground state they are no longer on resonance with the laser since this transition lays some 6.8 GHz away. So for each excited state the cases to come back into the F=2 ground state sum up to 10 (6+3+1), whereas the cases to get to the F=1 ground state sums up to 50 (25+25). That means only in 1/6 of all cases the atom can scatter again.

Once the atom is in the F=1 ground state it is no longer on resonance with the probing laser since this transition is 6.8 GHz detuned. So for each excited state the chances to go back into the F=2 ground state sum up to 10 (6+3+1), whereas the chances to get to the F=1 ground state sum up to 50 (25+25). That means only in $p_{scatt} = 1/6$ of all possibilities the atom can scatter again. The expectation value of the number of scattered photons per atom n_a can be calculated as

$$n_a = \sum_{k=1}^{\infty} k p_{scat}^{k-1} \tag{9.8}$$

$$= (1 - p_{scat})^{-2} \tag{9.9}$$

$$= 1.44. \tag{9.10}$$

The atom number is extracted from the total counts divided by 1.44 and by the overall detection efficiency of 0.8%. To get the full number of atoms in the guide, the guide current is scanned so that the center of the magnetic trap is shifted perpendicular to the chip. The guide current steps are chosen in such a way, that the shift of the guide is $\Delta r \approx 3.3$ µm for each step. Since the tapered fibre spot diameter is approximately 5 µm a certain overlap has to be taken into account. On first order the following formula can be taken for calculating the number of atoms in the whole guide:

$$m = \sum_{\forall i} c_i \frac{\Delta r}{2w_0} \frac{1}{p_{max}} \frac{1}{p_d} \frac{1}{n_{stat}}, \tag{9.11}$$

where m is the number of atoms in the guide, c_i the total count rate of one guide scan, $\Delta r/2w_0 \approx 3.3$ µm/5 µm is the overlap correction, $p_{max} \approx 1.44$ is the maximum number of scattered photons per atom for the transition, $p_d \approx 0.8\%$ is the detection efficiency and n_{stat} is the number of statistics taken. The measurement result for the complete guide is $m \approx (2.9 \pm 0.3) \times 10^5$ atoms. For a single shot only a fraction of the atoms in the guide are imaged. The number of atoms imaged at once strongly depends on the used laser power.

Scattered photons as a function of intensity and atom number As soon as the number of atoms is evaluated, the signal of the $|2, m_F\rangle \rightarrow |1, 1\rangle$ transition can be compared to the $|2, m_F\rangle \rightarrow |3, m'_F\rangle$ transition. The different count rate must originate from a different scattering rate per atom, which can be calculated for different laser intensities. Figure 9.16

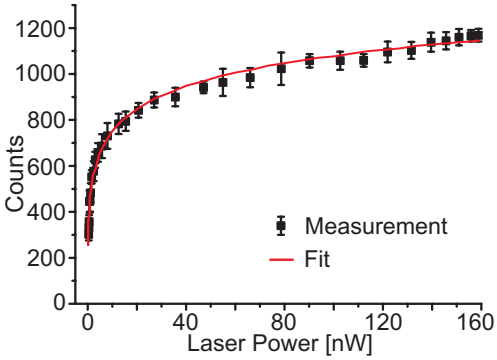

Figure 9.16: Count number plotted versus the laser intensity of the $|2, m_F\rangle \rightarrow |1, 1\rangle$ transition (mean over 8 statistics). Except for very low intensities ($\ll$ nW), every atom scatters the theoretical 1.44 photons per atom on average. One can calculate the radius r_0 of the Gaussian beam, where the intensity of the tapered fibre reaches atomic saturation s_0. A simple fit (red curve) is proportional to r_0^2. Note that s_0 for this transition is different to the saturation intensity of the other transitions.

shows the total counts as a function of the laser power. For intensities not much weaker than saturation intensity every atom of the $|2, m_F\rangle \rightarrow |1, 1\rangle$ transition scatters 1.44 photons/atom. The total scattering rate rises with increasing intensity. For laser powers above saturation intensity this rise originates from pure geometrical reasons. One can calculate the radius r_0 of the Gaussian beam of the tapered fibre, where the intensity has dropped to I_{max}/E^2 of the maximum intensity I_{max}. For a different laser intensity I' the radius r_0, where the intensity has dropped[16] to I_{max}/E^2 can be calculated to

$$r_0 \quad = \quad w_0\sqrt{1 + \ln\sqrt{s}}. \tag{9.12}$$

The theoretical curve is proportional to r_0^2 as a function of the laser power. Improvements in the model can be achieved by considering the volume below saturation and geometrical detection effects for higher intensities.

In section 9.4 both transitions are measured within the same set of parameters, which was the spectroscopy (Fig. 9.4). There the relative peak heights are measured to 0.025 / 1.0 for the $|2, m_F\rangle \rightarrow |3, -3\rangle$ (left peak) and 0.0148 / 1.0 for the $|2, m_F\rangle \rightarrow |3, 3\rangle$ (right peak) transition. Since the intensity stayed the same, geometrical effects become negligible. If 1.44 scattered photons per atom for the $|2, m_F\rangle \rightarrow |1, 1\rangle$ transition are assumed then the relative peak heights can be used to calculate the number of scattered photons for the $|2, m_F\rangle \rightarrow |3, -3\rangle$ ($|2, m_F\rangle \rightarrow |3, 3\rangle$). For the $|2, m_F\rangle \rightarrow |3, -3\rangle$ ($|2, m_F\rangle \rightarrow |3, 3\rangle$) transition 58 ± 2 (97 ± 3) scattered photons per atom are evaluated. The problem is the saturation intensity, which is different for different transitions and polarizations of light. It is hard to say, where the saturation intensity for the different transition lays. It was possible to change the peak heights by changing the incoming polarization. Thus this measurement is for a fixed incoming polarization. In the future one has to try to optimize the signal for the $|2, m_F\rangle \rightarrow |1, 1\rangle$ and then go to the $|2, m_F\rangle \rightarrow |3, 3\rangle$ transition and optimize the (right) peak.

9.7.3 Single atom detection efficiency and scattering rate

The third method to learn about the atom number in the guide is by a statistical calculation. This method will be derived in the following section. A Poissonian probability distribution with an expectation value of $\langle k\rangle = \lambda$ is typically used for describing a coherent light source. A laser well above threshold is such a light source. The probability for getting exactly k photons is

$$P(k, \lambda) = \frac{\lambda^k}{k!}e^{(-\lambda)}.$$

The variance is calculated to $var(k) = \lambda$. This gives the following important feature for photon counting

$$\frac{var(k)}{\langle k\rangle} = 1. \tag{9.13}$$

There are also events from dead-/background counts. Assuming m atoms are present in the detection area, the probability $P(n, \lambda)|_m$, that n photons are detected from m

[16] The radius where the intensity drops to I'/E^2 is always w_0.

atoms(+dead-counts/background) can be calculated to:

$$P(n,\lambda)|_m = \sum_{k=n}^{\infty} P(k,\lambda) \binom{k}{n} p_d^n (1-p_d)^{k-n} \tag{9.14}$$

$$= \frac{(p_d\lambda)^n}{n!} e^{(-p_d\lambda)}, \tag{9.15}$$

where p_d is the total detection efficiency and $\lambda = \sum_i \lambda_i$ the expectation value for different Poissonian distributed sources. This is possible, since the sum of (independent) Poissonian sources can be expressed as a single Poissonian distribution with the sum of the single expectation values as the new expectation value. For $\Delta t \geq 10$ µs and in saturation the expectation value of scattered photons from m atoms is $\lambda_1 = m \times n_a$, where the average scattering rate is n_a photons per atom. But the background sources and dead-counts can be included in $\lambda_2 = d_0 \Delta t / p_d$, where d_0 is the dead-count/background rate and Δt the width of the counting interval. The rate d_0 can be measured by integrating the counts over one second, while no atoms are present.

This leads to a first estimation which is summarized in tab. 9.7. One can read the table by choosing a column for a certain number of atoms. The values in the row yield the probabilities to have a certain number of detected photons for the chosen number of atoms.

The difference in **a)** and **b)** are the assumptions of exactly having m atoms with the photon detection probabilities of $p_d = 0.8\%$ and $p_d = 2 \times 4.16\%$. The latter p_d is the enhanced photon detection probability with two MM fibres. One can also calculate the

Probability to detect n counts, if m atoms are present.

Counts	0 atoms $p_d = 0.8\%$	1 atom $p_d = 0.8\%$	2 atoms $p_d = 0.8\%$	0 atoms $p_d = 8.32\%$	1 atom $p_d = 8.32\%$	2 atoms $p_d = 8.32\%$
0	99.7	45.9	21.1	99.34	0.03	9.7×10^{-6}
1	0.3	35.7	32.8	0.66	0.25	1.6×10^{-4}
2		13.9	25.5		1.0	1.3×10^{-3}
3		3.6	13.2		2.7	6.8×10^{-3}
>3	3×10^{-10}	0.8	7.3	2×10^{-8}	96.0	99.992

Table 9.7: Expected number of counts as a function of the number of atoms present. The values are given in per cent and are evaluated for an 10 µs interval and an expectation value of $n_a = 97 \pm 3$ scattered photons per atom (which was measured for the $|2,2\rangle$ to $|3,3\rangle$ transition). The background counts are $d_0 = 290$/s ($d_0 = 666$/s) and the photon detection probability of an emitted photon is $p_d = 0.8\%$ ($p_d = 8.32\%$) for the current case (enhanced case). With the enhancements also the background must be increased to $d_0 = 666$/s, which is the background rate times the relative increase in the MM acceptance plus the detector dead count rate.

expected number of counts as a function of the atom number. Table 9.8 summarizes the current case and the improved case.

Setting the threshold to ≥ 1 count, the detection probability for a single atom can be

	Current case		Enhanced case	
Number of atoms	Counts expected $p_d = 0.8\%$	P_{detect}	Counts expected $p_d = 2 \times 4.16\%$	$\bar{P}_{detect}$
0	0.003	0.3%	0.0067	99.33%
1	0.8	54.1%	8.1	3.1×10^{-4}
2	1.6	79.0%	16.1	9.7×10^{-8}
3	2.3	90.3%	24.2	3.0×10^{-11}
4	3.1	95.5%	32.3	9.5×10^{-15}
5	3.9	97.9%	40.4	3.0×10^{-18}
6	4.7	99.1%	48.4	9.3×10^{-22}

Table 9.8: Expected number of counts as a function of the number of atoms for an expected 97 photons per atom scattered. Two cases are given, one for a collection probability of $p_d = 0.8\%$ and for the proposed enhancements of two MM fibres $p_d = 2 \times 4.16\%$. Setting the threshold to ≥ 1 count, the probabilities to detect the atom(s) P_{detect} are given. For the proposed enhancements the probability NOT to detect $\bar{P}_{detect} = 1 - P_{detect}$ the atom(s) is given. For zero atoms there is a small probability of detection. That is the false detection rate of 0.3% and 0.67% for a time interval of 10 µs.

calculated as:

$$P_{detect} = 1 - P(0, n_a \times p_d) \tag{9.16}$$
$$= 1 - e^{-n_a \times p_d}. \tag{9.17}$$

For the setup a single atom detection probability of 54.1% is achieved. An enhanced setup yields a detection probability of 99.97%. The probability to get a signal, when no atom is present, is a false detection. The false detection rate is only 0.3% and 0.67% for a time interval of 10 µs. For a certain number of measured counts per time interval one can directly calculate the most probable atom number. This can be exploited for atom counting. Figure 9.17 shows the atom detection probabilities for different thresholds and different detectors as a function of the average number of detected photons ($p_d \times n_a$). What threshold is used, depends on the application. The more important it becomes to have a low false detection rate, the higher the threshold must be set. In Fig. 9.17 the atom detection probability is plotted for different detectors. How do the probabilities look like, if one wants to distinguish between different number of atoms? The cumulative probability to have a certain number of counts is plotted in Fig. 9.18 (for the enhanced detector with 2 MM fibres). One has to set additional thresholds. To distinguish between one and more atoms the the interval [1-11] counts for a single atom can be chosen. If there are more than 11 counts (and one only allows the information that it is greater than 11), one will classify the event as more than one atom. One can distinguish between two possible cases for the interval [1-11]:

- One declares a single atom, and it was a single atom E_1.
- One declares a single atom, and it was not a single atom $\bar{E}_1$.

For the interval >11 counts, two cases are possible:

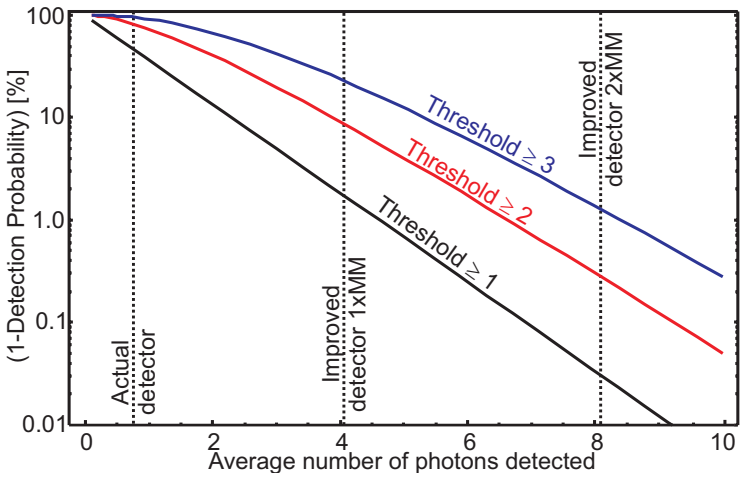

Figure 9.17: The probability not to detect a single atom is plotted as a function of the average number of detected photons ($p_d \times n_a$) in a 10 µs interval. Three cases are given for thresholds ≥ 1, ≥ 2 and ≥ 3. The current detector is indicated as well as the enhanced detectors with one (two) MM fibres with a higher NA. For the enhanced detector with 2 MM fibres the false detection rate is $0.67\%^{Threshold}$.

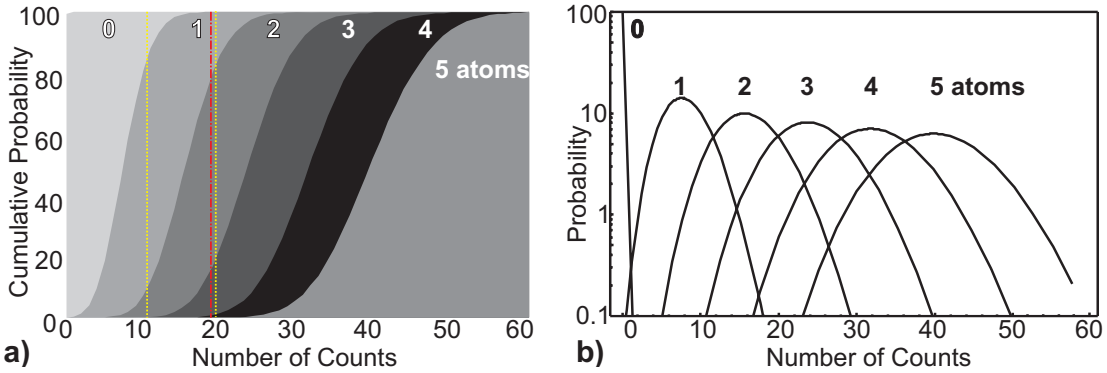

Figure 9.18: **a)** The cumulative detection probability is plotted as a function of the detected photon number for different atom numbers. E.g. in the interval [0-11] counts lay 88% (12%) of all possible counts for a single atom (2 atoms). The yellow (dotted) lines are optimal thresholds to distinguish between 1,2 and 3 atoms. The red (slash-dotted) line is the optimal threshold to distinguish between 1 and 3 atoms. **b)** The probability is plotted as a function of the measured number of counts for 0 to 5 atoms. The integral for each single curve yields 100%. Relative probabilities between curves of a different atom number can be used to find an optimal threshold. E.g. the intersection for 1 and 2 atoms is found for ≈ 11 counts. The probability to get 11 counts is therefore equal for 1 and 2 atoms.

- One declares more than a single atom, and there were more than a single atom E_m.
- One declares more than a single atom, and there was only a single atom $\bar{E}_m$.

With the help of the cumulative probabilities of Fig. 9.18 one can specify the values to $E_1 = 88\%$ and $\bar{E}_1 = 12\%$ for the first interval and $E_m = 88\%$ and $\bar{E}_m = 12\%$ when there were more than 11 counts.

Probabilities for a statistically distributed arrival of the atoms If the atoms, which arrive in the detection volume, are described by a Poissonian distribution with an average number of atoms $\bar{N}$, then the probability to have m atoms is

$$P(m, \bar{N})_{atom} = \frac{(\bar{N})^m}{m!} e^{(-\bar{N})} \tag{9.18}$$

To get to the photon distribution the double Poissonian distribution must be taken into account, where $P(n)$ is the probability to measure n photons ($\lambda = \sum_i \lambda_i$):

$$P(n) = \sum_{m=0}^{\infty} P(m,\bar{N})_{atom}\, P(n,\lambda)|_m \tag{9.19}$$

$$= \sum_{m=0}^{\infty} \frac{\left(\bar{N}\right)^m}{m!} e^{(-\bar{N})} \frac{(p_d\lambda)^n}{n!} e^{(p_d\lambda)}. \tag{9.20}$$

This is a summation over the complete atom number distribution times the probability to detect n photons for each number of atoms.

A helpful representation of the distribution is to use the generating function (Kask et al., 1999). The generating function of a distribution $P(n)$ is defined as

$$G(x) = \sum_{n=0}^{\infty} P(n)x^n. \tag{9.21}$$

For this case and using equation 9.19 one gets

$$G(x) = \sum_{n=0}^{\infty}\sum_{m=0}^{\infty} \frac{\left(\bar{N}\right)^m}{m!} e^{(-\bar{N})} \frac{(p_d\lambda)^n}{n!} e^{(p_d\lambda)} x^n \tag{9.22}$$

$$G(x) = \exp\left[\bar{N}\left(e^{\alpha(x-1)} - 1\right) + \gamma(x-1)\right], \tag{9.23}$$

where $\alpha = n_a p_d$ (p_d is the total detection efficiency and n_a the number of photons scattered per atom) and $\gamma = d_0\Delta t$ the background/dead-count rate in the evaluated time interval Δt. The variance as well as the expectation value can be expressed with the generating function of equation 9.21 as:

$$\langle n\rangle = \frac{d}{dx}G(x)|_{x=1} \tag{9.24}$$

$$\mathrm{var}(n) = \langle n^2\rangle - \langle n\rangle^2 = \frac{d^2}{dx^2}G(x)|_{x=1} + \frac{d}{dx}G(x)|_{x=1} \tag{9.25}$$

where the following expressions were used:

$$\frac{d}{dx}G(x)|_{x=1} = \sum_{n=0}^{\infty} nx^n P(n)|_{x=1} = \sum_{n=0}^{\infty} nP(n), \tag{9.26}$$

$$\frac{d^2}{dx^2}G(x)|_{x=1} = \sum_{n=0}^{\infty} n(n-1)x^{n-2} P(n)|_{x=1} = \sum_{n=0}^{\infty} (n^2-n)P(n). \tag{9.27}$$

With the generating function of equation 9.22 yields:

$$\langle n\rangle = \frac{d}{dx}G(x)|_{x=1} = \bar{N}\alpha + \gamma, \tag{9.28}$$

$$\text{with } \frac{d^2}{dx^2}G(x)|_{x=1} = \bar{N}\alpha + \bar{N}\alpha^2 + \gamma + \left(\bar{N}\alpha + \gamma\right)^2, \tag{9.29}$$

$$\mathrm{var}(n) = \bar{N}\alpha + \bar{N}\alpha^2 + \gamma. \tag{9.30}$$

The following ratio can be measured:

$$\frac{\mathrm{var}(n)}{\langle n\rangle} = \frac{\bar{N}\alpha(1+\alpha)+\gamma}{\bar{N}\alpha+\gamma}. \tag{9.31}$$

In most cases when the expected counts from the atoms are much larger than the counts from the background/dead-counts ($\bar{N}\alpha \gg \gamma$) the following approximation is valid:

$$\frac{\mathrm{var}(n)}{\langle n\rangle} = 1+\alpha. \tag{9.32}$$

The number of photons detected per atom $\alpha = n_a p_d$ can be determined by measuring this ratio. Furthermore the number of scattered photons n_a per atom can be calculated without the need to know the average number of atoms $\bar{N}$, if the photon detection probability p_d is known.

One can expand the calculations to a more general case, where the number of atoms in the detection volume is described by any statistical distribution. Then the variance over the mean for the number of detected photons becomes:

$$\frac{\mathrm{var}(n)}{\langle n\rangle} = 1+\alpha\frac{\mathrm{var}(N_{atoms})}{\langle N_{atoms}\rangle}, \tag{9.33}$$

where $\langle N_{atoms}\rangle$ is the average number of atoms in the detection volume and $\mathrm{var}(N_{atoms})$ the atom number variance. If α is known one can draw conclusions from the measurement with respect to the statistics of the atom arrival. Note that this equation yields the same result for an atomic beam which is described by a Poissonian distribution. Then $\mathrm{var}(N_{atoms})/\langle N_{atoms}\rangle$ is equal to one.

Figure 9.19 shows the analyzed data for 200 experimental cycles. The $|2,-2\rangle$ to $|3,-3\rangle$ (left peak) was used. In figure 9.19a) a representative cycle is depicted and in Fig. 9.19b) the variance is plotted as a function of the measurement time. The variance jumps from around 1 to 1.56 after 50 ms. This coincides with the release time of the atoms out of the trap. In 9.19**c** the variance is plotted as a function of the mean count number $\langle n\rangle$. The slope is $1+\alpha$, and α is the number of detected photons per atom. In this case 0.56 ± 0.07 photons per atom are detected. Estimating the photon detection probability to 0.8%, the average number of scattered photons per atom is 70 ± 9.

The analysis is repeated for different binnings in Fig. 9.20. When binning the data, one has to take into account the light fluctuations. In section 8.1.1 slopes of 3×10^{-3} for the worst case and 1.7×10^{-5} for the intensity stabilized light are measured. The binning in this case went as high as 25, that means in the worst case light fluctuations can contribute with $3\times10^{-3}\times25 \approx 7.5\times10^{-2}$ to the slope. The measured α can therefore be too high by a factor of 7.5×10^{-2}. Nevertheless the approximation is not completely invalid, even in the worst case. Applying a fit of the form

$$Y_{Data} = y_0 + A\,(1-\exp(-X_{Data}/\tau_i)) \tag{9.34}$$

to the data, the result is $\tau_i = (48 \pm 14)$ µs. For longer binning times the detected photons per atom level out and stay more or less constant. This points at a maximum interaction time of the atom with the light field in the order of τ_i. Note, that this is not equivalent to a

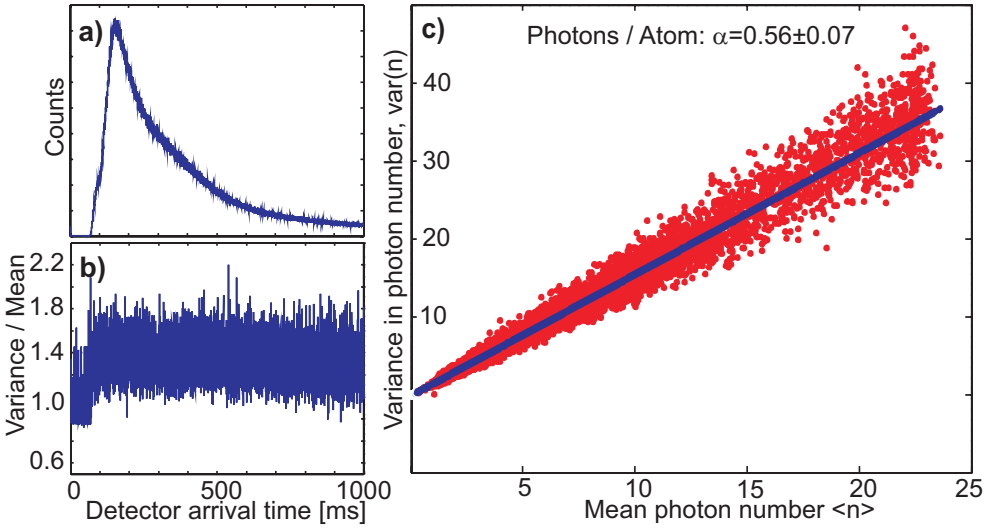

Figure 9.19: Number of detected photons per atom. **a)** shows one of the 200 cycles. In **b)** the variance is plotted as a function of measurement time. At a certain arrival time the variance/mean is increased. This arrival time coincides with the release of the atoms In **c)** the variance is plotted as a function of the mean count number $\langle n \rangle$. The slope is $1+\alpha$, and α is the number of detected photons per atom. The binning was set to 10, which corresponds to 100 µs. The light power was 1.4 nW and the total counts were 59k. Dividing 59k counts by the detection of 0.56 ± 0.07 photons/atom, yields $1.1 \pm 0.2 \times 10^5$ atoms. The $|2,-2\rangle$ to $|3,-3\rangle$ (left peak) was used. This yields a single atom detection probability for the left peak of 43%.

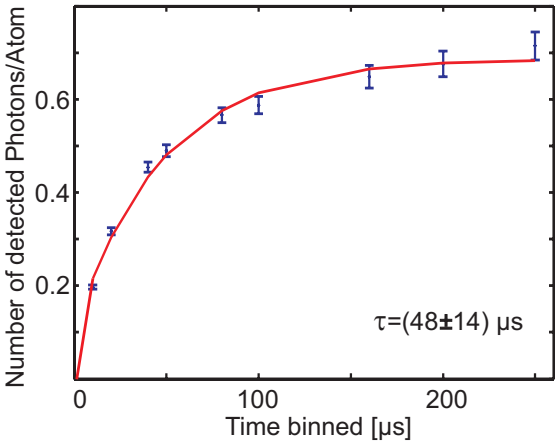

Figure 9.20: The calculated number of detected photons per atom is plotted as a function of the binning time. This measurement was done at 1.4 nW laser power. The curve rises quite fast. A fit of the function $y_0 + A\,(1-\exp(-X_{Data}/\tau_i))$ yields for $\tau_i = (48 \pm 14)$ µs. This indicates an interaction time of $\tau_i = (48 \pm 14)$ µs of the atoms with the light. At saturation intensity an atom can scatter $\Gamma/4 \approx 93$ photons per 10 µs.

full interaction, where an atom can scatter ≈ 93 photons per 10 µs at saturation intensity. The measurement is done at 4 times the saturation power. In 48 µs the maximum of the atom distribution moves approximately 4.8 ± 1.4 µm. This value corresponds to the beam diameter of the light.

Comparison of atom number in the magnetic guide Table 9.9 summarizes the number of atoms measured with the different methods. The errors given are only statistical errors from the different data sets. To estimate the systematic errors is more difficult. In the case of the F'=1 method the number of atoms strongly depends on the photon detection

assumption of $p_d = 0.8\%$. The number of atoms given is not the full number of atoms in

Method	Number of atoms
Absorption Imaging	$(1.0 \pm 0.2) \times 10^5$
F'=1 method	$(1.2 \pm 0.1) \times 10^5$
Statistics	$(1.1 \pm 0.2) \times 10^5$

Table 9.9: Only statistical errors are given. Systematic errors may be much higher. But within errors all three methods yield the same atom number in the guide, which are illuminated. More atoms are in the guide, but only a fraction is imaged at once. The exception is the absorption imaging, where the whole guide is illuminated. This number therefore becomes higher than 1.0×10^5. For a complete guide scan 2.9×10^5 atoms are estimated.

the guide, but only the fraction for a single shot and a certain probe laser intensity. The absorption imaging is a special case, where all atoms become imaged at once. Why this number has the same amplitude may result from different reasons. One reason can be the chip bonding (the wires connecting the chip to the mounting), which obstructed parts of the guide. Nevertheless all three methods yield the same atom number within errors.

To characterize the detector best is to use the $F' = 1$ method to find out the number of scattered photons per atom n_a. With the statistical approach $\alpha = n_a \cdot p_d$ can be measured. Both measurements therefore lead to a full characterization of the detector with n_a and p_d.

9.8 Tomography of the magnetic guide

Methods: Setting the magnetic guide trap bottom

So far the atomic signal is measured for different intensities, times, magnetic fields and laser detunings. The following section deals with the signal as a function of current in the magnetic guide. When scanning the current, a tomography of the atom distribution in the guide is acquired. The bias field B_{Bias} perpendicular to the guide and the guide current I_G defines the height of the magnetic guide minimum. The minimum is distant by r_0 from the surface of the wire. It can be calculated to be

$$r_0 = \frac{2I_G}{B_{\text{Bias}}}, \tag{9.35}$$

where I_G is given in Ampere, B_{Bias} in Gauss and r_0 in millimeter. The magnetic field B_{IP} parallel to the guide does not influence the height, it only lifts/decreases the trap bottom. Figure 9.21a) shows a measurement for a fixed guide current (0.61 A). The signal is plotted as a function of B_{IP}. The current of the guide is chosen in such a way, that the dip overlaps with the maximum of the total curve. One can identify a dip, when B_{IP} is zero, that means the total field $|B|$ is perpendicular to the guide. The dip is too broad to arise (only) from Majorana spin flips. Due to technical noise the spins are also flipped, if the B_{IP} is small enough. From the dip position, the strength of the used coils[17] can be evaluated. This

[17] Assuming a height of 62.5µm for the illuminating light, the superposition of the peak and the dip yields also the total strength of the magnetic field at that height. $B_{W0} = 2.88\text{G/A}$ and $B_{NS} = 2.56\text{G/A}$.

measurement was performed to set the trap bottom to a very low value, which becomes important with the RF-cooling techniques (induce spin flips by extra "technical noise").

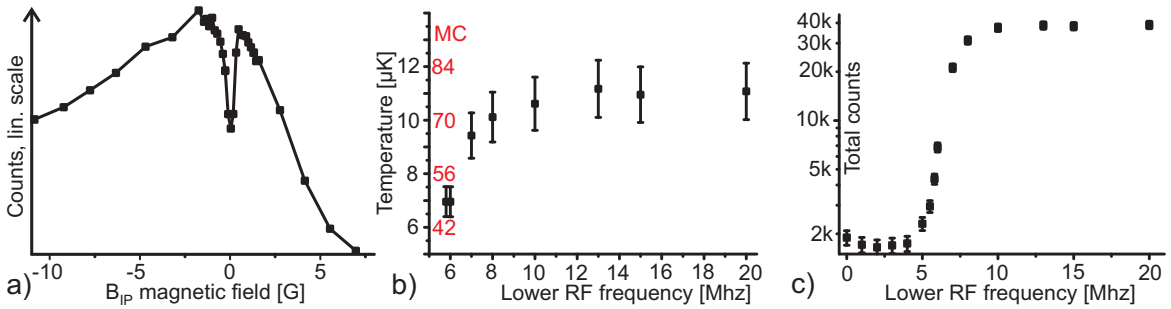

Figure 9.21: a) The plot shows the total counts as a function of B_{IP}. The dip occurs, when B_{IP} is zero, that means the total field is perpendicular to the guide. B_{Bias} then can be compensated by the guide, so no (or a small) magnetic field is left. When preparing the atoms in the chip-z the magnetic field was not perpendicular, so the influences between the guide and the chip-z trap can be distinguished. Technical noise can induce spin flips of the atoms and the atoms are no longer trapped. A minimum count rate can also be measured, when B_{IP} is set to zero during the chip-z time. **b)** Temperature of the atoms as a function of the lower RF frequency. The RF frequency starts at 20 MHz and the sweep takes 1.5 s. The distance of the chip-Z to the detection region is 5.5 ± 0.3 mm. The time of arrival of the peak can be measured more accurate than 10 ms. The temperature is given for the case of instantaneous release of the atoms. The Monte Carlo simulated temperatures are higher by a factor of 7. **c)** The total counts are plotted as a function of the lower RF frequency.

Methods: Reducing Temperature and number of atoms

A next step is to reduce the atom number and their temperature. This is achieved by coupling a RF-signal to the atom chip via a U-shaped wire structure close to the chip-Z structure.

In Fig. 9.21 b) and c) the influence of the RF frequency on the atom number and the temperature is depicted. Both values are plotted as a function of the lower RF frequency. The number of atoms and the temperature can be decreased with this method.

9.8.1 Tomography of the magnetic guide

With the help of the techniques to reduce atom number and temperature efficiently, the signal is measured as a function of the guide current and the B_Z (Up-Down) magnetic field. A schematic is drawn in Fig. 9.22 showing how the magnetic minimum shifts for the varying parameters. Changing the guide current sets the distance of the magnetic minimum to the chip, whereas changing the Up-Down magnetic field can shift the guide aside the wire. Also a comparison of the tomography with and without RF cooling will give evidence for the atomic distribution in the magnetic guide. Figure 9.23a) plots the counts as a function of the guide current and the time of flight. Additionally, plots of the counts versus the guide current for different times are shown. That means to determine the guide profile for different times. The counts are also plotted as a function of the time of flight for different

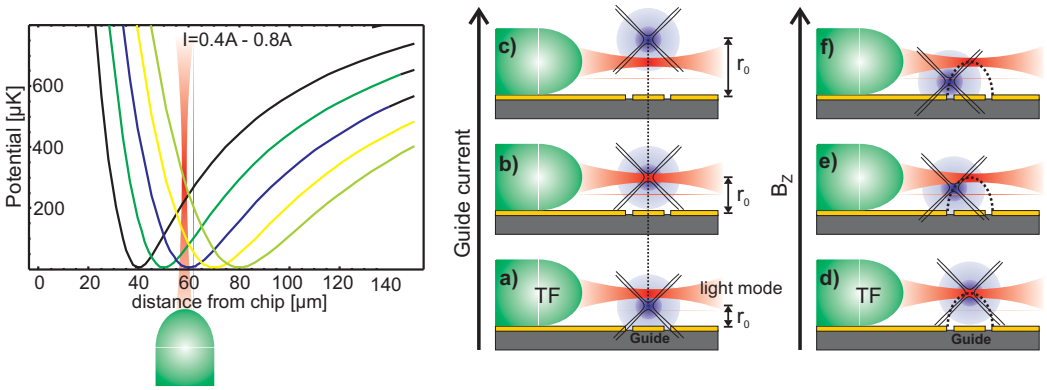

Figure 9.22: Left: The transversal magnetic potential is plotted for guide currents ranging from 0.4 A to 0.8 A. The tapered fiber is positioned at a height of 62.5 µm. Center/Right: The tapered fibre (TF) is mounted on the chip with its light mode shown. The interrupted golden structure in the middle is the guide wire structure. Above that structure a plot stands for the magnetic field minima (with indicated quadrupole field lines) **a)** depicts the guide at a certain height. If the guide current is increased also r_0, the distance of the magnetic trap minimum to the chip surface, is increased. **b)** has an optimal guide current whereas **c)** has a too high guide current. **d)-f)** shows a situation where the B_Z (Up-Down) offset field is increased. For **d)** the guide current is optimal and $B_Z = 0$. The minima now moves along a "squeezed" circle with its center in the guide. As the Up-Down field is increased the minima moves sidewards/downwards and closer to the guide.

guide currents, yielding an atomic time distribution profile for different magnetic fields (guide currents). Figure 9.23b) shows slices of the tomography along the guide current at

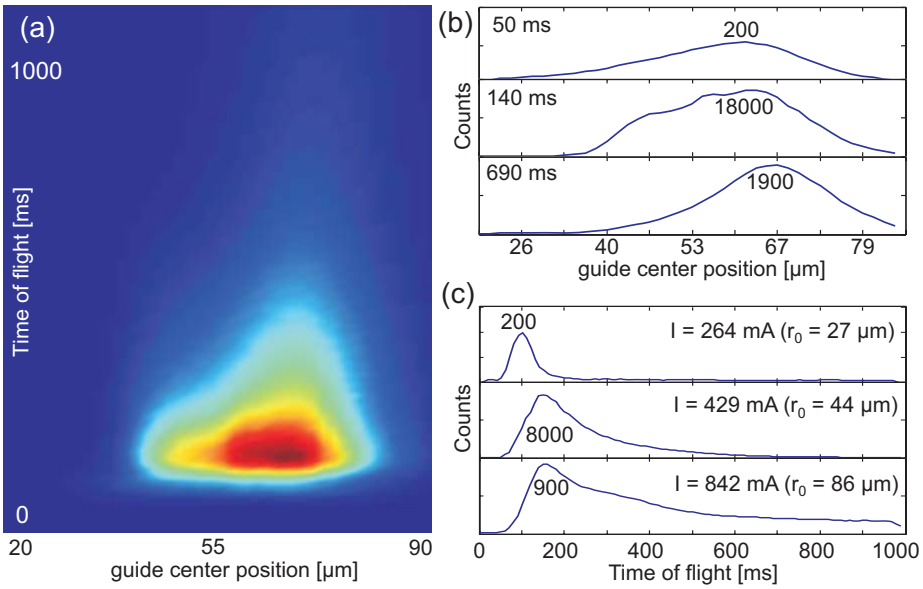

Figure 9.23: **a)** Counts as a function of the magnetic guide center position above the chip and the time of flight. Slices along the guide center positions at different times are shown in **b)**. In **c)** slices along the time axis at different guide center positions are evaluated. The maximum counts are also given for each curve.

different times. The later a cut is made in time, the higher the guide current for the count maximum is. An explanation can be that the atoms also transversally move in the guide. At low guide currents the atoms are closer to the chip surface. The probability that they hit the chip surface increases with time in the guide. Figure 9.23c) shows slices along the time axis for several guide currents. For low currents only the faster atoms are detected. This curve fits well to the 1D Maxwell-Boltzmann distribution plus an exponential decay with increasing time.

The same measurement is repeated for a magnetic field scan of B_z (Up-Down) and is plotted in Fig. 9.24. With increasing B_z the guide center can be shifted aside the wire. The minima now moves along a "squeezed" circle with its center in the guides' wire. As the Up-Down field is increased the minimum moves sidewards/downwards and closer to the guide. This is schematically drawn in Fig. 9.22.

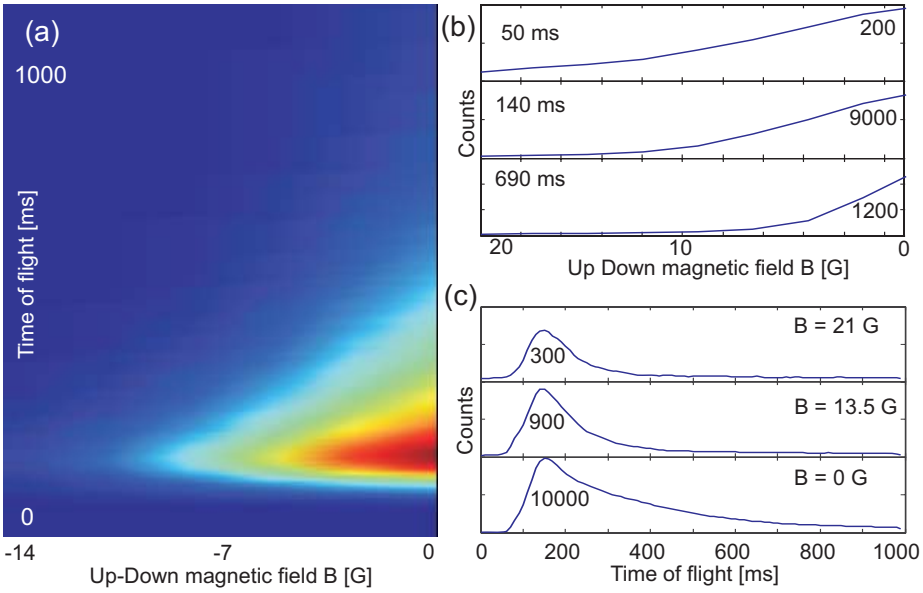

Figure 9.24: Counts as a function of the Up Down magnetic field and the time of flight. One cut is along the time axis, the other cut along the Up-Down magnetic field axis. Additionally the maximum counts are given for each peak.

9.8.2 Tomography for RF cooled atoms

The tomography so far was carried out with the atoms directly out of the chip-z trap. The atoms are "rather hot". In the following the results of the measurements for cooler atoms is shown. The measurements were done for the $|2, m_F\rangle \rightarrow |3, -3\rangle$ and $|2, m_F\rangle \rightarrow |3, 3\rangle$ transitions. Except for the absolute height the signal for the two peaks did not show any difference. Thus only the signals of one peak are compared. In Fig. 9.25 the atomic signal is plotted as a function of the guide current. Three different curves are shown, one was measured without Rf, one was measured with a frequency sweep from 20 MHz down to 7 MHz and one down to 6 MHz. The sweep time was set to 2.5 s. The signal's maxima shift to lower guide currents for lower Rf frequencies. In Fig. 9.25**(b)** The signal is plotted as a function of the guide current, but for three different times. All three graphs show the

signal without Rf. For the measurements with Rf the changes are the same. The maxima shift to higher guide currents for atoms arriving later at the detector. In Fig. 9.25**(c)** The signal is plotted as a function of time of flight. Two curves are shown for each of the three different guide currents. One was without a Rf field, the other was with a Rf sweep down to 6 MHz. The atoms with a Rf cooling are entering the detection area much later. This indicates a cooling effect. The amplitudes of the curves where a Rf sweep was applied, were multiplied by a factor of three to have a better visualization.

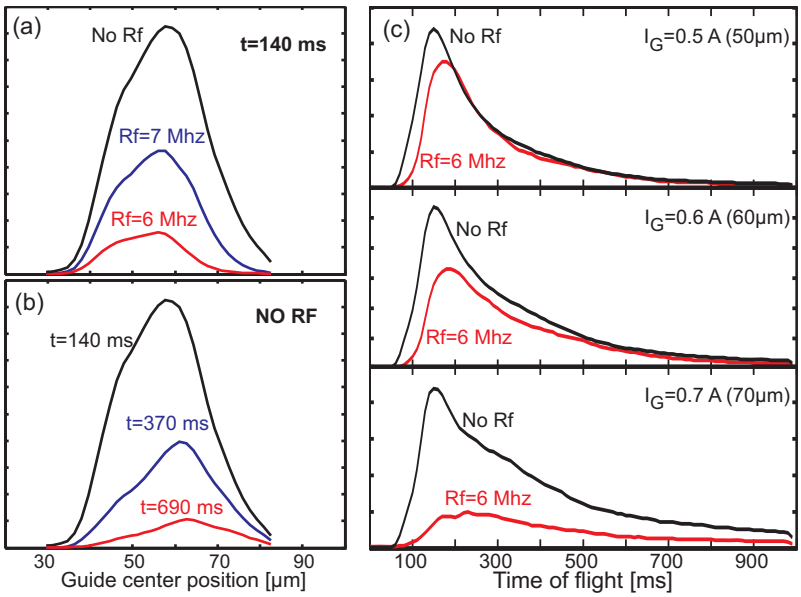

Figure 9.25: **(a)** The signal is plotted as a function of the guide current. Three different curves are shown, one was measured without Rf, one was measured with a frequency sweep from 20 MHz down to 7 MHz and one down to 6 MHz. The sweep time was set to 2.5 s. The signals' maxima shift to lower guide center positions (currents) for lower Rf frequencies. **(b)** The signal is plotted as a function of the guide current, but for three different times. All three graphs show the signal without Rf. The maxima shift to higher guide currents for atoms arriving later at the detector. **(c)** The signal is plotted as a function of time of flight. Two curves are shown for each of the three different guide currents. One was without a Rf field, the other was with a Rf sweep down to 6 MHz. (The amplitudes of the curves where a Rf sweep was applied, were multiplied by a factor of three to have a better visualization.) The atoms with a Rf cooling are entering the detection area much later. This speaks for a cooling effect.

Figure 9.26 shows the signal as a function of time of flight and guide current for different Rf sweeps. In the first row the signal is plotted as a function of guide current and time of flight. The difference in the tomographies are the used Rf sweeps. The first row shows the signal for no Rf **(a)**, 20 to 7 MHz **(b)**, 20 to 6 MHz **(c)** and 20 to 5 MHz **(d)**. The second row shows a division of the signal in the first row with the signal without a Rf sweep ($e = b/a$, $f = c/a$ and $g = d/a$). Red colors indicate a relative low loss in atoms compared to the blue regions. The "blue" channel at 100 ms hints at slower atoms with a Rf field than without a Rf field. That the cooling works can be seen by the shift of the peak to later arrival times. There is also a tendency for higher counts with Rf for small guide currents. This becomes understandable by the consideration that with Rf cooling

the transversal velocity becomes smaller too. Cooler atoms do not hit the chip (and get lost) that often. The blue region for high guide currents indicates hot atoms in the guide without Rf cooling, which are running up the magnetic potential.

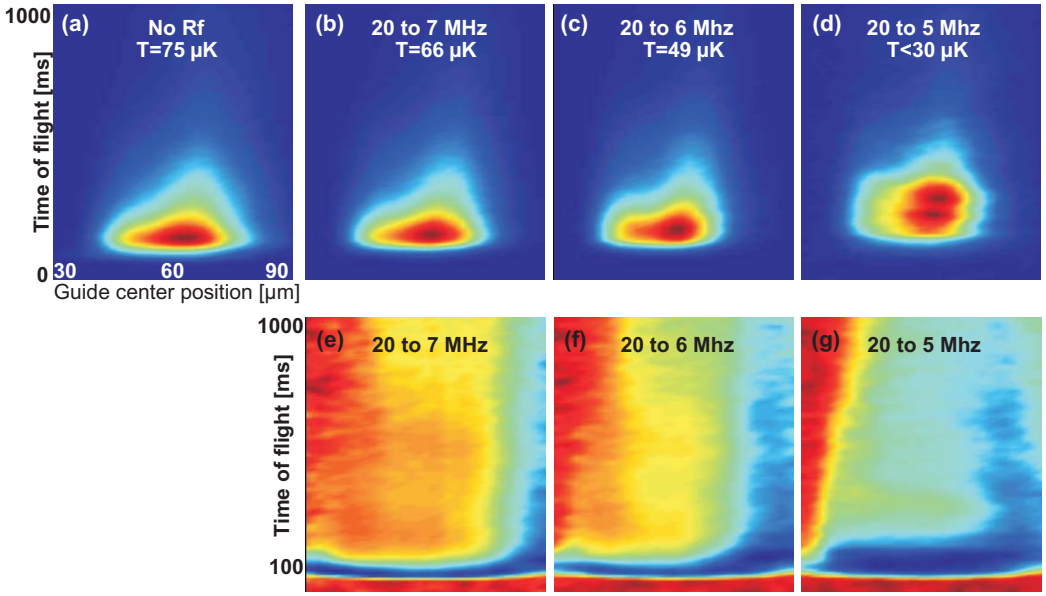

Figure 9.26: In the first row the signal is plotted as a function of the guide center position and time of flight. The difference in the tomographies are the used Rf sweeps. The first row shows the signal for no Rf **(a)**, 20 to 7 MHz **(b)**, 20 to 6 MHz **(c)** and 20 to 5 MHz **(d)**. The temperature for **(d)** is an upper estimate, since the structure has two peaks. The magnetic fields are $B_{IP} = -4.4$ G and $B_{\text{Bias}} = 20.0$ G. The total counts decrease as the lower RF frequency is reduced. The second row shows a division of the signal in the first row with the signal without a Rf sweep. Red colors indicate a relative low loss in atoms compared to the blue regions.

Atomic density distribution in a harmonic potential The density distribution of a thermal cloud in a harmonic potential is a Gaussian. The extension σ_i of the cloud in the i-direction is given by

$$\sigma_i = \frac{1}{\omega_i}\sqrt{\frac{2k_BT}{m_{Rb}}}. \tag{9.36}$$

ω_i is the trap frequency along the i-direction, k_B Boltzmann's constant, m_{Rb} the mass of rubidium and T the temperature. For the experimental parameters of $r_0 = 62$ µm, $B_{\text{Bias}} = 20$ G, $B_{IP} = |-4.4|$ G the radial trap frequency can be approximated to

$$\omega = \sqrt{\frac{\mu_B g_F m_F}{m_{Rb}}}\frac{B_{\text{Bias}}}{r_0\sqrt{B_{IP}}} \tag{9.37}$$

$$\approx 2\pi \times 2.0\text{kHz}. \tag{9.38}$$

The measured extensions of the atom cloud in the last section with guide scans are $\sigma_{guide} = [7.5, 12]$ µm. Taking into account the laser beam diameter of σ_{laser} =2.5 µm, the atomic cloud extension σ_{cloud} becomes $\sigma_{cloud} = \sqrt{\sigma_{guide}^2 - \sigma_{laser}^2} \approx [7.1, 11.7]$ µm.

With Eq. 9.36 one can calculate the extension for temperatures of $[40, 75]$ µK, which is measured for the different Rf cooled atoms. The extensions in the radial direction are $\sigma_{theo} = [6.9, 9.4]$ µm, which complies with the measured extension $\sigma_{cloud} = [7.1, 11.7]$ µm.

9.9 Conclusion

The fluorescence detector leads to many fascinating results. Here the different measurements and their results are summarized on how the pieces of information can be used for a most efficient fluorescence detector.

- The most important parameters of a fluorescence detector are the background and the measurement time. The background signal is minimized to 290 counts/s (+10 counts/s if the dipole laser is used). The highest background contribution is produced by the detector with a dead count rate of 250 counts/s. The background emerging from the probing light coupled into the tapered fibre is almost negligible. The impressive geometrical suppression factor is 3.0×10^{-10}. Less than one count per second contribute to the background signal for a probing laser power of 1 nW.

- To further minimize the background level a different version of the detector with dead counts of around 25 counts/s can be used. Another high background source is emerging mainly due to black body radiation. To produce the Rubidium vapor in the vacuum chamber a "dispenser" is heated. To minimize this background source the dispensers can be operated in a pulsed mode. That means they must be switched off a few seconds before the magnetic trapping of the atoms. For the MOT phase they must be heated up again.

- The number of atoms is measured with three different methods. The first one is the absorption imaging of the external camera system. Then the $|2, 2\rangle$ to $|1, 1\rangle$ transition is used to measure the atom number, since this transition scatters only 1.44 photons on average. The last one is a statistical approach, which uses Poissonian statistics to estimate the number of atoms. All three methods together yield an atom number of $(1.1 \pm 0.1) \times 10^5$.

- The number of scattered photons per atom can also be estimated. With the statistical approach 70 ± 9 scattered photons per atom and with the $|2, 2\rangle$ to $|1, 1\rangle$ transition 58 ± 2 scattered photons per atom can be calculated. In both cases the $|2, -2\rangle$ to $|3, -3\rangle$ transition was used. The number of scattered photons calculated from the statistical approach strongly depends on the detection efficiency p_d. Thus an error estimating p_d leads directly to an error in the number of scattered photons. For the $|2, 2\rangle$ to $|3, 3\rangle$ transition 97 ± 3 photons per atom is measured. From the statistical calculations one finds the typical interacting time of one atom (for the $|2, -2\rangle$ to $|3, -3\rangle$ transition) to be $\tau_i = (48 \pm 14)$ µs. In this time the atoms travel 4.8 ± 1.4 µm. This distance corresponds to the waist (diameter) of the laser beam.

- Geometrical effects of the collection volume of the MM fibre were investigated. Therefore the laser light was pulsed and compared to a continuous illumination of the atoms. At the beginning of the pulsed light an overshoot was visible. The decay

constant of that overshoot was $\tau = (480 \pm 80)$µs. In that time the atoms in the peak travel 48 ± 8 µm. This distance corresponds within errors to the length where the MM fibre has its maximum collection efficiency. From the ratio of the overshoot to the rest of the signal can be reasoned, that pulsed light has to be used for high laser powers, when large volumes are imaged. This is just due to geometrical reasons, since the atoms start to scatter already outside the optimal detection volume of the MM fibre for large laser powers . The overall number of scattered photons per atom can not be increased. For a laser power of 1.4 nW almost no overshot is measured. Thus the number of photons scattered per atom does not need to be corrected.

- Another important point is the detection efficiency of the fluorescence detector. In the current case it is 0.8%. This can be improved with existing technologies to a detection efficiency of over 8.3%.

- Therefore with the measured values one can estimate the detection probability for a single atom for the $|2,2\rangle$ to $|3,3\rangle$ (right peak) transition. The number of scattered photons per atom is $(97) \pm 2$. Setting the threshold to ≥ 1 counts the detection probability for single atoms gets $(54.1 \pm 2)\%$. For the enhanced detector with two MM fibres and a detection efficiency of $2 \times 4.16\%$, one has a single atom detection probability of >99.97%. But the background for the enhanced version will also increase. Assuming a background increase proportional to the gain in collection efficiency, the background rises to $(250 + \frac{2\times 4.16\%}{0.8\%}40)/s = 666/s$. The false detection rate is therefore increased from 0.3% to 0.67% per 10 µs interval.

- To find out the number of atoms, a statistical approach has to be used. The total number of atoms N can be calculated from the total counts divided by $\alpha = p_d \times n_a$. The values of the photon detection probability p_d and the number of scattered photons per atom n_a do not need to be known independently. Their product can be measured. To find out the number of scattered photons per atom n_a the $F\text{`} = 1$ method has to be used. This method is independent of the number of atoms and the detection efficiency p_d for a scattered photon, since only relative line strengths are measured. By performing those two measurements, one can find out N and n_a and therefore calculate p_d.

- Moreover the atomic distribution in the guide is measured. It fits very well to a 1D Maxwell-Boltzmann distribution. A Monte Carlo simulation showed typical temperatures of 40 to 75 µK in the magnetic guide. RF cooled atoms reach temperatures of <30 µK.

- A spectroscopic measurement of the $5^2S_{1/2}\,|F = 2, m_F\rangle \rightarrow 5^2P_{3/2}\,|F', m'_F\rangle$ transition with varying laser powers is performed. The non trapped atoms showed larger detunings, because they are repelled from the magnetic trap and thus reach higher magnetic fields. The detuning due to Zeeman level splitting is proportional to the magnetic field. The atoms do not necessarily need to stay trapped for a signal.

- The absolute magnetic field in the guide leads to a Zeeman-splitting and optical pumping. To avoid those effects in the future, one has to choose the smallest possible

remaining magnetic field at the guide center. It must be small enough, that the Zeeman-splitting is smaller than the natural line width of the atomic transition.

- Finally the magnetic guide was scanned for varying distances to the chip and for small shifts aside the chip wire. A tomography of the guide was made with the signal of the atoms. Several tomographies for different temperatures were compared. This helps to understand the distribution of the atoms in the guide as a function of temperature.

10 Absorption Detection

10.1 Overview

While fluorescence detection uses the spontaneously emitted light, the presence of an atom will also influence the driving field. This is described by the susceptibility of the atom. The imaginary part of the susceptibility describes the absorption, and the real part the phase shift on the driving field. By performing measurements on the driving field a complete atomic signature can be collected. The atomic density can be measured by monitoring the attenuation of the driving field. In the unsaturated case, this situation is described by Lambert-Beer law. The absorption signal provides a direct measure of the atomic column density. If the mean intensity of the incoming beam is known, the main uncertainty is determined by measuring the transmitted light. To reach unity detection efficiency in absorption imaging it seems natural to reduce the beam waist as much as possible. This is however not a successful strategy as pointed out by van Enk (van Enk, 2004, van Enk and Kimble, 2000, 2001). A strongly focused beam is not optimally overlapped with the radiation pattern of the atoms. The absorption cross section for such a strongly focused beam becomes smaller with a decreased spot size.

Another strategy to improve the sensitivity is to increase the measurement time. The scattered photons will however heat up the atoms and expel them from the observation window. If the atom is held by a dipole trap, the measurement time can be increased. There is no fundamental limit to the detection of a single atom via absorption, if it can be kept localized long enough.

In this chapter the fibre absorption detector is characterized with the help of different measurements. At the beginning a typical signal from the absorption detector for magnetically guided atoms is shown . The arrival time of the atoms agrees with a 1-D Maxwell-Boltzmann distribution. The standard measurement method is to keep all parameters constant and take the atom signal for one cycle, and change parameters only for the next experimental cycle. Therefore a timing information is always acquired.

Afterwards, the spectroscopy of the $|2, m_F\rangle \rightarrow |F', m'_F\rangle$ transition is taken and the measured values are compared to the fibre fluorescence detector. A next point is to determine the number of atoms in the magnetic guide. Two different methods are used. One is to use the absorption imaging with the external camera system, the other method is to use the $|2, m_F\rangle \rightarrow |1, 1\rangle$ transition to determine the number of atoms. The different methods are explained and their advantages and disadvantages are discussed in detail. Also the number of photons which are scattered per atom can be derived from these measurements.

Moreover the relative signal with and without atoms is analyzed for different laser powers. The expected signal to noise ratio is calculated and compared to the measurement. Optical pumping may be a problem for low laser intensities. This leads to the detection probability for a single atom and values are calculated for different setups. Finally several

tomographies of the magnetic trap are conducted. From these measurements pieces of information about the atomic distribution in the magnetic guide are acquired.

10.2 Setup

The absorption detector is made of a tapered fibre[1] and a MM fibre[2]. The two fibers face each other at a distance of ≈ 75 µm. The measured transmitted intensity is ≈ 95%. This allows only losses from reflections at the fiber facets. The setup of the absorption fibre detector is shown in Fig. 10.1. The distance of the tip of the tapered fibre to the center

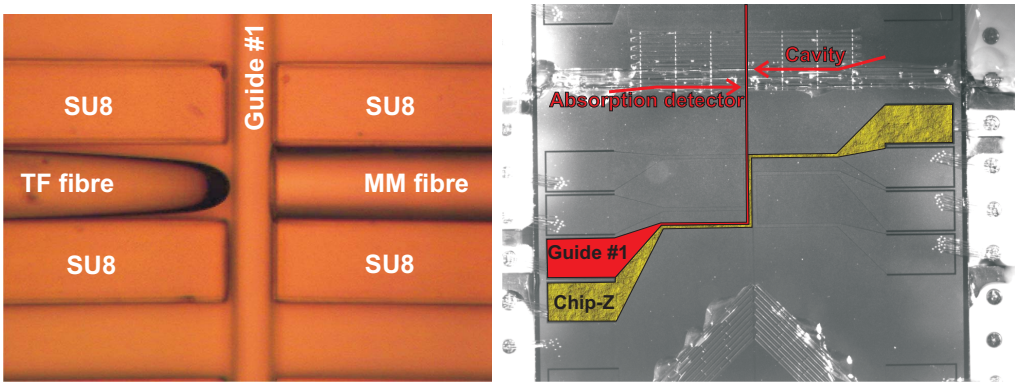

(a) Setup of the 0° fibre detector. (b) Overview of the chip.

Figure 10.1: Picture (a) shows the setup of the absorbtion detector. On the left side the tapered fibre is visible and is facing the MM fibre on the right side. In between the wire guide is also visible. The width of the wire is 50 µm. The distance of the tip of the tapered fibre to the center of the wire guide is ≈ 40 µm, which is its working distance. Picture (b) shows the chip from above. The 0° detector is embedded in the SU-8 structures at the top of the picture.

of the wire guide is ≈ 40µm, which is its working distance. The distance of the MM fibre facet to the center of the wire guide is 35 µm.

10.3 Typical signal

In the case of the absorption fibre detector, (almost) all the light is collected. So the signal has a certain level when there are no atoms. The signal level only depends on the light level, which is coupled into the tapered fibre. In Fig. 10.2 a typical signal with atoms is plotted as a function of the arrival time. As soon as atoms arrive in the detection volume, they scatter photons out of the transmitted light. This will be visible as a dip in the signal. The shape is very similar to the (inverted) fluorescence signal. Now the signal is made of a dip on a certain signal level, whereas for the fluorescence detector the signal formed a peak on the background signal.

[1] Working distance 40 µm.

[2] Thorlabs GIF625. Graded index multi mode fibre with 62.5 µm core diameter, NA=0.275 and with an attenuation of 3.6 dB/km $\sim 0.57 \times 10^{-3}$ loss per m.

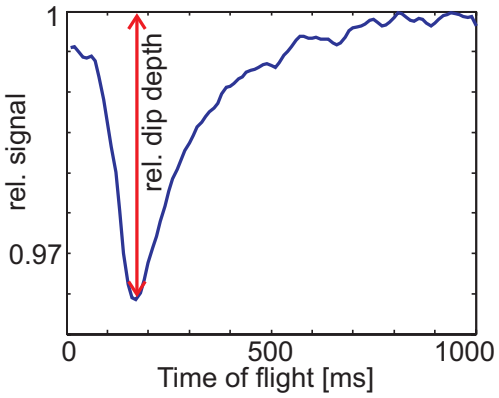

Figure 10.2: Typical absorption signal. The dip in the signal has a relative strength of a few per cent only. The shape is very similar to the (inverted) fluorescence signal. Now the signal is made of a dip on a certain signal level, whereas for the fluorescence detector the signal formed a peak on the background signal.

Noise reduction Background signals do not play a role for the absorption detector. Since the light level is quite high, noise on the light or on the electronic data acquisition chain are more severe than with the fluorescence detector. Connecting the computer via WLAN instead of ethernet, using a differential amplifier of the Labview Card and using the FEMTO[3] amplifier instead of the homebuilt[4] amplifier, the noise can be reduced by almost a factor of 100. Especially the use of a differential amplifier has the effect of getting rid of 50 Hz noise. See the Labview manual for further details (National Instruments, 2006).

Background The background is in the order of a few 100 photons per second. One picowatt of light at 780 nm contains about 4 million photons per second. So the background does not play a role for the absorption detector. Thus in most cases the IR-filter setup (see Fig. 8.3) can be left out, having 100% instead of 80% transmittance at that point of the setup.

10.4 Spectroscopy of the $|2, m_F\rangle \rightarrow |3, m'_F\rangle$ transition

The $|2, m_F\rangle \rightarrow |3, m'_F\rangle$ is the strongest transition. For the absorption detector it is important that the atoms scatter as many photons as possible. The fluorescence detector shows that the atomic levels are split in the magnetic field due to the Zeeman shift. To compare the absorption detector to the fluorescence detector a spectroscopic measurement is performed.

In Fig. 10.3 the relative dip depth is plotted as a function of the laser detuning. The peak's positions stay at the same value when compared to the fluorescence detector . Only the peak strengths change, but this may be due to polarization changes, as the angle of illumination for the atoms changes from 45° to 90°. A fit to the peaks of the $|2, -2\rangle$ to $|3, -3\rangle$ and $|2, 2\rangle$ to $|3, 3\rangle$ transitions yield detuning's of (-7 ± 1) MHz and (7 ± 1) MHz. This agrees with the fluorescence detector, where (-7.6 ± 0.1) MHz and (6.3 ± 0.1) MHz for those two peaks is measured. The higher errors of the absorption detector originate from the lower signal to noise ratio of the absorption detector.

[3]Femto variable-gain high-speed current amplifier DHPCA-100.
[4]Physikalisches Institut C17 I/U Converter.

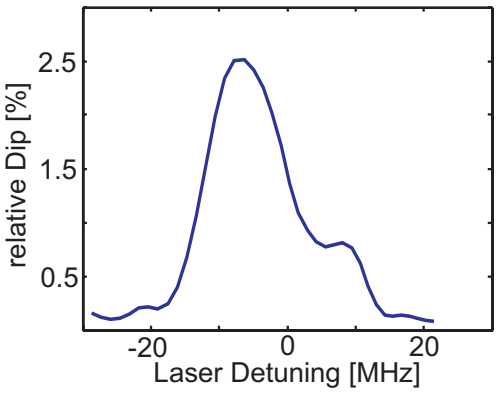

Figure 10.3: The $|2, m_F\rangle \rightarrow |3, m'_F\rangle$ transition is measured. The frequency of the laser was scanned over 50 MHz. The peaks are at $\pm(7 \pm 1)$ MHz. This agrees with the fluorescence detector, where the peaks are measured to be at (-7.6 ± 0.1) MHz and at (6.3 ± 0.1) MHz . The higher errors of the absorption detector originate from the lower signal to noise ratio for the absorption detector. The experimental values are $B_{\text{Bias}} = 20$ G, $B_{IP} = -4.4$ G of the offset fields, the guide's current is $I_{Guide} = 0.627$ A.

10.5 Determination of number of atoms in the detector

Two important quantities for the absorption detector are the number of atoms in the magnetic guide and the number of photons scattered per atom. The signal to noise ratio increases with both values. Two possibilities are available to measure the number of atoms in the detector. It can be measured by absorption imaging, which was already presented in tab. 9.6. Or it can be measured with the $|2, m_F\rangle \rightarrow |1, 1\rangle$ transition.

10.5.1 Number of atoms via the $|2, m_F\rangle \rightarrow |1, 1\rangle$ transition

A long measurement of 1340 consecutive experimental cycles is used to determine the number of atoms. The assumption is made, that each atom can scatter 1.44 photons on average. The power coupled in was kept constant at 150 pW.

In this case the number of atoms is a summation over the relative dip depth d_i for each time bin i times the number of photons $n_p \times \Delta t$ per time bin (of length Δt) and divided by the number of scattered photons per atom n_a. The number of photons n_p for a certain laser power P is given as

$$n_p = \frac{P}{h\nu},$$

where h is Planck's constant. In this case 150 pW corresponds to approximately 585 million photons per second. Additional corrections include the collection efficiency of 1.9% of the MM fibre (NA=0.275). Most of the scattered photons are lost into the solid angle of 4π, but 1.9% are collected again. Therefore a correction factor of $1/(1 - \frac{2\pi(1-\sqrt{1-NA^2})}{4\pi})$ must be applied. The number of atoms N is then

$$N = \sum_i \frac{d_i n_p \Delta t}{n_a(1 - \frac{2\pi(1-\sqrt{1-NA^2})}{4\pi})}. \tag{10.1}$$

The atom number was estimated via the $|2, m_F\rangle \rightarrow |1, 1\rangle$ transition to $(1.3 \pm 0.3) \times 10^5$. This number is comparable to the fluorescence detector, where $(1.1 \pm 0.1) \times 10^5$ atoms is measured.

10.5.2 Number of scattered photons per atom

To find out the number of scattered photons per atom for the $|2, m_F\rangle \rightarrow |3, m'_F\rangle$ transition, first the number of atoms is estimated via the $|2, m_F\rangle \rightarrow |1, 1\rangle$ transition. Then Eq. 10.1 is solved for the number of scattered photons per atom n_a. One finds $\approx 55 \pm 10$ scattered photons per atom for the $|2, -2 \rightarrow\rangle\ |2, -3\rangle$ transition (left peak), which agrees with the fluorescence detector (58 ± 2). It is important to mention, that the number of atoms is estimated via the $|2, m_F\rangle \rightarrow |1, 1\rangle$ transition only for one laser power. That means in this case that the geometrical effects will not cancel out, due to the larger illuminated volume with increasing laser power when dividing the signal of the $|3, m'_F\rangle$ and the $|1, 1\rangle$ transition. In principle the number of atoms should have been measured via the $|2, m_F\rangle \rightarrow |1, 1\rangle$ transition for each laser power. Then the signals should have been compared for the laser powers belonging together. Unfortunately one measurement for the $|2, m_F\rangle \rightarrow |1, 1\rangle$ transition took 1340 experimental cycles. This takes 8 hours of the experiment to run continuously. The probability for the lasers to fall out of lock increases exponentially with time.

10.6 Geometrical detection effects

Scattered light might kick out atoms before reaching the field of view of the MM fibre, since now the light is hitting the MM fibre directly. In the 90° detector the light can spread out, without hitting a fibre in its vicinity (typically > 200 µm). To check on how the atoms are lost due to photon scattering, a similar test as with the fluorescence detector is made. The dip depths of the signal with atoms is compared between full time illumination and illumination starting at the dip minimum. The dip depth stays the same, thus scattered light is no problem for the used probing light powers up to 3 nW. Pictures taken from below the chip with the camera system show no scattered light in the area of the absorption detector. An effect can not be detected here. The problem with the absorption detector is the high light amplitude hitting the detector, which results in a certain detector rise time. Thus any geometric effects can not be discovered, because they may be overlayed by detector effects.

10.7 Signal to noise ratio and relative dip depth as a function of laser power

The atomic density can be measured by monitoring the attenuation of the driving field. In the unsaturated case, this situation is described by Lambert-Beer law. To evaluate the performance of the fibre absorption detector measurements for different probing light powers are taken. For the fluorescence detector the signal height is measured as a function of the laser power, but for the absorption detector the measure will be a dip in a rather high signal. The dip depth can be related to the absolute signal and becomes the relative dip depth. If the mean intensity of the incoming beam is known, the main uncertainty is determined by measuring the transmitted light. This can be expressed by the signal to noise ratio (SNR). In the following section both quantities will be evaluated.

Relative dip depth Figure 10.4 shows a measurement of the relative dip depth as a function of the laser intensity. The measurement is carried out for the $|2,-2\rightarrow\rangle$ $|3,-3\rangle$ transition The laser power coupled in is $p = s \times p_0$, where p_0 is the saturation power for

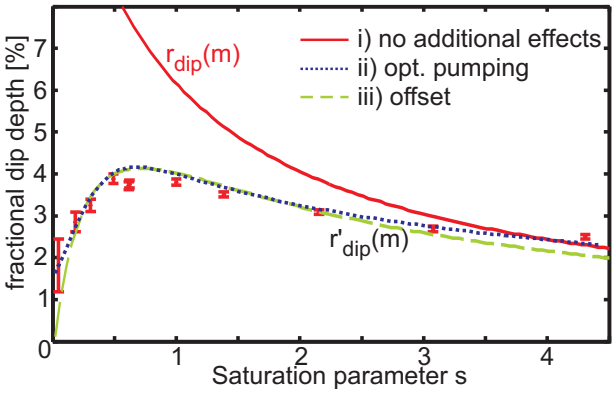

Figure 10.4: The relative dip depth is plotted as a function of the saturation parameter. The continuous red line is the theoretical estimate for the dip depth $r_{dip}(m)$. For low powers ($s < 2$) the measurement does not show the expected behavior. The blue dotted line (ii) shows a model fit for the dip depth if optical pumping is taken into account. The green dashed line (iii) evaluates a model fit for the dip depth r'_{dip}, if the real power for the atoms was smaller than the "measured" power. This can be some offset errors. The smaller the power, the stronger these effects will get.

the tapered fibre. s is the saturation parameter for the tapered fibre with $w_0 = 2.5$ µm. The scattering rate for N atoms S_{scatt} is

$$S_{scatt}(s) = N\frac{\Gamma}{2}\frac{s}{s+1}. \tag{10.2}$$

These photons are scattered into 4π. A small fraction is recollected again from the MM fibre, but will be neglected for the following calculations. If the recollection becomes stronger for other types of fibres, the effective scattering rate[5] will be smaller by $(1-\eta_{MM})$. η_{MM} is the MM fibre collection efficiency.

The relative dip depth matches the following expression:

$$r_{dip}(s) = \frac{S_{scatt}(s)}{s \times p_0 \times n_0} \tag{10.3}$$

$$= N\frac{\Gamma}{2}\frac{1}{(s+1)p_0 n_0}, \tag{10.4}$$

where n_0 is the number of photons per Watt and per second. This yields

$$n_0 = 1/(h\nu) \approx 3.92 \times 10^{18}/(\mathrm{Ws}), \tag{10.5}$$

where ν is the frequency for the relevant transition.

So for low laser powers ($s \rightarrow 0$) the curve rises and the relative dip depth r_{dip} approaches

$$N\frac{\Gamma}{2}\frac{1}{p_0 n_0} = N\frac{\sigma_0}{A}. \tag{10.6}$$

[5]The atomic scattering itself stays the same of course.

σ_0 is the on-resonance cross section[6], $A = \pi w_0^2$ the area of the Gaussian of the tapered fibre with the beam radius w_0. From the above formulas one also sees that the cross section is a function of laser power:

$$\sigma(s) = \sigma_0 \frac{1}{s+1}. \tag{10.7}$$

Taking a detuning $\Delta\omega$ with $\zeta = \Delta\omega/\Gamma$ into account, σ becomes

$$\sigma(s) = \sigma_0 \frac{1}{s+1+(2\zeta)^2}, \tag{10.8}$$

and therefore

$$r_{dip}(s) \quad = \quad N\frac{\sigma(s)}{A}. \tag{10.9}$$

All the formulas are valid only for $r_{dip} \ll 1$. The scattering rate then becomes

$$S_{scatt}(s) = N\frac{\Gamma}{2}\frac{s}{s+1+(2\zeta)^2}. \tag{10.10}$$

The measurement shows a different behavior. If the real power for the atoms was smaller than the "measured" power s', then the dip can be described by

$$r'_{dip}(s) \quad = \quad \frac{S_{scatt}(s)}{s' \times p_0 \times n_0} \tag{10.11}$$

$$= \quad r_{dip}(s)\frac{s}{s'}, \tag{10.12}$$

with $0 < s < s'$. This can be some offset errors, while measuring the power. For example light that is not resonant for the atoms. The smaller the power gets, the stronger the effect of the offset errors will get.

Another possibility for the aberration is to take into account the optical pumping. In paragraph 9.5.1 a model for a laser power dependent detuning is derived. For an offset error $r'_{dip}(s)$ approaches zero for $s \to 0$, but one measurement with the SPCM at 0.08 pW shows a dip of $\approx 1\%$. This speaks for optical pumping. Both effects are reasonable, only for $s \to 0$ they differ.

For the ideal case 0.8% absorption for a single atom and $s = 3/4$ are expected. If optical pumping from above is taken into account 0.47% absorption per atom is measured. That means that the measured dip of 4% is due to the presence of ≈ 8 atoms.

The data from the fluorescence detector shows, that every 10 µs 8 atoms enter the detection region around the peak arrival time[7]. But the atoms need 50 µs to cross the detection region. The situation can be handled mathematically by reducing the scattering rate to 1/5 for the whole time or by limiting the interaction time of the atom to 10 µs. For the calculations of the quality of the absorption detector 8 atoms can be assumed to be present all the time, since the loss of atoms is "compensated". Of course the question remains, why the atoms do scatter less than 100 photons although they stay longer in the light than 10 µs.

[6] σ_0 depends on the light polarization and the atomic transition.
[7] This corresponds to a density of $\approx 3 \times 10^{11}\mathrm{cm}^{-3}$.

Signal to noise ratio The most important quantity of the absorption detector is its signal to noise ratio (SNR) of a measurement. Figure 10.5 shows the SNR as a function of the saturation parameter s. The highest SNR is 10 for $s = 1.4$ at a time binning of 1 ms. The noise is also given as a function of the saturation parameter and is re-scaled to a bandwidth of one Hertz. The noise is rising linearly with the laser power, which is not the expected behavior for shot noise. The linear fit intersects the y-axis at $(1.7 \pm 0.3) \times 10^{-14}$ W/$\sqrt{Hz}$. That is within errors with the noise equivalent power of the photodiode of $(1.2 \pm 0.2) \times 10^{-14}$ W/$\sqrt{Hz}$, which is given in tab. 8.2. The signal to

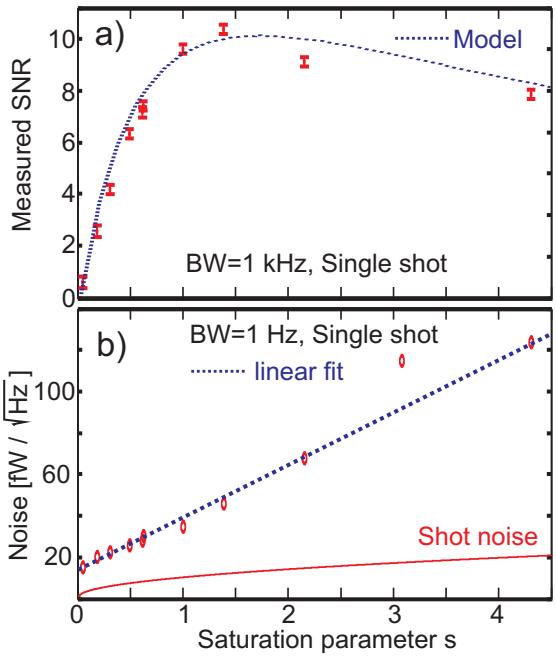

Figure 10.5: **a)** shows the measured SNR as a function of the laser power. The measurement is carried out for the $|2, -2 \rightarrow\rangle$ $|3, -3\rangle$ transition. The time binning was set to 1 ms. The maximum SNR is 10 at a saturation parameter of $s = 1.4$ (450 pW). In **b)** the measured noise is plotted. The noise is re-scaled to a bandwidth of one Hertz. It is rising linear with the laser power, which is not the expected behavior for shot noise. The linear fit intersects the y-axis at $(1.7 \pm 0.3) \times 10^{-14}$ W/$\sqrt{Hz}$. As a comparison the theoretical shot noise is included in the plot.

noise can be written with the signal without atoms S_{wo}, the signal with atoms S_w and the different noise contributions σ_i as:

$$SNR(s) = \frac{S_{wo}(s) - S_w(s)}{\sqrt{\sum_i \sigma_i^2(s)}}. \tag{10.13}$$

The amplitude of the difference of a measurement with atoms and without atoms is the quantity to be evaluated.

Let BW be the bandwidth of the measurement. With the sampling interval Δt it can be expressed as

$$BW = \frac{1}{\Delta t}. \tag{10.14}$$

The number of photons without atoms can be written as

$$S_{wo}(s) \;=\; s \times p_0 \times n_0 \times \Delta t, \tag{10.15}$$

and the number of photons with atoms as

$$S_w(s) \;=\; S_{wo}(s) - S_{scatt}(s) \times \Delta t. \tag{10.16}$$

Therefore the difference is

$$S_{wo}(s) - S_w(s) \quad = \quad S_{scatt}(s) \times \Delta t. \tag{10.17}$$

This is the amount of photons, which is removed (scattered) out of the photon stream. One of the noise contributions is the photon shot noise, which is just the square root of the number of photons

$$\sigma_1 = \sqrt{S_{wo}(s)}. \tag{10.18}$$

There may be many other noise contributions. If one can specify a function $d_i(m)$ for each noise source, then the noise can be written as

$$\sigma_i = d_i(s)\sqrt{\frac{1}{\Delta t}} n_0 \Delta t. \tag{10.19}$$

The functions $d_i(s)$ must be specified as $W/\sqrt{Hz}$. If one wants also to take a number of *stat* measurements into account (taking statistics), then the noise is reduced by a factor of $1/\sqrt{stat}$

$$\sigma_i' = \frac{\sigma_i}{\sqrt{stat}}. \tag{10.20}$$

The noise then becomes

$$\sqrt{\sum_i \sigma_i'^2} \quad = \quad \sqrt{\sum_i \left(\frac{d_i(s)\sqrt{\frac{1}{\Delta t}} n_0 \Delta t}{\sqrt{stat}} \right)^2} \tag{10.21}$$

In the following the experimental data will be applied to the formalism derived in this section. The photo detector contributed most of the noise. In Fig. 10.5**b)** the parameters can be determined. A linear function for $d_2(s)$ can be used. The y-intercept is $1.7 \times 10^{-14}\mathrm{W}/\sqrt{\mathrm{Hz}}$, the slope is $2.8 \times 10^{-14}\mathrm{W}/\sqrt{\mathrm{Hz}}$. Therefore for $d_2(s)$ can be written:

$$d_2(s) \quad = \quad (1.7 + s \times 2.8) \times 10^{-14} \frac{\mathrm{W}}{\sqrt{\mathrm{Hz}}}. \tag{10.22}$$

In Fig. 10.6 the SNR is plotted for the experimental data with the saturation power p_0 and n_0 the number of photons per Watt and per second and a single measurement ($stat = 1$). The SNR is given as:

$$SNR(s) \quad = \quad \frac{S_{scatt}(s) \times \Delta t}{\sqrt{\sqrt{S_{wo}(s)}^2 + \left(d_2(s)\sqrt{\frac{1}{\Delta t}} n_0 \Delta t \right)^2} \Big/ \sqrt{stat}}. \tag{10.23}$$

The noise figures are measured. The measurement and the theory with optical pumping (detuning) fit together. Table 10.1 compares the maximum SNR's for different conditions. The measurements suggest, that a major improvement in SNR can be achieved by a better photo detector. Then the SNR can become better by a factor of five at least. With the absorption detector again optical pumping plays a role for low intensities. The same methods of improvement as for the fluorescence detector can help here too. One has to use probing light intensities with $s \geq 1$ and the $|2,2 \rightarrow\rangle\ |3,3\rangle$ transition (right peak). Also the remaining magnetic field in the guide center must be as small as possible, that the Zeeman shift is smaller than the natural line width of the atom.

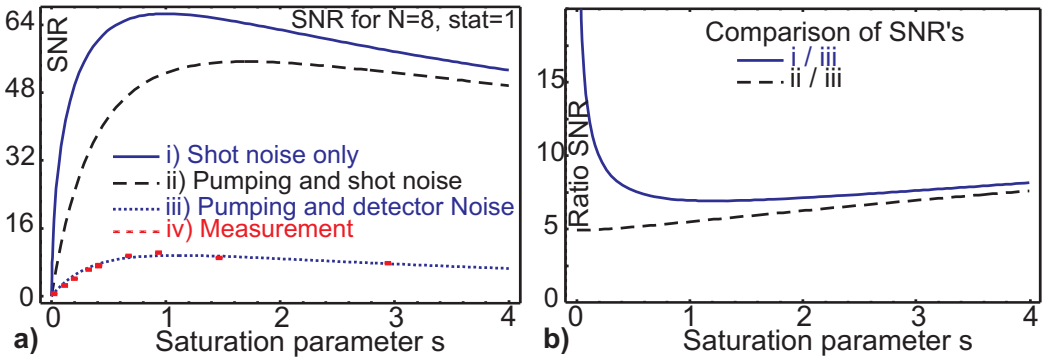

Figure 10.6: **a)** Different SNR's as a function of the saturation parameter s. The measurement is compared to theoretical SNR's for different conditions. SNR for i) shot noise only, ii) pumping plus shot noise and iii) pumping plus detector noise. **b)** compares i) and ii) to iii). With a better detector (shot noise limit), the SNR's can become better by a factor of 5 at least. The measurement is carried out for the $|2, -2 \rightarrow\rangle$ $|3, -3\rangle$ transition.

Condition	N=8 $\Delta t = 1$ ms	N=8 $\Delta t = 10$ µs	N=1 $\Delta t = 1$ ms	N=1 $\Delta t = 10$ µs
i)	66	6.6	8.2	0.8
ii)	55	5.5	6.8	0.7
iii)	9.5	1.0	1.2	0.12

Table 10.1: Comparison of the maximum SNR's for different conditions. Note that the maxima are not reached for the same saturation parameters. Only for i) the maximum is expected for a saturation parameter of $s = 1$. The number of repeated measurements is set to $stat = 1$. Maximum SNR for i) shot noise only, ii) pumping plus shot noise and iii) pumping plus detector noise. For iii) the measured parameters for the current setup are used. ii) is feasible with a better detector, but i) needs further investigation.

10.8 Tomography of the magnetic guide

A similar measurement to the one of the fluorescence detector was made with the absorption detector. The signal is measured as a function of the guide current. Figure 9.22 shows how the magnetic minimum shifts for the varying parameters. Changing the guide current sets the distance of the magnetic minimum to the chip. In Fig. 10.7 the signal is plotted as a function of the guide current and the time of flight. Additionally, plots with the counts versus the guide current for different times are shown. The guide profile is plotted for different times. The counts are also plotted as a function of time of flight for different guide currents, yielding an atomic profile for different magnetic fields (guide currents). On a first estimate, the absorption and the fluorescence detector yield the same tomography although the slices can not be made for the same times and guide center positions. The reason is the bad SNR of the absorption detector.

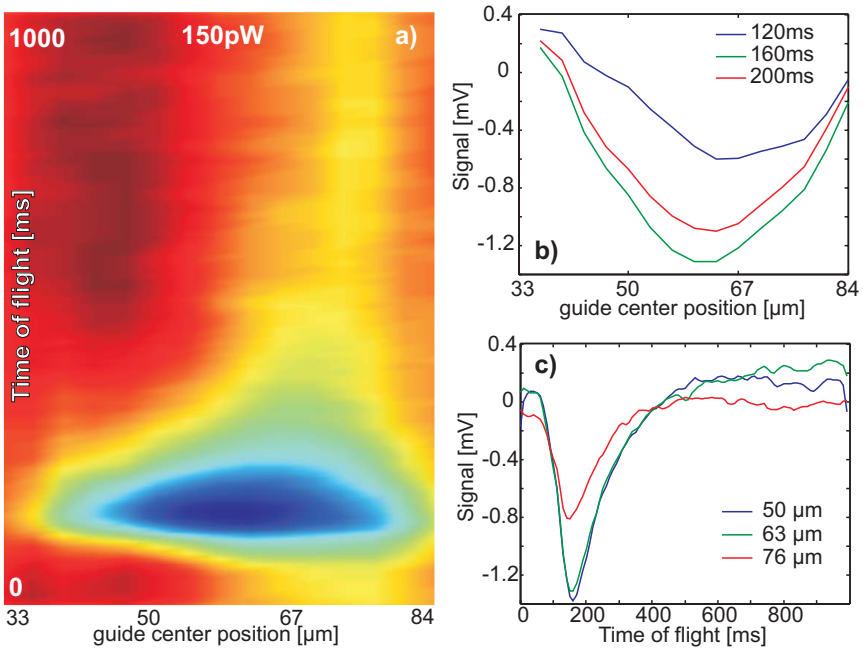

Figure 10.7: **a)** Signal as a function of the magnetic guide center position above the chip and the time of flight. The measurement was carried out at a power of 150 pW. Slices along the guide center positions at different times are shown in **b)**. In **c)** slices along the time axis at different guide center positions are evaluated.

10.9 Conclusion

The absorption detector was evaluated in this chapter. The theoretical model fits well to the measured data. Also the following points can be concluded:

- With a better detector (shot noise limit), the SNR's for this setup can become better by a factor of 5 at least. Finding a shot noise limited detector for a power of a few hundred pW is quite hard. This is an advantage with the fluorescence detector, where an almost noise free detector can be used.

- Since the $|2,-2\rangle$ to $|3,-3\rangle$ transition (left peak in the spectroscopy) is used, optical pumping must be taken into account. For very low powers the transition to the $|3,-3\rangle$ excited state is smaller than to the transition to $|3,3\rangle$. The atoms starting from the ground state $|2,2\rangle$ first must be optically pumped to reach the cycling transition from $|2,-2\rangle$ to $|3,-3\rangle$ (with several transitions with σ^- polarized light). And before the atoms end up in $|3,-3\rangle$ they are more detuned from the laser light resulting in a lower scattering rate.

- It is important to mention, that the atoms need ≈ 50 µs through the detection region. But the measurement only fits perfectly to the number of atoms, which arrive every 10 µs. Since the SNR stays unchanged there must be a loss of atoms at the same rate as the atoms arrive. That *will not* change the above calculations for the detector, but it will lead to almost the same result as for the fluorescence detector. At 150 pW the atom theoretically scatters ≈ 61 photons every 10 µs. $50/10 \times 61$ photons

are not measured, but $\approx 55 \pm 10$ photons per atom. The situation can be handled mathematically by reducing the scattering rate to 1/5 for the whole time or by limiting the scattering time to 10 µs. For the calculations of the quality of the absorption detector 8 atoms can be assumed to be present all the time, since the loss of atoms is compensated.

- Many reasons can contribute to the low scattering rate. Optical pumping can be an explanation, which will drastically change the scattering rate. This is important only for low powers ($s < 1$) and the $|2, -2 \rightarrow\rangle$ $|3, -3\rangle$ transition (left peak). Gravity needs more than 700 µs to pull non trapped atoms for 2.5 µm. If there is an acceleration due to directed scattering, the atom will be pushed for 2.7 µm for every 100 photons scattered . In this case the atom moves closer to the MM fibre.

- For $r_{dip} \ll 1$ and with Eq. 10.23 the following scaling laws for the SNR can be derived.

$$SNR \quad \propto \quad N\sqrt{\frac{stat}{BW}}. \tag{10.24}$$

The SNR rises linearly with the number of atoms. For the number of measurements $stat$ and the measurement time $\Delta t = 1/BW$ it rises only like a square root. When the detector is shot noise limited, then these are the parameters left for improvement.

11 Fibre detection improvements

11.1 Comparison of fluorescence and absorption detector

In the last chapters the performance of the fluorescence and absorption fibre detectors were evaluated. One weak point for both detectors is the interaction time of the atoms. The interaction time is limited to 10 - 50 µs and to less than 100 scattered photons per atom. The absorption detector has a SNR of 0.12 (0.7 / 0.8) for the current setup (with a better photo detector / the best case) and a single atom in the case of a sampling time of $\Delta t = 10$ µs. To have a reliable SNR of one, the interaction time has to be increased to 690 (20 / 16) µs).

For the fluorescence detector the SNR is already much greater than one, since the background level is so small. The detection probability plays a more important role. The detection probability can be increased with higher collection efficiencies of the MM fibres and integrating more than one MM fibre.

For the current setup for a detection probability (2σ) of $P_{detect} = 95.45\%$ for single atoms, the atom must be kept for 40 µs. The probability to get a background count is $P_{background} = 1.16\%$. The SNR for digital counting becomes:

$$SNR_{dig} = \frac{P_{detect}}{P_{background}}, \tag{11.1}$$

which in this case is 82. For the enhanced setup with two MM and a detection efficiency of $2 \times 4.16\%$ and $P_{background} = 0.253\%$ one can detect single atoms in 3.8 µs at a SNR of 377. Note that although the background is higher for the enhanced case, the result is still a higher SNR. That is due to the much smaller time interval needed for detection. Table 11.1 compares the absorption and fluorescence detector. It gives the necessary time Δt the atom must be hold at the detection volume to reach a SNR=2 (for the absorption detector) or single atom detection probability of 95.45% (for the fluorescence detector). Also the number of photons scattered in Δt are calculated.

If the time the atom stays in the detection volume can not be controlled, then still the enhanced fluorescence detector is enough to detect single atoms in 3.8 µs. The absolute magnetic field in the guide led to a Zeeman-splitting and optical pumping. To avoid those effects in the future, one must choose a smaller remaining magnetic field at the guide center. It has to be small enough, that the Zeeman-splitting is smaller than the natural line width of the atomic transition. This can lead to higher scattering rates.

The number of scattered photons needed is within the range of the measured number of photons per atom. The fluorescence detector is superior to the absorption detector by orders of magnitude. How to further improve the detectors is summarized in the following.

Both detectors gain in SNR when increasing the interaction time. The SNR scales as $\sqrt{\Delta t}$. This can be accomplished by additional magnetic traps at the location of the

Detector	Δt_{min}	p_{detect}	SNR	photons scattered
Fluorescence	40 µs	$\geq 95.45\%$	82	388
enhanced F.	3.8 µs	$\geq 95.45\%$	377	37
Absorption	2760 µs		2	27000
enhanced A.	80 µs		2	780

Table 11.1: Time Δt_{min} which is necessary for the different detectors to have $> 95.45\%$ detection efficiency (fluor. detector) or a $SNR \geq 2$ (absorb. detector). Δt_{min} is the time, where the atom scatters at the full scattering rate $\Gamma/2 \times s/(1+s)$. For the calculations a probing laser at saturation ($s = 1$) is used, thus ≈ 97 photons are scattered every 10 µs. (In the present setup, the time can not be controlled.) The times are given for the actual detectors and for the enhanced versions. For the fluorescence detector the enhanced version is two MM fibres and with a detection efficiency of $2 \times 4.16\%$. The enhanced absorption detector is with a shot noise limited detector. A high number of scattered photons can be a problem, since the atoms can fall into a dark state. The transition to the $F = 1$ ground state happens on average every 1000 transitions. To increase this number, one needs a laser pumping back the atoms into the $F = 2$ ground state. This is not a problem for the fluorescence detector, since the laser coupled into the tapered fibre does not contribute to the background signal when its power is lower than 1 nW.

detector or a dipole trap. The dipole trap is already "built-in", because of the use of a tapered fibre. The tapered fibre provides the focussing of the light. For the fluorescence detector an additional dipole laser is no problem. The dipole trap laser light can be in the 100 mW range without disturbing the signal, because of the geometrical suppression and the bandpass filters. For the absorption detector one needs extra filtering of the dipole light. To have a high efficiency of filtering one must probably use longer wavelengths.

The fluorescence detector can be further improved by increasing the detection efficiency with the help of two or several MM fibres or/and MM fibres with a higher numerical aperture.

For the absorption detector there are more improvements. One can think of using tapered fibers with a smaller Gaussian beam radius w_0. The SNR scales as $\propto 1/w_0$. Tapered fibers producing a fifth of the currently used beam radius are available. For "virtually" increasing the scattering cross section of the atom a cavity can be used. The photons interact with the atom several times. If the cavity has a finesse of F, the SNR scales as $\propto \sqrt{F}$.

In the following preliminary measurements to the two suggested improvements will be evaluated. Increasing the time the atom spends in the detection volume can be increased with a dipole trap. For improving the absorption detector, a cavity can be used.

11.2 Dipole trap

In the last section it was concluded, that increasing the interaction time can enhance the single atom detection. Two different dipole lasers are used for pilot tests for dipole trapping atoms. The first (second) laser has a wavelength of 840 nm (786 nm) and $P = 20$ mW ($P = 6$ mW) can be coupled into the tapered fibre. The beam radius of the tapered fibre is specified for 780 nm as $w_0 = 2.5$ µm. It changes slightly for different wavelengths like $w_0(\lambda) = w_0\lambda/780\,\text{nm}$. The dipole potential depth scales like $U \propto P/(\Delta \times w_0^2)$. Δ

is the frequency detuning of the dipole laser from the atomic transition. Thus even for lower powers it may be advantageous to use wavelengths closer[1] to 780 nm. But the dipole wavelength must still be high enough, to use the full filtering capacity of the optical bandpass filters.

A measurement with the dipole laser at 786 nm is performed. The imaging laser is scanned over 50 MHz for the $|2, m_F\rangle \rightarrow |3, m'_F\rangle$ transition. The measurements were performed for three different probing laser powers (150 pW, 1.0 nW, 3.0 nW). The power of the dipole laser stays constant at 6 mW, which is 40 million times more power than used for the probing light at 150 pW. For each power two measurements are made, one with the dipole laser on and one with the dipole laser off. Figure 11.1 shows these measurements. If the dipole laser is on, the peaks are shifted to the blue. The effect is strongest for low

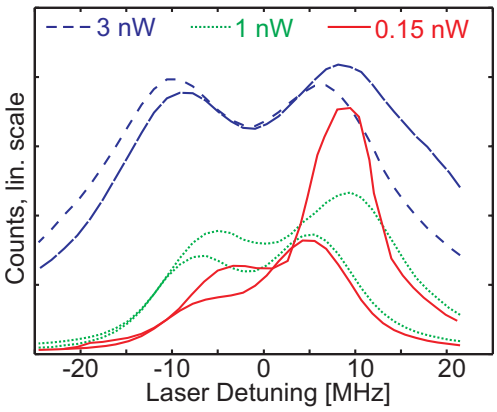

Figure 11.1: A laser scan over 50 MHz was performed for the $|2, m_F\rangle \rightarrow |3, m'_F\rangle$ transition for three probing laser powers (150 pW, 1.0 nW, 3.0 nW). For each probing power there are two measurements, one with and one without the dipole trap laser. In each case with the dipole laser on, the maximum count rate is shifted to higher frequencies (to the blue). The shifts are summarized in tab.11.2.

imaging beam powers. The reason is that the atoms scatter only close to the beam axis of the tapered fibre. When they are close to the axis also the dipole potential will be maximally. For higher imaging laser powers, the atoms will already start to scatter when the dipole potential gets negligible. The relative shifts are summarized in tab.11.2. At

	$\|3, -3\rangle$	$\|3, 3\rangle$
150 pW	4.2 MHz	4.1 MHz
1 nW	2.0 MHz	4.1 MHz
3 nW	1.1 MHz	2.5 MHz

Table 11.2: Relative shifts for the left ($|3, -3\rangle$) and right ($|3, 3\rangle$) peak. The biggest shift occurs for a laser power of 150 pW, where both peaks are shifted by over 4 MHz. The dipole potential is maximal only along the emitted beam. It decays exponentially like the intensity of the Gaussian beam. At a greater distance than $\pm w_0$ from the beam axis the dipole potential can be neglected.

150 pW both peaks are shifted by over +4 MHz. The dipole potential is maximal along

[1] One must keep in mind, that in principle one has to take all possible transitions of Rb 87 into account. The next stronger transition is at 795 nm. If the dipole laser is at 786 nm, the transition at 795 nm leads to a repelling dipole potential. Since the laser is closer to the stronger transition at 780 nm and because the potential scales like $\propto 1/\Delta$ there is still an attractive potential. Of course there are more transitions, but they are less than 1/1000 in strength. If one does not directly hit such a transition, it adds scarcely anything to the potential. The relevant lines are listed for example in (NIST, Version 2.0, 2002).

the emitted beam axis. Radially it decays exponentially like the intensity of the Gaussian beam. Earlier it was mentioned, that the atoms can be excited by the imaging laser far outside if powers were high enough. For an imaging power of 150 pW the highest measured shift is over 4 MHz. For low imaging laser powers the atoms reach the region within the beam waist. There they sense the dipole potential and their transition frequencies are shifted. The maximum dipole potential for the given parameters is $U_{dip} = -1.1$ mK resulting in a maximum shift of 23 MHz. The trap frequencies are $\omega_r = 2\pi \times 41$ kHz and $\omega_z = 2\pi \times 2.9$ kHz. The atoms cross the dipole potential at different positions, thus an average shift will be the result. Only a small fraction of the atoms will cross the dipole trap at the center and enter the maximum dipole potential.

For low imaging powers one can calculate the average frequency shift of the atoms. Let the z-axis be into the direction of the atomic movement. The column density is $\rho_C(x, y)$ and the integration over the guide cross section yields $\int_{-\infty}^{\infty} \mathrm{dx} \int_{-\infty}^{\infty} \mathrm{dy} \rho_C(x, y) = N$. N is the total number of atoms which contribute to the signal. That simplification to 2D is valid, since the atoms "hit" the dipole beam from the side. For pulsed operation, one has to take the atomic volume density at a certain time in the dipole beam and integrate over the volume. The average frequency shift $\Delta\nu$ can be calculated to:

$$\Delta\nu = \frac{1}{N} \int_{-\infty}^{\infty} \mathrm{dx} \int_{-\infty}^{\infty} \mathrm{dy} U_{dip}(x, 0, y) \rho_C(x, y). \tag{11.2}$$

$U_{dip}(x, y, z)$ is the dipole potential (in Hz). Note that the y-variable is used as the z-variable of the dipole potential since the dipole beam is intersecting the magnetic guide under 90°. Another assumption was the intersecting of the atomic beam center with the dipole beam axis. Offsets can be easily integrated into the formulas. Their only use here would be to let the formulas look more complicated. The density profile of a thermal cloud of atoms in a harmonic potential is Gaussian. Using a double exponential for the column density is therefore a good approximation. It is given by

$$\rho_C(x, y) \quad = \quad \frac{N}{2\pi\sigma_x\sigma_y} \exp\left(-\frac{x^2}{2\sigma_x^2} - \frac{y^2}{2\sigma_y^2}\right). \tag{11.3}$$

For the numerical calculation $\sigma_x = \sigma_y = 6.6$ µm is used. The σ fits to the dipole measurement and the measured σ for the cloud extension in the magnetic guide. The calculated frequency shift is then $\Delta\nu = 4.2$ MHz.

Even for $\sigma > w_0$ it is possible to probe the light field. Figure 11.2 shows the average frequency shifts as a function of the vertical offset and the horizontal offset of the atomic beam and the laser beam axes. The shifts for different σ are normalized to their maximum to compare the curves.

With the dipole light continuously on, the atoms can not be trapped. They "roll" through the dipole potential. To catch atoms, one has to pulse the dipole laser and try to catch an atom at the beam center. The pulsed operation was tried several times, but no signal was acquired which suggested the capture of any atoms. This will be a project for the future. Maybe one should test a tapered fibre with a smaller beam radius to have a higher trap frequency in the longitudinal direction too.

The following points can be concluded from the dipole trapping efforts.

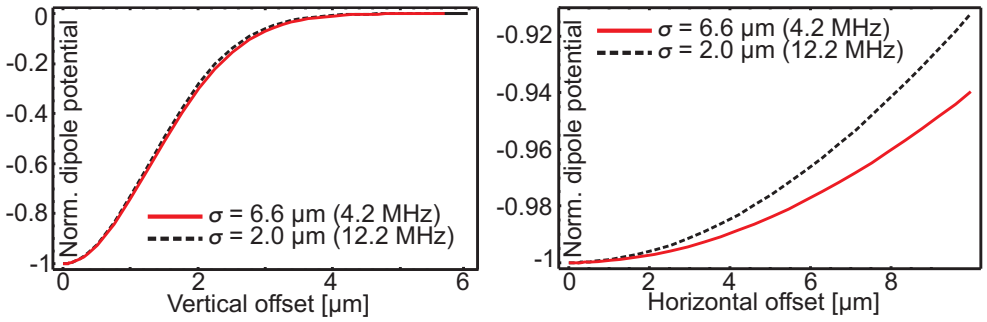

Figure 11.2: The normalized dipole potential is plotted as a function of the vertical and horizontal offsets. The average frequency shift is just the negative dipole potential. Two curves are plotted. The average shift is 4.2 MHz (12.2 MHz) for a cloud extension of $\sigma = 6.6$ µm ($\sigma = 2.0$ µm). The difference in the curve shape for the two σ is rather small. Against horizontal offsets the frequency shift is rather robust, since in the direction of the laser beam the gradient is small. Thus it is possible to probe the dipole potential even with widespread atomic ensembles. One only has to take care to have illumination with the imaging laser all the time.

- One nW has to be the upper limit for the imaging laser power. The increase in signal for higher powers is just due to imaging more atoms in the guide. But the goal must be to have a high detection efficiency as possible.
- Both lasers have to be pulsed. The dipole trap laser must be pulsed, since otherwise the atoms just "roll" through the dipole potential. The imaging laser must also be pulsed. Otherwise the atoms scatter before their arrival at center of the dipole trap.
- The loading of the dipole traps must be reconsidered. Maybe the loading must be accomplished out of an optical molasses or out of a 3D magnetic trap directly at the center of the dipole trap. Also the longitudinal confinement can not be proved with a measurement.
- The measured frequency shift in the spectroscopy with the dipole laser on is 4.2 MHz. This agrees with a model of a thermal atomic ensemble, which density distribution is Gaussian. When the atoms sense the dipole potential an average frequency shift is the result, since the atoms cross the dipole potential at different positions (depths). The theoretical shift for an atomic cloud extension measured in the magnetic guide agrees with the measured shift of 4.2 MHz.

11.3 Fibre cavity

Since the SNR scales like $\propto \sqrt{F}$ a fibre cavity is integrated right after the absorption detector. In the following preliminary tests to detect atoms with that cavity are described.

11.3.1 Temperature dependence

Because of the gap in between the two fiber pieces, the cavity actually is made of 3 cavities. That is why the peak heights and positions behave a bit more complicated, than with a

normal cavity (e.g. see Fig. 6.5). The parameters of the cavity are summarized in table 11.3 At the beginning the fibre cavity had a finesse of 70. But probably after a sightly

Parameter	Value
Finesse	$\mathcal{F} = 16.0 \pm 2.2$
FSR	FSR= (512 ± 11) MHz
Length	$L = c/(2n\,FSR) = (20.2 \pm 0.5)$ cm
Refractice Index	n=1.45

Table 11.3: Parameters of the integrated fibre cavity (with the speed of light c).

too high bakeout temperature (after closing the vacuum chamber) over the recommended limit of 90°C, the cavity was misaligned.

Temperature sensitivity If the cavity is on resonance for a fixed laser wavelength, then it will be on resonance again if the length changed by (a multiple) of $\Delta L = \lambda/(2n)$. The coefficient of thermal expansion for fused silica is $\alpha = 0.5 \times 10^{-6}/K$. Since the fibre is firmly attached to the chip, one can conclude that the fibre follows the chip. The silicon chip has a coefficient of thermal expansion[2] of $\alpha_{Si} = 3.0 \times 10^{-6}/K$. If the temperature changes by ΔT, then the fibre cavity will change its length. The relative length change is $\Delta L/L = \alpha_{Si} \times \Delta T$. Therefore the temperature needed for a shift of one FSR can be calculated:

$$\frac{\lambda}{2n} = L\alpha_{Si} \times \Delta T_{FSR} \tag{11.4}$$

$$\Rightarrow \Delta T_{FSR} = \frac{\lambda}{2n\alpha_{Si}L}. \tag{11.5}$$

It is feasible to determine the cavity's peaks position better than FWHM/10. That means, the temperature change needed for a change in resonance of FWHM/10 is

$$\Delta T_{min} = \frac{\Delta T_{FSR}}{10\mathcal{F}} \tag{11.6}$$

$$= \frac{\lambda}{2n\alpha_{Si}L}\frac{1}{10\mathcal{F}} \tag{11.7}$$

$$= 18.7\,\text{mK}, \tag{11.8}$$

where the FWHM of a cavity resonance is connected to the Finesse via $FWHM = FSR/\mathcal{F}$. The smallest chip temperature changes which can be measured with the cavity are $\Delta T_{min} = 18.7$ mK. Here the used length was $L = 0.03$ m, which is the part of the fibre sticking to the chip. This is valid for time scales $\ll$ minutes. For long time scales, e.g. when the whole setup changes its temperature, one has to take the α of the fibre with $L = 0.202$ m into account[3]. The fibre not attached to the chip has an acrylate coating. Acrylates usually have much higher coefficients of thermal expansion. How the connection

[2] Note: α strongly depends on the doping of the silicon. Thus the used α for silicon here may be wrong by a factor of 3.

[3] α for L=(20-3) cm and α_{Si} for 3 cm to be correct.

of the glass fibre with the acrylate coating behaves is unknown. To estimate a lower limit on the temperature sensitivity, the α of the glass alone is used. Then overall temperature changes of the whole experimental setup of $\Delta T_{min} = 16.7$ mK are the lower limit.

This will make it quite hard to run longer measurements, since the room temperature was stabilized to 20 ± 2 °C. Fluctuation periods were typically in the range of 5-6 hours. Thus after 16.7mK/(2000mK/6h) ≈ 3 min the cavity resonance moves 1/10 FWHM. This sensitivity to temperature changes must be kept in mind.

Even the lasers lead to a heating of the cavity/chip system. The chip's mass is $m = 1.22$ g, the specific heat capacity for silicon is $\rho_{Si} = 0.70\,\mathrm{kJ/kg/K}$. The temperature increase can be expressed with the deposed energy ΔE as

$$\Delta T = \frac{\Delta E}{\rho_{Si} m}. \tag{11.9}$$

The deposed energy is $\Delta E = a_{surf} I_{Laser} t$, where the laser power hitting the chip was $I_{Laser} = 0.25W$, the exposure time $t = 8s$ and the unknown absorption coefficient a_{surf} of the chip surface. The measured temperature increase was 20 mK. The absorption coefficient can be expressed as

$$a_{surf} = \frac{\Delta T \rho_{Si} m}{I_{Laser} t} \approx 0.9\%. \tag{11.10}$$

Thus the chip surface absorbed 0.9% of the laser power. Note that many unknowns, like the effective α are distorting this measurement. Also the heat transferred to the mounting is completely neglected. Thus the 0.9% are a lower estimate. But it can be used as rule of thumb. Moreover it is impossible to decide, whether the whole golden chip surface was heated up or the structures on the chip alone. The reflectance of gold mirrors is usually above 98% (Melles Griot, 2006).

Temperature measurements During an experimental cycle the chip changes temperature. A wire for creating the magnetic field for the magnetic trap is running right under the gap of the cavity. Up to 0.8 A of current was pushed through that wire. The resistive load leads to the heating of the chip. Also the other used current carrying structures on or beneath the chip lead to a periodic heating of the chip. Through the U-copper structure beneath the chip run 50 A during MOT phase. All those temperature changes will be measurable with the resonance shifts of the cavity. Figure 11.3 shows the cavity resonance shift for the chip-z, the wire guide and both together. The measurement was performed via scanning the cavity(or laser) over two FSR's. The scanning rate was 20 Hz. The transmittance of the cavity then was recorded continuously for 18 s. That is almost one full experimental cycle (except the MOT phase). A program later tracks the peaks and can plot the position of a certain peak over the recorded time. If the model explained in (Groth et al., 2004) is taken for the thermal properties of an atom chip, the temperature of the wire guide heats up by $\Delta T \approx 1.04\,\mathrm{K}$. For the chip-Z the temperature increase is $\Delta T \approx 1.64\,\mathrm{K}$. The golden wires heat up within a few ms.

Without heat transfer to the chip mounting, the total energy deposed due to ohmic losses by the chip-z (wire guide) heats up the complete chip by $\Delta T = 0.86\,\mathrm{K}$ ($\Delta T = 0.42\,\mathrm{K}$). If both run simultaneously, then the sum of the single contributions is $\Delta T = 1.28\,\mathrm{K}$. This

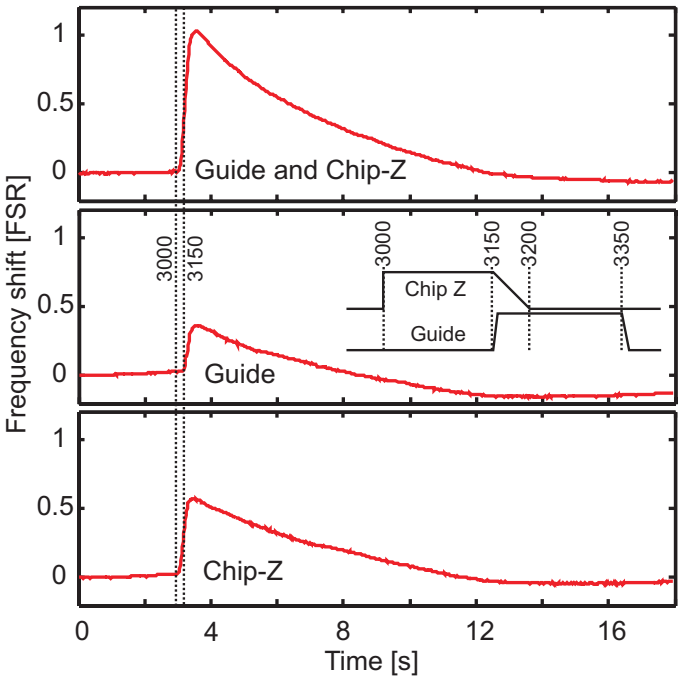

Figure 11.3: The cavity resonance shift is plotted over time. The different plots show the shift for switching the chip-z, the wire guide and both together. The inset shows the timing of the currents through the wires. The chip-z is switched on at 3000 ms, stays on until 3150 ms and is then ramped down in 50 ms. The guide is ramped up in 10 ms at 3150 ms, stays on for 190 ms and is then ramped down in 10 ms. A typical time scale to cool down is ≈ 6 s.

can be seen as a lower limit, since local heating leads to higher expansions closer to the cavity. The different properties for the structures of the atom chip are summarized in tab.11.4. The measured ΔFSR for the chip-z (wire guide) were 0.57 (0.36).

Parameter	Chip-Z	Wire guide	Unit
Width	250	50	µm
Height	2.7	2.7	µm
Length	29	27.5	µm
Resistivity	0.0244	0.0244	Ωmm^2/m
Resistance	1.04	5.0	Ω
Time on	175	200	ms
Energy deposit	0.73	0.36	J
ΔFSR	0.57	0.36	
ΔT_{needed}	2.5	1.2	°K
Theoretical wire heating			
ΔT	1.4	0.9	°K
$\Delta\bar{T}$	1.2	0.8	°K

Table 11.4: Properties for the chip-Z and wire guide. The thermal properties and the resulting resonance shift of the cavity are given for a typical experimental cycle with the cavity. ΔT_{needed} is the temperature increase needed to explain the measured FSR. The used length was $L = 0.03$ m and the coefficient of thermal expansion of silicon $\alpha_{Si} = 3.0 \times 10^{-6}/K$ was used. The temperature change was also calculated (Groth et al., 2004). The difference may be the result of the uncertainty in α_{Si} as mentioned earlier.

The temperature increase needed on the length of the attachment on the chip is 2.5 K (1.2 K) for the chip-z (guide) with the used coefficient of thermal expansion of silicon $\alpha_{Si} = 3.0 \times 10^{-6}/K$. The theory in Groth et al. (2004) yields a heating of 1.4 K (0.9

K) for the chip-Z (wire guide). Solving the heat transfer equation, the average increase in temperature is 1.2 K (0.8 K) over the full 3 cm. That is about one half of the needed temperature increase to explain the frequency shifts. As mentioned at the beginning of this chapter, the α of the silicon of the used chip is not known. Thus only a standard value for silicon can be used.

Locking technique The cavity can be scanned over 7 FSR's with an actuator attached to it. Locking is accomplished via a lock-in technique. The current of the laser coupled into the cavity is modulated by 30-100 kHz. The transmitted cavity signal is then fed to a lock-in amplifier[4], which generates an error signal. Together with the PID card the error signal can be used to keep the cavity on resonance. Unfortunately the drifts during the MOT phase are larger than the 7 FSR covered by the actuator. This is caused by the heating of the copper-U structure beneath the chip. The cavity can not be locked for a complete experimental cycle. Nevertheless it is possible to keep the cavity on resonance (at least for the important time periods).

During the MOT phase the cavity lock is switched off. To switch off and on the PID lock, the the PID card[5] has to be modified. During the chip-Z phase, one second before the guide is switched on, the integral part of the PID card is activated. The PID card tries to lock the cavity on a resonance. Due to the different heating during that one second before the guide is on, the cavity always comes into resonance again before the second elapses. This resonance instantaneously makes the PID card to follow that resonance with the help of the cavity actuator. Thus it is possible to keep the cavity locked on resonance for 2s. After the 2 seconds the guiding of the atoms is finished anyhow and the PID card can be switched off again. The actuator goes back to the set voltage and the PID card waits for the next experimental cycle. This method worked continuously for several thousand measurement runs.

For atom detection there was no evidence for a signal from atoms. The data from the complicated system of three coupled resonators must be further analyzed. Another difficulty is the small gap between the two fibres. The fibre has a diameter of 125 µm, whereas the gap is only 6 µm wide. How the atoms are affected by the fibre facets is unknown. A possible solution is to prepare cooler atoms or even a Bose-Einstein condensate. This makes it easier to have a precise spatial confinement of the atoms, without possibly loosing them at the fibre facets. The experiments showed, that the vertical position of the atoms is accurate within a few µm. A remaining problem is to have a first estimation on the height of the atoms. Therefore a fluorescence or absorption detector can be placed at the same height prior to the cavity to optimize the magnetic guide's position first.

[4] FEMTO LIA-BVD-150-H lock-in amplifier.

[5] U6(MAX4690) has to be used. The second switch of the U6 has to be connected in parallel to the K3 relay's (pins 4 and 5). Connecting the MAX4690 to the computer control, it can be used to switch off the integral part of the PID card. That has the same effect as switching off the I-part manually. The layout diagram can be found in appendix B.

Part IV

Conclusion

12 Summary

For quantum information processing and computation (QIPC) several prerequisites must be fulfilled (DiVincenzo, 2000). One of the essential ingredients is to detect single quanta (qubits) with high fidelity. The key question to be answered is how to perform such measurements using a robust and scalable technology based on cold neutral atoms. Ultra-cold atoms can be trapped and manipulated using miniaturized atom chips (Folman et al., 2002). A prerequisite for exploiting single atoms held by atom chips in quantum information schemes is the ability to efficiently detect these atoms, which remained unsolved until this thesis was written.

This thesis was focussed on the miniaturization and integration of detectors for the detection of neutral atoms on an atom chip. For this purpose three different detectors were developed for atom detection by absorption or fluorescence. A fluorescence detector was realized by mounting a tapered lensed fibre perpendicular to a multi-mode collection fibre. For the absorption detector a multi-mode fibre was placed in-line with a tapered lensed fibre. A tunable cavity detector was built from two single mode fibres mounted on the chip surface. Each integrated detector has been evaluated by several characterization measurements.

To be able to test the individual detectors for atom detection an experimental apparatus providing an ultra-high-vacuum (UHV) was constructed. A magneto-optical trap (MOT) and lasers were built to deliver and investigate ensembles of rubidium-87 atoms. The associated electronic laser stabilization was developed and frequency stabilities of better than one MHz were achieved. A structure for the generation of a magnetic quadrupole field, Ioffe-traps and for providing a UHV compatible mounting for the atom chip was designed. The constructed atom chip was equipped with different magnetic micro-traps to trap and transfer a cold ensemble of rubidium atoms to the different integrated fibre detectors. From the MOT up to 10^5 atoms with typical temperatures of 50 µK were transferred to the detectors.

The fibre detectors were integrated on the atom chip by mounting them on the planar surface of the atom chip with lithographically defined retaining structures. Those structures allow a very accurate and stable passive fiber alignment with accuracies better than a few ten nanometers, which was confirmed by measurements on the fiber cavity. Long term stabilities of over one year were observed.

For the fluorescence detector the background count rate is one of the most important limitations. With the used single photon counting module the background count rate was reduced from 10^8 to 290 counts per second. Another important quantity is the number of scattered photons per atom, which directly affects the single atom detection probability. To estimate this quantity a spectroscopic measurement of the $|2, m_F\rangle \rightarrow |3, m'_F\rangle$ transition of the rubidium D2-line was carried out. The highest scattering rate of 97 photons per atom was achieved for the cycling transition from $|2, 2\rangle$ to $|3, 3\rangle$. For the fluorescence detector this yields a single atom detection probability of more than 54%, which corresponds on average

to 0.8 counts per atom. Geometrical detection effects for different light intensities were examined. Only high probing laser powers significantly above the atomic saturation caused a decrease in the detection efficiency. With the help of the characterization measurements it was possible to figure out the optimum conditions for the operation of such a detector. The fluorescence detector allowed the performance of quantitative measurements for the magnetically guided atoms on a single atom level and to study fundamental properties of the confined atoms.

Secondly the integrated absorption fibre detector was tested. Similar measurements were carried out as for the fluorescence detector. Additionally the signal to noise ratio (SNR) was evaluated. For a SNR of unity 8 atoms must be present in 10 µs. A possible technical improvement for the absorption detector is a better photo-detector. With a shot-noise limited detector, the SNR can be immediately improved by a factor of 5.

Both integrated detectors can be improved by increasing the number of scattered photons per atom and by increasing the interaction time to overcome the present limit of 97 scattered photons per atom. A possible solution is to hold the atom with dipole traps to increase their interaction time. Therefor first measurements on trapping the atoms with a dipole trap were performed. Theoretical predictions of the dipole potential generated by the tapered fibres were confirmed by measurements with the atoms.

Moreover the absorption detector can be enhanced by a cavity. The photons are given multiple chances to interact with an atom located in the cavity. For this reason the fibre cavity was tested. It was stabilized and the drifts due to temperature changes were evaluated. The temperature increase of the atom chip during operation was indirectly measured with the help of the fibre cavity with a sensitivity of better than 18 mK. A preliminary evaluation on atom detection with the cavity is shown in Fig. 12.1.

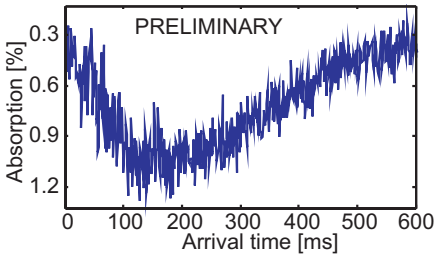

Figure 12.1: The absorption in the cavity detector is plotted as a function of the arrival time of the atoms at the cavity. No real quantitative numbers can be given. The result here is preliminary and will be further analyzed.

In this thesis three different detectors were developed and integrated for the first time on an atom chip. The most promising detector is the fluorescence detector. When 97 photons are scattered per atom, single atoms can be detected with a probability of more than 54%. For future projects this detector with a rather small numerical aperture (NA=0.275) with an overall photon collection and detection efficiency of 0.8% leading to 0.8 counts per atom can be improved by increasing the numerical aperture of the collection fibre. Using one (two) commercially available multi-mode fiber(s) with a NA of 0.6 the photon detection efficiency can be increased to 4.2% (8.4%) leading to 4 (8) counts per atom. For a threshold of one detected count the two facing multi-mode collection fibers yield a single atom detection probability of >99.97% and a false detection probability of 0.67%.

The background rate, which is responsible for the false detection probability of an atom, can be further decreased by an order of magnitude by using higher quality photon counters. Commercially available detectors for our wavelength go down to a dark count rate of less

than 25 counts per second. The technology is available and can be directly implemented into the existing experiment.

In this regime even atom counting turns out to be realistic. This becomes of especial interest when probing Bose-Einstein condensates on a single atom level. Detailed information about phase transitions and interatomic interactions can be provided. Furthermore ultra-cold atoms in optical lattices can be studied for a wide range of applications with this kind of detector. Nondestructive optical measurements become feasible for the investigation of phase transitions between a Mott insulator and superfluid states (Mekhov et al., 2007).

Other groups working on the implementation of QIPC with ionized atoms also benefit of miniaturized and integrated detectors. Leading groups in this area plan to integrate such a detector.

In the future the integration of the detectors could go one step further by using the same lithographic methods as for the atom chip fabrication, allowing a more automated fabrication. This field is quite evolved in the telecommunications sector, where wave guides, resonators as wavelength multiplexer, or Bragg-gratings acting as mirrors in wave guides are already in use in highly integrated devices. Adapting those abilities to our wavelengths and in combination with the atom chip, the integration of scalable and stable QED schemes will become possible.

Part V

Appendices

A Properties of rubidum 87

Rubidium is a chemical element of the alkali metal group and it has the atomic number 37. The symbol is "Rb". As all alkali metals it is highly reactive. An (almost) exhaustive summary of the physical and atomic properties of rubidium is given in (Steck, 2001). Some important properties are summarized in table A.1

D-2 line($5s^2S_{1/2} \rightarrow 5p^2P_{3/2}$)	λ_0		780.2	nm
natural lifetime	τ	$\equiv 1/\Gamma$	27.02	ns
natural line width	$\Gamma/2\pi$		5.89	MHz
saturation intensity	I_0	$\equiv \pi hc\Gamma/3\lambda_0^3$	1.67	mW/cm^2
Laser cooling (D-2 line):				
Doppler-temperature	T_D	$\equiv \hbar\Gamma/2k_B$	146	μK
typ. Doppler-velocity	v_D	$\equiv \sqrt{2k_BT_D/M}$	16.7	cm/s
recoil temperature	T_R	$\equiv (\hbar k_L)^2/Mk_B$		
		$= 2E_R/k_B$	361	μK
recoil velocity	v_R	$\equiv \hbar k_L/M$	5.88	mm/s
recoil frequency	ω_R	$\equiv E_R/\hbar = \hbar k_L^2/2M$	$2\pi\times$ 3.77	kHz
thermal deBroglie	Λ	$\equiv h/\sqrt{2\pi Mk_BT}$	15.5	nm (T_D)
wavelength			312	nm (T_R)
Gravitation:	Mg/k_B		1.03	mK/cm
	Mg/h		21.4	MHz/cm
	Mg/μ_B		15.3	G/cm
general constants:	h/k_B		48.0	μK/MHz
	k_B/h		20.8	kHz/μK
	μ_B/h		1.40	MHz/G
	μ_B/k_B		67.2	μK/G
			0.67	K/T
	g		0.98	(cm/s)/ms

Table A.1: Properties of rubidium, values taken from Barwood et al. (1991), Volz and Schmoranzer (1996).

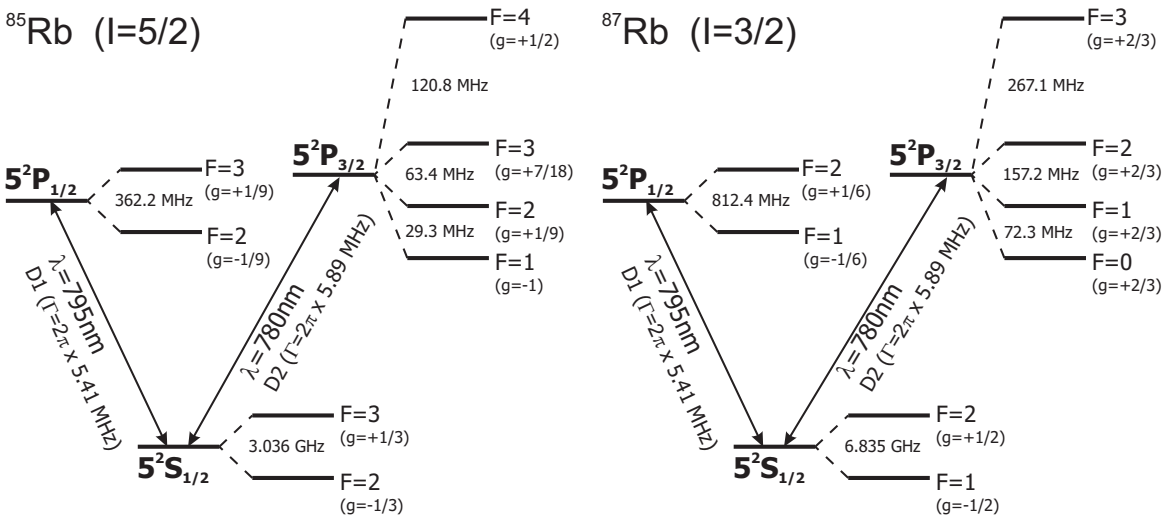

Figure A.1: Level diagram of the two rubidium isotopes. Frequency differences (Arimondo et al., 1977), natural line widths (NIST, Version 2.0, 2002) and g-factors of the the levels are given.

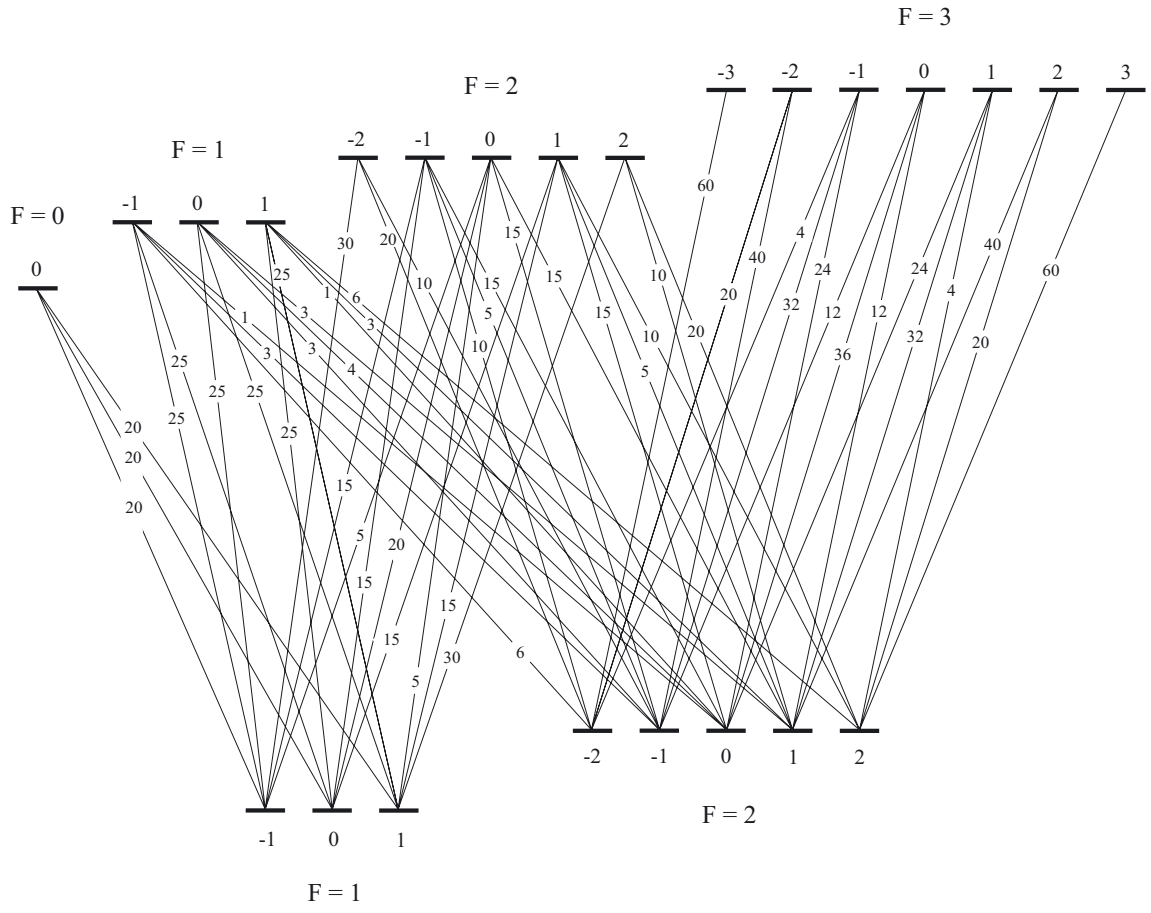

Figure A.2: Squares of the Clebsch-Gordon coefficients of the D_2 line of rubidium 87 (Schuster, 2002).

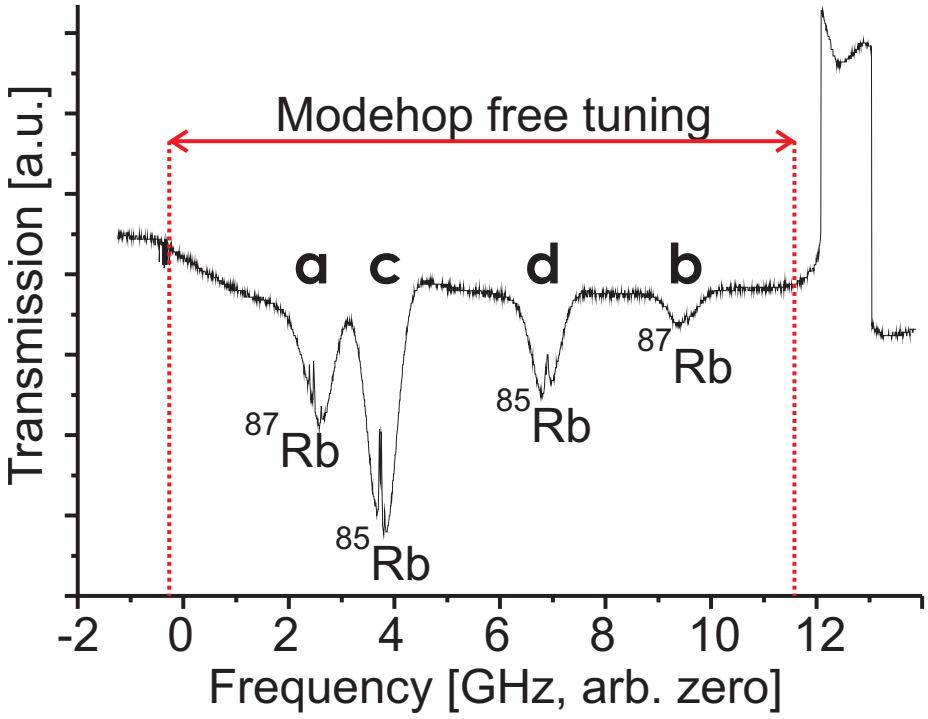

Figure A.3: Four Doppler valleys of the D2 line of ^{85}Rb and ^{87}Rb. The spectroscopy was done with one of the grating stabilized laser diodes and additional current feed forward.

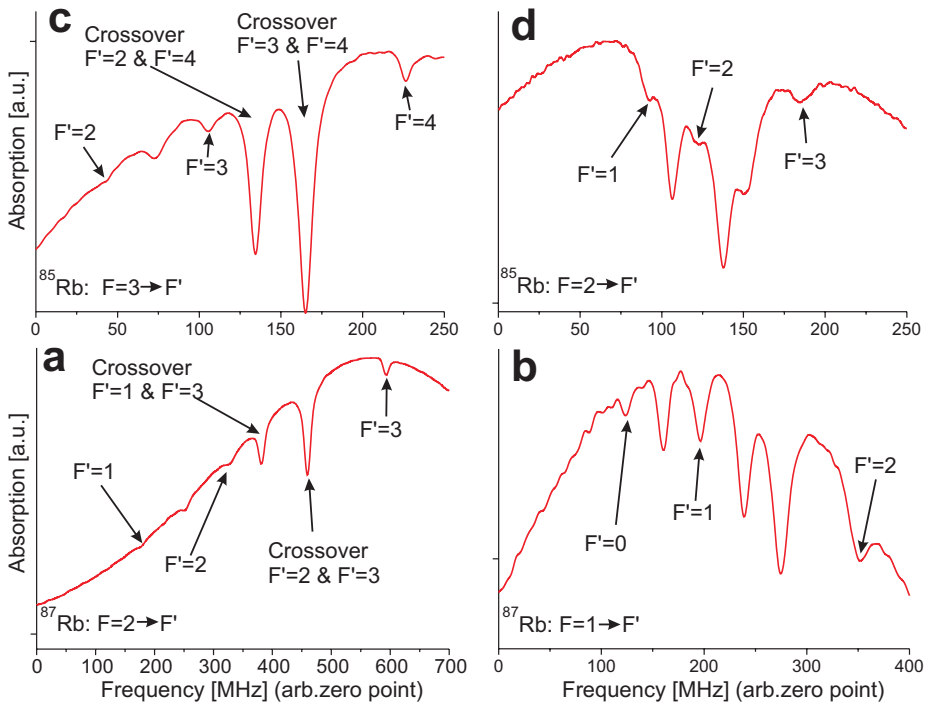

Figure A.4: Details of the spectroscopy of the D2 line. Note that now the absorption is plotted and not the transmittance.

B Laser Lock Electronics

The layout diagrams for the electronics of the laser lock system is collected on the following pages. For most parts the construction was carried out during this thesis. The ingenious development of course was undertaken by Mr.Rusnyak of the Elektronikwerkstatt des Physikalischen Instituts Heidelberg. All the single modules are placed into the A368 Lock-Box. Because of the modular design a lock system for the specific needs can be put together. The cards themselves are designed in a way, that the components can be easily changed to cover different frequency ranges. The following circuit diagrams will be given.

- A368E FM-Lock.
- A368G FO-Lock.
- A368F PI-Regulator.

Additionally the FM lock can be operated by a crystal oscillator, a fixed voltage-controlled oscillator (VCO), a VCO tunable with an external voltage, and an external frequency source. The externally tunable VCO can be used to use a reflectometer for the operation of an EOM, which center frequency can drift in the kHz regime. The (plug-in) parts afterwards must be adjusted to the desired frequency range.

The FO lock can be outfitted with different parts, so the frequency tuning range and the frequency offset of the slave to the frequency master laser can be chosen. With additional external mixing the upper frequency offset can be in the GHz range (the photo-detector is then the limit). The frequency can be typically tuned over > 400 MHz, if the following parts are used (Minicircuits: VCO POS800W, phase detector MPD21, low pass LP400). A useful rule of thumb for choosing the frequency of the major parts is:

$$f_{VCO} \geq f_{Phasedetector} = f_{Lowpass}.$$

Two outputs are provided for both locking cards, one slow output and one fast output with a prefixed filter chain. The slow output can be used for the actuator feedback, whereas the fast output can be used for a fast current feedback. The filter chain can be adjusted to modify the phase and amplitude response of the laser diode. The split ratio between the two outputs can be changed by changing the capacity (C52). When leaving out the capacity the whole frequency spectrum (DC-5 MHz) of the error signal will be forwarded to the “slow” output.

The following items are available, but will not be given here (initiated during this thesis, but completely developed by Mr.Rusnyak).

- A368H Counter (50 MHz-1 GHz).
- A368I ± 15 V Adaptor (Power source for photodiodes).

- A368K Avalanche Photodiode Bias-Supply (180-240 V).

Additionally a commercial lock-in amplifier (LIA-BVD-150-H Lock-In Amplifier, FEMTO Messtechnik GmbH, Berlin, Germany.) can be used in the lock electronics frame.

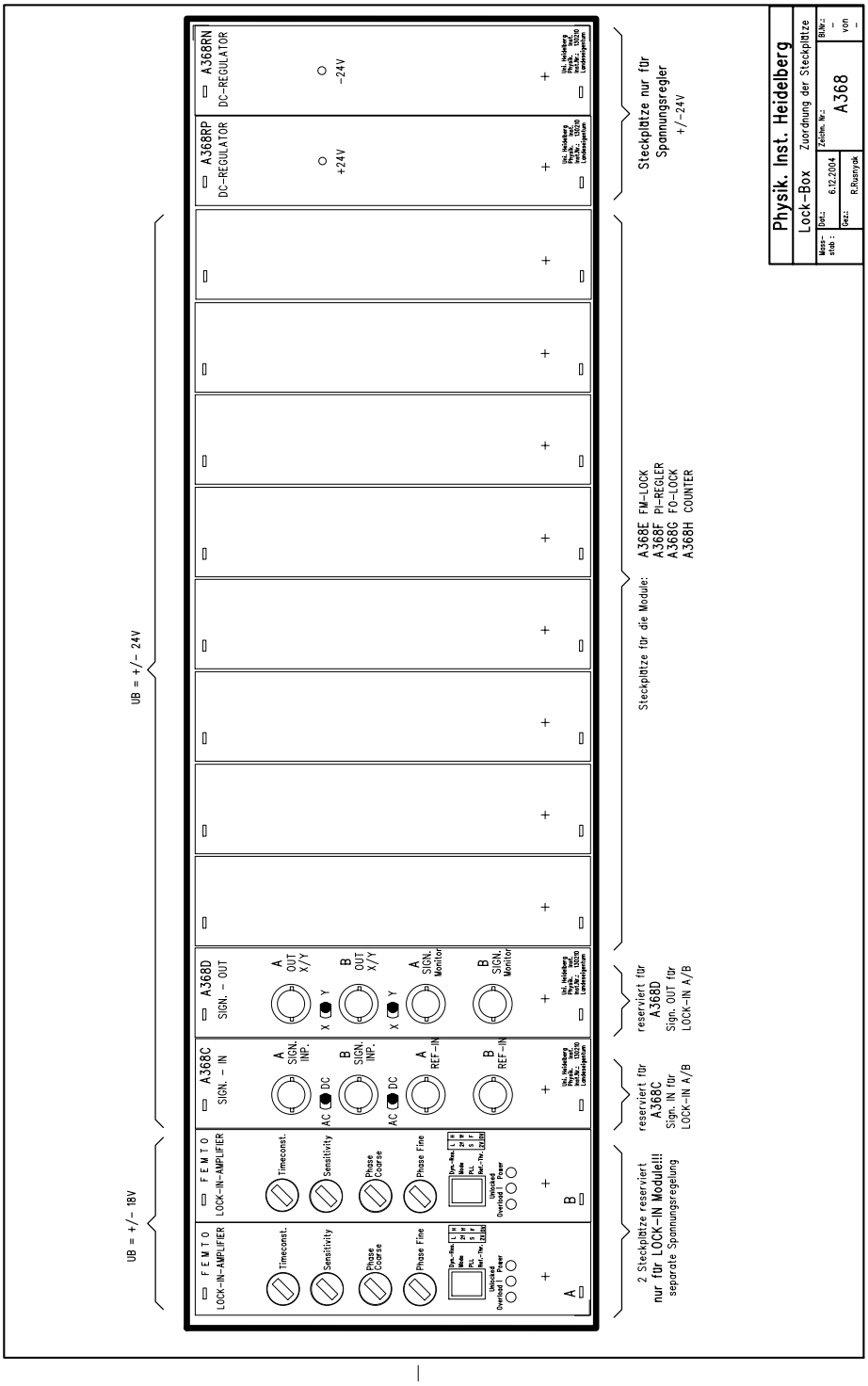

Figure B.1: Main frame for the lock electronics.

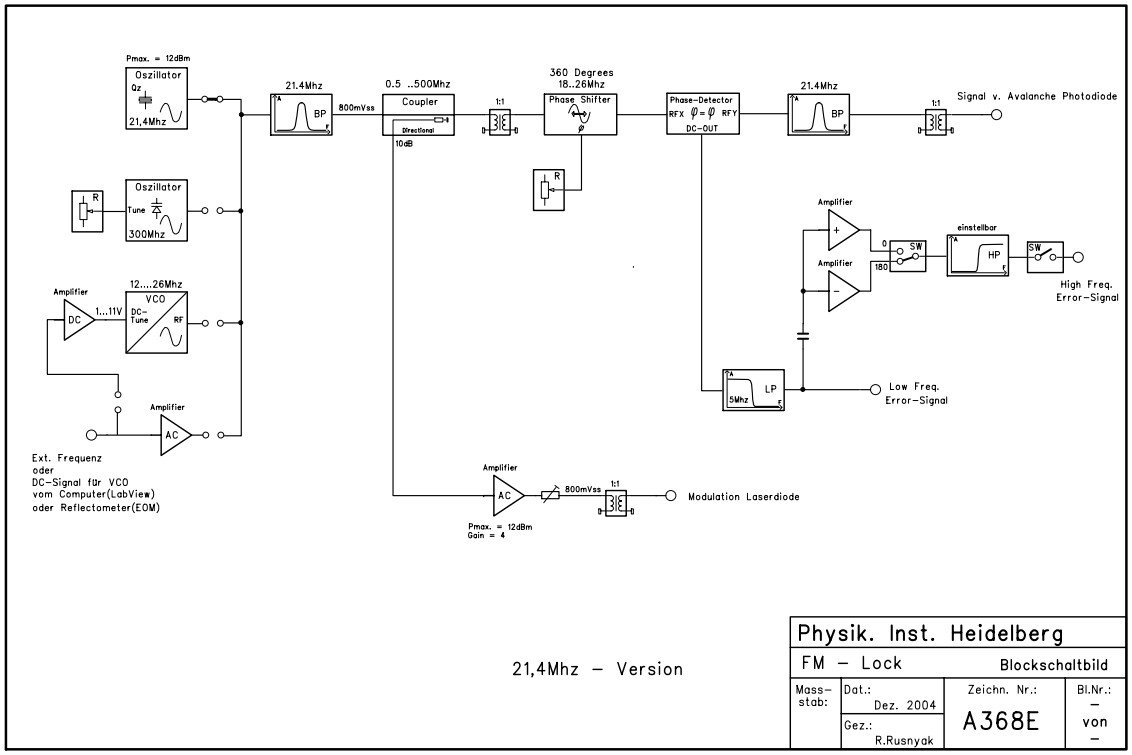

Figure B.2: FM lock schematics.

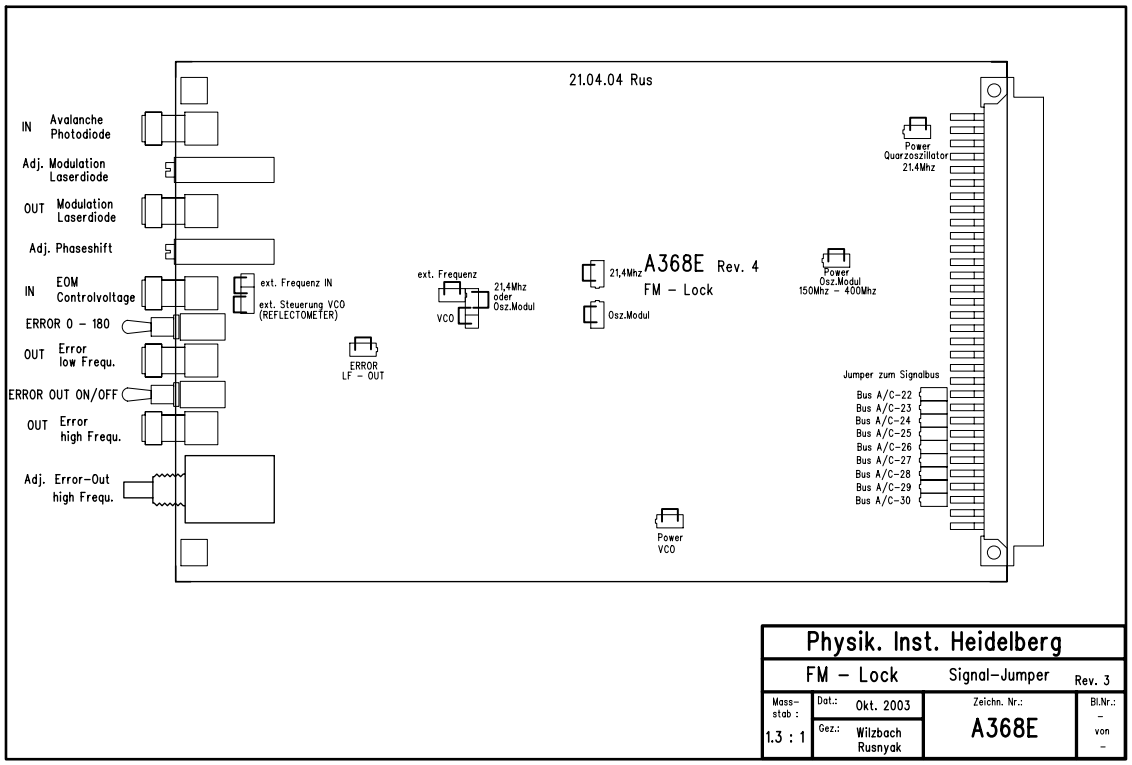

Figure B.3: FM lock jumper settings.

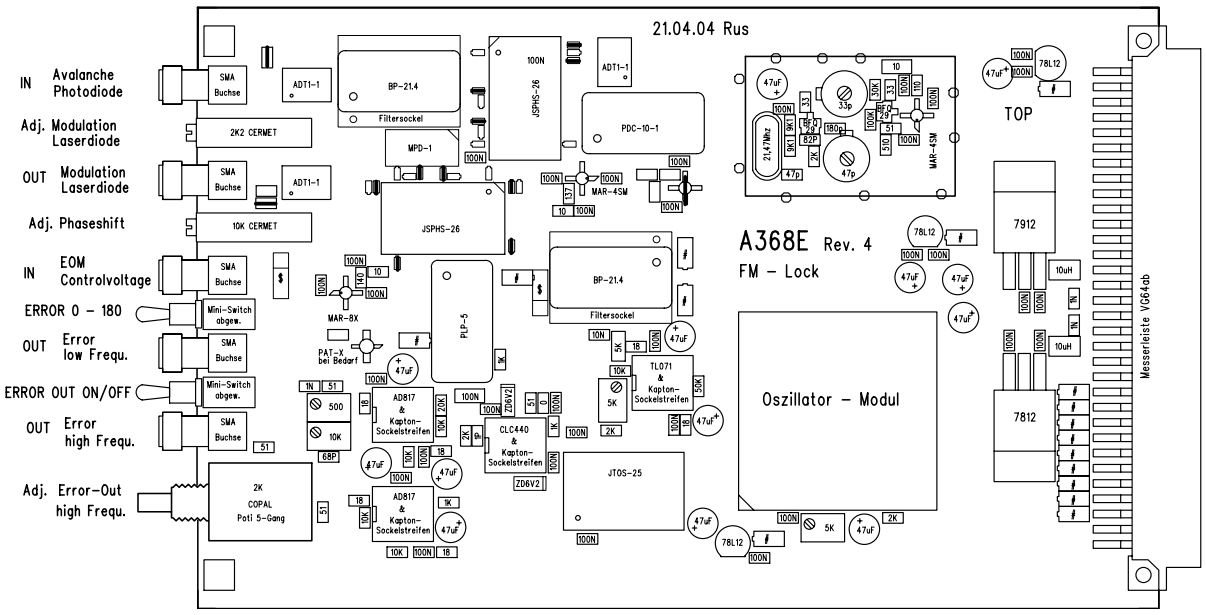

Figure B.4: FM lock layout diagram.

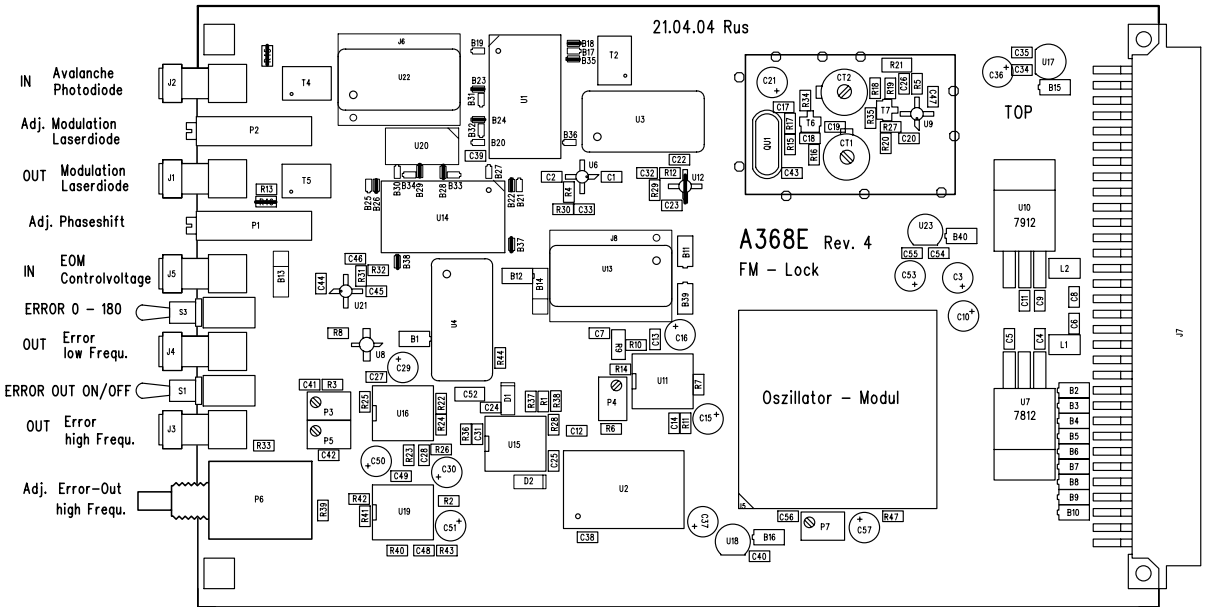

Figure B.5: FM lock block diagram.

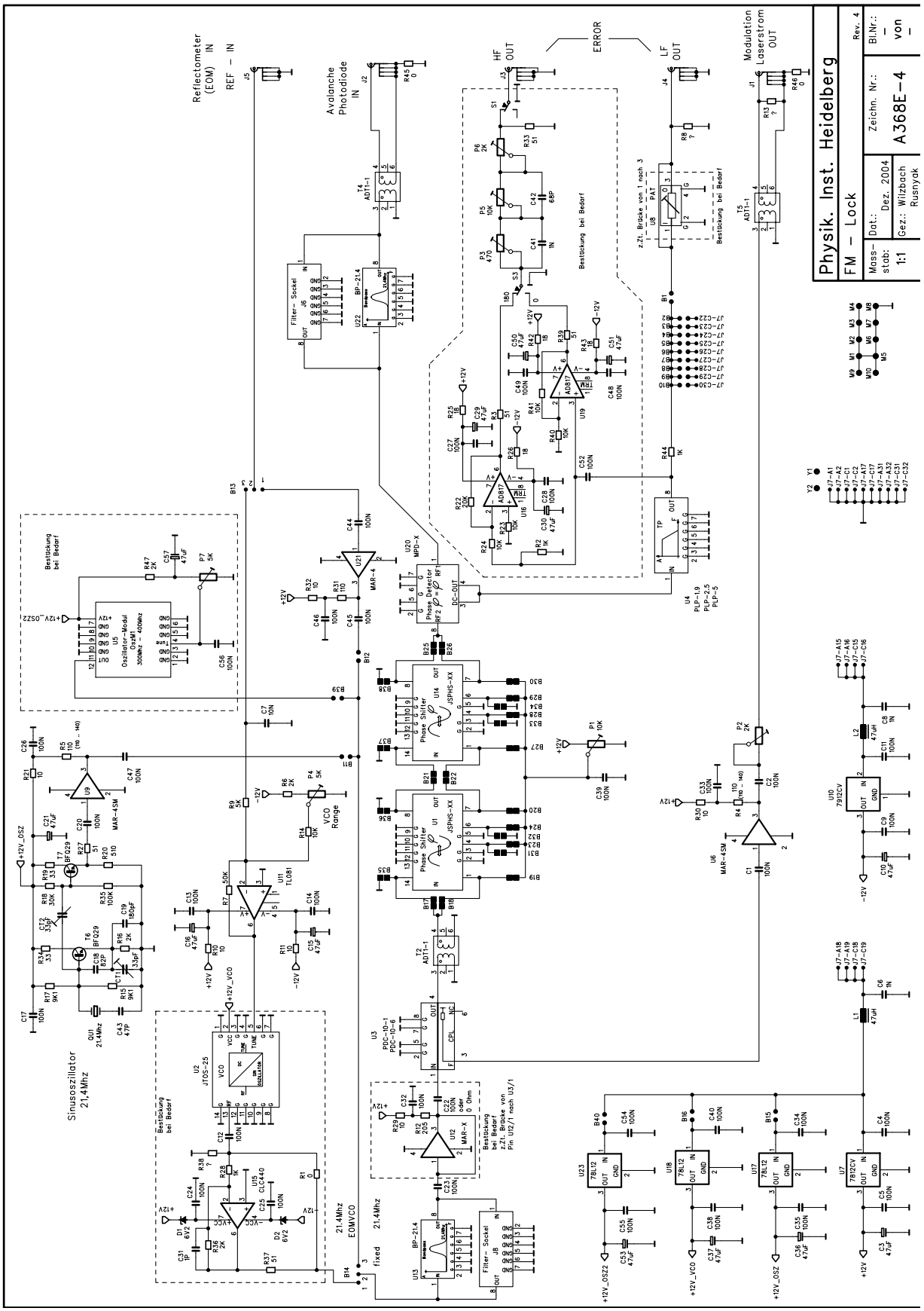

Figure B.6: FM lock circuit diagram.

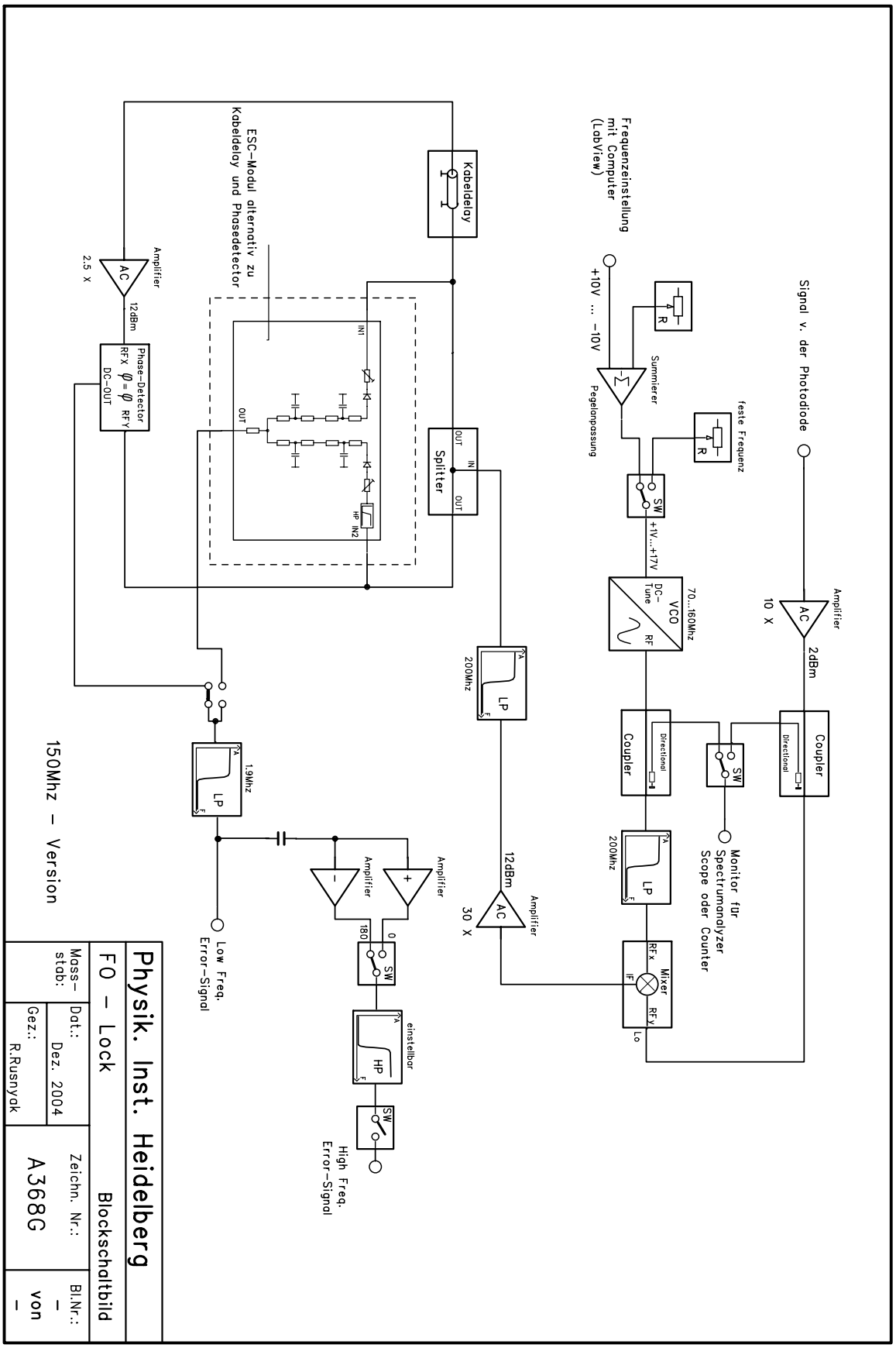

Figure B.7: FO lock schematics.

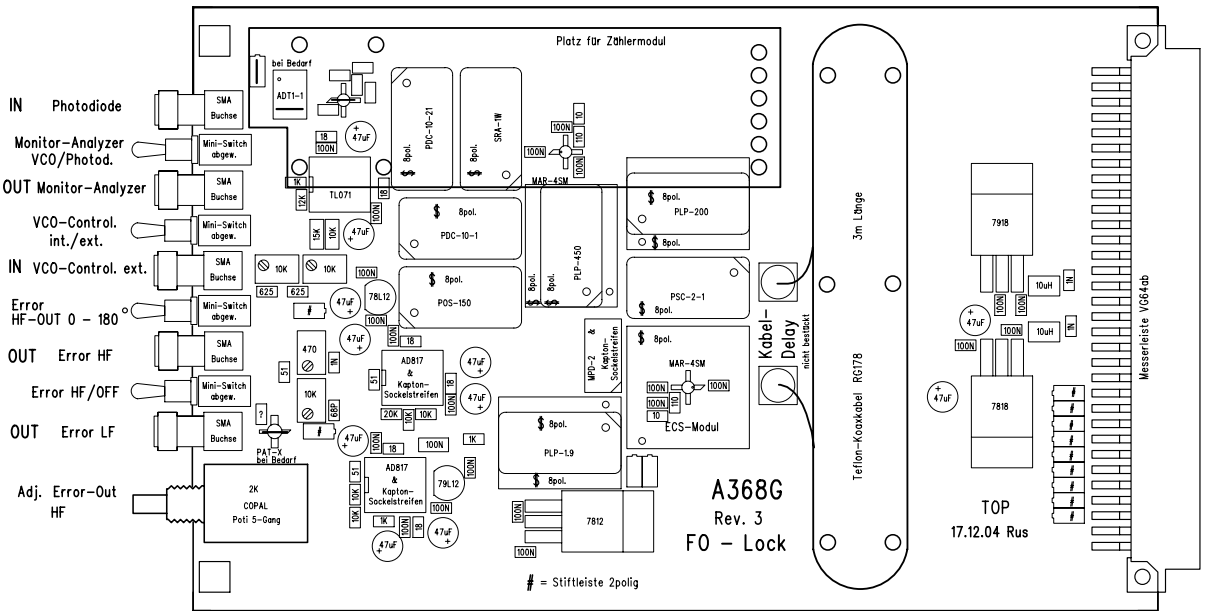

Figure B.8: FO lock block diagram.

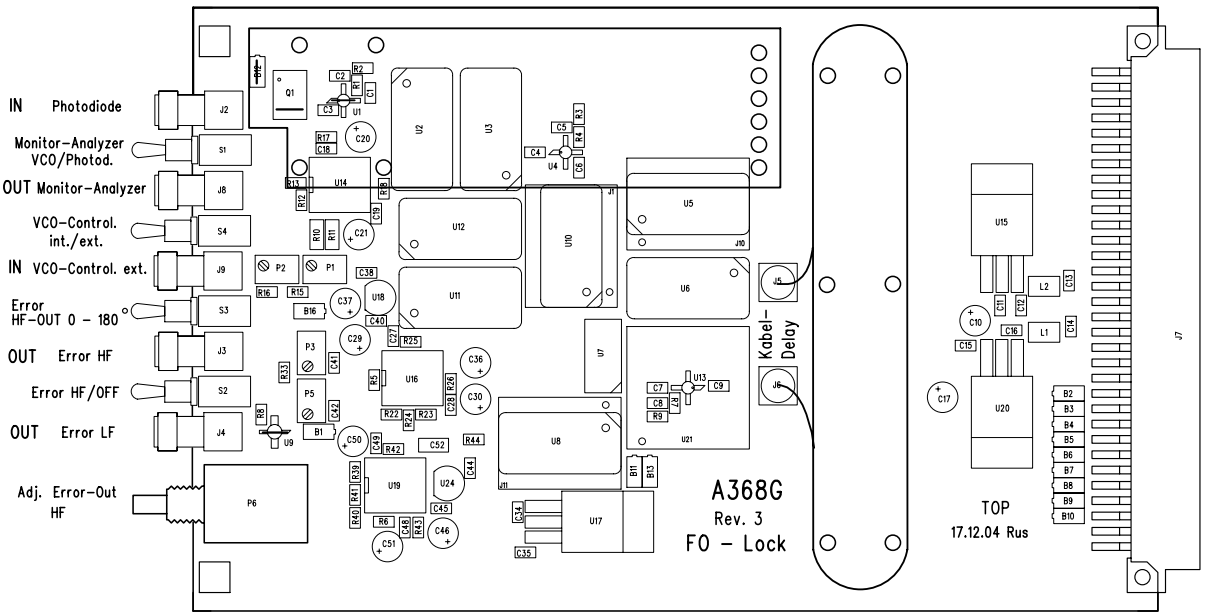

Figure B.9: FO lock block diagram.

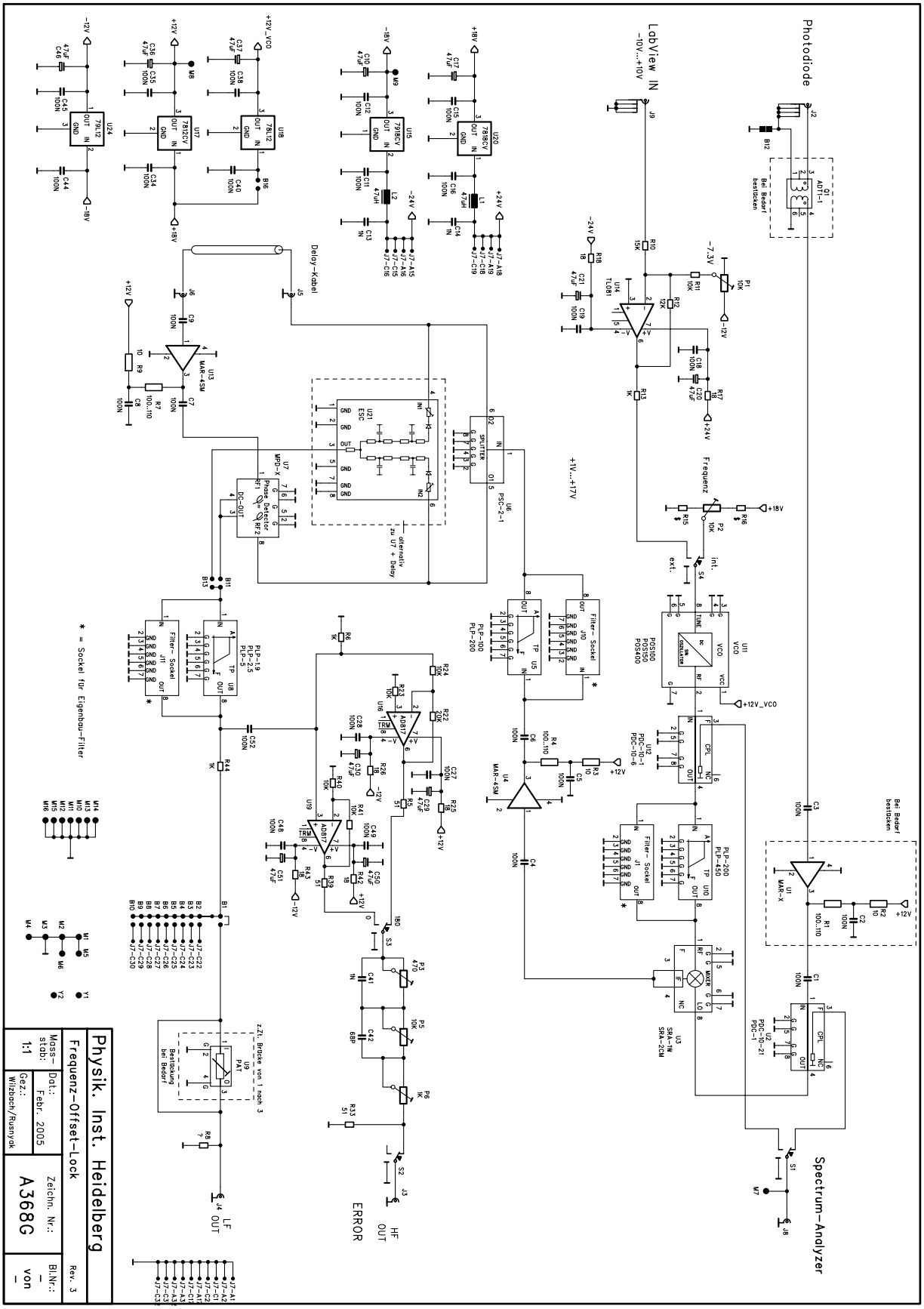

Figure B.10: FO lock circuit diagram.

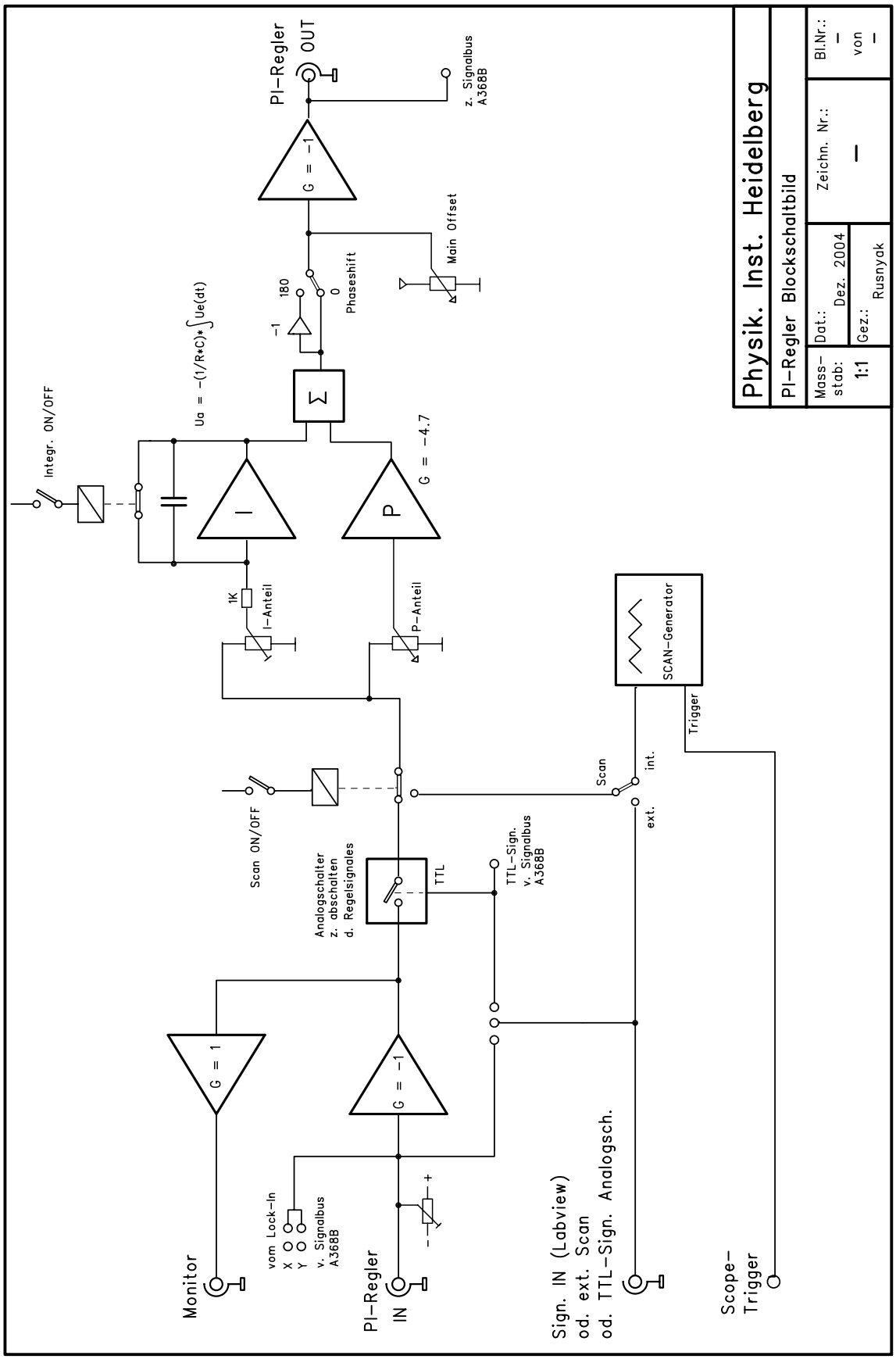

Figure B.11: PI regulator schematics.

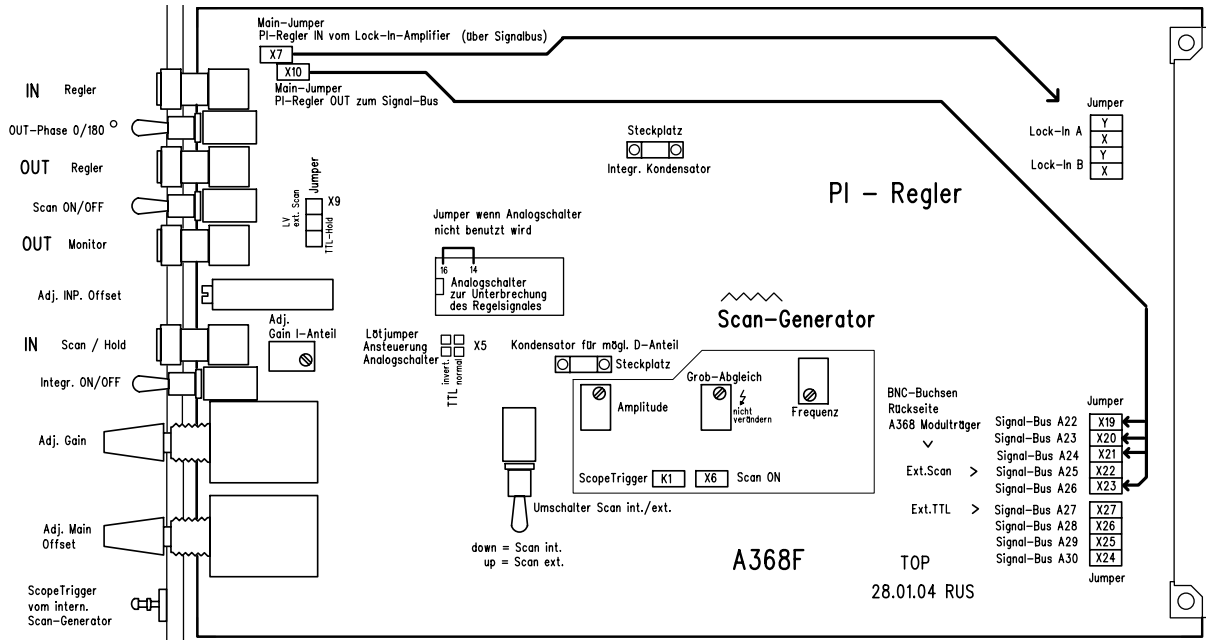

Figure B.12: PI regulator possible adjustments.

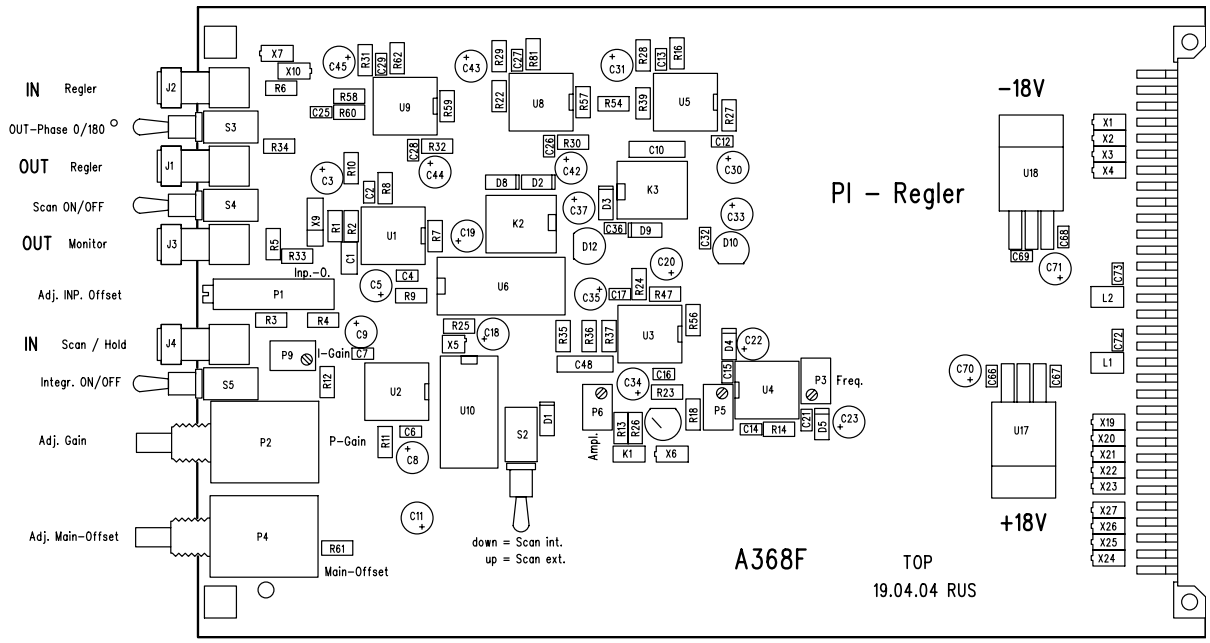

Figure B.13: PI regulator block diagram.

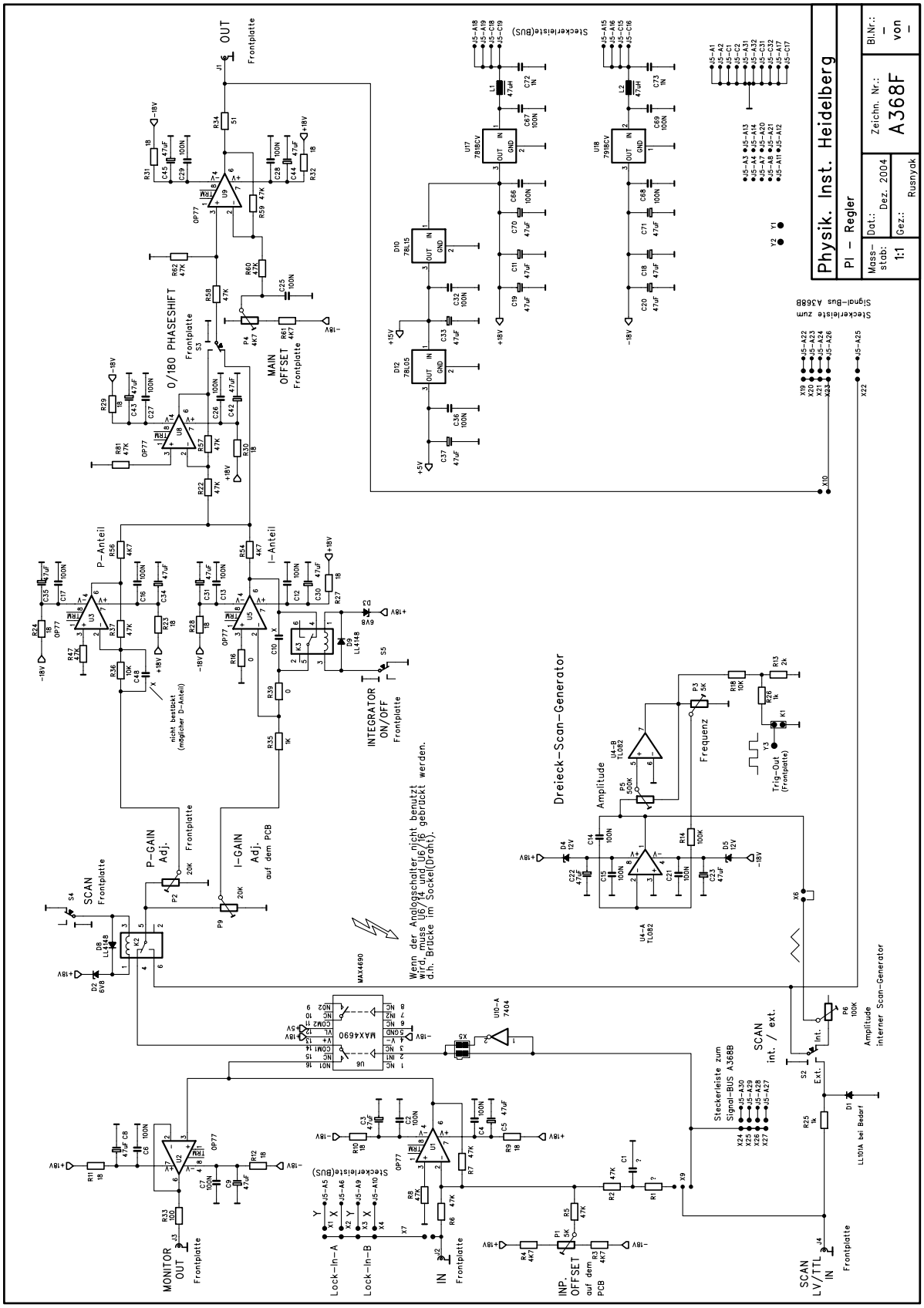

Figure B.14: PI regulator circuit diagram.

C Chip Mounting Technical Drawings

The technical drawings of the chip mounting will be summarized here. A total overview is given in C.1. In chapter 4.2 an explanation of the different structures is given .

Here technical drawings of the upper Shapal block and the copper structures beneath the chip are given. The other components will be omitted, since of no relevance. The dimensions of the copper structures are needed for calculations of the magnetic fields.

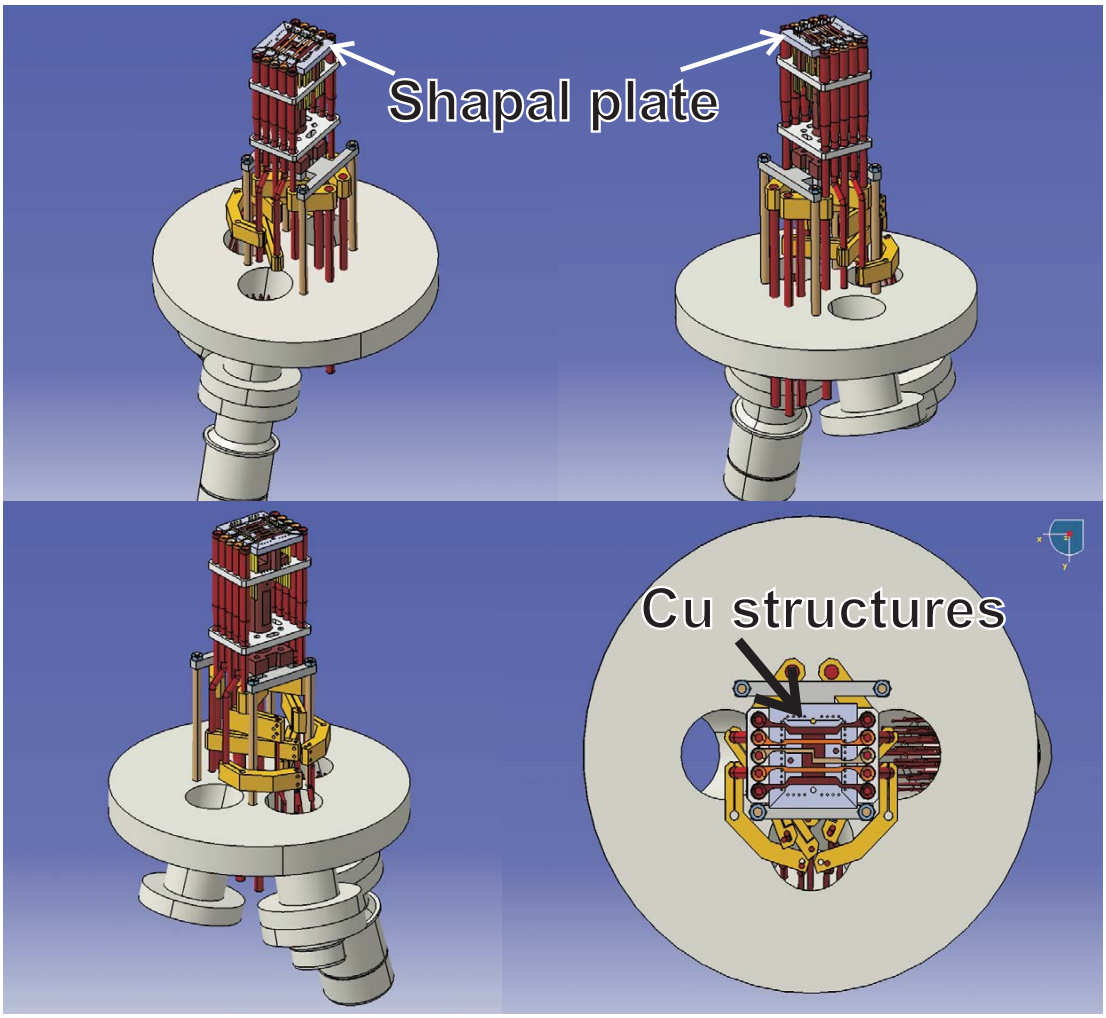

Figure C.1: Overview of the complete chip mounting. The technical drawings of the parts marked here will be given in this chapter.

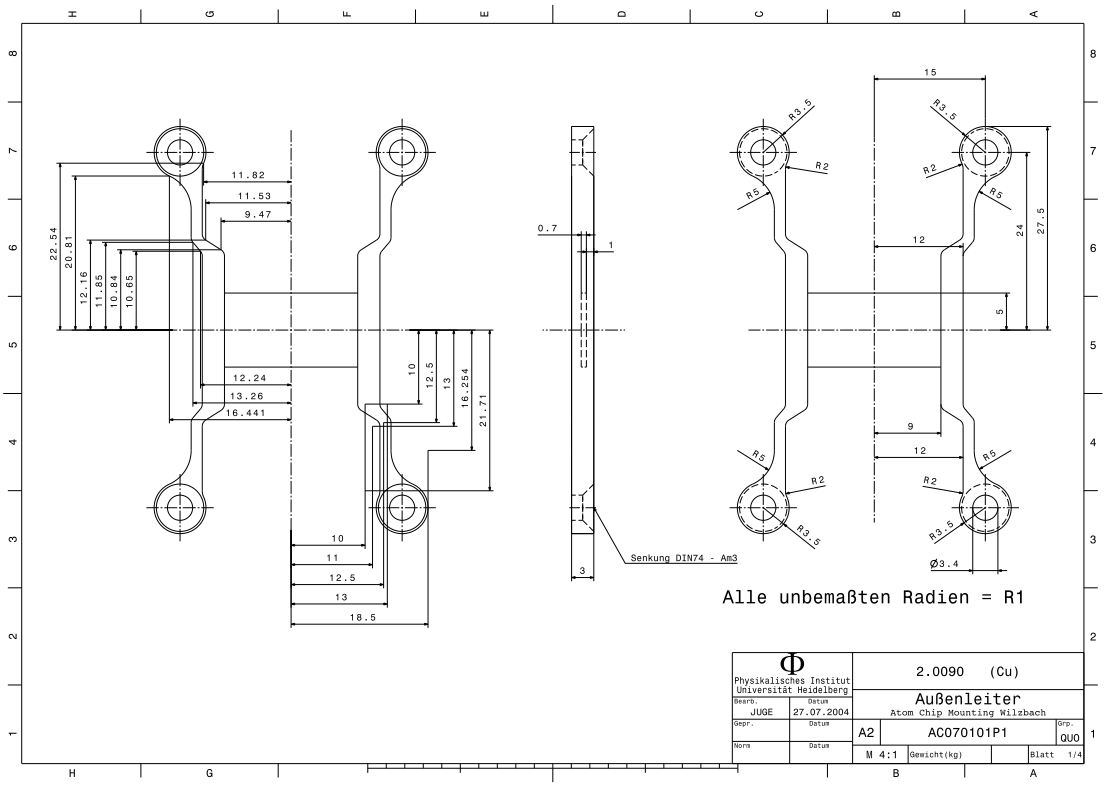

Figure C.2: Copper H-structure beneath the chip. Half of the H is uses as a "U" to create the quadrupole fields for the U-MOT.

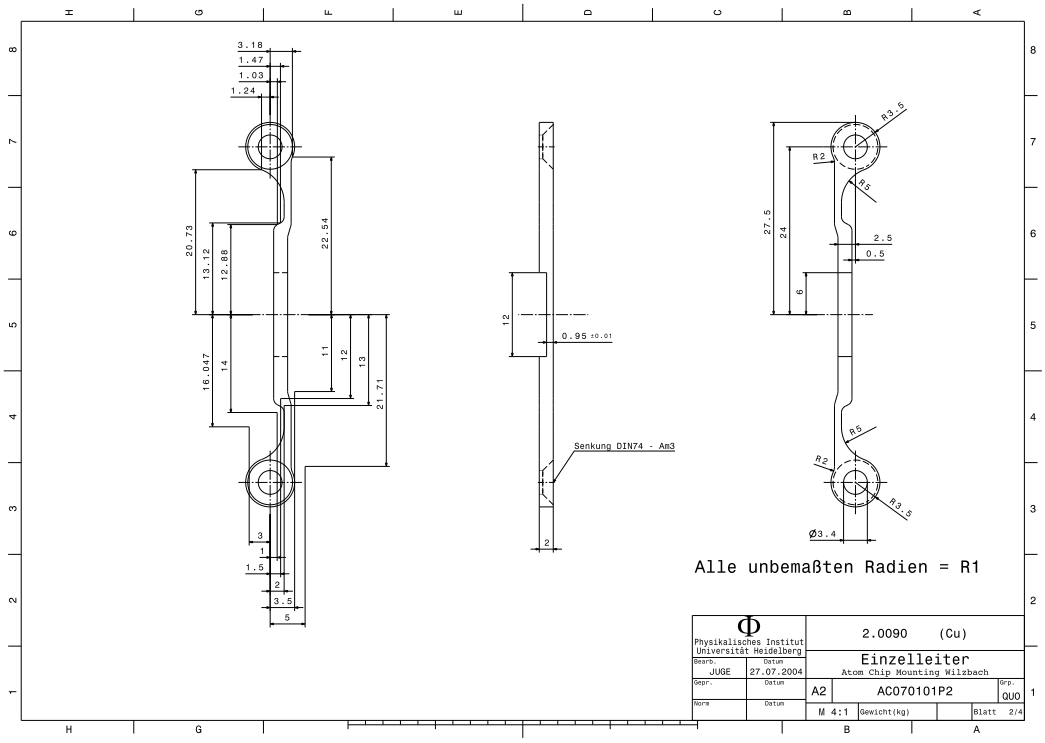

Figure C.3: Copper I-structure beneath the chip. Together with the copper-Z the two I-structures can be used to compress the magnetic Ioffe trap.

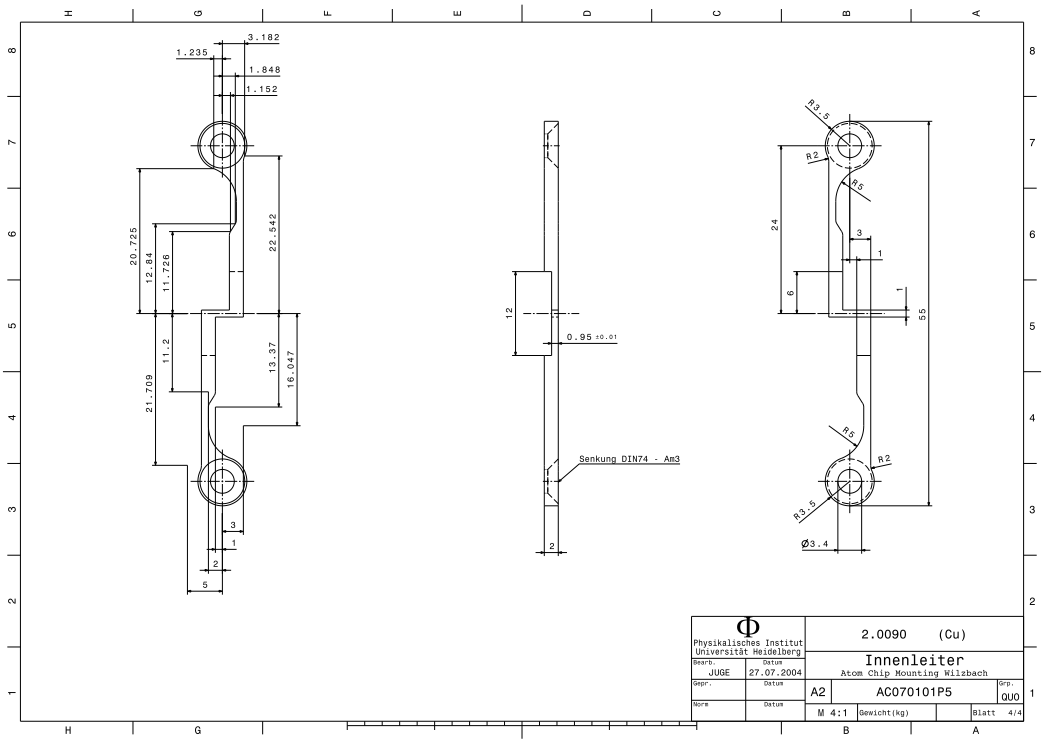

Figure C.4: Copper Z-structure beneath the chip. This structure is usually used for initially (magnetically) trapping the atoms after the MOT phase.

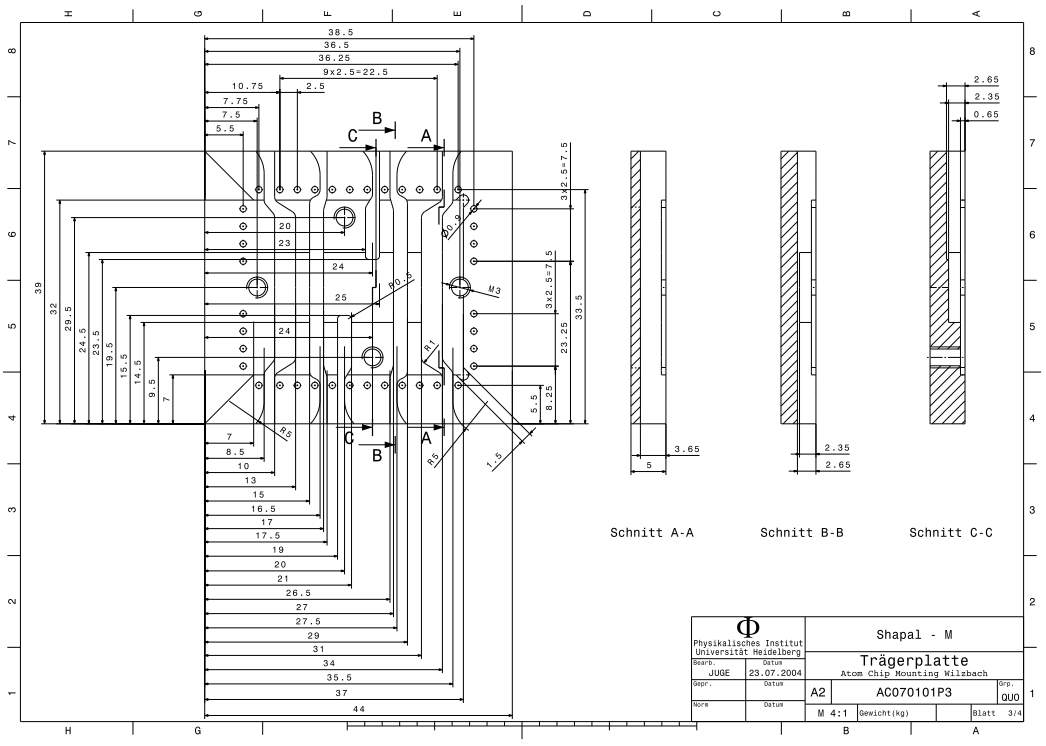

Figure C.5: Shapal carrier plate. This structure holds the copper structures and the atom chip.

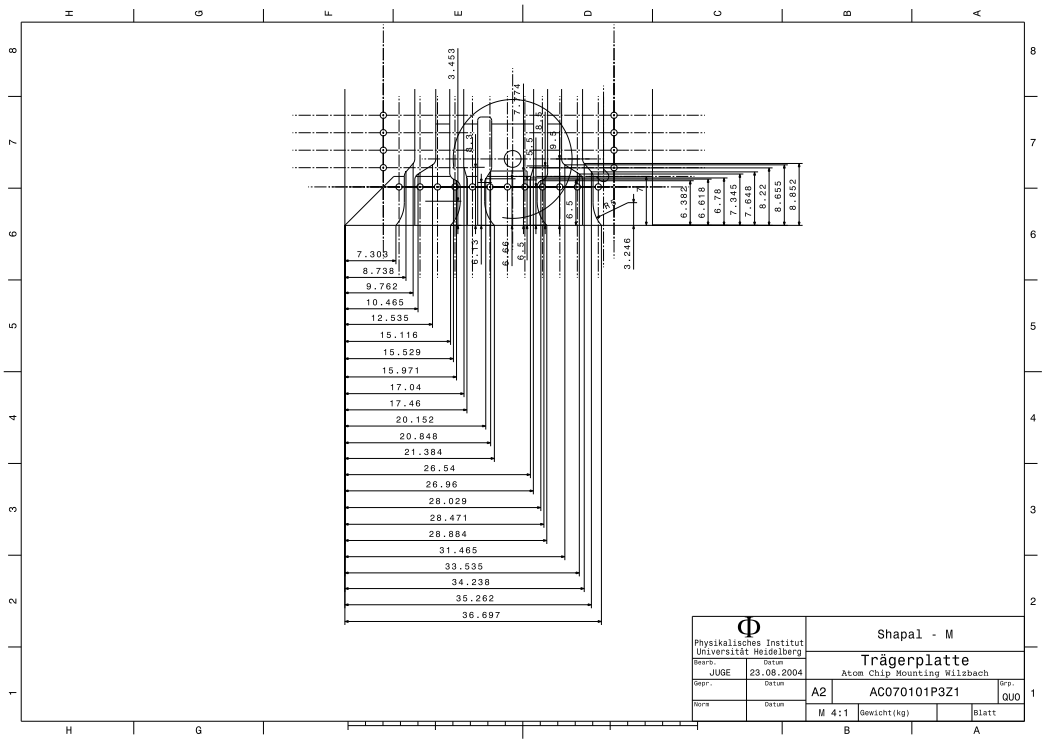

Figure C.6: Shapal carrier plate. This structure holds the copper structures and the atom chip.

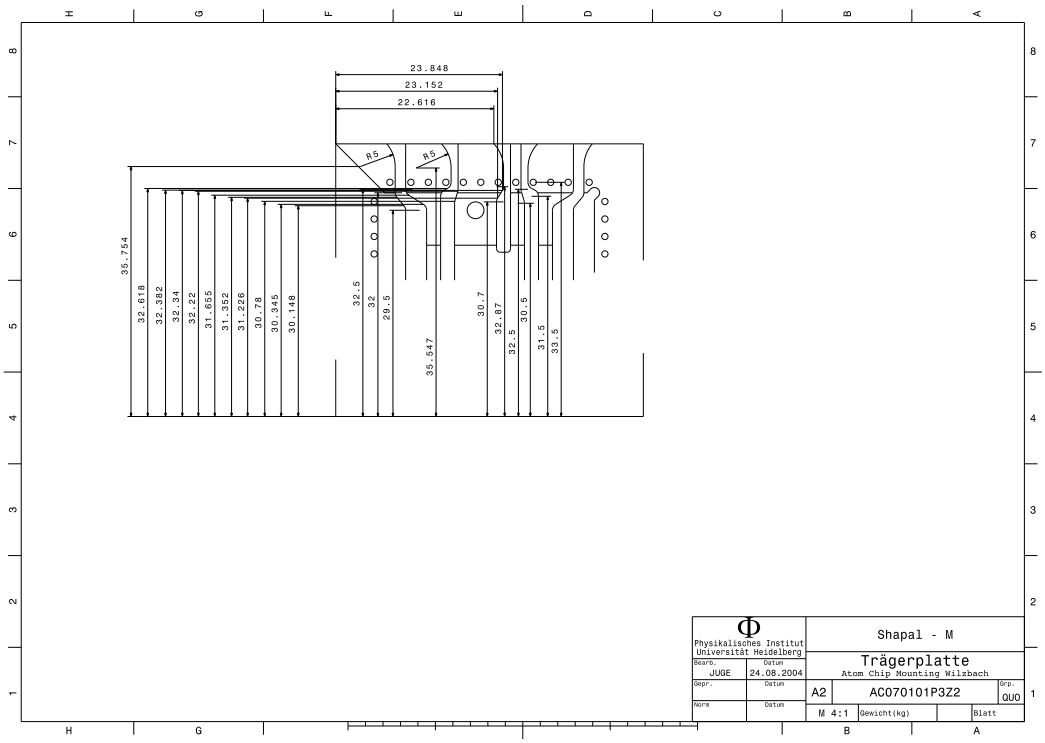

Figure C.7: Shapal carrier plate. This structure holds the copper structures and the atom chip.

D Vacuum Chamber Technical Drawings

Technical drawings of the vacuum chamber. As long as the chamber is in use, it can be useful to have the dimensions for future constructions. Only the drawings for the main chamber and the big window flange are given.

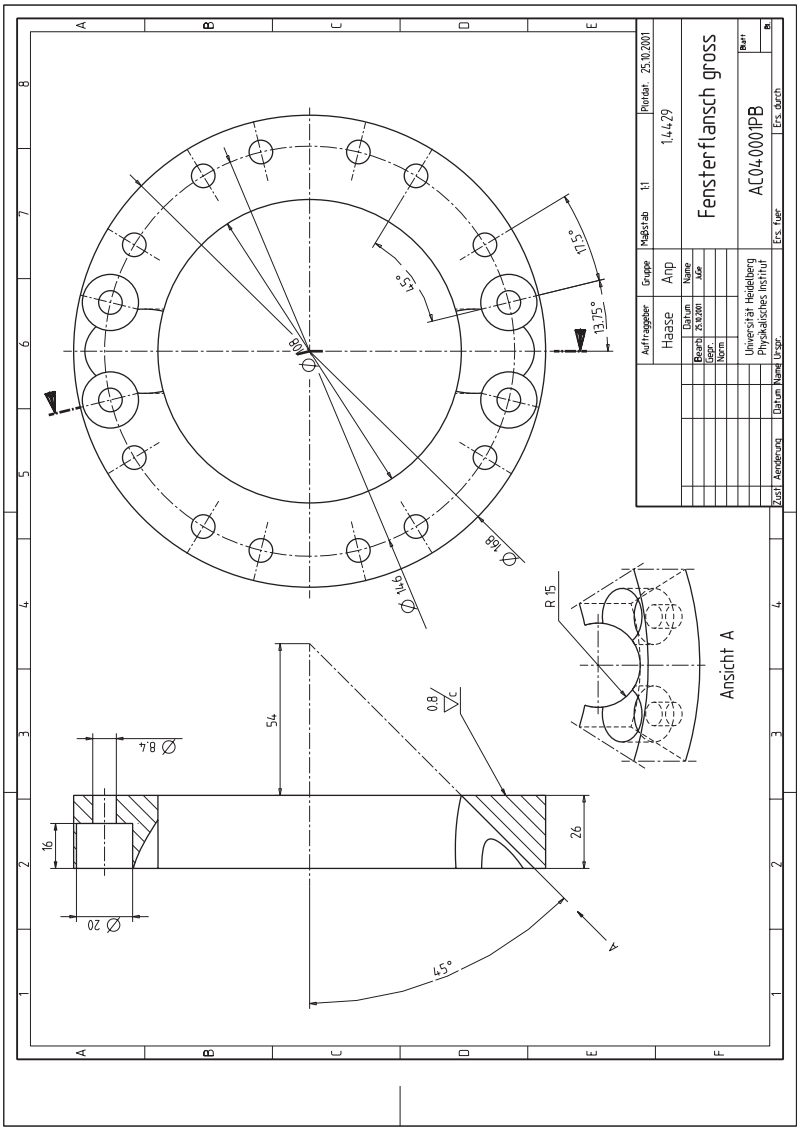

Figure D.1: Technical drawing of the big window.

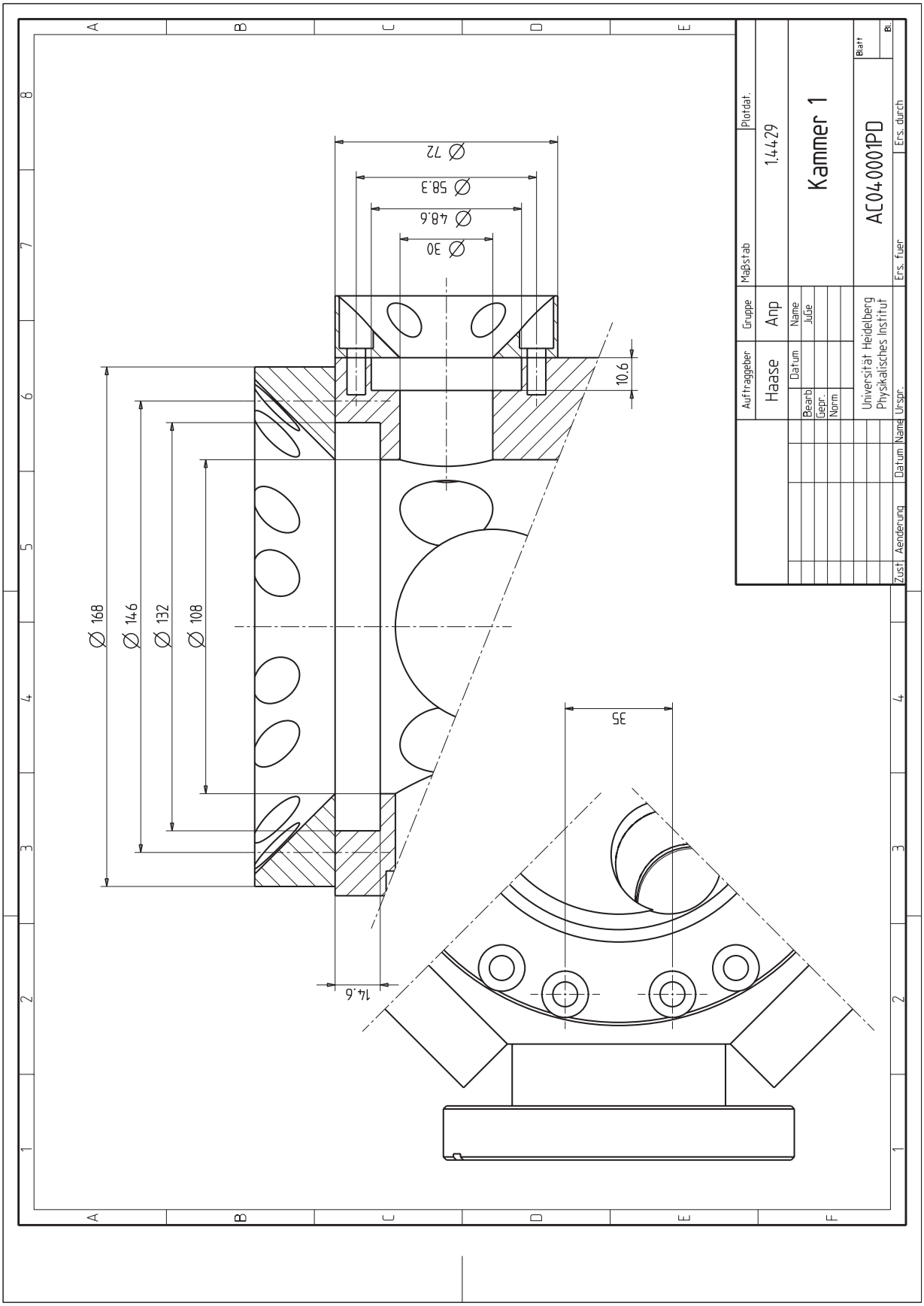

Figure D.2: Technical drawing of the vacuum chamber.

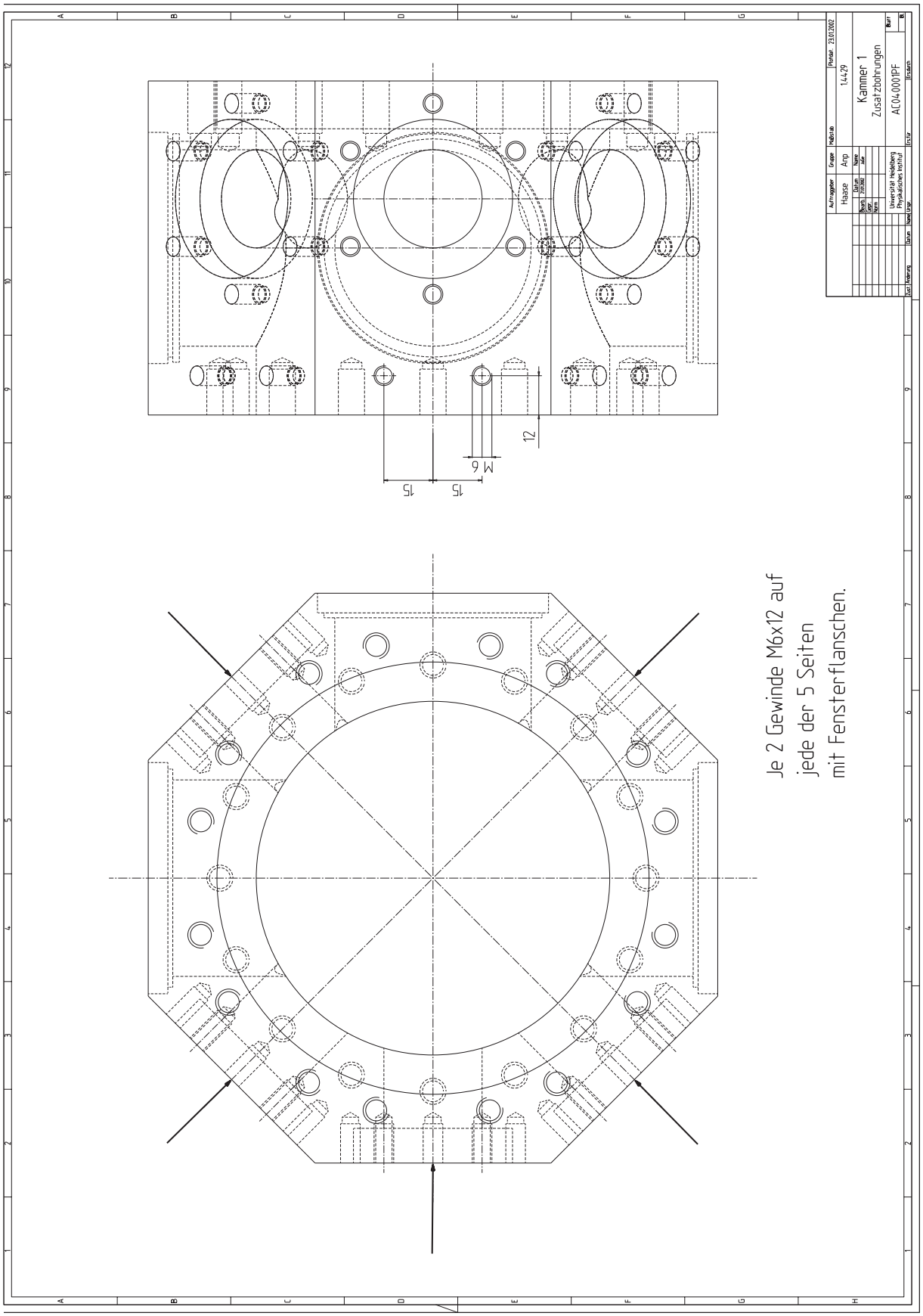

Figure D.3: Technical drawing of the vacuum chamber.

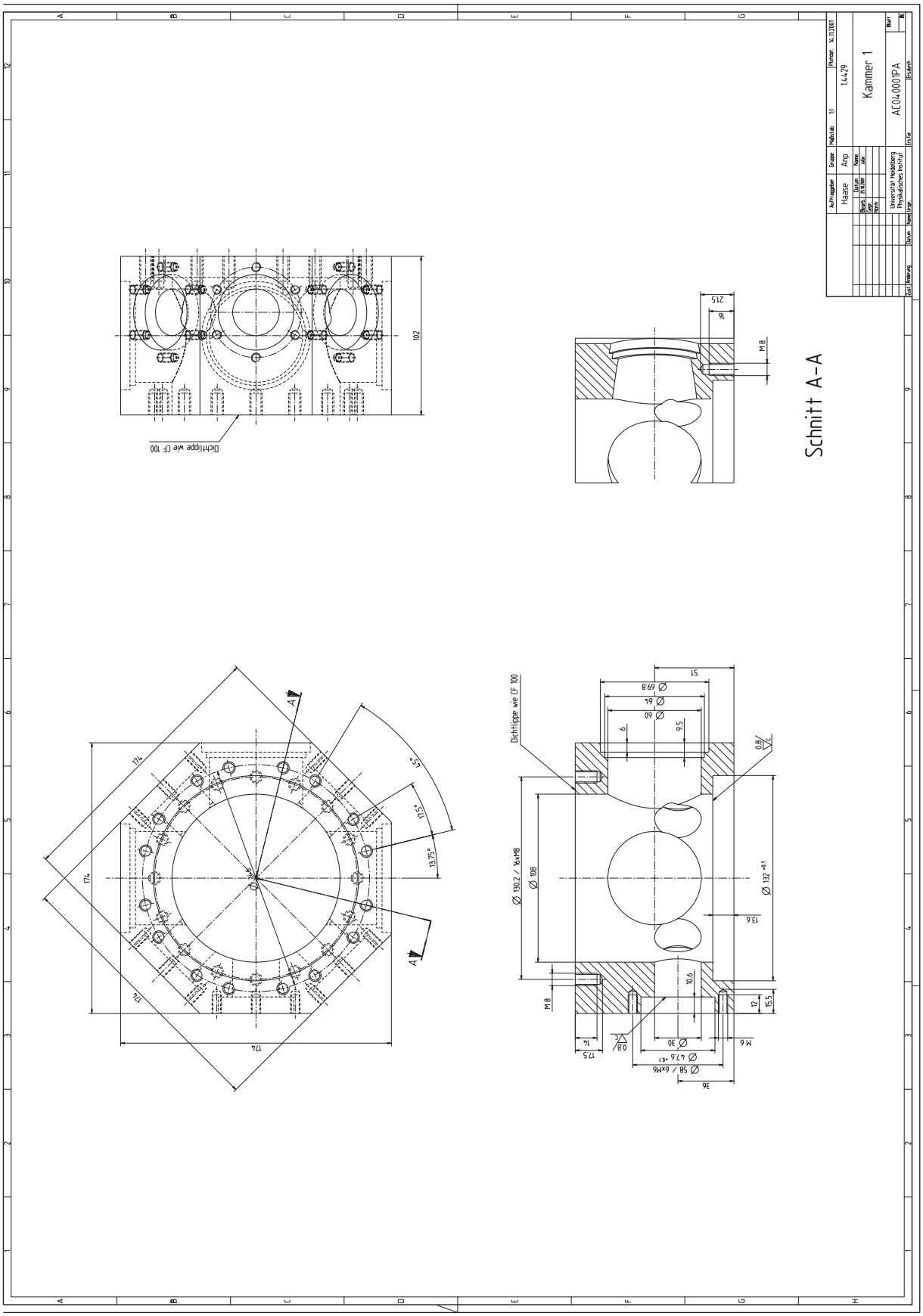

Figure D.4: Technical drawing of the vacuum chamber.

E Acknowledgement

Last but not least some words to thank all the people contributing to the success of this thesis.

- Thank you very much, Jörg, for supervising this thesis and allowing me all the scientific freedom to develop this nice experiment. It was a *cool* experience ;)
- Professor Ullrich I would like to thank for furnishing a second opinion on this thesis. One can not take it for granted, that you willingly took over such a load of extra work - thanks a lot!
- I appreciated the cooperation with the electronics and mechanical workshop, who did more than "just" their job! Special thanks to Mr."Termine nur über meinen Anwalt" Stahl; Mr. Giesser who really can define the word "**Fein**mechaniker" not only with words; to Mr. "frag doch mal den" Rusnyack for developing the best available technology in electronics.
- Thanks to all former PhD candidates of this group for teaching me the basics of the cold atom business. **THE** atom chips were built by Sönke, thanks a lot for the uncountable atom chips you provided!
- Particularly I want to thank Xiyuan Liu and Prof. Brenner of the University of Mannheim for the fruitful cooperation in designing and building all kinds of SU-8 structures and special lenses.
- I also thank all my diploma students for putting so much effort into the experiment. Thanks Christian, Michael and Kai for recycling photons.
- Moreover I thank Björn (Höli) and Dennis (Böli) for all the effort they put into our experiment. Thanks for proof reading my thesis and the tons of suggestions and for the nice time also beyond work.
- Danke, Mama und Papa. Ohne Eure Unterstützung wäre diese Arbeit nicht möglich gewesen.
- Thank you very much Ela for all your support and patience and being the best wife on the world...
- Last but not lest I would like to thank the Studienstiftung des deutschen Volkes not only for their financial support during this thesis.

Bibliography

E. R. I. Abraham and E. A. Cornell.
Teflon feedthrough for coupling optical fibers into ultrahigh vacuum systems.
Appl. Opt., 37:1762–1763, 1998.

M. Anderson, J. Ensher, M. Matthews, C. Wieman, and E. Cornell.
Observation of Bose-Einstein condensation in a dilute atomic vapor.
Science, 269:198, 1995.

M. R. Andrews, M. O. Mewes, N. J. van Druten, D. S. Durfee, D. M. Kurn, and W. Ketterle.
Direct, nondestructive observation of a Bose condensate.
Science, 273:84, 1996.

E. Arimondo, M. Inguscio, and P. Violino.
Experimental determinations of the hyperfine structure in the alkali atoms.
Reviews of Modern Physics, 49:31, 1977.

D. Armani, T. Kippenberg, S. Spillane, and K. Vahala.
Ultra-high-Q toroid microcavity on a chip.
Nature, 421:925, 2003.

V. Bagnato, G. Lafyatis, A. Martin, E. Raab, R. Ahmad-Bitar, and D. Pritchard.
Continuous stopping and trapping of neutral atoms.
Phys. Rev. Lett., 58:2194, 1987.

G. Barwood, P. Gill, and W. Rowley.
Frequency measurements on optically narrowed Rb-stabilised diodes at 780nm and 795nm.
Appl. Phys. B, 53:142, 1991.

C. Becker.
Eine neuartige magneto-optische Falle für Atomchip Experimente.
Master's thesis, Universität Heidelberg, 2002.

T. Bergeman, G. Erez, and H. Metcalf.
Magnetostatic trapping fields for neutral atoms.
Phys. Rev. A, 35:1535, 1987.

P. R. Berman.
Cavity Quantum Electrodynamics.
Academic press, San Diego, 1994.

F. Bertinetto, P. Cordiale, G. Galzerano, and E. Bava.
Frequency Stabalization of DBR Diode Laser Against Cs Absorption Lines at 852 nm Using the Modulation Transfer Method.
IEEE Transactions on Instrumentation and Measurement, 50(2):490–492, 2001.

G. Bjorklund.
Frequency-modulation spectroscopy: a new method for measuring weak absorptions and dispersions.
Optics Letters, 5(1):15–17, 1979.

G. Bjorklund, M. Levensen, W. Lenth, and Ortiz.
Frequency Modulation (FM)Spectroscopy.
Applied Physics B, 32:145–152, 1983.

E. Black.
An introduction to Pound-Drever-Hall laser frequency stabalization.
Amercian Journal of Physics, 69(1):79–87, 2001.

C. Bradley, C. Sackett, J. Tollett, and R. Hulet.
Evidence of Bose-Einstein condensation in an atomic gas with attractive interactions.
Phys. Rev. Lett., 75:1687, 1995.

G. Camy, C. Borde, and M. Ducloy.
Heterodyne saturation spectroscopy trough frequency modulation of the saturating beam.
Optics Communications, 41(5):325–330, 1982.

D. Cassettari, B. Hessmo, R. Folman, T. Maier, and J. Schmiedmayer.
Beam splitter for guided atoms.
Phys. Rev. Lett., 85:5483, 2000.

S. Chu.
The manipulation of neutral particles.
Reviews of Modern Physics, 70:685, 1998.

S. Chu, L. Hollberg, J. E. Bjorkholm, A. Cable, and A. Ashkin.
Three-dimensional viscous confinement and cooling of atoms by resonance radiation pressure.
Physical Review Letters, 55:48–51, 1985.

C. Cohen-Tannoudji.
Manipulating atoms with photons.
Reviews of Modern Physics, 70:707, 1998.

J. Dalibard and C. Cohen-Tannoudji.
Laser cooling below the doppler limit by polarization gradients: simple theoretical models.
Journal of the Optical Society of America B, 6:2023, 1989.

K. Davis, M. Mewes, M. Andrews, N. van Druten, D. Durfree, D. Kurn, and W. Ketterle. Bose-Einstein condensation in a gas of sodium atoms, journal = Phys. Rev. Lett., year = 1995, volume = 75, pages = 3969,.

N. H. Dekker, C. Lee, V. Lorent, J. Thywissen, S. Smith, M.Drndic, R. Westervelt, and M. Prentiss.
Guiding neutal atoms on a chip.
Phys. Rev. Lett., 84:1124, 2000.

J. Denschlag, D. Cassettari, A. Chenet, S. Schneider, and J. Schmiedmayer.
A neutral atom and a wire: towards mesoscopic atom optics.
Appl. Phys.B, 69:291, 1999a.

J. Denschlag, D. Cassettari, and J. Schmiedmayer.
Guiding neutral atoms with a wire.
Physical Review Letters, 82:2014, 1999b.

D. P. DiVincenzo.
The physical implementation of quantum computation.
Fortschritte der Physik, 48:771–783, 2000.

R. W. P. Drever, J. Hall, F. Kowalski, J. Hough, G. Ford, A. Munley, and H. Ward.
Laser phase and frequency stabalization using an optical resonator.
Appl. Phys. B, 31:97, 1983.

M. Ducloy and D. Bloch.
Polarization properties of phase-conjugate mirrors: Angular dependence and disorienting collision effects in resonant backward four-wave mixing for Doppler-broadened degenerate transitions.
Physical Review A, 30(6):3107–3122, 1984.

D. Duffy, O. S. J. McDonald, and G. Whitesides.
Rapid prototyping of microfluidic systems in poly(dimethylsiloxane).
Anal. Chem., 70:4974, 1998.

B. Engeser.
Optische Abbildung einer atomaren Dichteverteilung.
Master's thesis, University of Heidelberg, 2002.

S. Eriksson, M. Trupke, H. F. Powell, D. Sahagun, C. D. J. Sinclair, E. A. Curtis, B. E. Sauer, E. A. Hinds, Z. Moktadir, C. O. Gollasch, and M. Kraft.
Integrated optical components on atom chips.
Eur. Phys. J D, 35:135, 2005.

M. Feld and V. Letokhov.
Laser Spectroscopy.
Scientific American, December 1973.

M. Finn, G. Greenless, T. Hodapp, and D. Lewis.
Real-time elimination of dead-time and afterpulsing in counting systems.
Rev. Sci. Instrum., 59:2457–2459, 1988.

R. Folman, P. Krüger, D. Cassettari, B. Hessmo, T. Maier, and J. Schmiedmayer.
Controlling cold atoms using nanofabricated surfaces: Atom chips.
Phys. Rev. Lett., 84:4749, 2000.

R. Folman, P. Krüger, J. Denschlag, C. Henkel, and J. Schmiedmayer.
Microscopic atom optics: From wires to an atom chip.
Advances in Atomic and Molecular Physics, 48:263, 2002.

J. Fortagh, A. Grossmann, and C. Zimmermann.
Miniaturized wire trap for neutral atoms.
Phys. Rev. Lett., 81:5310, 1998.

Goodfellow.
Datasheet for aluminium nitride.
http://www.goodfellow.com, 2007.

S. Gov, S. Shtrikman, and H. Thomas.
Magnetic trapping of neutral particles: Classical and quantum-mechanical study of a Ioffe-Pritchard type trap.
J. Appl. Phys., 87:3989, 2000.

R. Grimm, M. Weidemüller, and Y. Ovchinnikov.
Optical dipole traps for neutral atoms.
Advances in Atomic, Molecular and Optical Physics, 42:95, 2000.

S. Groth.
Development, Fabrication and Characterisation of Atom Chips.
PhD thesis, University of Heidelberg, 2006.

S. Groth, P. Krüger, S. Wildermuth, R. Folman, T. Fernholz, D. Mahalu, I. Bar-Joseph, and J. Schmiedmayer.
Atom chips: Fabrication and thermal properties.
Applied Physics Letters, 85(14):2980–2982, 2004.

A. Haase.
Single atom detection in low finesse cavities.
PhD thesis, Universität Heidelberg, 2005.

A. Haase, D. Cassettari, B. Hessmo, and J. Schmiedmayer.
Trapping neutral atoms with a wire.
Phys. Rev., page 043305, 2001.

A. Haase, B. Hessmo, and J. Schmiedmayer.
Detecting magnetically guided atoms with an optical cavity.
Opt. Lett., 31:268, 2006.

W. Hänsel, P. Hommelhoff, T. Hänsch, and J. Reichel.
Bose-Einstein condensation on a microelectronic chip.
Nature, 413:498, 2001a.

W. Hänsel, J. Reichel, P. Hommelhoff, and T. W. Hänsch.
Magnetic conveyor belt for transporting and merging trapped atom clouds.
Phys. Rev. Lett., 86:608, 2001b.

E. Hecht.
Optik.
Oldenbourg, Germany., 2005.
ISBN 978-3486273595.

D. Heine.
Integrated optics and atomic physics.
PhD thesis, University of Heidelberg, 2007.

C. Henkel, J. Schmiedmayer, and C. Westbrook, editors.
Special Issue: Atom chips, volume 35, 2005. Eur. Phys. J. D.

L. Hillesheim and D. Müller.
The photon counting histogram in fluorescence fluctuation spectroscopy with non-ideal photodetectors.
Biophysics Journal, 85:1948–1558, 2003.

P. Hommelhoff, W. Hänsel, T. Steinmetz, T. W. Hänsch, and J. Reichel.
Transporting, splitting and merging of atomic ensembles in a chip trap.
New J. Phys., 7:3, 2005.

J. J. Hope and J. D. Close.
Limit to minimally destructive optical detection of atoms.
Phys. Rev. Lett., 93:80402, 2004a.

J. J. Hope and J. D. Close.
General limit to nondestructive optical detection of atoms.
Phys. Rev., A71:043822, 2004b.

P. Horak, B. G. Klappauf, A. Haase, R. Folman, J. Schmiedmayer, P. Domokos, and E. A. Hinds.
Possibillity of single-atom detection on a chip.
Phys. Rev., A67:043806, 2003.

E. Jaatinen.
Theoretical determination of maximum signal levels obtainable with modulation transfer spectroscopy.
Optics Communications, 120:91–97, 1995.

S. Kadlecek, J. Sebby, R. Newell, and T. G. Walker.
Nondestructive spatial heterodyne imaging of cold atoms.
Opt. Lett., 26:137, 2001.

P. Kask, K. Palo, D. Ullmann, and K. Gall.
Fluorescence-intensity distribution analysis and its application in biomolecular detection technology.
Proceedings of the National Academy of Sceinecs of the United States of America, 96 (24):13765–13761, 1999.

W. Ketterle.
When atoms behave as waves: Bose-Einstein-condensation and the atom laser.
Nobel Lecture, December 2001.

M. Key, I. G. Hughes, W. Rooijakkers, B. E. Sauer, E. A. Hinds, D. J. Richardson, and P. G. Kazansky.
Propagation of cold atoms along a miniature magnetic guide.
Phys. Rev. Lett., 84:1371, 2000.

P. Krüger, X. Luo, M. Klein, K. Brugger, A. Haase, S. Wildermuth, S. Groth, I. Bar-Joseph, R. Folman, and J. Schmiedmayer.
Trapping and manipulating neutral atoms with electrostatic fields.
Phys. Rev. Lett., 91:233201, 2003.

K. Lee, J. Kim, H. Noh, and W. Jhe.
Single-beam atom trap in a pyramidal and conical hollow mirror.
Opt. Lett., 21:1177, 1996.

D. Leibfried, M. D. Barrett, T. Schaetz, J. Britton, J. Chiaverini, W. M. Itano, J. D. Jost, C. Langer, and D. J. Wineland.
Toward Heisenberg-limited spectroscopy with multiparticle entangled states.
Science, 304:1476, 2004.

V. Letokhov and V. Chebotayev.
Nonlinear laser spectroscopy.
Springer series in optical sciences. Springer, Berlin, 4. edition, 1977.

P. Lett, W. Phillips, S.Rolston, C. Tanner, R. Watts, and C. Westbrook.
Optical molasses.
Journal of the Optical Society of America B, 6:2084, 1989.

B. Lev, K. Srinivasan, P. Barclay, O. Painter, and H. Mabuchi.
Feasibility of detecting single atoms using photonic bandgap cavities.
Nanotechnology, 15, 2004.

X. Liu, K. H. Brenner, M. Wilzbach, M. Schwarz, T. Fernholz, and J. Schmiedmayer.
Fabrication of alignment structures for a fiber resonator using deep UV-lithography.
Applied Optics, 2005.

R. Long, T. Steinmetz, P. Hommelhoff, W. Hänsel, T. W. Hänsch, and J. Reichel.
Magnetic microchip traps and single atom detection.
Phil. Trans. R. Soc. Lond., 361:1375, 2003.

J. E. Lye, J. J. Hope, and J. D. Close.
Rapid real-time detection of cold atoms with minimal destruction.
Phys. Rev., A69:023601, 2004.

I. B. Mekhov, C. Maschler, and H. Ritsch.
Probing quantum phases of ultracold atoms in optical lattices by transmission spectra in cavity quantum electrodynamics.
Nature Physics, 3:319 – 323, 2007.

Melles Griot.
Reflectance of gold coated mirrors.
www.mellesgriot.com, 2006.

H. Metcalf and P. van der Straten.
Laser Cooling and Trapping.
Springer, New York, Berlin, Heidelberg, 1999.

A. Migdall, J. Prodan, and W. Phillips.
First observation of magnetically trapped neutral atoms.
Phys. Rev. Lett., (54):2596, 1985.

J. D. Miller, R. A. Cline, and D. J. Heinzen.
Far-off-resonance optical trapping of atoms.
Phys. Rev., A47:4567, 1993.

Y. Miroshnyenko, D. Schrader, S. Kuhr, W. Alt, I. Dotsenko, M. Khudaverdyan, A. Rauschenbeutel, and D. Meschede.
Continued imaging of the of a single neutral atom.
Opt. Express, 11:3498, 2003.

D. Müller, D. Anderson, R. Grow, P. Schwindt, and E. Cornell.
Guiding neutal atoms around curves with lithographically patterned current-carrying wires.
Phys. Rev. Lett., 83:5194, 1999.

J. Müller.
Cumulant anaylsis in fluorescence fluctuation spectroscopy.
Biophysics Journal, 86:3981–3992, 2004.

Z. Moktadir, E. Koukharenka, M. Kraft, D. M. Bagnall, H. Powell, M. Jones, and E. A. Hinds.
Etching techniques for realizing optical micro-cavity atom traps on silicon.
J. Micromech. Microeng., 14:82, 2004.

D. Müller, E. A. Cornell, M. Prevedelli, P. D. D. Schwindt, A. Zozulyaand, and D. Z. Anderson.
Waveguide atom beam splitter for laser-cooled neutral atoms.
Opt. Lett., 25:1382, 2000.

National Instruments.
DAQ M Series.
National Instruments, Austin, Texas, USA, 371022g-01 edition, November 2006.

NIST.
Atomic spectra database.
http://physics.nist.gov/PhysRefData, Version 2.0, 2002.

Optische Interferenz Bauelemente GmbH, 2004.
For further details: http://www.oib-jena.de.

H. Ott, J. Fortagh, G. Schlotterbeck, A. Grossmann, and C. Zimmermann.
Bose-Einstein condensation in a surface microtrap.
Phys. Rev. Lett., 87:230401, 2001.

PCO AG.
Pixelfly qe data sheet.
For further details: http://www.pco.de, 2007.

K. Petermann.
Laser diode modulation and noise.
Kluwer Academic Publishers, Dordrecht, The Netherlands, 1988.
ISBN 90-277-2672-8.

W. Phillips.
Laser cooling and trapping of neutroal atoms.
Reviews of Modern Physics, 70:721, 1998.

P. W. H. Pinkse, T. Fischer, P. Maunz, and G. Rempe.
Trapping an atom with single photons.
Nature, 404:365, 2000.

D. Pritchard.
Cooling neutral atoms in a magnetic trap for precision spectroscopy.
Phys. Rev. Lett., 51:1336, 1983.

C. Raab, J. Bolle, H. Oberst, J. Eschner, F. Schmidt-Kaler, and R. Blatt.
Diode laser spectrometer at 493 nm for single trapped Ba+ ions.
Applied Physics B, 67:683–688, 1998.

E. Raab, M. Prentiss, C. A., S. Chu, and D. Pritchard.
Trapping of neutral sodium atoms with radiation pressure.
Physical Review Letters, 59:2631, 1987.

R. Raj, D. Bloch, J. Snider, G. Camy, and M. Ducloy.
High-Frequency Optically Heterodyned Saturation Spectroscopy Via Resonant Degenerate Four-Wave Mixing.
Physical Review Letters, 44(19):1251–1254, 1980.

J. Reichel, W. Hänsel, and T. Hänsch.
Atomic micromanipulation with magnetic surface traps.
Phys. Rev. Lett., 83:3398, 1999.

G. Reymond, N. Schlosser, I. Protsenko, and P. Grangier.
Single-atom manipulations in a microscopic dipole trap.
Phil. Trans. R. Soc. Lond. A, 361:1527, 2003.

L. Ricci, M. Weidemüller, T. Esslinger, A. Hemmerich, C. Zimmermann, V. Vuletic, W. König, and T. Hänsch.
A compact grating-stabilized diode laser system for atomic physics.
Optics Communications, 117:541–549, June 1995.

M. Rosenblit, P. Horak, S. Helsby, and R. Folman.
Single-atom detection using whispering-gallery modes of microdisk resonators.
Phys. Rev., A70:053808, 2004.

M. Saruwatari and K. Nawate.
Semiconductor laser to single-mode fiber coupler.
Appl. Opt., 18:1847, 1979.

A. Schenzle, R. DeVoe, and R. Brewer.
Phase-modulation laser spectroscopy.
Physical Review A, 25(5):2606–2621, 1982.

N. Schlosser, G. Reymond, I. Protsenko, and P. Grangier.
Sub-poissonian loading of single atoms in a microscopic dipole trap.
Nature, 411:1024, 2001.

N. Schlosser, G. Reymond, and P. Grangier.
Collisional blockade in microscopic optical dipole traps.
Phys. Rev. Lett., 89:023005, 2002.

S. Schneider.
Bose Einstein Kondensation in einer magnetischen Z-Falle.
PhD thesis, University of Heidelberg, 2003.

S. Schneider, A. Kasper, C. vom Hagen, M. Bartenstein, B. Engeser, T. Schumm, I. Bar-Joseph, R. Folman, L. Feenstra, and J. Schmiedmayer.
Bose-Einstein condensation in a simple microtrap.
Phys. Rev. A, 89:023612, 2003.

T. Schumm, S. Hofferberth, L. M. Andersson, S. Wildermuth, S. Groth, I. Bar-Joseph, J. Schmiedmayer, and P. Krüger.
Matter-wave interferometry in a double well on an atom chip.
Nature Physics, 1:57, 2005.

J. Schuster.
Stosslawinen in einem Bose-Einstein-Kondensat.
PhD thesis, University of Munich, 2002.

M. Schwarz.
Aufbau eines Glasfaserresonators zur Detektion einzelner atome auf einem Atomchip.
Diplomarbeit, University of Heidelberg, 2004.

V. Seidemann, J. Rabe, M. Feldmann, and S. Büttgenbach.
SU8-micromechanical structures with in situ fabricated movable parts.
Microsyst. Tech., 8:348, 2002.

K. Shimoda.
High-Resolution Laser Spectroscopy.
Topics Applied Physics. Springer, Heidelberg, 1976.

J. H. Shirley.
Modulation transfer processes in optical heterodyne saturation spectroscopy.
Optics Letters, 7(11):537–539, 1982.

A. E. Siegman.
Lasers.
University Science Books, Mill Valley, 1986.

D. Steck.
Rubidium 87 d line data.
http://steck.us/alkalidata, 2001.

O. Stern.
Ein Weg zur experiemtellen Prüfung der Richtungsquantelung im Magnetfeld.
Zeits.Phys., 7:249, 1921.

O. Stern and W. Gerlach.
Der experimentelle Nachweis der Richtungsquantelung.
Zeitschrift für Physik, 9:349, 1922.

C. Sukumar and D. Brink.
Spin-flip transitions in a magnetic trap.
Phys. Rev. A, 56:2451, 1997.

J. Supplee, E. Whittaker, and W. Lenth.
Theoretical description of frequency modulation and wavelength modulation spectroscopy.
Applied Optics, 33(27):6294–6303, 1994.

L. D. Turner, K. P. Weber, D. Paganin, and R. E. Scholten.
Off-resonant defocus-contrast imaging of cold atoms.
Opt. Lett., 29:232, 2004.

S. J. van Enk.
Atoms, dipole waves, and strongly focused light beams.
Phys. Rev. A, 69:043813, 2004.

S. J. van Enk and H. J. Kimble.
Single atom in free space as a quantum aperture.
Phys. Rev. A, 61:051802, 2000.

S. J. van Enk and H. J. Kimble.
Strongly focused light beams interacting with single atoms in free space.
Phys. Rev. A, 63:023809, 2001.

U. Volz and H. Schmoranzer.
Precision lifetime measurement on alkali atoms and on helium by beam-gas-laser spectroscopy.
Physica Scripta, 48:65, 1996.

K. Wicker.
Micro Cavities for Cavity QED.
Diplomarbeit, University of Heidelberg, 2006.

C. Wieman and E. Cornell.
Nobel lecture: Bose-einstein condensation in a dilute gas, the first 70 years and some recent experiments.
Reviews of Modern Physics, 74:875, 2002.

C. Wieman, D. Prichard, and D. Wineland.
Atom cooling, trapping, and quantum manipulation.
Rev. Mod. Phys., 71:253, 1999.

C. E. Wieman.
Using diode lasers for atomic optics.
Review of Scientific Instruments, 62(1):1–20, 1991.

S. Wildermuth, P. Krueger, C. Becker, M. Brajdic, S. Haupt, A. Kasper, R. Folman, and J. Schmiedmayer.
Optimized magneto-optical trap for experiments with ultracold atoms near surfaces.
Phys. Rev. A., 69:030901, 2004.

M. Wilzbach.
Aufbau eines Experiments zur minaturisierten und integrierten Detektion neutraler Atome.
Master's thesis, University of Heidelberg, 2002.

M. Wilzbach, P. Domokos, T. Fernholz, R. Folman, S. Groth, A. Haase, C. Hock, P. Horak, B. Klappauf, M. Schwarz, and J. Schmiedmayer.
Integration of light and atom optics on an atom chip.
AIP Conf. Proc., 709:443, 2004.

M. Wilzbach, A. Haase, M. Schwarz, D. Heine, K. Wicker, X. Liu, K.-H. Brenner, S. Groth, T. Fernholz, B. Hessmo, and J. Schmiedmayer.
Detecting neutral atoms on an atom chip.
Fortschr. Phys., 54:746 – 764, 2006.

D. Wineland and W. Itano.
Laser cooling of atoms.
Physical Review Letters A, 20:1521, 1979.

www.hamamatsu.com.
Frequently asked questions.
Internet, 2007.